NASA CR-120842
MRC-SL-345

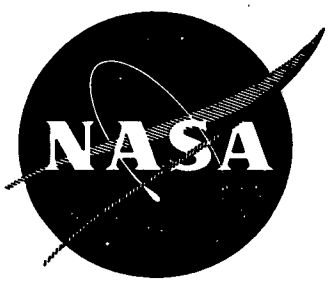

OPTICAL INTERFEROMETRY STUDY OF FILM FORMATION IN LUBRICATION OF SLIDING AND/OR ROLLING CONTACTS

by

E.O. Stejskal and A. Cameron
MONSANTO RESEARCH CORPORATION

prepared for

NATIONAL AERONAUTICS AND SPACE ADMINSTRATION

NASA Lewis Research Center
Contract NAS3-12418

FOREWORD

The research described herein, which was conducted under NASA contract NAS3-12418, was conducted by Monsanto Research Corporation partly in the Monsanto Company Research Center in St. Louis, Missouri and partly in the Lubrication Laboratory of the Department of Mechanical Engineering, Imperial College, London, England. The work done in St. Louis, which consisted largely of the procurement, synthesis, and characterization of the test fluids, was supervised by Dr. Frank S. Clark. The work done in London, under the supervision of Dr. A. Cameron, Director of the Lubrication Laboratory, is made up of the research of Mr. C. R. Gentle, film thickness and traction in point contacts, Mr. D. Wymer, film thickness in line contacts, Mr. G. Paul, refractive index in point contacts, and Mr. R. S. Day, soft film studies. This project was managed by the NASA Project Manager, Mr. W. R. Loomis, Fluid System Components Division, NASA-Lewis Research Center.

The glass transition/crystalline freezing data were obtained from Mobil Research and Development Corporation and are the work of Dr. L. W. Manley and Dr. J. F. Gyer. Discussions with Dr. Welford of the Applied Optics Section, Physics Department, Imperial College were most helpful.

TABLE OF CONTENTS

TABLE OF CONTENTS (Continued)

TABLE OF CONTENTS (Continued)

TABLE OF CONTENTS (Continued)

TABLE OF CONTENTS (Continued)

LIST OF ILLUSTRATIONS

LIST OF ILLUSTRATIONS (continued)

LIST OF ILLUSTRATIONS (continued)

LIST OF ILLUSTRATIONS (continued)

LIST OF ILLUSTRATIONS (continued)

LIST OF ILLUSTRATIONS (continued)

LIST OF ILLUSTRATIONS (concluded)

LIST OF TABLES

ABSTRACT

Seventeen fluids of widely varying physical properties and molecular structure were chosen for study. Film thickness and traction were measured simultaneously in point contacts by interferometry, from which a new theory of traction was proposed. Film thickness was measured in line contacts by interferometry and electrical capacitance to establish correlation between these two methods. An interferometric method for the absolute determination of refractive index in the contact zone was developed and applied to point contact fluid entrapments. Electrical capacitance was used to study the thickness and properties of the soft surface film which sometimes forms near a metal-fluid interface.

SUMMARY

The principal purpose of this work has been to extend the use of optical interference patterns developed in the Hertzian region between lubricated bearing surfaces to determine fluid film thickness and bearing surface contours to temperatures, loads, speeds, atmospheres, etc. comparable to those found in practical devices, especially aircraft engines. Additionally, for the better understanding of the experimental method as well as the properties of the fluid films produced, several collateral experiments have been done: Traction has been measured simultaneously with film thickness in point contacts. Film thickness in line contacts has been measured simultaneously by optical interference and by electrical capacitance. An interferometric method for the absolute determination of refractive index of the fluid in the contact zone has been developed. The existence and properties of the soft surface film which sometimes forms near a metal-fluid interface has also been investigated. For the purpose of this work, a variety of pure fluids of widely varying physical properties and molecular structure were assembled. The most significant findings of this work are summarized below.

A new approach to traction has been developed based on the concept that the fluid turns into either a glass or a solid in the Hertzian zone. The properties of the fluid in the middle of the contact (where traction is determined) bear almost no relation to the properties in the inlet zone (where film thickness is determined). The importance of the pressure-viscosity coefficient to traction is thus questioned.

Line contact has been brought into the realm of optical elastohydrodynamics (EHD) and behaves as expected. Use of a silica layer deposited over the semi-transparent metal surface required for optical EHD film thickness measurements has permitted electrical capacitance measurements of film thickness to be made simultaneously on rough surfaces, a measurement never before achieved. The asperity contact which is detected apparently occurs just outside the Hertzian region. Within the Herztian region, the asperities are flattened sufficiently to prevent contact and permit good optical EHD pictures.

Using a new interferometric technique, the fluid refractive index in a point contact entrapment has been studied. Analysis of the fluid behavior eventually has led to fluid viscosities estimated as much as three orders of magnitude higher than ever before reported, all with one drop of fluid.

The soft film studies have resulted in definitive evidence for the existence of soft films $\sim$100 nm thick and also evidence for fluid viscosity increase near solid surfaces.

1. INTRODUCTION

For many years there has been speculation on the state of lubrication between heavily loaded counterformal contacts such as are found in gears, rolling bearings, cams, tappetts, etc. The theory available up to 1949 indicated that no appreciable oil film would exist. In 1949, Ertel and Grubin,[1] employing a masterly simplification, showed that an oil film could in fact be formed between the surfaces. The full solution, confirming this approximate method for line contacts, was subsequently given by Dowson and Higginson[2] in 1960. A large surge of interest was generated and much work was done on the investigation of such elastohydrodynamic (EHD) films. In 1961, Crook[3] measured the film thickness between rolling contacts by electrical capacity and Sibley and Orcutt[4] did the same by means of an x-ray method. The theory and practice of line contacts were found to agree very well.

Point contacts were a different story. The theory was (and is) extremely involved and neither x-rays nor capacitance were really very adequately suited to the measurement of film thickness, though they were in fact used. However, in 1966 Cameron and Gohar[5] published a paper showing how optical interferometry could be used for the precise measurement of the film thickness between a ball and a plane. Their method was considerably improved by Foord, Hammann, and Cameron,[6] working both in the Lubrication Laboratory at Imperial College, London and at Monsanto Company in St. Louis. This work has been continued at the Imperial College by other workers.[7-8]

The work to be described in this report is concerned primarily with a detailed study of the formation of an oil film between a sphere and a plane, under conditions approaching those found in real bearings. The work has been aimed at understanding rolling elements both from the mechanical point of view and with an eye to understanding the role played by the fluid. It was decided to study a series of fluids of widely differing chemical structures and physical properties in order to examine the validity of the various theories of non-Newtonian and relaxational behavior of fluids which have been proposed to occur in the contact region.

Fortunately, it was also decided to include a study of traction in the project. The traction study has led to some useful findings and a completely new theory of traction based on the formation of a granular phase in the fluid. The reasons for including traction were twofold. First, in fast running bearings, skidding is a major cause of failure and hence the influence of

traction is important. Secondly, traction drives are increasingly being used to replace toothed gearing and fluid coupling in many applications.

While point contact and traction were the main targets of the project, other areas were considered. The correlation between various methods of film thickness measurement were to be studied with a line contact machine. This was in fact achieved and is the first such correlation so far published.

Further, an optical method was devised to measure the refractive index in an EHD contact. By its success this has made film thickness measurements by interferometry into an absolute method. All the other techniques at present available require a knowledge of some property---dielectric constant or x-ray absorbence---in the pressure zone. The interferometer method can now give absolute results.

This study has led on---since the termination of the contract---to the development of an absolute high pressure viscometer running to 10^7 poise and 11 x 10^8 N/m^2 (160,000 psi).

A further part of the work was designed to investigate the very contentious question of a change in viscosity near the metal surface.

This work may be said to be the first study of oil film formation and of lubricated traction at medium pressures, 7 x 10^8 N/m^2 (100,000 psi), with a wide range of molecular shapes as lubricants that has ever been attempted.

Part of the contract was to supply a test rig (point contact) to NASA similar to the principal rig developed for this project and capable of running to extreme conditions. A special support for the ball allowed high temperatures [up to 316°C,] (600°F) to be attained and a sapphire disk permitted high loads [up to 10^9 N/m^2 maximum Hertz and higher (150,000 psi)]. The disk was so arranged that various atmospheres could blanket the contact. A brake was used to enable traction to be applied and measured.

This project, which was undertaken by Monsanto Research Corporation, was carried out partly in the Monsanto Company Research Center in St. Louis and partly in the Lubrication Laboratory of the Imperial College in London, under a subcontract to Monsanto Research Corporation.

2. TEST FLUIDS

The seventeen fluids selected for study are listed in Table 1. Listed also are the code letters (a through q) by which they will be identified throughout the remainder of this report whenever it is more convenient to omit their names.

These fluids were selected to provide a wide variety of physical properties and molecular structures in different combinations. It is evident from this list that the molecular structures differ greatly; the tabulations of physical properties given later show the variation of physical properties.

2.1 PROCUREMENT

The test fluids were obtained from a variety of sources.

Two of the fluids were synthesized for the project (see Section 2.2):

fluid i., di(2-ethylhexyl)-3,3,4,4-tetramethyladipate, and
fluid o., 1,1,7-trihydroperfluoroheptylperfluoroglutarate.

Seven of the fluids were supplied by Monsanto Company from supplies on hand:

fluid a., pentaerythritoltetravalerate,
fluid f., cyclododecylcyclododecane,
fluid g., dihydrocedrene,
fluid h., di(2-ethylhexyl)adipate,
fluid k., 1,4-bicyclohexylbutane,
fluid m., 2-ethylhexyldiphenylphosphate, and
fluid n., 3,3'dichlorodiphenylether.

Four fluids purchased from Eastman Chemical Company:

fluid c., squalane,
fluid d., octacosane,
fluid j., bicyclohexyl, and
fluid l., oleic acid.

The remaining four fluids were purchased from other commercial sources :

Table 1

THE SEVENTEEN TEST FLUIDS

fluid a.	pentaerythritoltetravalerate
fluid b.	polyethyleneglycol
fluid c.	squalane
fluid d.	octacosane
fluid e.	polychlorotrifluoroethylene oil
fluid f.	cyclododecylcyclododecane
fluid g.	dihydrocedrene
fluid h.	di(2-ethylhexyl)adipate
fluid i.	di(2-ethylhexyl)3,3,4,4 tetramethyladipate
fluid j.	bicyclohexyl
fluid k.	1,4-bicyclohexylbutane
fluid l.	oleic acid
fluid m.	2-ethylhexyldiphenylphosphate
fluid n.	3,3'-dichlorodiphenylether
fluid o.	1,1,7-trihydroperfluoroheptylperfluoroglutarate
fluid p.	dimethylsilicone (100 cS)
fluid q.	dimethylsilicone (1000 cS)

fluid b., polyethylene glycol,
from Union Carbide Company as UCON-LB165,
fluid e., polychlorotrifluoroethylene oil,
from 3M Company as KEL-F775, and
fluid p., dimethylsilicone (100 cs), and
fluid q., dimethylsilicone (1000 cs),
from Dow-Corning Corporation.

The purity of these fluids was such that further purification was not necessary except for the removal of trace surface active impurities and dissolved gases immediately prior to study. Where such last-minute purification was required, it is described in detail, in the sections to follow.

2.2 SYNTHESIS

2.2.1 Synthesis of 1,1,7-Trihydroperfluoroheptylperfluoroglutarate

We prepared this compound by a standard esterification of perfluoroglutaric acid with 1,1,7-trihydroperfluoroheptanol.

$$HO_2C\text{-}(CF_2)_3CO_2H + 2\ CF_2H\text{-}(CF_2)_5\text{-}CH_2OH \xrightarrow{\text{acid}}$$

perfluoro-glutaric acid

1,1,7-trihydroper-fluoroheptanol

$$CF_2H(CF_2)_5\text{-}CH_2\text{-}O\text{-}\overset{O}{\overset{\|}{C}}\text{-}(CF_2)_3\text{-}\overset{O}{\overset{\|}{C}}\text{-}O\text{-}CH_2(CF_2)_5\text{-}CF_2H + 2H_2O$$

1,1,7-trihydroperfluoroheptylperfluoroglutarate

Experimental:

Perfluoroglutaric acid (50 g, 0.21 mole, Pierce Chemical Co.), freshly distilled alcohol (146 g, 0.44 mole, Du Pont), xylene (220 ml) and p-toluenesulfonic acid catalyst (1 g) were charged to a round-bottomed flask joined to a Dean-Stark trap. The reaction produced 7 ml of water, 95% of the expected amount. After three aqueous washes, distillation through a Todd column gave 113 g of product (b p 145°/0.2); this is a 62% conversion based on the acid.

The analyses of the main cut were as follows:

C-H Analysis	% C	% H
found	25.92, 26.09	0.74, 0.68
theory	26.28	0.70

Gas-Liquid Chromatography (GLC)

99.9+% pure (single peak) when run in methyl acetate solvent

Nuclear Magnetic Resonance (NMR)

spectrum consistent with the ester structure
no acid or alcohol protons present
ratio of methylene protons to terminal protons (by integrated areas) 1.9:1 - theory 2:1 - agreement satisfactory

2.2.2 Synthesis of di(2-ethylhexyl)-3,3,4,4-tetramethyladipate

We prepared this ester in two steps starting with commercially available 3,3-dimethylacrylic acid. The first step was esterification of this acid with 2-ethylhexanol in the presence of trifluoroacetic anhydride.[10,11]

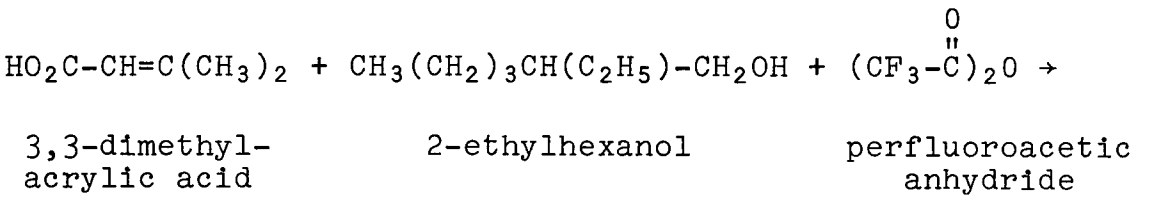

3,3-dimethylacrylic acid — 2-ethylhexanol — perfluoroacetic anhydride

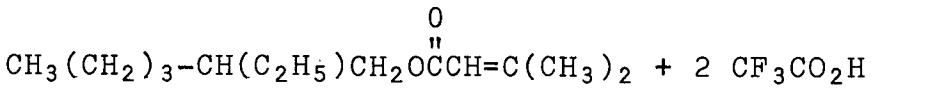

2-ethylhexyl-3,3-dimethylacrylate — perfluoroacetic acid

The second step was electrohydrodimerization of the above acrylate to di(2-ethylhexyl)-3,3,4,4,-tetramethyladipate:

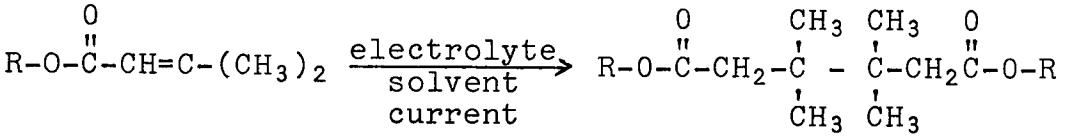

(R = 2-ethylhexyl)

The scope, apparatus, and procedure for this reaction are described in the literature.[12,13]

Experimental:

Step 1: Preparation of 2-ethylhexyl-3,3-dimethylacrylate

2-Ethylhexanol (136.5 g, 1.05 mole) was added dropwise under nitrogen to a solution of 3,3-dimethylacrylic acid (105.0 g, 1.05 mole) in 331.3 g of trifluoroacetic anhydride. The temperature was kept below 45° with an ice bath. Then 1260 ml of 10% sodium hydroxide was added dropwise. After twenty minutes, the organic layer was combined with a chloroform extract of the aqueous layer, washed twice with 300 ml of water, dried and distilled. This gave a typical yield of 170 g (76%) of acrylate (b.p. 88°/1.0).

	% C	% H
Found	73.6, 73.3	11.5, 11.3
Theory	73.5	11.3

Step 2: Synthesis of di(2-ethylhexyl)-3,3,4,4,-tetramethyladipate

The following reagents were charged to the electrolysis cell:

2-ethylhexyl-3,3-dimethylacrylate	40 g.
dimethylformamide	120 ml.
tetraethylammonium tosylate	30 g.
water	5 ml.

One amp was passed through the cell for 2-3/4 hours at 30-35° and a pH ∿8. Two layers formed even with an addition of another 10 ml of dimethylformamide. Normal work-up and distillation gave 7 g (17% conversion) of 97% pure di(2-ethylhexyl)-3,3,4,4-tetramethyladipate (b.p. 213-4°/0.2). A forecut of unreacted acrylate and 2-ethylhexyl-3-methylbutyrate accounted for 70% of the starting ester. Redistillation raised the purity of the adipate to >99%.

	% C	% H
Found	73.1	11.8
Theory	73.5	11.4

The mass spec of this adipate showed no parent ion; ions indicative of the proposed structure included:

m/e		
	297	(loss of one alcohol group by alpha cleavage at the carbonyl)
	213	half-dimer
	185	McLafferty rearrangement and loss of octyl from m/e 297
	167	loss of octyl alcohol from m/e 297

2.3 PHYSICAL PROPERTIES

In the analysis and interpretation of the several kinds of film thickness and traction data which are the object of the remainder of this report, certain physical properties of the test fluids are of use. Some of these properties have been obtained and are tabulated below.

In Table 2, density and kinematic viscosity as a function of temperature are given for each of the seventeen fluids. Density was determined by weighing a known volume of fluid; kinematic viscosity was measured by means of conventional Ostwald - type viscometers. Table 3 lists the specific heat and thermal conductivity of some of the test fluids also as a function of temperature. The specific heat was measured with a differential scanning calorimeter. This is a relative method using a standard sapphire specimen for comparison. The thermal conductivity was measured by the transient hot-wire method. Table 4 gives the bulk modulus as a function of temperature for some of the test fluids. These are the isothermal secant values. The pressurization was to $0.480 \times 10^8 N/m^2$ (7000 psi) in each case.

Furthermore, because of the possibility of glass formation in the Hertzian region, the low temperature calorimetric behavior of the test fluids is also of interest, especially when glass transitions occur. The NASA Project Manager was able to obtain these data from the Mobil Research and Development Corporation. The results of that measurement are summarized as follows. A differential scanning calorimeter was used to obtain both heating and cooling curves between -140°C and room temperature (or above if necessary). Based on these curves, the fluids were divided into three categories:

Table 2

DENSITY AND KINEMATIC VISCOSITY OF THE TEST FLUIDS

Fluid	Density (g/cm^3)				Kinematic Viscosity (cs)			
	Ambient, °C	37.8°C (100°F)	98.9°C (210°F)	148.9°C (300°F)	Ambient, °C	37.8°C (100°F)	98.9°C (210°F)	148.9°C (300°F)
pentaerythritoltetra-valerate	1.0146-25.6	0.997	0.953	0.911	26.98-25.6	16.71	3.61	1.75
polyethyleneglycol	0.9813-23.9	0.966	0.917	0.882	61.62-25.0	35.60	6.84	3.16
squalane	0.8075-26.1	0.794	0.758		32.55-25.6	20.30	4.18	
octacosane			0.755	0.723			3.82	2.02
polychlorotrifluoro-ethylene oil	1.950-25.0	1.915	1.829	1.753	266.1-25.0	96.95	6.02	2.00
cyclododecylcyclo-dodecane	0.936-25.0	0.9191	0.8837	0.8526	1515.6-25.0	379.2	12.17	3.58
dihydrocedrene	0.9224-24.4	0.909	0.868		6.76-26.1	5.03	1.73	
di(2 ethylhexyl)-adipate	0.9217-25.6	0.905	0.865		12.18-25.6	8.22	2.38	
di(2 ethylhexyl)-3,3, 4,4-tetramethyl-adipate	0.951-25.6	0.9187	0.8754		39.75-25.0	22.35	4.26	
bicyclohexyl	0.8834-25.0	0.872	0.830		3.96-26.1	3.06	1.22	
1,4-bicyclohexylbutane	0.878-25.6	0.860	0.815		11.08-25.6	7.43	2.21	
oleic acid	0.8853-24.4	0.878	0.836	0.802	32.48-24.4	20.06	4.80	2.23
2-ethylhexyldiphenyl-phosphate	1.0866-25.0	1.071	1.024		16.27-25.6	10.01	2.42	
3,3'-dichlorodiphenyl-ether	1.2813-25.0	1.272	1.213		6.07-24.4	3.68	1.29	
1,1,7-trihydroper-fluoroheptylper-fluoroglutarate	1.8024-24.4	1.763	1.664		32.83-25.6	18.22	2.94	
dimethylsilicone (100 cs)	0.967-24.4	0.947	0.896	0.856	101.0-25.6	80.11	32.45	18.10
dimethylsilicone (1000 cs)	0.9723-24.4	0.954	0.904	0.867	1028.5-25.6	810.9	323.3	178.5

Table 3

THERMAL CONDUCTIVITY AND SPECIFIC HEAT OF THE TEST FLUIDS

Fluid	Thermal Conductivity (cal/°C/cm/sec) x 10^5			Specific Heat (cal/°C/g)		
	37.8°C (100°F)	98.9°C (210°F)	148.9°C (300°F)	37.8°C (100°F)	98.9°C (210°F)	148.9°C (300°F)
pentaerythritoltetravalerate	34.58	31.85		0.403	0.496	0.561
polyethyleneglycol	34.22	32.94		0.482	0.513	0.526
squalane	32.13	30.04		0.512	0.572	
octacosane		37.49	34.84		0.717	0.723
polychlorotrifluoroethylene oil	16.84	15.98		0.235	0.281	
cyclododecylcyclododecane	26.58	25.56		0.499	0.504	0.583
dihydrocedrene	22.51	21.51		0.530	0.535	
di(2-ethylhexyl) adipate	33.50	31.55		0.538	0.568	
di(2-ethylhexyl)-3,3,4,4-tetra-methyladipate	30.72	28.97		0.442	0.523	
bicyclohexyl	27.05	25.08		0.467	0.513	
1,4-bicyclohexylbutane	28.38	26.77		0.440	0.517	
oleic acid	38.78	35.98		0.494	0.508	0.648
2-ethylhexyldiphenylphosphate	30.72	28.54		0.365	0.424	
3,3'-dichlorodiphenylether	27.70	26.66		0.308	0.419	
1,1,7-trihydroperfluoroheptylper-fluoro glutarate	21.92	20.44		0.294	0.325	
dimethylsilicone (100 cs)	37.22	34.73		0.398	0.419	0.443
dimethylsilicone (1000 cs)	38.28	35.94		0.382	0.420	0.435

Table 4

BULK MODULUS B, $N/m^2 \times 10^{+8}$ (psi $\times 10^{+3}$), FOR THE TEST FLUIDS

pentaerythritoltetravalerate

B	T
20.6 (298)	22.8°C (73°F)
18.8 (273)	51.7°C (125°F)
15.8 (229)	93.3°C (200°F)
14.6 (211)	118.3°C (245°F)

polyethylene glycol

B	T
19.0 (275)	22.8°C (73°F)
17.1 (248)	47.8°C (118°F)
16.0 (232)	66.7°C (152°F)
14.3 (208)	97.2°C (207°F)
12.8 (186)	125.6°C (258°F)

squalane

B	T
17.1 (248)	22.8°C (73°F)
15.9 (230)	51.7°C (125°F)
14.1 (204)	93.3°C (200°F)
11.5 (167)	135°C (275°F)

polychlorotrifluoro-ethylene oil

B	T
19.8 (287)	22.8°C (73°F)
16.9 (245)	62.8°C (145°F)
14.0 (203)	104.4°C (220°F)
13.0 (189)	121.1°C (250°F)
11.9 (172)	148.9°C (300°F)

dihydrocedrene

B	T
20.5 (297)	22.8°C (73°F)
17.2 (249)	65.6°C (150°F)
15.4 (224)	93.3°C (200°F)
12.6 (182)	148.9°C (300°F)

oleic acid

B	T
18.8 (272)	23.9°C (75°F)
17.6 (256)	51.7°C (125°F)
15.3 (222)	93.3°C (200°F)
13.0 (189)	135°C (275°F)

2-ethylhexyldiphenyl phosphate

B	T
21.7 (315)	22.8°C (73°F)
19.4 (282)	65.6°C (150°F)
17.8 (258)	93.3°C (200°F)
15.4 (223)	123.9°C (255°F)

3,3'-dichlorodiphenylether

B	T
25.9 (376)	22.8°C (73°F)
22.7 (329)	46.1°C (115°F)
21.7 (315)	71.1°C (160°F)
18.8 (273)	112.8°C (235°F)
17.4 (253)	145°C (275°F)

1,1,7-trihydroperfluoro-heptylperfluoro glutarate

B	T
16.6 (241)	22.8°C (73°F)
14.6 (212)	51.7°C (125°F)
12.0 (174)	82.2°C (180°F)
9.93 (144)	121.1°C (250°F)

dimethyl silicone (100 cs)

B	T
11.6 (169)	22.8°C (73°F)
11.0 (159)	42.8°C (109°F)
9.10 (132)	93.3°C (200°F)
8.14 (118)	121.1°C (250°F)
7.45 (108)	143.3°C (290°F)
7.38 (107)	148.9°C (300°F)

dimethyl silicone (1000 cs)

B	T
12.3 (179)	23.9°C (75°F)
11.8 (171)	71.1°C (160°F)
11.2 (162)	93.3°C (200°F)
11.1 (161)	121.1°C (250°F)

Glassy fluids

Pentaerythritoltetravalerate
Polyethyleneglycol
Squalane
Cyclododecylcyclododecane
Dihydrocedrene
Di(2-ethylhexyl)adipate
Di(2-ethylhexyl)-3,3,4,4-tetramethyladipate
2-Ethylhexyldiphenylphosphate

Super cooling or semi-crystaline fluids

3,3-Dichlorodiphenylether
1,1,7-Trihydroperfluoroheptylperfluoroglutarate
Dimethylsilicone (100 cs)
Dimethylsilicone (1000 cs)
Polychlorortrifluoroethylene oil

Crystalline fluids

Bicyclohexyl
1,4-Bicyclohexylbutane
Octacosane
Oleic acid

Tables 5, 6, and 7 summarize the features seen in the calorimeter curves.

Table 5

LOW TEMPERATURE TRANSITIONS OF THE GLASSY (NON-CRYSTALLINE) FLUIDS

Fluid	Tg from Heating Curve Peak (°C)	Melting Range (°C)		Notes on Melting Behavior
pentaerythritol-tetravalerate	-86	-5	-5	The melting range for this group is a set of slope changes which imply altered rate of change of heat capacity (Cp) with temperature. Molecular aggregation and altered viscosity-Temperature behavior are likely associated with this temperature range.
polyethylene glycol	-76	-13	+2	
squalane	-96	-57	-12	
cyclododecylcyclo-dodecane	-46	-16	+9	No crystalline order is detectable under the test conditions.
dihydrocedrene	-107	-40	+8	
di(2-ethylhexyl)-adipate	-100	-40	+1	
di(2-ethylhexyl)-3,3,4,4,tetramethyl-adipate	-86	-39	+4	
2-ethylhexylphenyl-phosphate	-79	-35	+13	

Table 6

LOW TEMPERATURE TRANSITIONS OF THE SUPERCOOLING (SEMI-CRYSTALLINE) FLUIDS

Fluid	Tg from Heating Curve Peak (°C)	Melting Range (°C)		Notes on Melting Behavior
3,3'dichlorodiphenyl-ether	-74	-47	+11	Broad melt, poorly crystalline, mainly glassy material.
1,1,7trihydroperfluoro-heptylperfluoro-glutarate	-89	-62	+11	Super cools, crystallizes on heating -62 to -5; pk-58 melts -5 to +11, pk +6.
dimethylsilicone (100 cs)	-121	-98	-22	Super cools, crystallizes on heating -98 to -51. Melts in two phases -51 to -22, pks -45, -35.
dimethylsilicone (1000 cs)	-121.5	-105	-33	Super cools, crystallizes on heating -105 to -50.5. Melts in two phases -50.5 to -33, pks -44, -36.5.
polychlorotrifluoro-ethylene oil	-65	-43	+5	Broad melt, poorly crystalline, stress cracking at -89 and -124 on cooling.

Table 7

LOW TEMPERATURE TRANSITIONS OF THE CRYSTALLINE FLUIDS

Fluid	Tg from Heating Curve Peak (°C)	Melting Range (°C)		Notes on Melting Behavior
bicyclohexyl	-94	-40	+8	Melts in two phases pks -13, +4
1,4 bicyclohexyl-butane	-86	-16	+21	Melts as single peak +15
octacosane	-32	+13	+72	Melts in two phases +57, +67
oleic acid	-114	-62	+14	Melts as two phases -47, +6

3. FILM THICKNESS AND TRACTION IN POINT CONTACTS

3.1 TEST APPARATUS

3.1.1 General

The apparatus used throughout the tests was basically a refinement of earlier "ball and plate" rigs, such as those used by Cameron and Gohar,[5] and Foord, Wedeven, Westlake and Cameron.[7] In essence, a lubricated steel ball was used to drive a transparent, optically flat plate mounted in a freely moving air bearing. Using white-light interferometry it was possible to observe directly the thickness of the lubricating film in the contact under conditions of pure rolling, pure sliding or any combination. In addition, the tractive force and load on the ball were measured, together with the surface speeds and temperatures of the lubricated elements.

3.1.2 Optical

The optical arrangement at the lubricated contact was as shown in Fig. 1. The interference is caused by light being reflected partly from the polished surface of the 25.4 mm (1 inch) diameter type 52100 steel ball and partly from the semi-reflecting underside of the optically flat glass disk. To optimise the visibility of the interference fringes, it was necessary to choose firstly the type of interferometry required, in order to calculate the degree of reflectivity needed at the surfaces.

Since the thickness of lubricant inside the contact was the main optical concern, it was decided to use white light interferometry. This was because it was possible to identify a number of different color fringes to every order of interference, as opposed to just one fringe per order with monochromatic light. Hence measurements of thickness could be more precise. It was later found that four colors were readily distinguishable, although this was largely the observer's personal choice, and these were:

Yellow/orange
Cherry Red
Dark Blue
Apple Green

in order of increasing thickness, from zero.

The choice of white light limited the number of observable orders of interference to four or five, since beyond this the colors overlap to reform white light. This set a maximum of

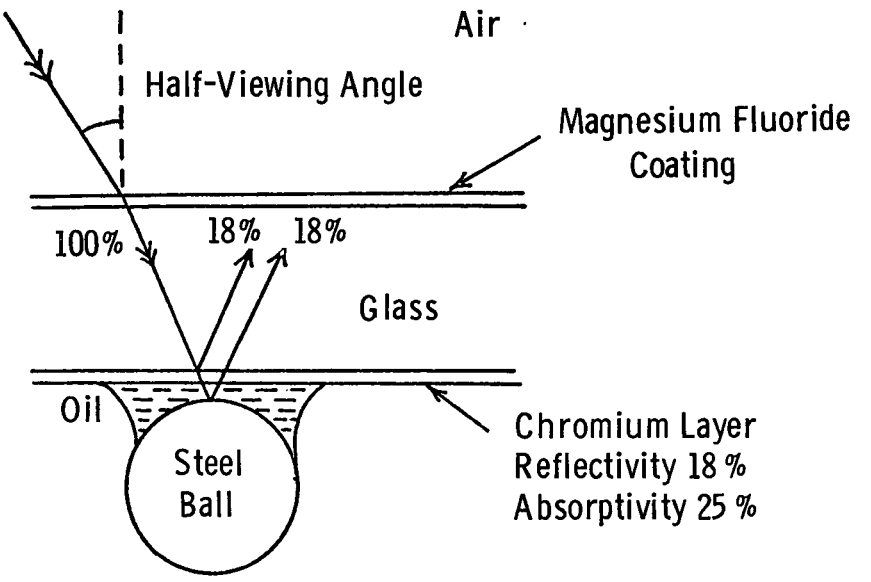

Figure 1. Optical arrangement

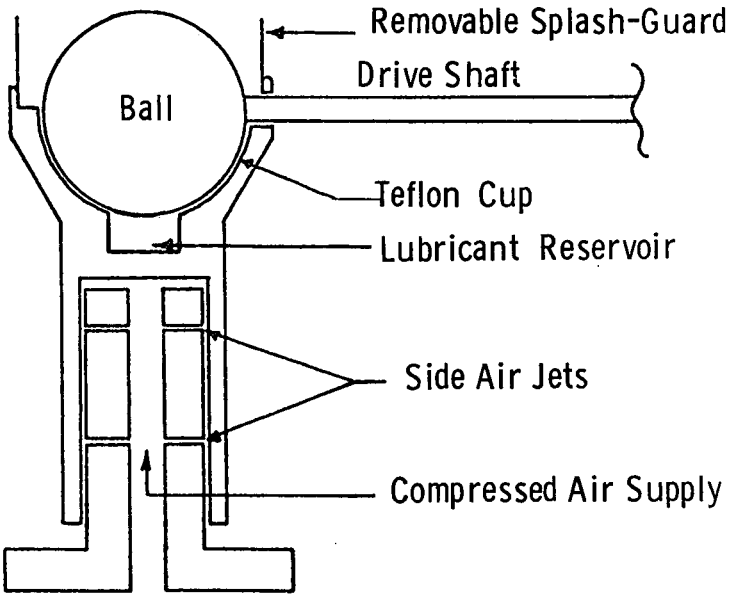

Figure 2. Loading system

about 10^{-6} m (10^4Å) on film thickness, but this was adequate over the ball speed range used. It also meant that the actual "Newton's Rings" pattern outside the contact, particularly in the wake of the ball, was difficult to observe.

White light also implied the use of two-beam interferometry, with less precisely defined interference peaks, but nevertheless, the resolution of 1/20 of a fringe, generally accepted for this method,[14] was easily adequate. For two-beam interferometry, the two rays reflected from the ball and the plate must be of equal intensity, and this fact allowed the calculation of desired reflectivity. The ball was as highly polished as possible to minimise surface roughness effects and the reflectivity was found to be 60% in oil. The optimum value for the semi-reflecting surface was calculated to be 18% reflectivity and 25% absorptivity. The absorption was present because the semi-reflection was achieved by vacuum depositing a 20 nm (200Å) layer of chromium on the underside of the glass disk. This had the added attraction of more closely simulating the real situation of metal to metal contact. Finally to eliminate spurious reflections from the top surface of the disk, an anti-reflection coating of magnesium fluoride was deposited on to it.

For good interference, the incident light must be collimated to give an approximately parallel beam. In the case of white light, the degree of collimation required is high and a half-cone angle of 3° is necessary.[14] This was achieved very conveniently by using a stereoscopic microscope of 80X; one branch for observation, and one branch for illumination. This consisted in principle of a pair of Gallilean telescopes viewing the contact through one large objective lens. A beam of approximately parallel light shone down one branch (with the eyepiece removed) emerged from the telescope in a narrower parallel beam. This was then automatically directed onto the contact by the objective lens. The collimation angle was governed mainly by the telescope diameter 1 x 10^{-2}m and the working distance 9.1 x 10^{-2}m which gives approximately 3° for the half-cone angle. The half-viewing angle caused by the illumination being on a separate path was 6° but this introduces an inaccuracy of only 0.5%, which is well inside experimental limits. The light itself was provided by a 12V d.c. incandescent filament lamp with a ground-glass screen and condensing lens.

3.1.3 Speed Control and Measurement

The drive mechanism was largely as shown in Fig. 2. The steel ball was used to drive the disk, since it was much easier to mount the disk in an approximately frictionless air bearing. A shaft was attached rigidly to the ball by means of a spark-eroded hole located as accurately as possible along a radius. The shaft

in turn was attached via a constant velocity universal joint to a 30V d.c. motor. This had a generator integral to its construction and hence could be used in conjunction with a solid-state feedback system of speed control. The result was a continuously variable speed range from 6-6000 RPM, (up to 7.6m/s, 300in/s). Speed measurement was by a digital tachometer, activated by voltage pulses from a magnetic transducer which monitored a 100-toothed steel gear wheel mounted on the motor shaft. The accuracy of reading the speed was good provided the wheel was turning fast enough. This caused difficulties at low speeds, but was overcome by the addition of a 20:1 gearbox for this range. The gearbox also helped increase the torque available at these low speeds beyond the actual motor maximum of 0.085Nm (12 oz-in). The overall accuracy of control and reading was then found to be better than 1 in 500.

The speed of the disk was measured also by a digital method. However, the problem of low speed measurement was here overcome by using a photoelectric pulse producer, since this was not speed dependent. This consisted of a light beam focused onto a series of 100 silvered strips placed on the black-coated edge of the disk. The reflected pulses were monitored by a photo-transistor circuit.

3.1.4 Loading

The ball was loaded against the glass disk by means of a hemispherical cup coated with polytetrafluorethylene (Teflon) as shown in Fig. 2. This was situated on a very close fitting piston-and-cylinder arrangement, activated by compressed air. Side jets ensured that there was negligible friction at the piston, and very little air flowed out, so the load was calculated assuming a hydrostatic condition, (i.e. load = piston area x air pressure), with allowance made for the weight of the cup etc. The air pressure and hence the load, was controlled by a needle valve.

The cup itself was divided into two parts by a small trough, adjacent to the equator of the rotating ball. The trough was 0.5×10^{-2}m in depth and served the dual purpose of minimising the effect on the lubricant of frictional heating in the cup, and also forming a lubricant reservoir of a few cm^3 capacity. To prevent excessive spraying of lubricant from the cup at high speed, a stainless steel surround could be fitted over the rim once the ball was in position.

The only substances in contact with the lubricants in the cup were Teflon and stainless steel, which were considered corrosion resistant under the operating conditions. The disk was of selected float glass capable of loading to $6.9 \times 10^8 N/m^2$ (100,000 psi).

3.1.5 Bearing

It was essential that the disk should rotate freely, for accurate measurement of transmitted torque. Therefore, the disk was supported by an air bearing. The final design was an elegant simplification of earlier ones in that the optical flatness of the disk was utilised by making the underside of the disk into one of the bearing surfaces. For this reason, the disk was larger than originally intended, being 20.3 cm (8 in) in diameter, with the extra width used in the bearing. The disk was therefore floated on a ring of vertical air jets, and radially located by a sphere and cup air bearing as shown in Fig. 3. The spherical bearing surface was a slice from a 5.35 cm (2.5 in) ball bearing ball, cemented accurately to the center of the disk. The cup was formed from epoxy resin moulded around the ball slice, and supported in a brass screw mount. The clearance between bearing surfaces was adjustable by means of the screw mount, in order to give virtually frictionless rotation of the disk. The compressed air supply was at a pressure of 5.5×10^5 N/m^2 (80 psi) and was filtered and dried before passage to the bearing along 6 mm (0.25 in) bore air lines. The whole bearing was moveable along the direction of the motor drive shaft to allow the ball to run along a number of tracks on the disk at varying radius should the chromium semi-reflecting layer become scratched at any time.

3.1.6 Temperature Control and Measurement

Facility was made to raise the temperature of the ball environment, by means of a 1.5 kW heating element located underneath the brass floor of the test enclosure (Fig. 3). The enclosure was insulated below this, and also round the edge by asbestos compound integral to the construction. In addition, a two-section cowl of similar insulating material could be positioned over the glass disk, with suitable gaps for interferometric observations and measurement of disk speed.

The heat transfer to the ball and disc was largely via the surrounding atmosphere. The enclosure walls as a whole were therefore at a considerably higher temperature than the contact. Owing to the large thermal capacity of the metal structure of the enclosure, and the good insulation of the walls, the temperature of the contact remained constant to within ±1.1°C (±2°F) for the duration of a test run, if the heating was stopped once the desired temperature was reached. The temperature could be raised to about 170°C, although it was difficult to achieve any previously chosen temperature accurately. However, this did not matter since the temperature of the fluid was measured to within 0.5°C (1°F) using an electronic thermometer with a copper/constantan thermocouple dipping into the fluid. The thermocouple bead was

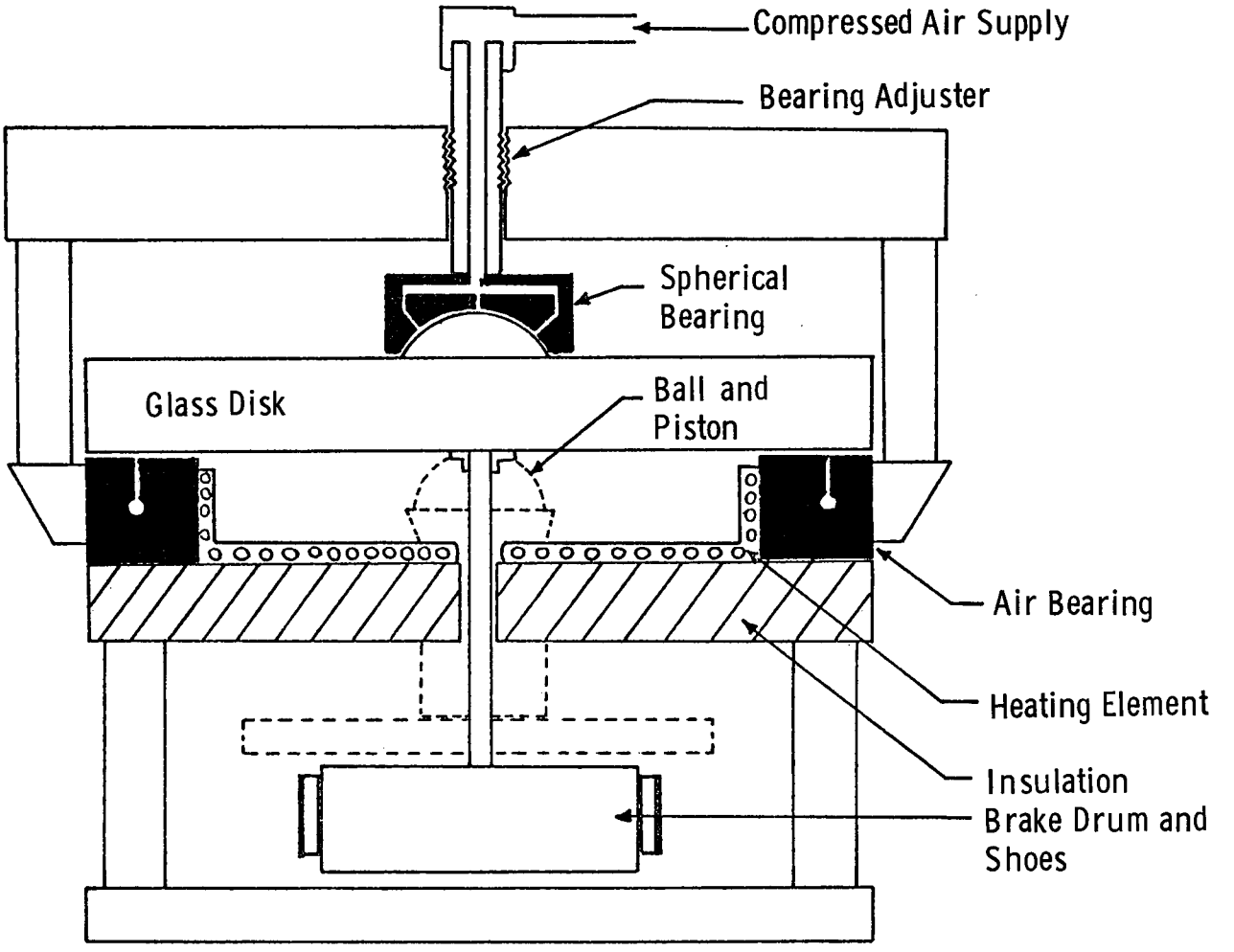

Figure 3. Schematic diagram of EHD test apparatus

only 1.27 μm (0.005 in) in diameter and therefore could be located very close to the contact inlet without disrupting fluid flow appreciably. No variation could be found between the temperatures of the ball, the disk and the fluid, so they were assumed equal. The limiting useful temperature was set by the effective viscosity and α value of the fluid. If the oil was too thin the speed required to obtain a graph of H* vs U* was beyond the capacity of the motor. For this reason temperatures beyond 170°C were not required.

The only inlets to the test enclosure once the disk was in position were through the passages allowed for the drive shaft and torque measurement shaft. It was therefore possible to eliminate almost all the air if desired from the enclosure simply by introducing a supply of oxygen-free nitrogen from a pressurized cylinder. This quickly displaced air from the enclosure and, by keeping the flow continuous and slightly above atmospheric pressure, it also flushed out the small amount of air leaking from the loading piston. The excess pressure also made sure that little air leaked in from the bearing surface.

The actual percentage of oxygen in the atmosphere of the enclosure was measured continuously by feeding some of it to an oxygen content analyser. This worked by measuring galvanometrically the change in magnetic reluctance of two large coils, as paramagnetic oxygen was passed between them. It was found that an oxygen concentration of 0.1% was achieved after about 30 secs.

3.1.7 Traction Measurement

Previous rigs were unsuitable for traction measurements because no account could be made of frictional losses involved with rotating the ball in the loading cup. This was overcome by mounting the loading piston, gearbox and motor all on a sub-plate which was floated on an air pad. Any tangential traction force transmitted by the ball therefore could be measured by the force of reaction exerted on the floating plate. In this way, frictional losses in the cup, gearbox and motor were automatically eliminated from consideration.

The reaction force on the floating plate was measured by means of strain gauges. The plate was located in an approximately central position over the air pad by a spring steel strip at the opposite end from the loading piston, as shown in Fig. 4. The stiffness of this was selected to allow a transverse motion of the ball of ±0.5 cm for the maximum expected tractive force of 4.45 N (1 lbf). Since the effective length of the sub-plate from ball to spring steel strip was approximately 0.3 m, the angular displacement was small, and proportional to the transverse force. The strain gauges were mounted on a low-stiffness steel U-shaped strip fixed rigidly at one end to the sub-plate and

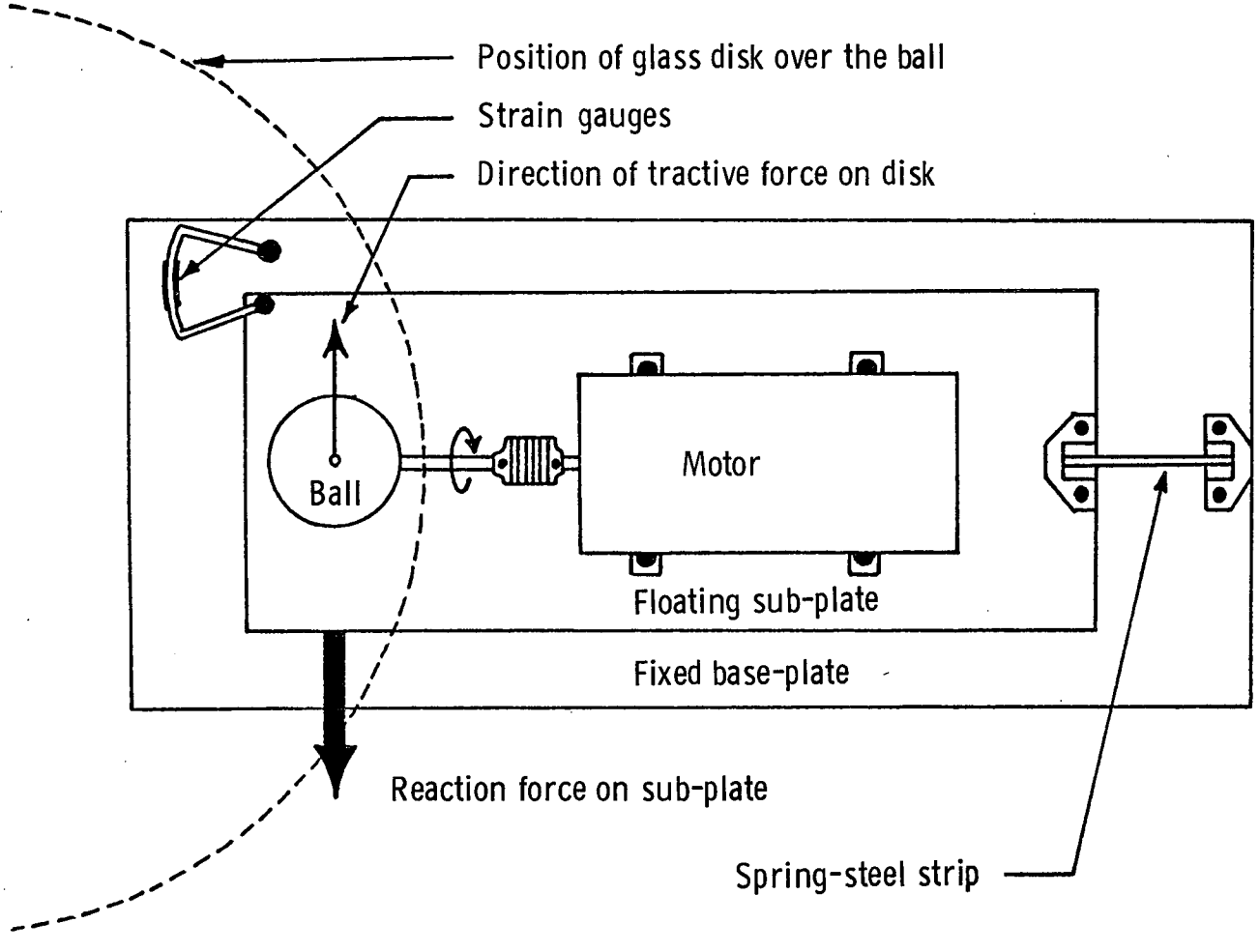

Figure 4. Plan view of floating sub-plate assembly

flexibly at the other end to the stationary base-plate. One gauge was in extension on the outer surface of the curved steel strip while the other was in compression on the inner surface. Two identical gauges were mounted close by on a similar mounting strip to act as a dummy resistor to compensate for temperature fluctuations. The four gauges were used in a Wheatstone Bridge circuit, with the out-of-balance current across the bridge being amplified using an integrated circuit device. It was possible by this method to calibrate an ammeter reading directly as a measurement of tractive force. The calibration was checked periodically throughout the series of tests in case of changes occurring in the amplifier characteristics, the stiffness of the system, or the voltage of the supply to the bridge.

The fact that the stiffness of the system was so high meant that it was possible to ignore the effect on force readings of the motor leads, and the small air line to the piston, provided they moved easily.

The transmission of force across the contact relied on there being a velocity difference between the ball and disk at the contact. This was produced by applying a variable braking force to the disk by means of a metal stalk along its principal axis (Fig. 3). This stalk was attached by means of a boss cemented to the underside of the disk. It proved impossible to locate it very accurately on the axis of rotation, mostly because this axis was in turn determined by the large ball slice cemented to the top surface of the disk. For this reason, the torque applied to the stainless steel brake drum on the stalk was not measured, since it would have been impossible to align brake shoes free to rotate on the same axis. Instead it was simple to apply a steadily variable braking force via spring loaded Teflon shoes on either side of the drum.

3.2 CALIBRATION PROCEDURE

3.2.1 Traction Measurement

The galvanometer indicating the output from the strain gauge bridge amplifier was calibrated directly in terms of the tractive force acting at the point contact. A known calibrating force therefore had to be applied horizontally, parallel to the direction of motion of the rotating ball surface. This was carried out by replacing the ball and piston with a rigid vertical rod and fastening to this a length of thread held in tension by a variable load acting via a pulley.

The bridge was initially balanced by means of a 25-turn screw potentiometer to give a central reading. Subsequent readings were taken for a range of weights up to 0.454 kg (1 lb) for both load-

ing and unloading. The response of the system as a whole was found to be linear over this region and showed no signs of saturation.

Such calibrations were repeated periodically during the sequence of tests since it was necessary to lower the stiffness of the system for some low traction lubricants.

3.2.2 Film Thickness Measurement

The calibration procedure adopted was based on a method used by Wedeven.[9] In this a known load was applied to the ball against the disk and the gap between the two surfaces outside the actual contact was calculated using the Hertz equation

$$h = \frac{ap_{max}}{E'} \left[- \left(2 - \frac{r^2}{a^2}\right) \cos^{-1} \frac{a}{r} + \left(\frac{r^2}{a^2} - 1\right)^{\frac{1}{2}} \right] \qquad (1)$$

where h = separation of the two surfaces
E' = reduced Young's modulus for glass and steel
r = radial distance from center of contact
a = Hertz contact radius
$p_{max} = \frac{3}{2} \left[\frac{W}{\pi a^2} \right]$ = max. Hertz contact pressure
W = load.

By observing the interference fringes or rings outside the contact with a filar eyepiece and travelling microscope the radius for each order of each color could be measured accurately. When substituted in the above equation, it was possible to compute the thickness in air corresponding to each color, giving the following:

1st order	Yellow	2.0×10^{-7}m
	Red	2.7
	Blue	3.4
	Green	4.3
2nd order	Yellow	4.7
	Red	5.6
	Blue	6.1
	Green	6.7
3rd order	Yellow	7.6
	Red	8.6
	Blue	9.0
	Green	9.6
4th order	Yellow	10.5
	Red	11.5
	Green	12.5

The method of loading in this case was simply to balance the ball on a scale pan using an equal weight on the opposite side; then place an extra 0.1 kg weight in the opposite pan to make the ball touch the disk, placed over it, with load W = 0.1 kg.

It must be stressed again that these results apply only to the particular apparatus used since there is a phase change for the light at the disk and ball surfaces which depends on the materials used, and also the identification of colors is personal to the individual observer.

3.3 EXPERIMENTAL PROCEDURE

3.3.1 Purification and Degassing

The fluids used in the tests were originally very pure, but owing to the length of the total series of tests it was necessary to remove products of oxidation and hydrolysis etc. immediately prior to their actual use. Also since one of the variables to be investigated in the tests was the blanketing atmosphere, it was necessary to degas the fluids to avoid contamination of the atmosphere and hasten the equilibration between the fluid and the atmosphere.

Decontamination procedure was suited to the chemistry of the fluid in question. For the hydrocarbons, (Fluids c,d,f, g,j,k) the principal contaminants were the result of air oxidation. The following procedure removed these impurities:

Store over silica gel.
Pass the fluid over a small silica gel column under nitrogen within two days of actual use.
Store in the dark in the absence of oxygen.

For the esters (Fluids a,h,i,o) there was the additional problem of hydrolysis back to acid and alcohol. Fortunately it was shown by titrating for acid before and after extracting any acid with 5% aqueous lye that there was negligible impurity due to hydrolysis. (This was later confirmed by experiments on the soft film apparatus). Purification therefore simply followed the hydrocarbon procedure.

Fluid m was purified by a similar method, except that alumina was used instead of silica gel.

It was not considered necessary to purify the six remaining fluids either because they were unlikely to decompose, or because they were unlikely to develop impurities which would alter their properties in any significant way.

The degassing procedure exploited the fact that gas solubility in a liquid decreases markedly when the liquid freezes or is cooled to a solid glassy state. Cooling to drive off dissolved

gases was preferable to heating in that it does not promote decomposition in the process. For the test fluids that were not appreciably volatile at room temperature, the following procedure was employed.

Place the fluid in a glass vessel connected to a cold-trapped vacuum pump.
While pumping, freeze the fluid with solid carbon dioxide in an acetone slurry.
Then warm to room temperature.
Repeat this freeze-thaw cycle ten times to remove the dissolved gases.

For volatile fluids (g,j,k,n) pumping was only carried out when the fluid was frozen, and the vessel was isolated by a vacuum stop-cock for the rest of the process, to avoid heavy evaporation loss of the fluids.

3.3.2 Cleaning of Apparatus

The only parts of the apparatus to come in contact with the fluids were the ball, the disk, the loading cup and the splash guard. These were all washed in acetone or benzene in between tests to remove excess fluid remaining from the previous test. Following this they were transferred to an ultrasonic degreasing machine for a more thorough cleaning, and then stored in a desiccator.

Originally it was intended to clean the surfaces even further by means of a soft glow vacuum discharge apparatus. However, while waiting to try such a procedure, it was demonstrated on the soft film apparatus that if any of the fluids did produce surface films, their shear strength was very low (about 1 N/m^2). This could have no effect on traction measurements, and since the ultrasonic machine already eliminated the effect of impurities on bulk properties of the fluids, it was decided to cut out the lengthy vacuum discharge procedure.

3.3.3 Film Thickness Measurements

The procedure used for film thickness measurements was as follows:

With the ball placed in the loading cup and the shaft fastened to the motor via the universal joint, the reservoir was filled with lubricant. For thick fluids, some was also spread in a ring on the disk, following approximately the track of the ball.
The thermocouple bead was then pressed lightly against the ball surface, close to the contact inlet, and held in place by a mounting on the splash guard.

The disk was then placed in position, and the spherical air bearing was clamped over it. The air supply was turned on and the bearing clearance was adjusted to give free rotation.

With the disk stationary, the ball was loaded until it touched the disk lightly. The ball and disk were then rotated slowly by means of the motor until there was an even spread of lubricant along the track. This was particularly important for thick fluids.

The load was increased to the chosen value, and the contact region was brought into focus in the microscope.

Actual recordings were then taken of the digital tachometer reading corresponding to a particular color fringe as the speed was increased. As many fringe orders as possible were observed. The readings were checked as the speed was reduced.

The temperature was monitored throughout the test, on the electronic thermometer. If the temperature rose by more than 1°C, the test was temporarily stopped, but after a little practice the tests could be performed so fast that the temperature rise was negligible in most cases.

At the end of the test, the ball was lowered from the disk before the motor was switched off, to minimize the risk of scratching the disk.

For higher temperature tests, the asbestos compound cover was placed over the disk, and the whole apparatus was heated up slowly before the test started. The ball was turned slowly without loading against the disk, to ensure that the thermocouple showed the actual fluid temperature. When the required temperature was reached, the heating was stopped and the test carried out, once again as quickly as possible.

In all these tests, the traction facility was not exploited and the motor sub-plate was not floated on the air pad. The film thickness measured was that of the large flat central region of the contact. It was impossible to observe accurately the film thickness at the rear of the contacts, since the fringes were so condensed that they became merged and gave indistinct colors. For the same reason it was not practicable to observe the cavitation in the wake of the ball. It was possible to observe the fluid inlet boundary, and if this started to approach the contact region, indicating the onset of starvation, then the test was stopped.

For tests run under nitrogen atmosphere, the nitrogen was allowed to flow for about 1 minute to reach the allowed concentration of oxygen, before any results were taken. No difference could be detected between results taken in air and results taken in nitrogen, outside the normal range of variation of experimental results.

3.3.4 Measurement of Sliding

For measurement of sliding it was necessary to record the speeds of the disk and the ball simultaneously. This was difficult to carry out directly, but was finally overcome. The method

was to measure firstly the motor speed, which remained very constant owing to the feedback system, throughout the variations of torque imposed on it. The digital tachometer was then used to measure the ratio of disk speed to ball speed by counting the number of pulses from the disk speed transducer occurring during a large fixed number of counts from the motor speed transducer. The actual surface speed of the ball was calculated knowing the motor speed and the ball radius. The disk surface speed was calculated from the ratio measured on the tachometer by assuming that it was equal to the ball speed for conditions of zero traction i.e. zero slip. This assumption was thought to be justified since the speed ratio and strain gauge output remained constant for large variations of load and rolling speed. This was interpreted as showing negligible effect of rolling friction.

Having measured the motor speed and speed ratio between the ball and disk, it was possible to calculate the ball surface speed U_1 and the disk surface speed U_2. Hence the sliding velocity (U_1-U_2) could be derived. It was found more useful in many cases to consider the sliding velocity as a fraction of the rolling velocity. Therefore if the rolling velocity is interpreted as $\frac{1}{2}(U_1+U_2)$ i.e. the speed at which oil enters the contact, then the slide/roll ratio Σ becomes:

$$\Sigma = 2\,\frac{(U_1-U_2)}{(U_1+U_2)} \qquad (2)$$

Ideally the rolling velocity should have been kept constant, but this would have been difficult and would probably have entailed a separate drive to the disk.

3.3.5 Measurement of Traction

The amount of sliding was gradually increased up to the maximum value of $\Sigma = 2$, by applying a braking force to the drum. This force produced a reaction force on the floating sub-plate which was monitored via the strain gauge meter. In practice the force was increased so as to make the meter read on successive divisions from zero up to the value at total slip with the disk stationary. For each value of tractive force thus obtained, a value of the speed ratio was noted. Care was taken to ensure that the reading of the ratio was constant by allowing the counting procedure to repeat itself two or three times. By reference to the calibration experiment it was possible to derive values of tractive force against values of slide/roll ratio. Since the experiments were carried out at varying loads, it was found more meaningful to divide the tractive force F by the load W to give a coefficient of traction (or friction) of $f = F/W$.

3.4 ANALYSIS OF RESULTS

3.4.1 Film Thickness/Speed Results

The EHD film thickness has been shown to depend by a power law on the rolling speed. Hence a plot on logarithmic axes of film thickness against rolling speed will give a straight line whose slope is the value of the power index. Therefore all film thickness results were plotted as straight lines by this method and the graph slopes were measured. The load was kept constant at 22.2 N (5 lbf) which is equivalent to a maximum Hertz pressure of 4.56×10^8 N/m^2 (66,170 psi).

3.4.2 Pressure Viscosity Coefficient

From the film thickness/speed results it was also possible to calculate the pressure/viscosity coefficient α, using an empirical equation formulated by Westlake.[8] This is as follows:

$$H^* = K(U^*)^a(W^*)^b(G^*)^c, \qquad (3)$$

where $H^* = \frac{h_o}{R}$ film thickness parameter,

$U^* = \frac{\eta_o \bar{u}}{E'R}$ speed parameter,

$W^* = \frac{W}{E'R^2}$ load parameter,

$G^* = \alpha E'$ materials parameter.

Since Westlake's work was under almost exactly similar conditions, the values of the coefficients a,b,c and k obtained in Ref. 8 were used directly in a computer program to find α, using experimental values of h_o and $\bar{u}$.

These coefficients were

$$K = 62U^{*-0.063}$$

$$a = \left(\frac{1}{90} \log_{10} W^*\right) + 0.89 \qquad (4)$$

$$b = \left(\frac{1}{43} \log_{10} U^*\right) + 0.303$$

$$c = 0.55$$

The manufacturer determined for us the elastic constants of the glass. These were

$$E_{glass} = 7.58 \times 10^{10} \text{ N/m}^2 \quad (11.0 \times 10^6 \text{ psi})$$
$$\sigma_{glass} = 0.25$$

and they were used to calculate the reduced Young's modulus.

The only difficulty involved was that the experimental measurements were of ball speed and optical film thickness. The actual film thickness h_o was found from the relationship

$$h_o = \frac{\text{optical thickness}}{\text{refractive index}}$$

The refractive index of the fluids therefore had to be known at the conditions of pressure and temperature present in the contact. Since the refractive index measuring apparatus was still largely experimental, it was decided to measure the refractive indices in a conventional Abbé refractometer at the correct temperature and then calculated the value for the appropriate pressure using the Lorentz-Lorenz equation:

$$n_p = \frac{(1+2A)^{\frac{1}{2}}}{(1-A)}, \tag{5}$$

where $$A = \frac{\rho_p}{\rho_o} \frac{n_o^2-1}{(n_o^2+2)} . \tag{6}$$

The pressure value used in the calculations was the maximum Hertzian pressure p_{max}, and the density ratio was found from the bulk modulus.

The experimental readings of film thickness and speed were taken from the central region of the graph, rather than choose an actual pair of readings since this reduced the errors. It is difficult to estimate the errors involved in the calculated values of the pressure/viscosity coefficient, but they will be approximately the same as those in Westlake's work, which are estimated by comparison with other methods of measuring the coefficient. The value of α and the graph slopes are presented in Table 8.

Table 8

SUMMARY OF FILM THICKNESS DATA

Fluid	Rolling Speed (m/s) at Optical Thickness ($\times 10^{-7}$m) of 2.0	2.7	3.4	4.3	4.7	T°C	Slope	n_p	α ($psi^{-1} \times 10^{-4}$)
a	0.52	0.85	1.2	1.8		38.5	0.66	1.55	0.51
	0.33	0.46	0.73	1.1		24.5	0.66	1.56	0.50
b	0.36	0.56	0.8	1.1		38.0	0.70	1.52	0.91
	0.19	0.29	0.39	0.53		22.5		1.57	0.98
c	0.80	1.2	1.7	2.5		37.0	0.65	1.53	0.84
	0.44	0.72	1.0	1.4		23.0		1.59	0.74
e	0.031	0.048	0.066	0.093	0.115	36.4	0.66	1.48	2.5
	0.019	0.012	0.018	0.027	0.039	20.5		1.52	2.1
f	0.48	0.80	1.05	1.6	1.9	54.0		1.62	2.1
	0.11	0.18	0.26	0.40	0.47	38.3	0.65	1.67	2.7
	0.017	0.027	0.040	0.057	0.067	21.0		1.71	2.5
h	3.1	4.5	6.1	8.5		39.0	0.66	1.51	0.43
	1.4	2.2	3.3	4.3		23.0		1.56	0.52
i	0.52	0.86	1.25	1.86	2.20	37.5	0.59	1.54	0.94
	0.27	0.44	0.66	0.96	1.15	24.0		1.59	0.85
k	2.1	3.7	5.3	8.2		38.0	0.54	1.52	0.76
	1.4	2.5	3.7	5.7	6.8	25.0		1.56	0.59
l	0.04	0.073	0.113	0.165	0.186	39.0	0.54	1.55	0.63
	0.023	0.037	0.056	0.082		25.0	0.60	1.59	0.75
m	1.45	2.40	3.30	4.8	5.5	38.0	0.69	1.59	1.25
	0.71	1.08	1.53	2.1	2.5	24.0		1.64	1.73
o	0.29	0.49	0.73	1.09	1.30	38.5	0.58	1.40	1.19
	0.13	0.23	0.34	0.50	0.59	22.0		1.43	1.08
p	0.25	0.40	0.57	0.68		38.0	0.66	1.54	0.52
	0.19	0.30	0.44	0.62		20.5		1.59	0.67
q	0.094	0.132	0.18	0.24		38.0	0.70	1.54	0.13
	0.075	0.102	0.14	0.18		20.5		1.59	0.16

W = 44.5N $p_{max}=4.57\times10^{8}N/m^2$

3.4.3 Traction Results

It was found most meaningful to plot the results of traction as dimensionless quantities, since comparisions could then be made more easily. The parameters chosen for this were

$$\text{Traction coefficient } f = \frac{\text{traction force}}{\text{load}} = \frac{F}{W}$$

$$\text{and Slide/roll ratio } \Sigma = (U_1 - U_2)/\tfrac{1}{2}(U_1 + U_2)$$

It was found that f varied in the range 0-0.1 and Σ varied from 0 up to 2, the latter corresponding to total sliding with the disk stationary and $U_2 = 0$.

By referring to the graphs (see Section 3.6) it can be seen that:
(1) all curves approximate straight lines near the origin;
(2) the initial slopes do not depend on the rolling speed, except through the ratio Σ;
(3) the curves approach a plateau region for large values of Σ; and
(4) none of the curves exhibits a peak, although more than one value of Σ is sometimes obtained at f_{max}.

Therefore the graphs could largely be characterized by two measurable quantities: firstly the initial slope of the straight line part of the graph of f against Σ, and secondly the maximum value of f achieved in the plateau region.

It was noticed that graphs exhibiting this plateau region were very similar to plots of shear stress against shear strain (comparable axes to f and Σ) for loosely packed powders.[15] An attempt was therefore made to analyze the data further in terms of a powder model. This predicted that

$$A = \ln(1 - f/f_{max}), \quad A = \text{const.} \qquad (7)$$

Therefore in addition to the above graphs, this relation was also plotted for those fluids where a plateau was formed and the plateau height f_{max} could be measured. All such plots gave straight lines, so the powder model was developed and is presented below.

The values of A and f_{max} for each fluid are presented in Table 9.

Table 9

SUMMARY OF TRACTION DATA

Fluid	$f_{max} \times 10^{-3}$	$A \times 10^{-2}$	T°C	W N
a	12.5	1.5	35.0	44.5
	17.0	1.5	25.0	44.5
b	33.0	6.4	38.0	66.7
	33.0	3.6	38.0	44.5
	43.0	8.3	25.0	66.7
	43.0	5.4	24.0	44.5
c	40.0	2.5	37.0	44.5
	40.0	3.7	25.0	44.5
e	84.0	25.0	39.0	66.7
	84.0	25.0	38.0	44.5
	90.0	25.0	21.5	66.7
	90.0	25.0	23.5	44.5
f	62.5	17.0	21.5	66.7
			39.0	44.5
			53.5	
h	11.2	1.1	40.0	44.5
	14.8	1.4	25.0	44.5
i	28.0	2.4	36.0	44.5
	32.0	3.7	24.8	44.5
k	17.5	5.2	38.0	44.5
	19.5	4.2	27.0	44.5
l	11.5	1.8	39.0	44.5
	11.5	3.6	20.0	66.7
				44.5
m	25.5	2.5	38.0	44.5
	27.5	3.8	25.0	44.5
o	30.0	4.9	33.0	44.5
	37.5	5.9	24.0	44.5
p	25.0	2.2	40.0	66.7
	17.0	2.0	40.0	44.5
	25.0	4.0	22.0	66.7
	17.0	3.8	22.0	44.5
q	23.0	3.5	38.0	66.7
	18.0	2.5	38.0	44.5
	31.0	4.4	21.0	66.7
	23.0	3.4	21.0	44.5

3.5 THEORETICAL EVALUATION OF TRACTION BEHAVIOR

The results confirm the conclusion of Jefferis and Johnson[16] that initially the traction coefficient is proportional to the slide/roll ratio:

$$f \propto \Sigma = \frac{U_1 - U_2}{\bar{u}} . \tag{8}$$

If the situation were Newtonian then the traction should be predicted by:

$$f \propto \eta \frac{U_1 - U_2}{h_o} ; \tag{9}$$

and since $h_o \propto (\bar{u})^{0.7}$

$$f \propto \eta \frac{U_1 - U_2}{(\bar{u})^{0.7}} . \tag{10}$$

To resolve Eqs. 8 and 10, the apparent viscosity must depend on the rolling speed

$$\eta_{app} \propto (\bar{u})^{-0.3}$$

This fact emerges as the greatest difficulty in the traction problem. Some authors[17,18] have tried to solve the problem in a Newtonian manner by considering that the frictional heating of the fluid lowers the viscosity, but since this is negligible for small Σ the problem is not resolved.

Dyson[19] has identified the apparent viscosity with actual viscosity for a Barlow-Lamb fluid, but met with little success in fitting theory to experiment. The fact that all the fluids behave in the same way makes this approach seem more unlikely.

Johnson has pointed out in the discussion to Ref. 20 that fluids in EHD contacts exhibit traction properties similar to granular solids.

This idea is followed through to see what it would predict and how the experimental results are correlated. As is stated later whether it is the correct explanation or not needs further study.

Suppose the high pressure fluid in the contact can be considered as a loose packed powder. The microscopic structure could be stylized as in Fig. 5. Consider just one "column" of granules of diameter D. The structure will support normal load and the height will be governed by inlet conditions. The force required to lean the column over will be negligible, but the column will fracture somewhere along its length as it passes through the contact when the ends have a relative displacement of one granule diameter D. Once fractured, the column breaks up into disordered particles which have an observed coefficient of friction which is constant as in the granular case.

For the contact as a whole, the problem resolves to what proportion of particles are ordered (no friction force) and what proportion are disordered (constant coefficient of friction f).

For distance x into the contact (see Fig.6) the relative displacement of the column ends is:

$$(U_1 - U_2)\frac{x}{\bar{u}} = \Sigma\, x \tag{11}$$

Disordered particles will be either totally inside or outside the contact zone, therefore y must be some integer multiple of D.

$$y = ND \tag{12}$$

There must be some value of Σ, say Σ_o below which this condition is not satisfied, i.e. there is a minimum value of Σ before any traction occurs, as suggested by Plint.[21] This is given by $\Sigma_o x = D \times 1$ and for $x = 2a$,

$$\Sigma_o = D/2a. \tag{13}$$

In general,

$$y = ND = \Sigma_{N-1}\,(2a-\{N-1\}D). \tag{14}$$

Consider y increases by D as a result of an increase in Σ, $\delta\Sigma$:

since $(N+1)D = \Sigma_N(2a-ND)$,

$$\delta\Sigma = \frac{(N+1)D}{2a-ND} - \frac{ND}{2a-(N-1)D}. \tag{15}$$

But $(2a-ND) = x$, so provided $D \ll x$, it follows that

$$\delta\Sigma = D/x. \tag{16}$$

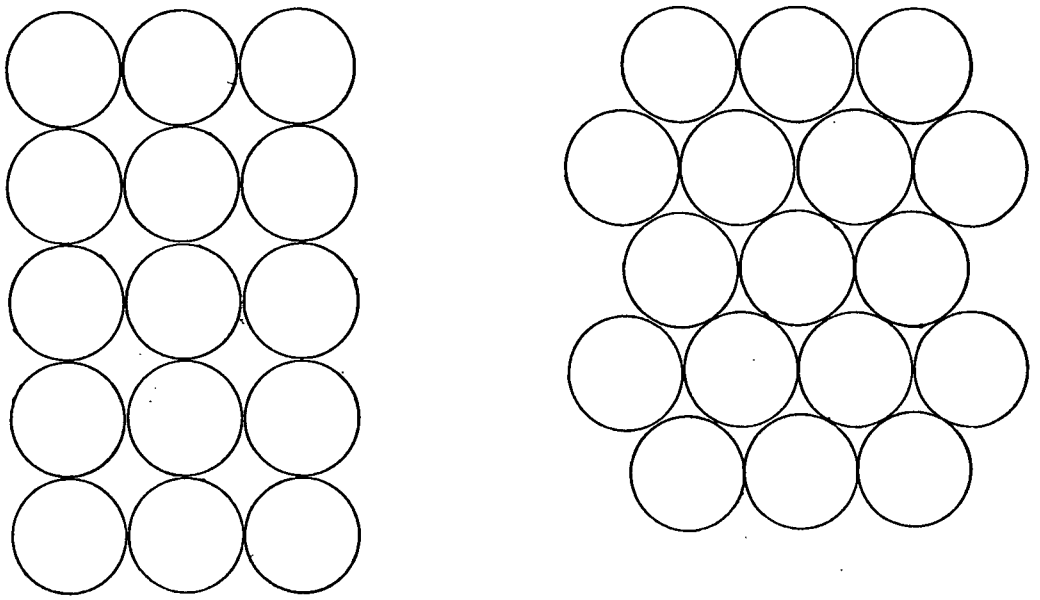

Figure 5. Stylized diagram of packing

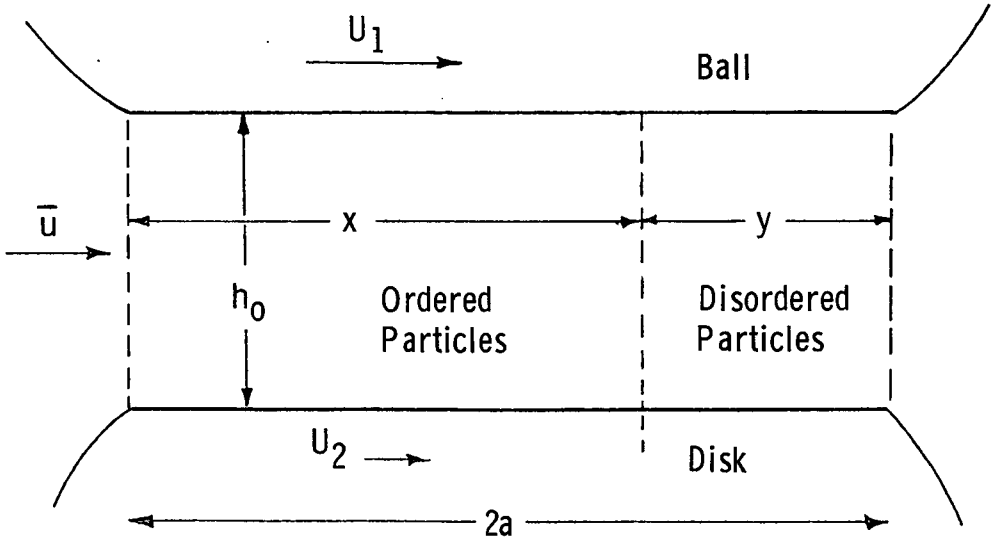

Figure 6. Contact area nomenclature

But D is a steady increment in y, and is therefore proportional to $-\delta x$. Thus $AD = -\delta x$, where A is a proportionality constant, and:

$$A\delta\Sigma = -\delta x/x \tag{17}$$

$$\text{Since } \Sigma = \Sigma_o \text{ for } x = 2a$$

$$x/2a = \exp\left[-A(\Sigma-\Sigma_o)\right] \tag{18}$$

This is the proportion of ordered particles, the proportion of disordered particles is:

$$1-(x/2a) = 1-\exp\left[-A(\Sigma-\Sigma_o)\right]; \text{ thus} \tag{19}$$

$$f = f_{granule}\{1-\exp\left[-A(\Sigma-\Sigma_o)\right]\}, \text{ and} \tag{20}$$

$$1-f/f_{max} = \exp\left[-A(\Sigma-\Sigma_o)\right]. \tag{21}$$

Since the particle diameter would be very small, then Σ_o is also very small and Σ plotted against $\log(1-f/f_{max})$ is a straight line of slope A.

This analogy with loose packed powder seems useful and gives quite a good fit with experimental fact, but actual evidence of granules has not been produced. The most likely cause of such particles (should they exist) is that nucleation centers appear in the fluid as it vitrifies under the extreme pressure of the contact. The effect of this glass transition has already been pointed out by Poon in the discussion to Refs. 16 and 21. Also Jacobson[22] has considered the effects of lubricants solidifying in EHD contacts.

Some evidence has been found for vitrification with the present apparatus. This was a series of tests with the fluid 5-phenyl 4-ether involving film thickness/speed measurements for a range of pressures and temperatures. For each temperature and pressure, three film thicknesses were chosen and the corresponding film speeds were read from a graph of results. The ball speeds, multiplied by the ambient viscosity at the contact temperature were then plotted against contact temperature for the three values of film thickness and resulted in three straight lines as shown in Fig. 7. These all cut the temperature axis at one point precisely. Since the viscosity cannot be zero at that temperature, it follows that the film speed need only be zero to give any film thickness. This can only be interpreted as infinite viscosity for the fluid i.e. vitrification, so the intercept of temperature corresponds to the glass transition point at the contact pressure. This is borne out by the fact that the

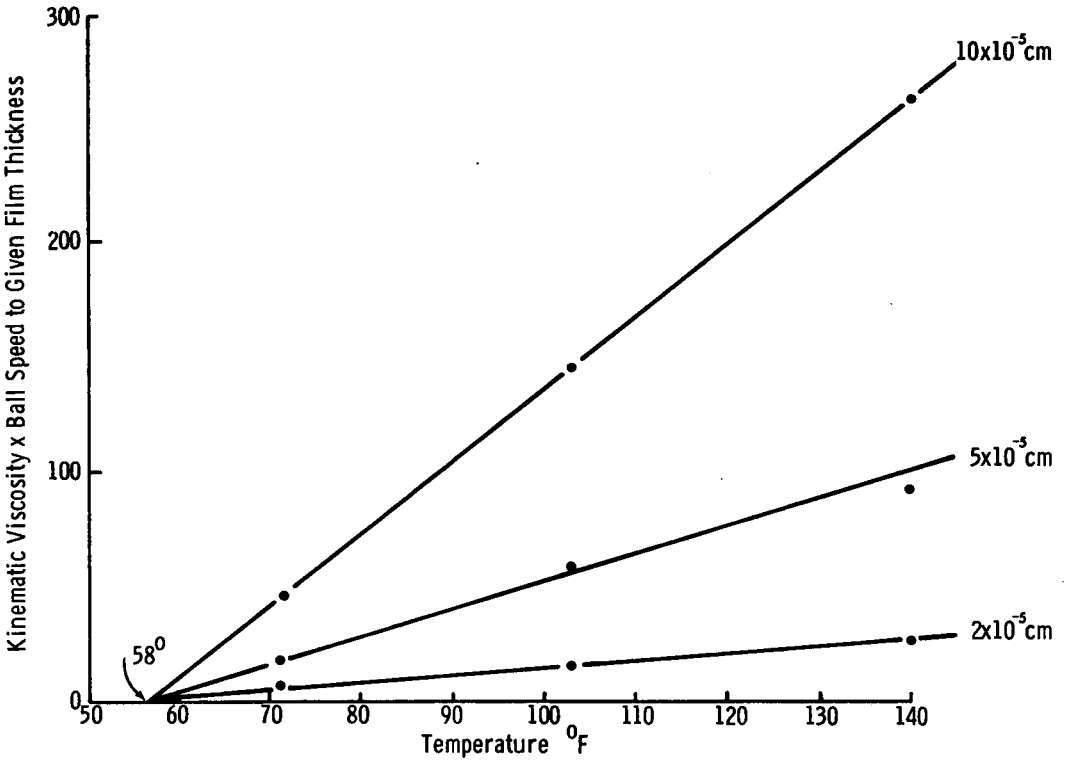

Figure 7. Results for 101,500 psi Hertzian stress

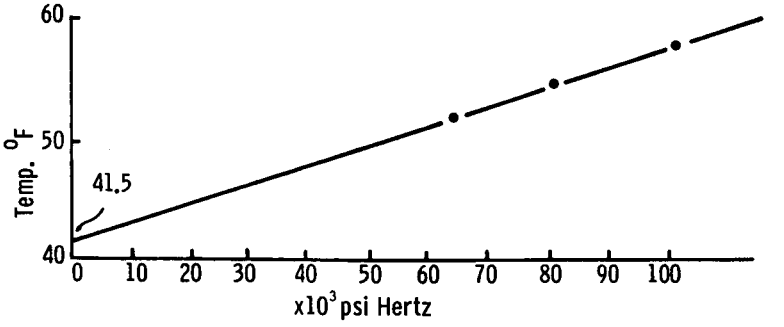

Figure 8. Plot for prediction of pour point at zero pressure

intercept temperatures plotted against pressure meet up with the glass transition temperature at ambient pressure in Fig. 8, in excellent agreement with the quoted pour point of the fluid 40°F. Unfortunately little work was done on this line of approach with the actual test fluids.

An interesting extension of the analogy of powders is that at higher pressures than considered here, the fluids would presumably behave like close-packed powders. In this case the ordered particles would exhibit an elastic force which would contribute to the coefficient of friction. Since this would decay when the order is lost as Σ increases, there would be a peak in the traction curve, and the same "ceiling" as at low pressure, which is in keeping with experimental results.

Close packed powders exhibit large volume increases when sheared, so the ultimate test of the analogy would be to look for some such effect during shearing at high pressures (about $15 \times 10^8 N/m^2$).

3.6 TRACTION DATA

A tabulation of the full array of traction data collected is given in Table 10 and also in Figs. 9 through 32.

It will be noted that fluids d, g, j, and n (see Table 1) have been omitted. These fluids gave films too thin to permit measurement of either film thickness or traction within the available speed range. (Fluid g did give marginally measureable film thickness, only).

Table 10

TRACTION DATA

Pentaerythritoltetravalerate

$f \times 10^{-3}$	Σ							
0.0	0.0	0.0	0.0	0.0	0.0	0.0	0.0	0.0
2.0	0.10	0.13	0.14	0.10	0.10	0.11	0.09	0.09
4.0	0.22	0.22	0.28	0.20	0.23	0.22	0.16	0.16
6.0	0.37	0.33	0.44	0.32	0.36	0.32	0.23	0.25
8.0	0.54	0.49	0.68	0.55	0.46	0.41	0.32	0.34
10.0	0.73	0.67	1.00	0.85	0.57	0.51	0.47	0.44
11.0				1.10				
12.0	0.96	1.05	1.27	1.49	0.72	0.78	0.82	0.67
12.5	2.00	2.00	2.00	2.00				
16.0					1.40	1.30	1.38	1.32
17.0					2.00	2.00	2.00	2.00
T°C	34.5	35.5	34.7	36.5	24.5	25.3	26.0	26.0
U_1 m/s	0.53	0.70	0.95	1.33	0.32	0.50	0.67	0.82
W N	44.5							

Polyethylene Glycol

$f \times 10^{-3}$	Σ							
0.0	0.00	0.00	0.00	0.00	0.00	0.00	0.00	0.00
1.4					0.002	0.003	0.002	0.004
2.1	0.008	0.009	0.025	0.018				
2.8					0.005	0.006	0.008	0.010
4.2	0.015	0.017	0.033	0.033	0.008	0.009	0.013	0.016
5.7					0.013	0.012	0.020	0.021
6.4	0.024	0.022	0.060	0.062				
7.1							0.023	0.025
8.5	0.031	0.033	0.073	0.074	0.020	0.018	0.029	
10.6			0.088	0.083				
11.4					0.026		0.042	0.046
12.8	0.050	0.055	0.119	0.114				
14.2					0.034	0.028	0.056	0.061
17.0	0.066	0.075	0.166	0.162	0.048	0.050	0.083	0.073

Table 10 continued

Polyethylene Glycol (continued)

$f \times 10^{-3}$	Σ							
19.8					0.058	0.060		
21.3	0.132	0.114	0.249					
22.7					0.070	0.074	0.123	0.109
25.5	0.158	0.150	0.361	0.351	0.093	0.090		
28.4					0.098	0.110	0.222	0.219
29.8	0.226	0.240						
31.2							0.516	0.369
31.9			0.758	0.915				
34.0	0.376	0.350	2.00	2.00	0.178	0.180	2.00	2.00
38.2	0.486	0.500						
39.6					0.387	0.420		
42.6	0.805	0.890			0.690	0.650		
44.7	2.00	2.00						
45.4					2.00	2.00		
T°C	24.0	24.0	38.3	38.2	25.0	25.0	38.2	38.0
U_1 m/s	0.20	0.33	0.22	0.28	0.20	0.33	0.22	0.28
W	44.5N				66.7N			

Squalane

$f \times 10^{-3}$	Σ			
0.00	0.00	0.00	0.00	0.00
2.1	0.009	0.011	0.015	0.020
4.3	0.018	0.028	0.037	0.046
6.4	0.025	0.035	0.050	0.058
8.5	0.040	0.050	0.060	0.071
10.6	0.057	0.067	0.109	0.102
12.8	0.085	0.077	0.127	0.133
14.9	0.102			
17.0	0.124	0.122	0.173	0.188
21.2	0.156	0.149	0.231	0.257
25.5	0.207	0.244	0.353	0.364
29.8	0.281	0.309	0.473	0.574

Table 10 continued

Squalane (continued)

$f \times 10^{-3}$	Σ			
34.0	0.389	0.457	0.631	0.812
38.2	0.490		1.024	1.145
40.3			2.00	2.00
42.4	0.815	0.871		
44.5	2.00	2.00		
T°C	25.0	25.0	37.0	36.0
U_1 m/s	0.258	0.545	0.565	0.830
W	44.5N			

Polychlorotrifluoroethylene Oil

$f \times 10^{-3}$	Σ							
0.0	0.00	0.00	0.00	0.00	0.00	0.00	0.00	0.00
2.8	0.0012	0.0005		0.0006		0.0010		0.0009
4.3			0.0010		0.0013		0.0017	
5.7		0.0010		0.0012		0.0021		0.0017
8.5	0.0016	0.0018	0.0022		0.0035	0.0029	0.0034	0.0026
11.4				0.0026		0.0037		0.0034
13.7		0.0024			0.0050		0.0049	
14.2		0.0032				0.0045		0.0042
17.0	0.0046	0.0040	0.0045	0.0042	0.0064	0.0053	0.0068	0.0049
22.7		0.0062		0.0065		0.0080		0.0072
25.5	0.0077		0.0073		0.0081		0.0093	
28.4		0.0080		0.0073		0.0102		0.0090
34.0	0.0101	0.0100	0.0099	0.0096	0.0132	0.0129	0.0130	0.0117
40.0		0.0116		0.0123		0.0159		0.0144
42.5	0.0149		0.0138		0.0192		0.0182	
45.4		0.0153		0.0157		0.0206		
51.0	0.0224	0.0179	0.0196	0.0196	0.0267	0.0247	0.0249	0.0231
56.8		0.0230		0.0224		0.0337		0.0294
59.5	0.0329		0.0278		0.0394		0.0351	
62.5		0.0257		0.0298		0.0447		0.0400
68.0	0.0421	0.0385	0.0433	0.0410	0.0655	0.0724	0.0587	0.0593

Table 10 continued

Polychlorotrifluoroethylene Oil (continued)

$f \times 10^{-3}$	Σ							
73.7		0.0517		0.0636		0.1225		0.1050
76.5	0.107		0.0773		0.144		0.0984	
79.3		0.0790		0.107		0.2077		0.2065
85.0	0.219	0.138	0.154	0.199	0.300	0.424	0.351	0.382
88.0		0.248	0.526	0.600	also 2.00			
90.7	2.00	2.00	2.00	2.00				
T°C	21.0	21.5	23.5	24.0	38.0	39.0	38.0	39.5
U_1 m/s	0.0175	0.0175	0.0665	0.0665	0.094	0.094	0.133	0.133
W N	44.5	66.7	44.5	66.7	44.5	66.7	44.5	66.7

Cyclododecylcyclododecane

$f \times 10^{-3}$	Σ					
0.00	0.00	0.00	0.00	0.00	0.00	0.00
2.8			0.0030		0.0025	
4.3				0.0035		0.0040
5.7	0.0051		0.0050		0.0050	
8.5		0.088	0.0080	0.0085	0.0075	0.0070
11.4	0.0118		0.010		0.010	0.011
17.0	0.0178	0.0178	0.014	0.013	0.0160	0.014
22.7	0.0223		0.020		0.022	
25.5		0.0269		0.021		0.026
28.4	0.0340		0.025		0.0285	
34.0	0.0411	0.0329	0.031	0.034	0.039	0.037
39.8	0.0504		0.039		0.045	
42.5		0.0530		0.052		0.056
45.4	0.0671		0.046		0.0687	
51.0	0.0802	0.0733	0.063	0.096	0.103	0.097
56.8			0.097		0.161	
59.5		0.1121		0.186		0.306
62.5	2.00	2.00	0.252 also 2.00	0.41	2.00	2.00
T°C	21.5	21.5	39.5	39.0	53.5	53.5
U_1 m/s	0.011	0.0175	0.0812	0.0542	0.287	0.068
W N	66.7	44.5	66.7	44.5	66.7	44.5

Table 10 continued

Di(2-ethylhexyl)adipate

$f \times 10^{-3}$	Σ					
0.00	0.00	0.00	0.00	0.00	0.00	0.00
0.8	0.049	0.052	0.038	0.050	0.044	0.042
1.6	0.076	0.074	0.069	0.085	0.089	0.111
2.4	0.111	0.115	0.116	0.146	0.154	0.180
3.2	0.149	0.147	0.165	0.212	0.241	0.302
4.9	0.221		0.235	0.415	0.419	0.455
6.5	0.308	0.319	0.335	0.551	0.578	0.579
8.2	0.386	0.459	0.522	0.751	0.791	0.818
9.8	0.568	0.676	0.671	0.969	1.00	1.200
11.4	0.760	0.814	0.914	2.00	1.909	2.00
13.0	0.929	0.989	0.999		2.00	
14.7	1.910	2.00	2.00			
	2.00					
T°C	25.0	25.0	25.0	42.0	38.0	40.0
U_1 m/s	0.933	1.24	1.57	2.00	2.32	2.86
W N	44.5					

Di(2-ethylhexyl)-3,3,4,4-tetramethyl adipate

$f \times 10^{-3}$	Σ					
0.00	0.00	0.00	0.00	0.00	0.00	0.00
2.0	0.016	0.011	0.018	0.021	0.022	0.031
4.0	0.036	0.018	0.033	0.037	0.049	0.060
6.0	0.058	0.040	0.049	0.070	0.075	0.090
8.0	0.078	0.064	0.064	0.104	0.111	0.117
10.0	0.104	0.086	0.076	0.127	0.155	
12.0	0.122	0.106	0.095	0.161	0.201	0.201
16.0	0.195	0.153	0.138	0.298	0.323	0.335
20.0	0.299	0.204	0.208	0.434	0.505	0.611
24.0	0.484	0.355	0.341	0.682	0.792	1.098
28.0	0.733	0.597	0.791	1.128	1.178	
29.0				2.00		2.00
30.0					2.00	
32.0	2.00	2.00	2.00			
T°C	24.8	24.8	24.8	37.0	35.4	36.5
U_1 m/s	0.198	0.323	0.475	0.223	0.402	0.595
W N	44.5					

Table 10 continued

Bicyclohexylbutane

$f \times 10^{-3}$	Σ					
0.0	0.0	0.00	0.00	0.00	0.00	0.00
0.8	0.013	0.009	0.011	0.005	0.013	0.009
1.6	0.019	0.018	0.017	0.015	0.019	0.018
2.4	0.028	0.026	0.032	0.028	0.028	0.028
3.2	0.045	0.041	0.043	0.036	0.043	0.041
4.9	0.051			0.055	0.057	0.051
6.5	0.076	0.070	0.084	0.075	0.077	0.086
8.2	0.098	0.106	0.125	0.095	0.090	0.113
9.8	0.142			0.149	0.155	0.159
11.4	0.165			0.203	0.189	0.196
13.0	0.190	0.181		0.340	0.345	0.406
14.7	0.254				0.481	0.710
16.4	0.342	0.338	0.361	0.59	0.878	0.882
18.0		0.562	0.648	2.00	2.00	2.00
19.6	0.717 2.00	1.064 2.00	2.00			
T°C	27.0	27.0	27.0	38.0	38.0	38.0
U_1 m/s	0.975	1.235	1.650	1.485	1.955	2.325
W N			44.5			

Oleic Acid

$f \times 10^{-3}$	Σ								
1.4	0.016		0.019		0.019				
2.1		0.026		0.050		0.047	0.063	0.084	0.131
2.8	0.039		0.042		0.054				
4.3	0.095	0.047	0.094	0.123	0.089	0.134	0.173	0.262	0.303
5.7	0.190		0.184		0.160				
6.4		0.267		0.230		0.252	0.299	0.427	0.411
7.1	0.316		0.277						
8.5		0.783	0.833	0.469	0.657	0.558	0.505	0.588	0.859
9.9			2.00						
10.6				1.038			0.792	1.016	1.311
11.4	2.00	2.00		2.00					2.00
12.8					2.00	2.00	2.00	2.00	
T°C	19.0	19.0	20.0	20.0	21.3	21.0	38.0	39.0	38.0
U_1 m/s	0.040	0.040	0.087	0.087	0.138	0.138	0.282	0.618	0.933
W N	66.7	44.5	66.7	44.5	66.7	44.5	44.5	44.5	44.5

Table 10 continued

2-Ethylhexyldiphenylphosphate

f x 10^{-3}	Σ					
0.00	0.00	0.00	0.00	0.00	0.00	0.00
2.0	0.009	0.017	0.018	0.037	0.033	0.037
4.0	0.029	0.035	0.038	0.062	0.061	0.069
6.0	0.042	0.054	0.062	0.099	0.088	
8.0	0.081	0.076	0.102	0.145	0.128	0.128
10.0	0.105	0.099	0.148	0.179	0.180	0.212
12.0	0.140	0.128	0.182	0.306	0.255	0.310
16.0	0.204		0.303	0.510	0.513	0.440
20.0	0.307	0.327	0.513	0.699	0.668	0.741
24.0	0.615	0.635	0.702		1.215	0.989
26.0				2.00	2.00	2.00
28.0	2.00	2.00	2.00			
T°C	24.0	25.0	24.0	38.0	38.0	38.0
U_1 m/s	0.521	0.665	1.045	1.045	1.280	1.765
W N			44.5			

1,1,7-Trihydroperfluoroheptylperfluoroglutarate

f x 10^{-3}	Σ					
0.0	0.0	0.0	0.0	0.0	0.0	0.0
2.0	0.008	0.005	0.006	0.009	0.011	0.011
4.0	0.014	0.014	0.014	0.020	0.022	0.019
6.0	0.019	0.023	0.020	0.031	0.035	0.031
8.0	0.027	0.027	0.029	0.042	0.045	0.042
10.0		0.039	0.040	0.062	0.060	0.053
12.0	0.046	0.050	0.060	0.085	0.079	0.077
16.0	0.063	0.076	0.082	0.141	0.102	0.125
20.0	0.096	0.132	0.109	0.172	0.137	0.220
24.0	0.145	0.201	0.189	0.293	0.245	0.381
28.0	0.404	0.340	0.338	0.546	0.670	0.980
30.0				0.778	2.00	2.00
32.0	0.564	0.551	0.685	2.00		
36.0		1.070	1.232			
38.0	2.00	2.00	2.00			
T°C	23.0	24.0	25.0	34.5	32.6	33.2
U_1 m/s	0.157	0.259	0.419	0.267	0.455	0.675
W N			44.5			

Table 10 continued

Dimethylsilicone (100 cS)

f x 10^{-3}	Σ									
0.0	0.0	0.0	0.0	0.0	0.0	0.0	0.0	0.00	0.00	0.00
1.4		0.004		0.005		0.007		0.015		0.022
2.1	0.017		0.010		0.028		0.030		0.037	
2.8		0.010		0.013		0.017		0.030		0.029
4.2	0.039	0.017	0.040	0.019	0.076	0.029	0.119	0.041	0.123	0.051
5.7		0.028		0.028		0.047		0.065		0.091
6.4	0.079		0.079		0.119		0.260		0.221	
7.1		0.040		0.045		0.059		0.109		0.116
8.5	0.207	0.061	0.142	0.050	0.235	0.090	0.355	0.171	0.360	0.192
9.8		0.081		0.074				0.240		0.230
10.6	0.308		0.257		0.320				0.468	
11.4		0.119		0.092		0.194		0.270		0.271
12.8	0.336		0.401		0.485		0.711		0.811	
14.2		0.165		0.145		0.32		0.350		
14.9	0.666						0.940		1.11	
17.0	2.00	0.194	1.023 2.00	0.254	1.57 2.00		2.00	0.476	2.00	0.445
19.8		0.316		0.433		0.501		0.814		
22.7		0.712		0.553						
25.5		2.00		0.850 2.00		2.00		2.00		2.00
T°C	21.0	21.4	21.5	22.4	23.0	23.0	39.0	39.5	39.5	41.0
U_1 m/s	0.053	0.053	0.107	0.107	0.178	0.178	0.142	0.142	0.186	0.186
W N	44.5	66.7	44.5	66.7	44.5	66.7	44.5	66.7	44.5	66.7

Dimethylsilicone (1000 cS)

f x 10^{-3}	Σ									
0.0	0.0	0.0	0.0	0.0	0.0	0.0	0.0	0.0	0.0	0.0
1.4		0.004		0.004		0.010		0.013		0.009
2.1	0.016		0.011		0.023		0.013		0.016	
2.8		0.007		0.008						
4.2	0.027	0.013	0.026	0.014	0.038	0.028	0.091	0.031	0.055	0.027
5.7		0.020		0.023		0.041		0.053		0.056
6.4	0.105		0.053		0.137		0.169		0.173	
7.1		0.031		0.031		0.068		0.099		0.073

Table 10 concluded

Dimethylsilicone (1000 cS) (continued)

$f \times 10^{-3}$										
8.5	0.112	0.047	0.130	0.046			0.282	0.145	0.266	0.145
9.8		0.063		0.061		0.175		0.196		0.181
10.6					0.351		0.438		0.382	
11.4		0.097		0.081		0.270		0.306		0.271
12.8	0.297		0.210		0.621		0.586		0.589	
14.2		0.153		0.113		0.439		0.454	0.834	0.422
17.0	0.606	0.224	0.511	0.193	2.00		0.964	0.689	2.00	0.549
19.8	0.779	0.344		0.277			2.00	0.959		0.786
22.7	2.00	0.437	2.00	0.382		2.00		2.00		2.00
28.4		0.790		0.920						
31.2		2.00		2.00						
T°C	21.3	21.3	21.3	21.3	38.0	38.0	38.0	38.0	37.5	38.0
U_1 m/s	0.040	0.040	0.054	0.054	0.017	0.017	0.035	0.035	0.049	0.049
W N	44.5	66.7	44.5	66.7	44.5	66.7	44.5	66.7	44.5	66.7

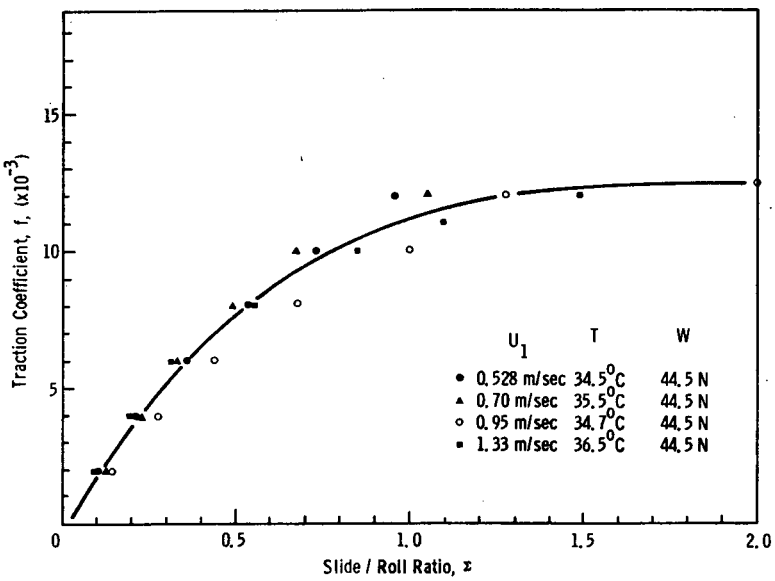

Figure 9. Traction coefficient against slide/roll ratio for pentaerythritoltetravalerate

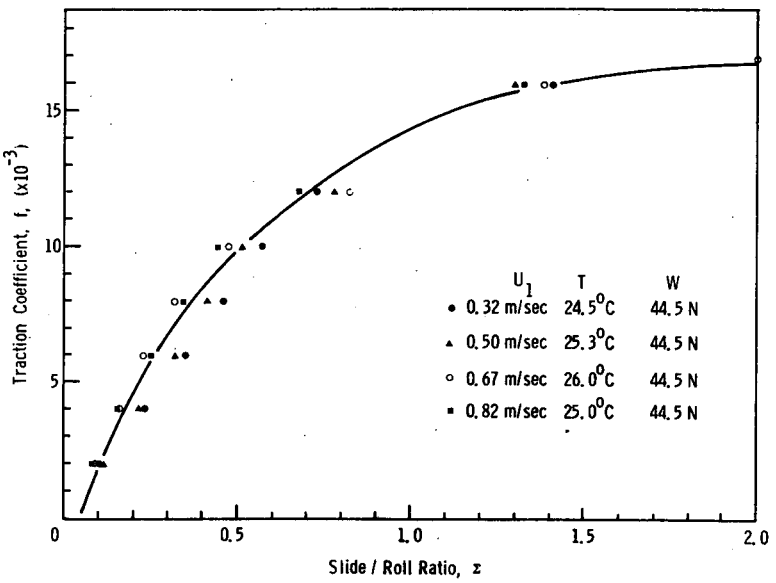

Figure 10. Traction coefficient against slide/roll ratio for pentaerythritoltetravalerate

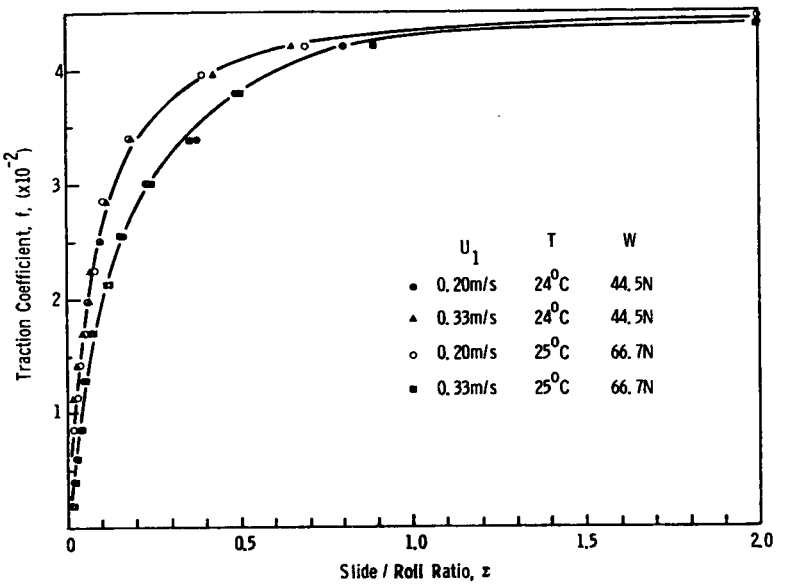

Figure 11. Traction coefficient against slide/roll ratio for polyethylene glycol

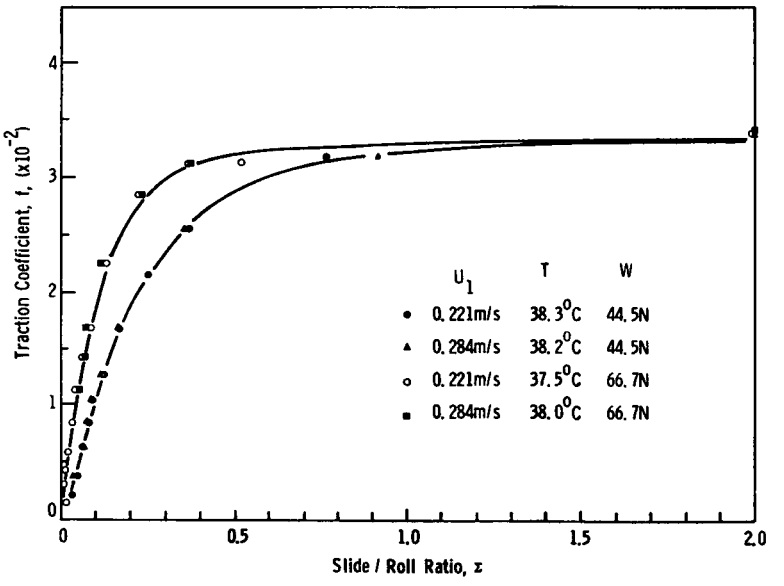

Figure 12. Traction coefficient against slide/roll ratio for polyethylene glycol

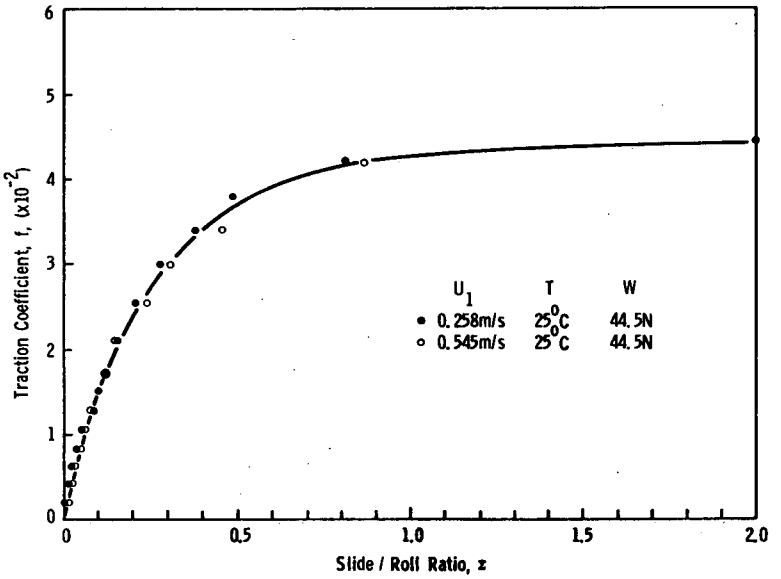

Figure 13. Traction coefficient against slide/roll ratio for squalane

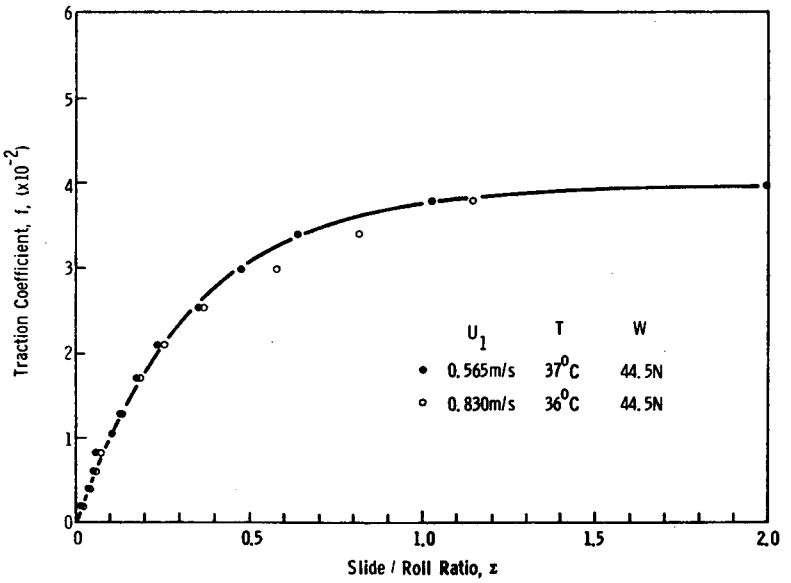

Figure 14. Traction coefficient against slide/roll ratio for squalane

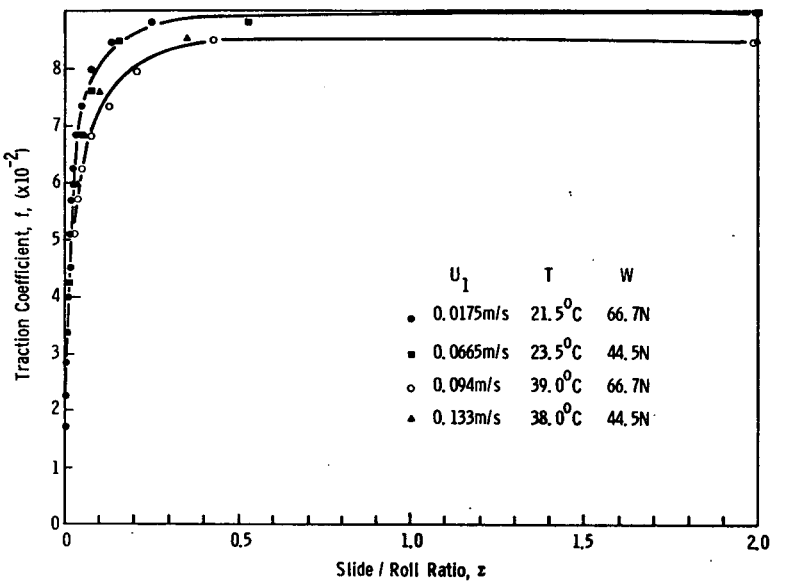

Figure 15. Traction coefficient against slide/roll ratio for polychlorotrifluoroethylene oil

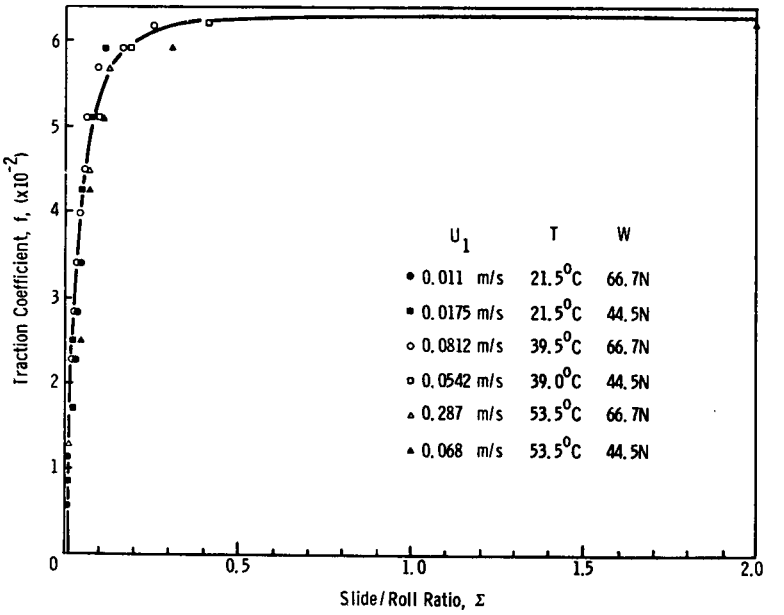

Figure 16. Traction coefficient against slide/roll ratio for cyclododecylcyclododecane

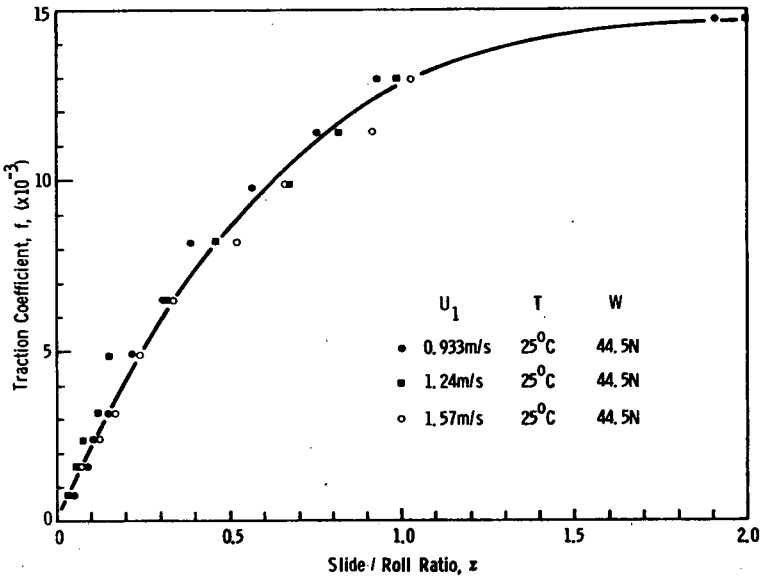

Figure 17. Traction coefficient against slide/roll ratio for di(2-ethylhexyl)adipate

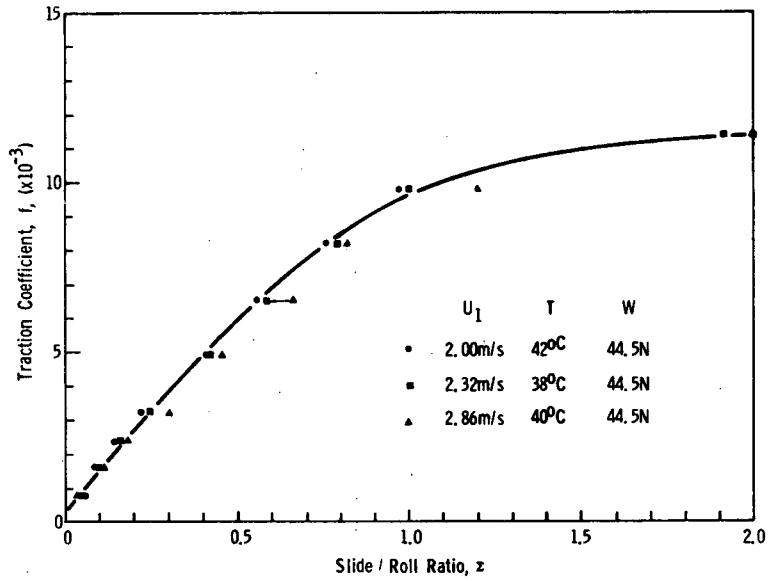

Figure 18. Traction coefficient against slide/roll ratio for di(2-ethylhexyl)adipate

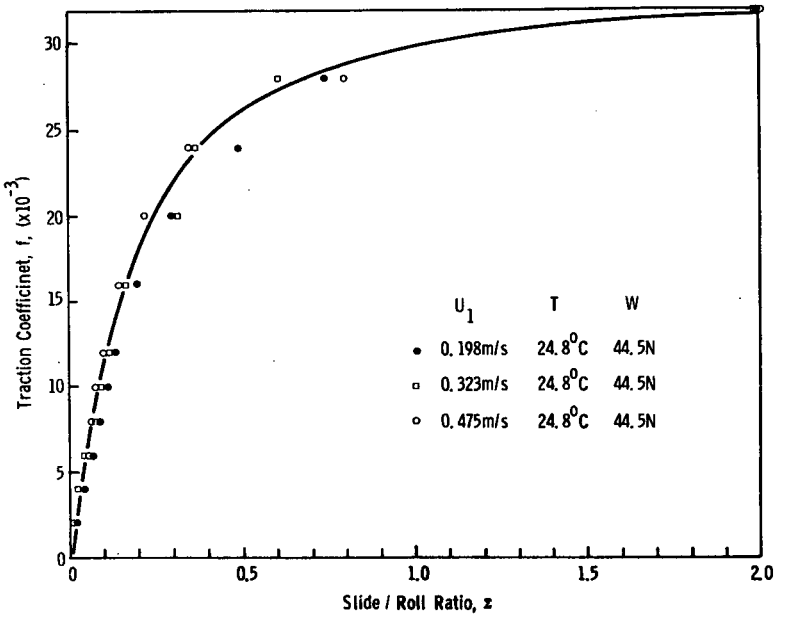

Figure 19. Traction coefficient against slide/roll ratio for di(2-ethylhexyl)-3,3,4,4-tetramethyladipate

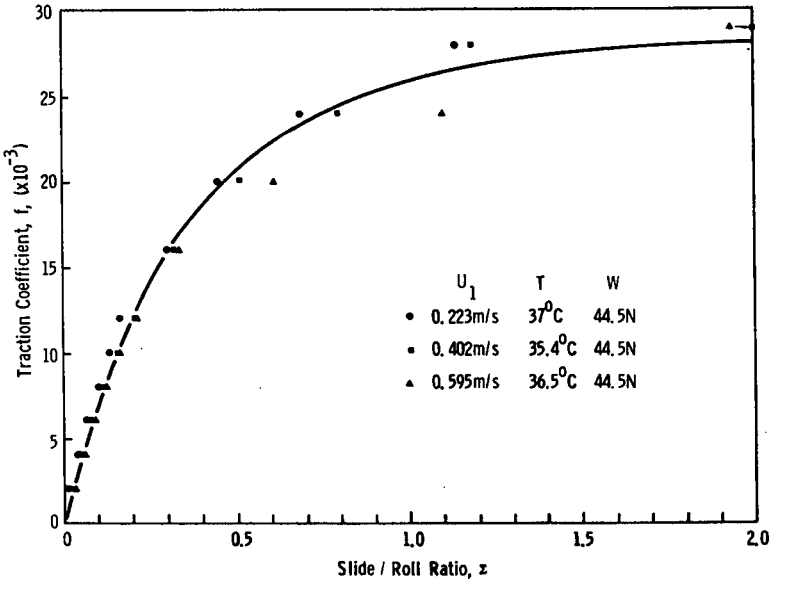

Figure 20. Traction coefficient against slide/roll ratio for di(2-ethylhexyl)-3,3,4,4-tetramethyladipate

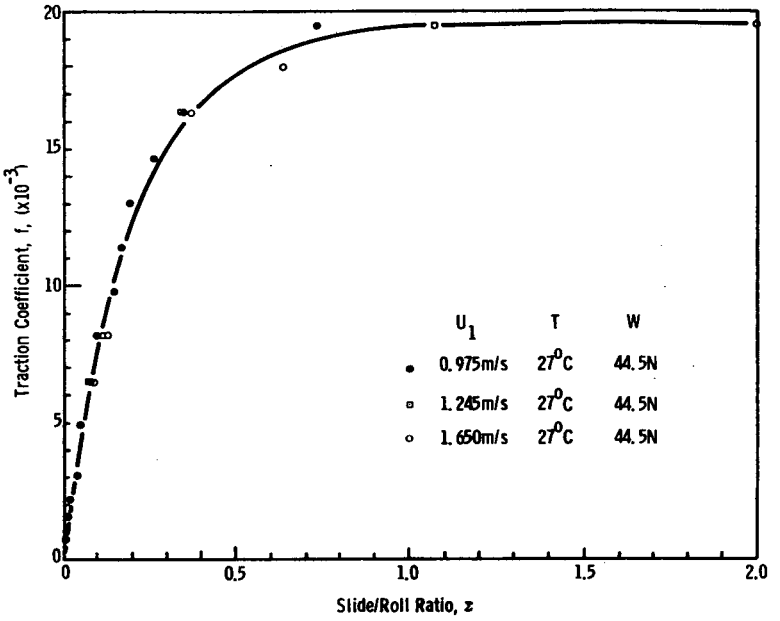

Figure 21. Traction coefficient against slide/roll ratio for bicyclohexylbutane

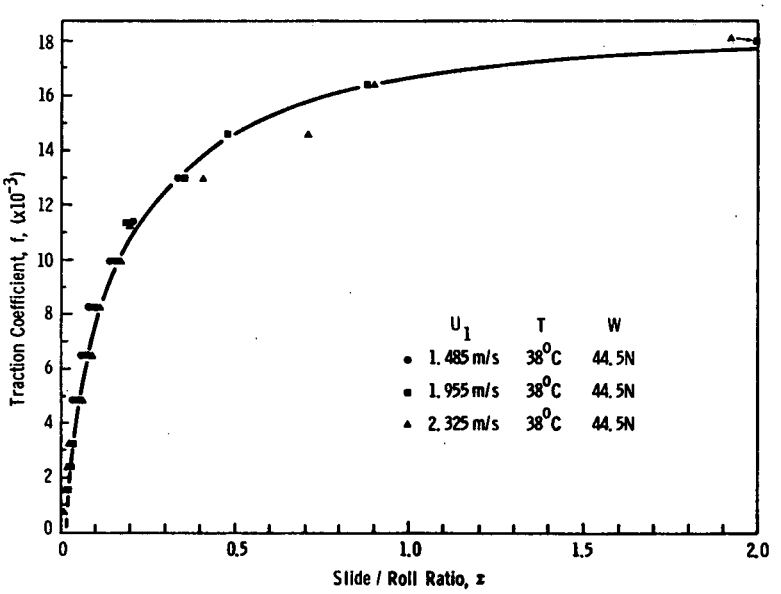

Figure 22. Traction coefficient against slide/roll ratio for bicyclohexylbutane

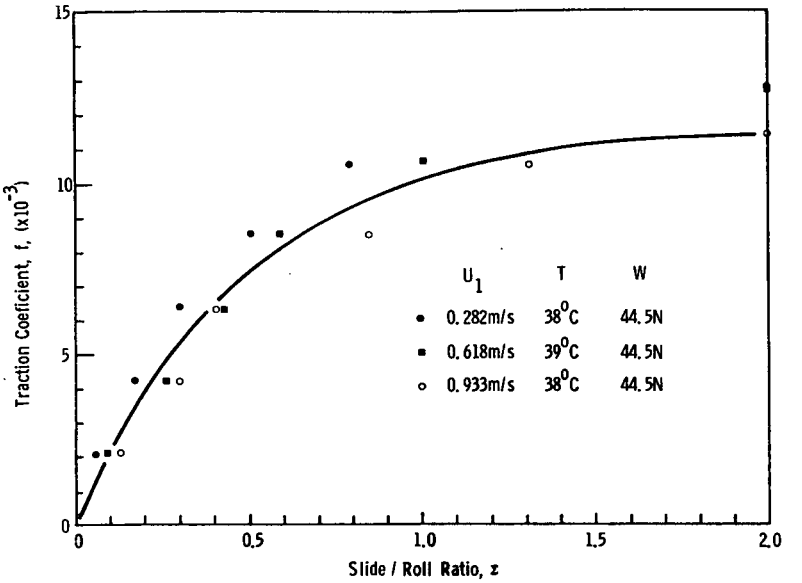

Figure 23. Traction coefficient against slide/roll ratio for oleic acid

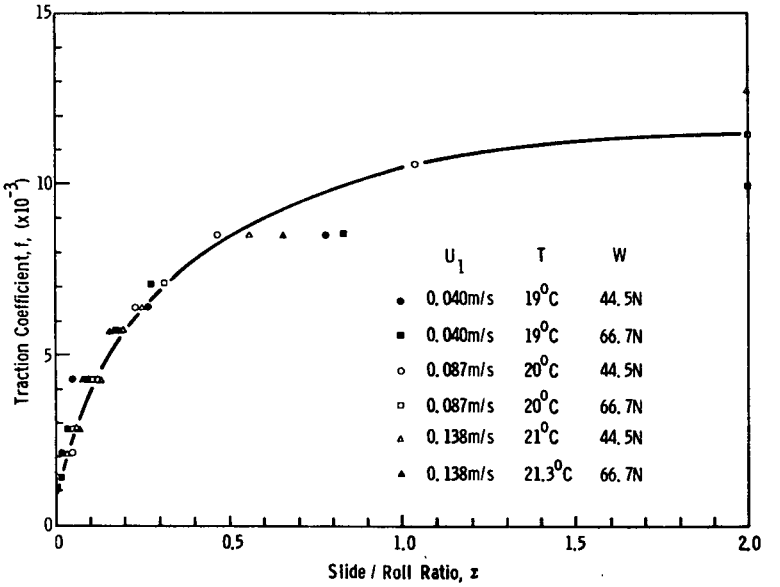

Figure 24. Traction coefficient against slide/roll ratio for oleic acid

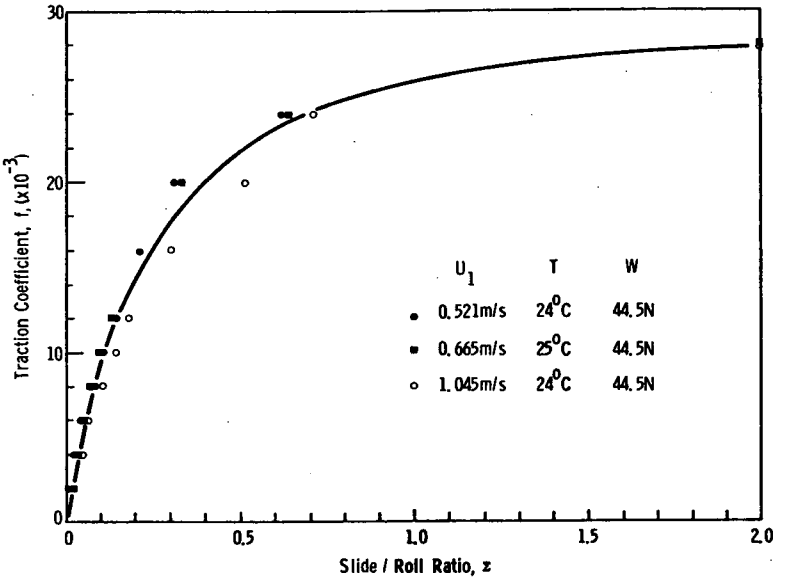

Figure 25. Traction coefficient against slide/roll ratio for 2-ethylhexyldiphenylphosphate

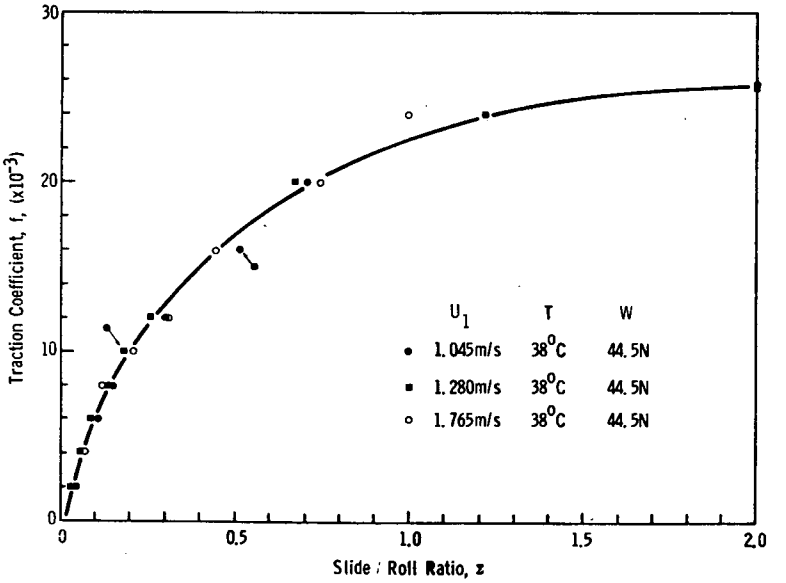

Figure 26. Traction coefficient against slide/roll ratio for 2-ethylhexyldiphenylphosphate

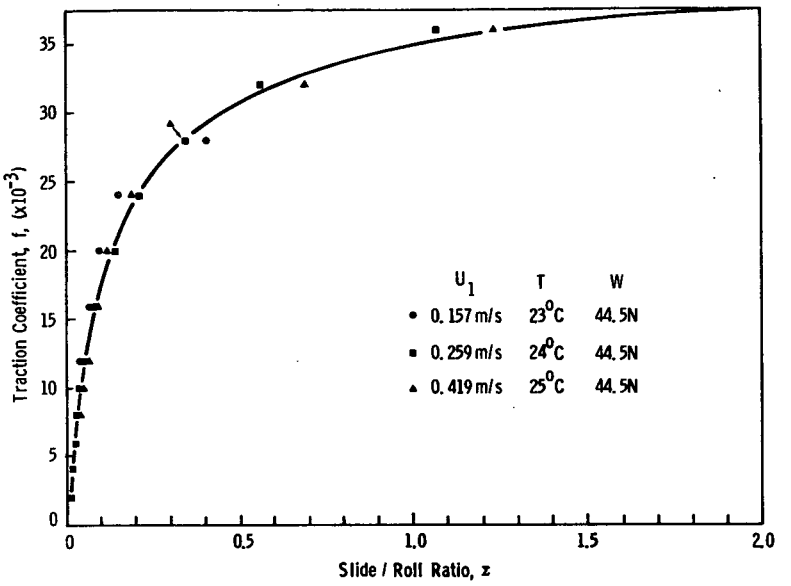

Figure 27. Traction coefficient against slide/roll ratio for 1,1,7-trihydroperfluoroheptylperfluoroglutarate

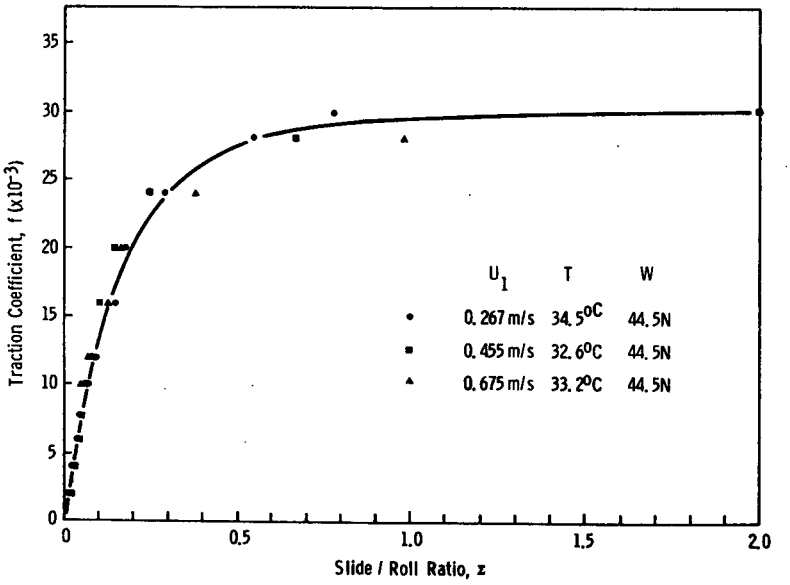

Figure 28. Traction coefficient against slide/roll ratio for 1,1,7-trihydroperfluoroheptylperfluoroglutarate

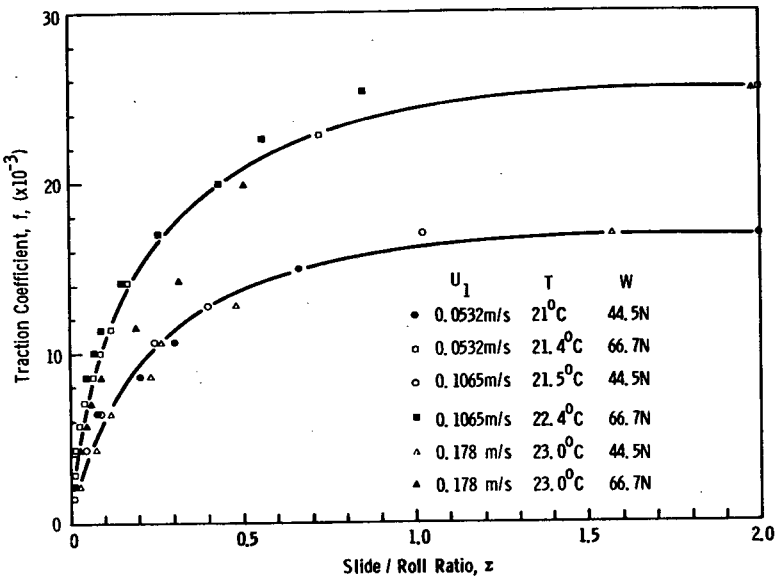

Figure 29. Traction coefficient against slide/roll ratio for dimethylsilicone (100 cS)

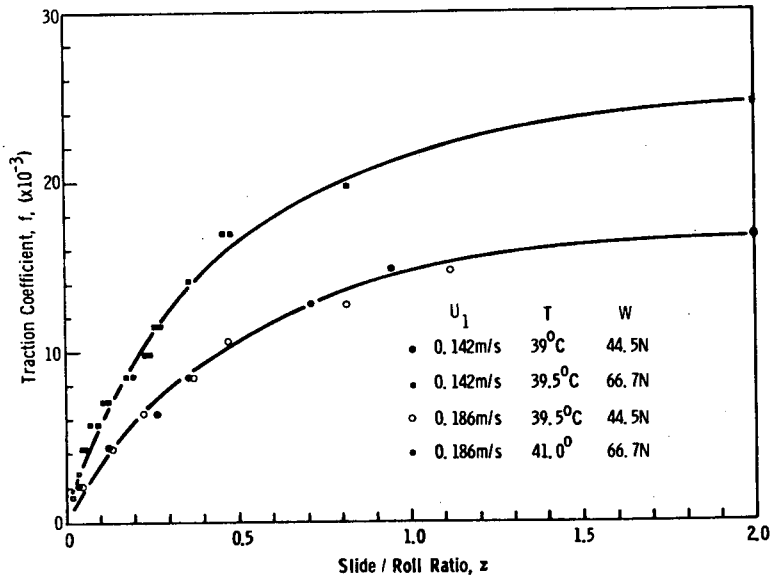

Figure 30. Traction coefficient against slide/roll ratio for dimethylsilicone (100 cS)

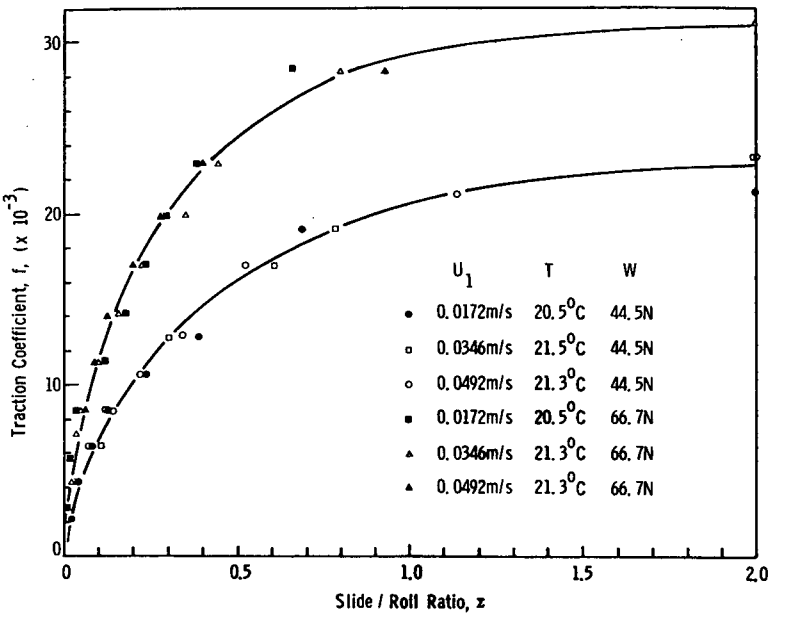

Figure 31. Traction coefficient against slide/roll ratio for dimethylsilicone (1000 cS)

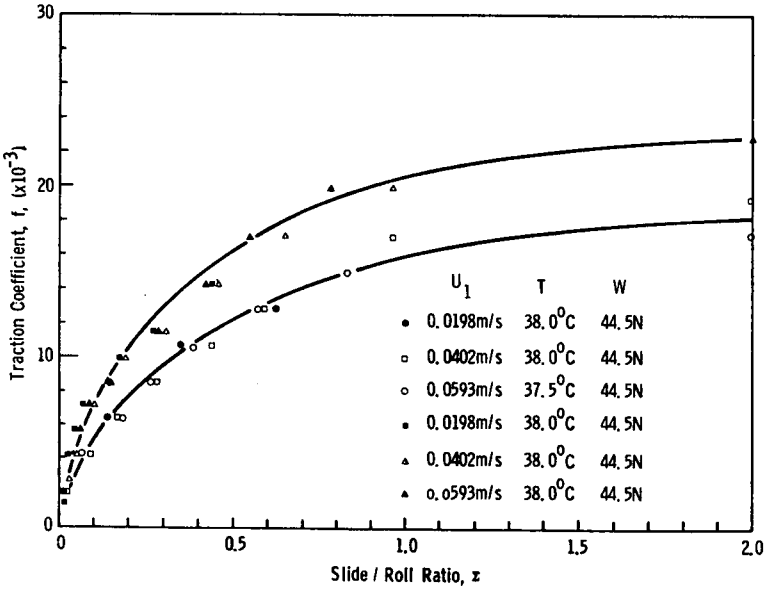

Figure 32. Traction coefficient against slide/roll ratio for dimethylsilicone (1000 cS)

4. FILM THICKNESS IN LINE CONTACTS

4.1 SCOPE OF WORK

An elastohydrodynamic line contact between a tapered roller and a glass disk was studied under conditions of almost pure rolling using four of the test fluids supplied for evaluation (a,b,e and q). Film thickness and shape were measured by optical interferometry. Film thickness was simultaneously measured by a capacitance method, and the results of the two methods were compared. Loads of up to 2,420 N (540 lbf) were applied giving a maximum Hertz pressure of up to $8.89 \times 10^8 Nm^{-2}$ ($128,850$ lbf-in^{-2}). Measurement of the low voltage electrical resistance of the oil film gave some information on asperity contacts, and the effect of the roller end profile on film shape was also investigated.

4.2 TEST RIG

4.2.1 General Description

Fig. 33 shows a schematic view of the rig. The single tapered roller runs between an upper, flat glass disk and a lower, angled steel race. The steel race is driven via a light chain from a motor and gearbox. The roller is kept in one position by a restraining arm, causing the glass disk to counter-rotate. The glass disk is loaded locally against the roller by a pneumatic loading device acting through an oil hydrostatic thrust bearing. The steel race is supported by a heavy series ball thrust bearing.

The glass disk is attached by a self aligning bearing to a central shaft, which is free to move vertically in a guide (Fig. 34). This allows the glass disk to align itself with the roller. Perfect alignment is essential for uniform load distribution along the length of the contact. The weight of the glass, central shaft and other attachments is supported by an adjustable compression spring.

The steel race is fitted with an oil seal at its center and a lip around its perimeter in order to keep the lubricant in good supply around the contact. It has nonetheless proved difficult to maintain fully flooded conditions at high speeds, and this has made it difficult to make measurements at mean surface speeds above 1.25 m/s (50 in/s).

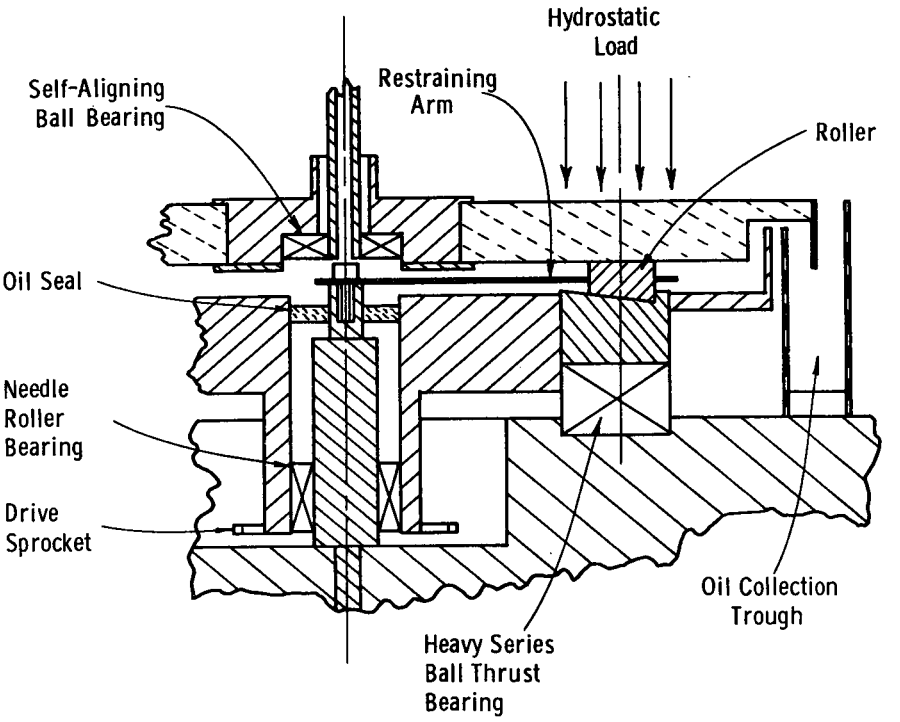

Figure 33. Schematic view of line contact rig

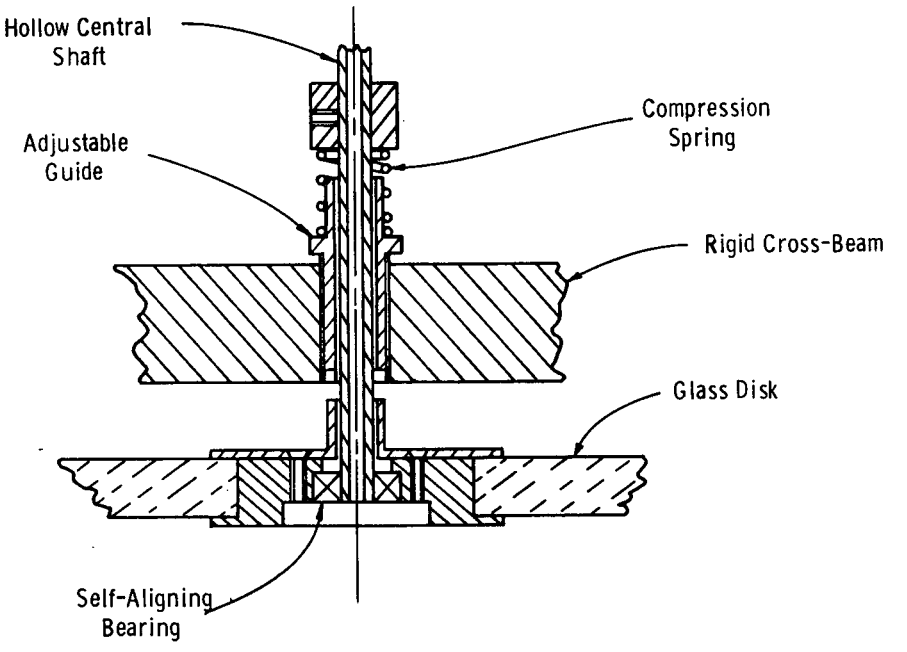

Figure 34. Method of mounting glass disk

The contact is viewed through the loading systems and glass disk using a specially designed long working distance microscope and incident illuminator. A semi-reflecting layer of chromium is vacuum deposited onto the lower surface of the glass disk, to allow the formation of interference fringes. Electrical connections are made to the roller and chromium coating via mercury contacts to allow measurement of capacitance and resistance across the film.

4.2.2 Motor Drive and Speed Measurement

The steel race is driven by a 1/5 H.P. D.C. electric motor via a 50:1 worm gearbox and chain drive. The size of the chain sprocket on the gearbox can be altered to give a 1:1 or 2:1 ratio, giving an overall speed reduction of 50:1 or 100:1. The motor speed is controlled by a rectified autotransformer giving a speed range of about 500:1 with an accuracy of about 2% over all except the lower end of the range. A thyristor control with tachometer feedback would have been more precise, but it was found to cause too much electrical disturbance when making capacitance measurements.

The speed of the steel race was measured by a magnetic transducer positioned next to a 120 tooth gearwheel on the motor shaft. The transducer output was fed into a digital counter, which displayed the number of pulses received per minute. Knowing the speed reduction ratio, the speed of the race was easily found. The speed of the glass disk was measured by timing a given number of revolutions.

Assuming no slip takes place, the geometry predicts that the speeds of the disk and steel race should differ by less than 1%. This is within the limits of accuracy of speed measurement and is therefore neglected. Within the ranges of load and speeds used, the slip between the steel race and glass disk was found to be always less than 5%, and in most cases was less than 2%. Although the speed of the roller could not be measured directly, it seemed safe to assume that its speed was near the average of its upper and lower races, and so no significant error would be introduced by estimating the mean surface speed in the contact to be that of the lower race. All subsequent speed measurements were therefore taken directly from the digital counter.

4.2.3 Loading System

4.2.3.1 General Description

Fig. 35 shows a diagram of the loading system. It consists of a piston and cylinder arrangement, operated by pneumatic pressure, pushing downwards on to the glass via a single pocket hydrostatic thrust bearing. In order to follow any runout in the rotating parts underneath without load fluctuation, the piston must be able to slide with very little friction, and for this reason it is located in the cylinder by a double row air journal bearing, the piston itself acting as the inner member. A neoprene rolling diaphragm acts as a seal at the top, and the air pressure inside the piston acts as a supply for the air bearing. The hydrostatic bearing and the top casing are fitted with glass "windows" to allow the contact to be viewed with the microscope.

4.2.3.2 Piston and Air Bearing

The pressure inside the piston is continuously variable from 0 to 8.275×10^5N m^{-2} (120 lbf in^{-2}) by an accurate pressure controller. This gives a maximum downward force of 2,420 N (540 lbf). The air bearing consists of two rows of 12 holes accurately drilled to 3.56×10^{-4}m (0.014 in). The clearance in the bearing is about 5.08×10^{-5}m (0.002 in). At low loads, the air bearing has to operate below the pressure for which it is designed, but this is not important because at such loads the compliance of the hydrostatic bearing is large enough to take up the run-out without drastic load fluctuations.

4.2.3.3 Hydrostatic Thrust Bearing

This is a single rectangular pocket bearing with an effective load carrying area of approximately $6.45 \times 10^{-4}m^2$ (1 in^2). At the maximum load of 2,420 N (540 lbf) the required oil pressure is about 3.08×10^6N.m^{-2} (450 lbf in^{-2}). The oil supply is provided by a two stage gear pump running at 900 rpm. The output is about $1.5 \times 10^{-4}m^3/s$ (2 imperial gallons per minute).

The oil is cooled and filtered, and the supply to the bearing is regulated by orifice restrictors, (Fig. 36). One restrictor is in the supply line and prevents the flow from exceeding the rate of return from the collection trough when the load is zero. The other restrictor is placed in a by pass line to ensure that the flow to the bearing is enough to generate a film thickness of about 2.54×10^{-5}m (0.001 in) when the bearing is under maximum load.

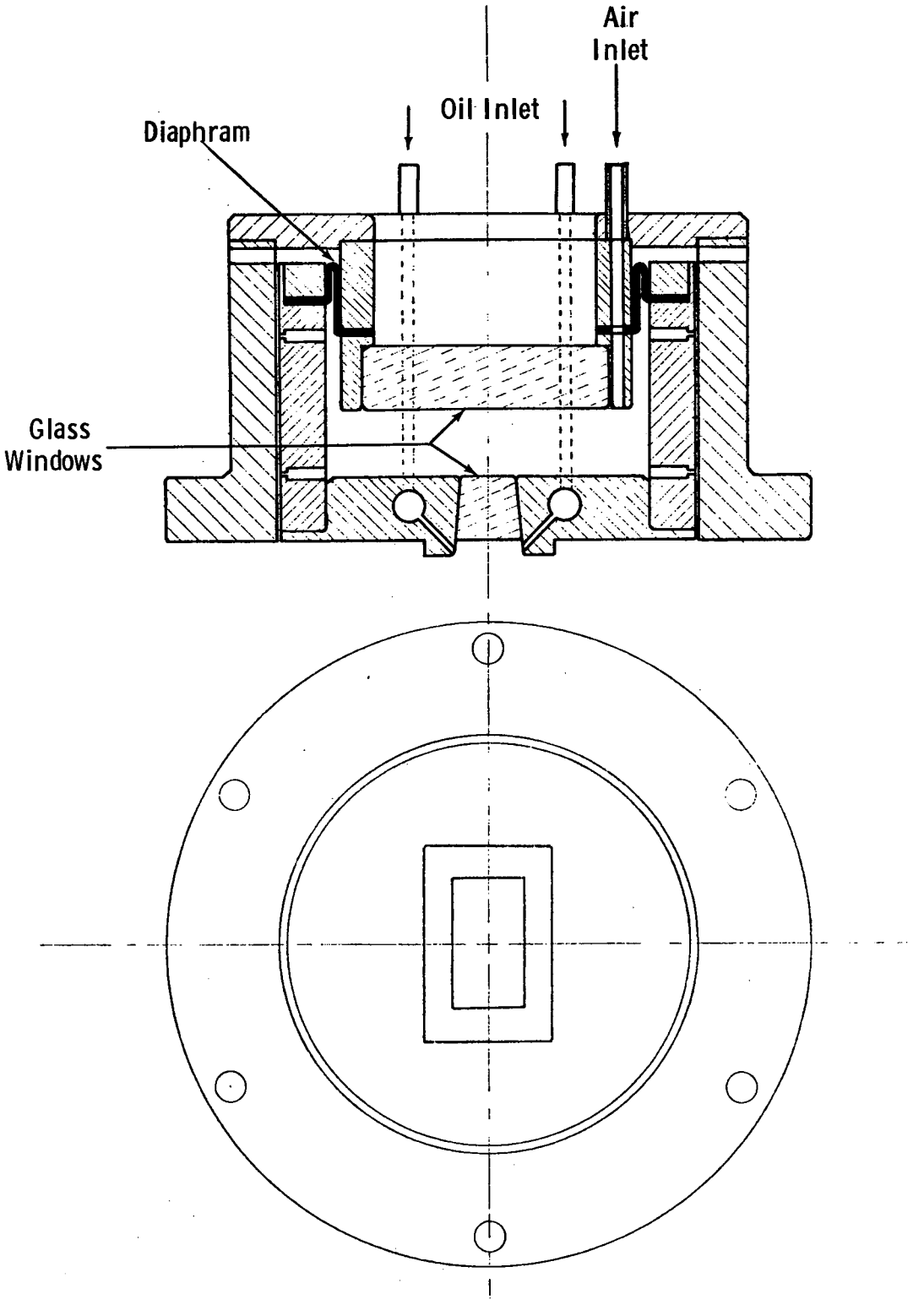

Figure 35. Loading system

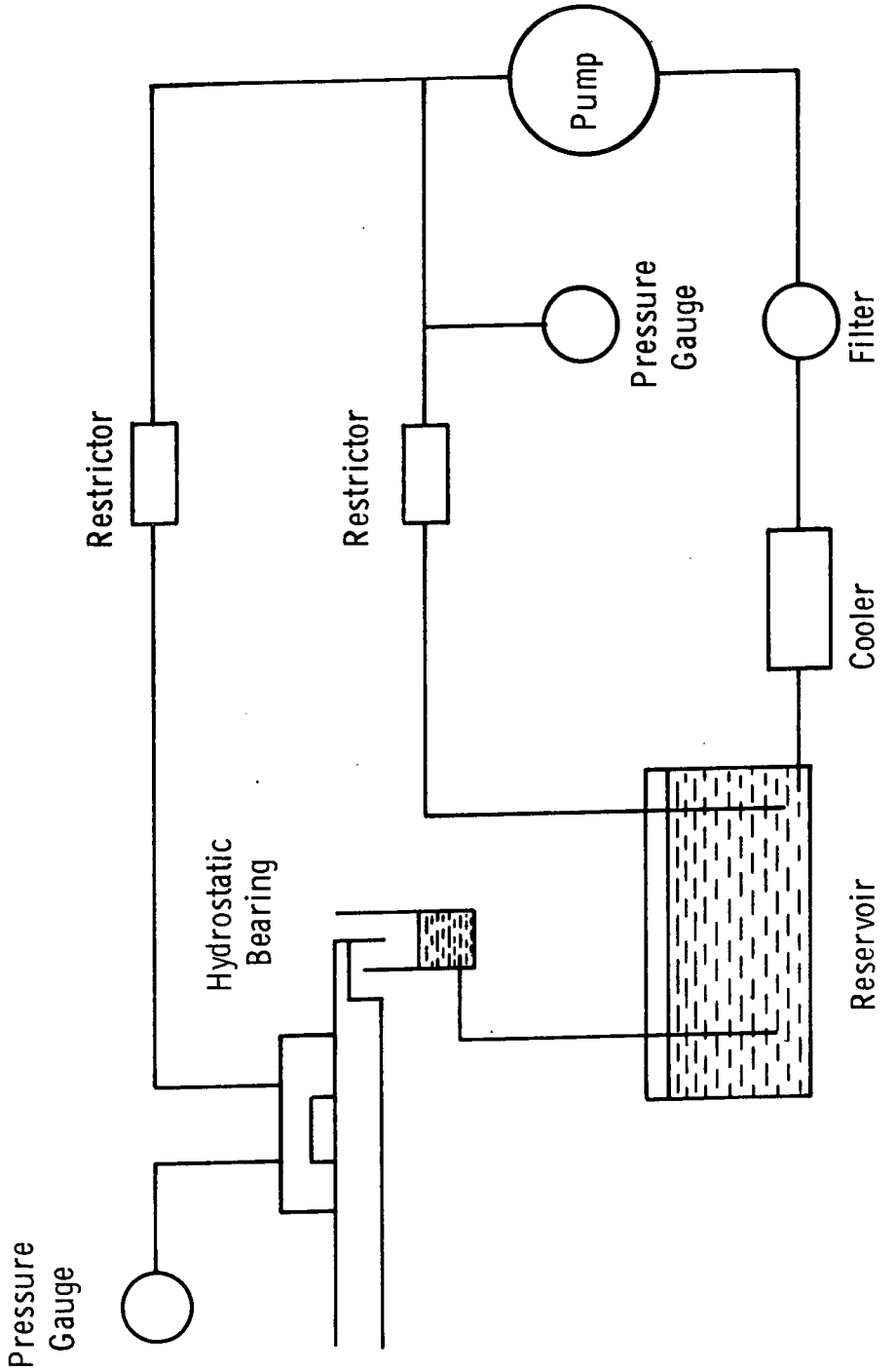

Figure 36. Hydraulic circuit

4.2.4 Optical System

4.2.4.1 Formation of Interference Fringes

The roller surface is highly polished to provide good reflectivity. This is achieved using diamond paste, and the surface roughness is estimated at 2.54×10^{-8}m (1 microinch) center line average. It is not possible to obtain as good a finish as that on steel balls because of the difficultv in preserving the geometry. The reflectivity is estimated at 50% at best in oil compared with about 60% for a 2.54×10^{-2}m (1 in) ball, and a few scratches are also visible.

The glass disk is optically polished, and the faces are parallel to within 2.54×10^{-6}m (0.0001 in.). The lower face is coated with a semi-reflecting layer of chromium, vacuum deposited while the glass is hot (140°) to provide greater adhesion. The layer gives about 44% transmission and 22% reflection in air. These values change to about 52% and 14% respectively in oil. Assuming 50% reflection at the roller surface, this gives two interfering beams of almost equal intensity, which is the condition for maximum fringe visibility.

Two beam interference fringes are formed in the usual way (see Fig. 37) between the chromium layer and the roller surface, following the relation:

$$N\lambda = 2\,nh \cos \theta + \phi, \qquad (21A)$$

where h is the thickness at the Nth dark fringe, and ϕ is a constant to account for the phase change at the chromium layer. (The phase change at the steel surface is assumed to be π). This relation relates to monochromatic fringes, using light of wavelength λ. Most of the measurements were made using duochromatic light (red and green). The effect of this is to produce two sets of fringes superimposed on one another, and the resulting pattern contains various mixtures of red and green fringes. This makes fringe order more easily identifiable and was first used by Wedeven.[9]

The chromium layer is covered by a layer of silicon oxide* of thickness 198nm (1980 Å). This is used for capacitance measurements, and being transparent, has no effect optically apart from acting as a 'spacer' layer. Its effect is automatically taken into account during fringe calibration.

---

* Vacuum deposited film of silicon oxide have the general composition SiO_n where n is between 1 and 2.

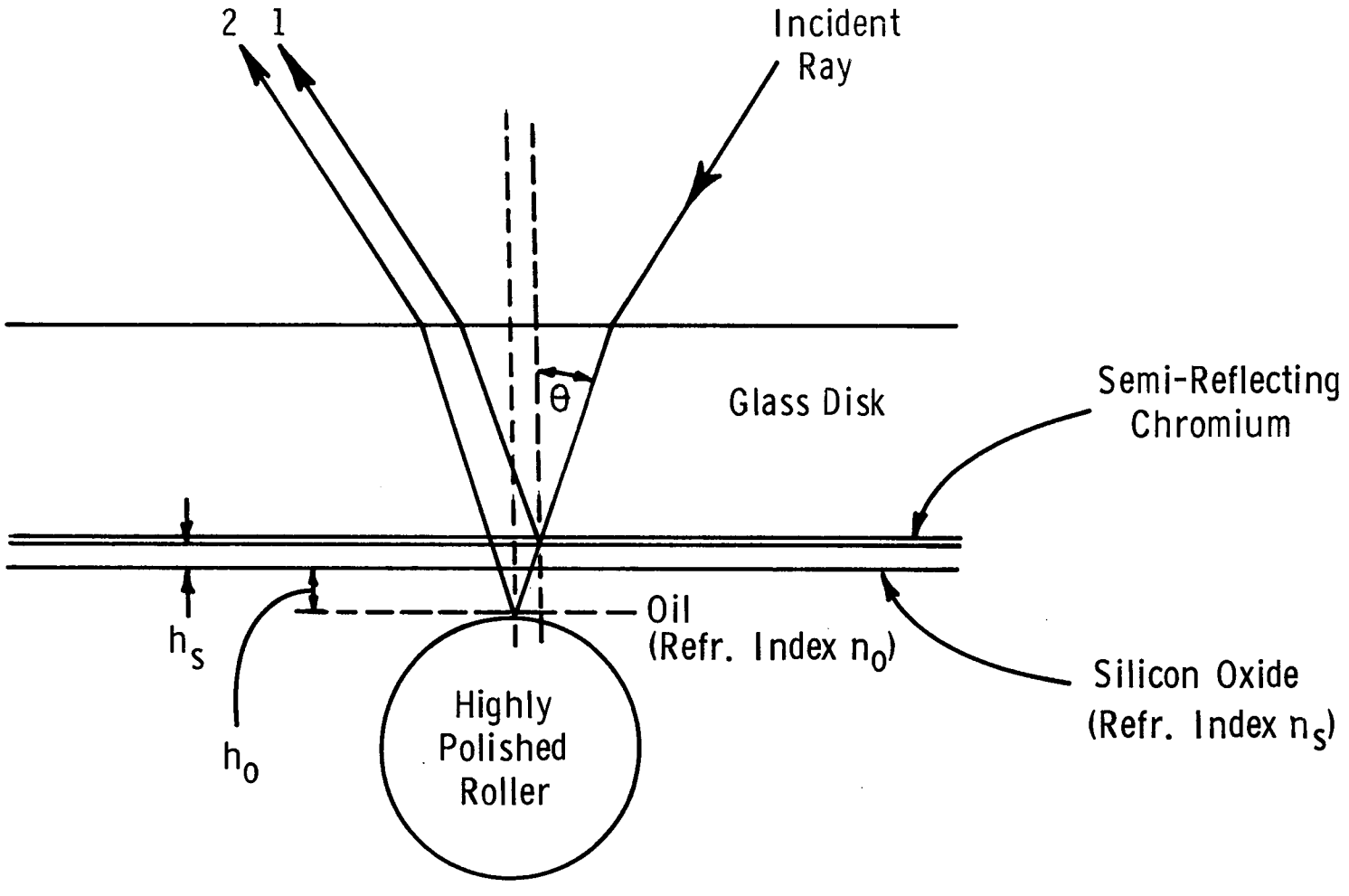

$$N\lambda = 2nh \cos\theta + \phi, \text{ where } nh = n_0h_0 + n_sh_s$$

Figure 37. Formation of two-beam interference fringes

4.2.4.2 Microscope and Illuminator

A magnification of up to X200 is required, and the working distance has to be about 5.08 x 10^{-2}m (2 in) in air due to the space taken up by the loading system. No commercial microscope satisfied these requirements, and so a special purpose microscope was designed and built. A schematic diagram is shown in Fig. 38. The objective lens (A) is a conventional X 10 achromatic doublet scaled up four times. This has the effect of increasing the working distance from 1.27 x 10^{-2}m (1/2 in) to about 5.08 x 10^{-2}m (2 in) while keeping the same magnification. However, the tube length now becomes about 5.08 x 10^{-1}m (20 in) which is inconvenient. A pair of lenses (B,C) are therefore introduced which considerably shorten the physical tube length without affecting the optical tube length. A conventional eye piece (D) is used to provide secondary magnification of up to X 20.

Incident illumination is provided via a 45° semi-reflecting mirror, coated with titanium dioxide, The light source is a 100 watt, 12 volt quartz iodine lamp, (for visual work) or a 100 joule xenon flash tube (for high speed photography). The collimator is a modification of a design by Hopkins, described in Ref. 9, which gives control over the size of field and the degree of collimation. The latter also affects the intensity of illumination.

All glass/air interfaces are coated with quarter-wavelength thicknesses of magnesium fluoride to cut down reflections.

High speed photographs are taken using a 35 mm single lens reflex camera with an adaptor and extension tubes to fit the microscope tube. If the eyepiece is retained, the field of view is rather small, and best results are obtained without an eyepiece. In this case, the magnification is determined by the length of extension tubes. A xenon flash tube gives a maximum of 100 joules in 1 millisecond. The discharge is run from a 1,000 volt discharge unit, having a bank of six 33 μF capacitors. The energy of the discharge can be varied by altering the number of capacitors connected, and this method is used to obtain the correct exposure. Black and white photographs are taken using a nominally 400 A.S.A. film which is uprated to 650 A.S.A. by using a high speed developer.

Duochromatic light for visual work is produced by inserting a Wratten 77A filter in the collimator tube. This gives two discrete wavelengths at 546 and 630 nm (5460 and 6300 Å). For black and white photography an additional filter, Wratten 74, is inserted. This blocks the red light, leaving only the green at 546 nm (5460 Å).

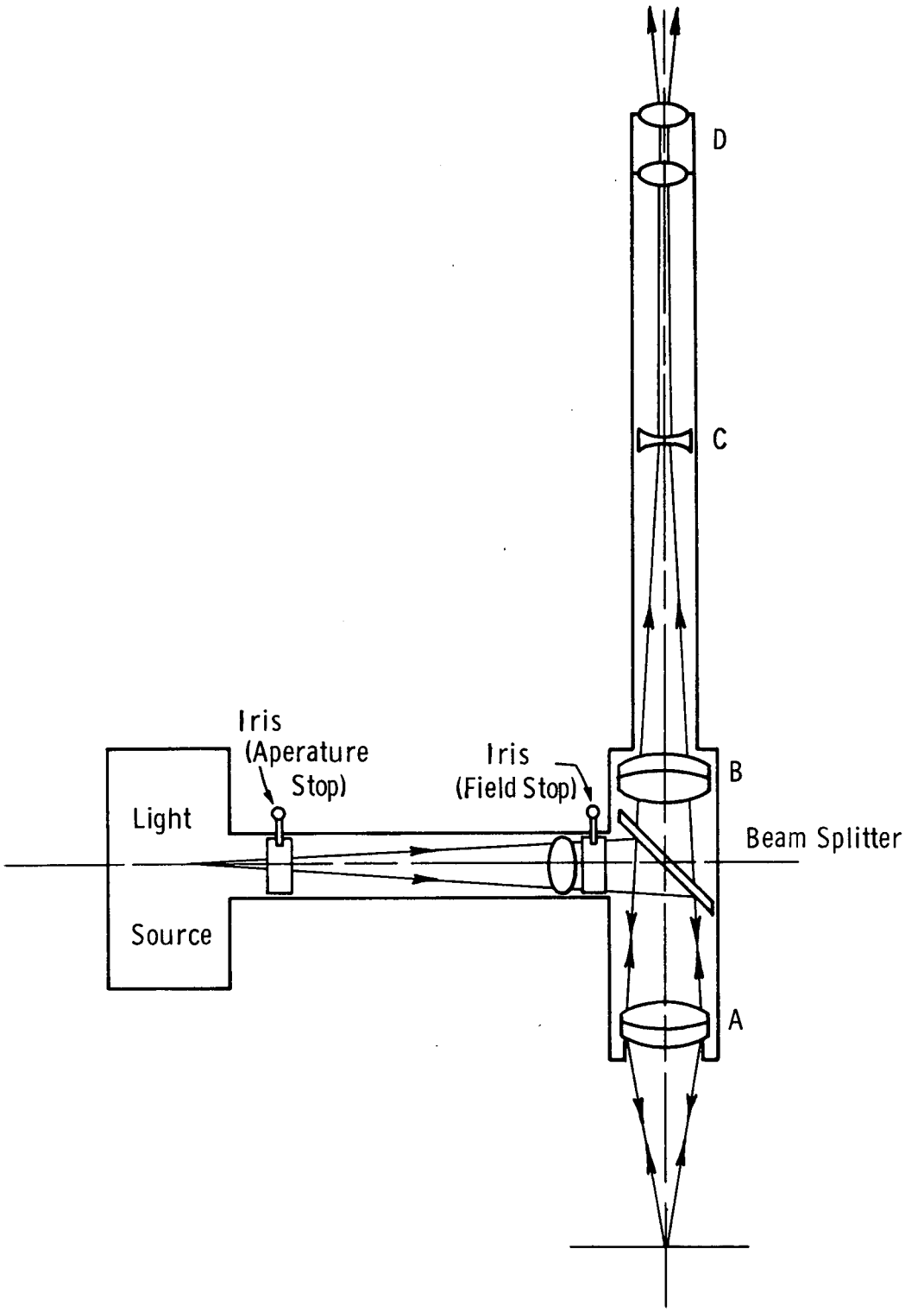

Figure 38. Long-working-distance microscope (schematic)

4.2.5 Electrical Connections

Electrical connections are made to the roller and chromium layer by means of mercury contacts, shown diagrammatically in Fig. 39.

The roller has a hole through the center into which is pressed a copper sleeve, closed at one end. The closed end is soldered to the roller. The copper sleeve contains a small amount of mercury, and a copper wire intrudes into the open end and makes contact with the mercury. It has been found that there is no need to seal the mercury in, because it wets the copper and is thus held inside by its own surface tension.

The central region of the chromium layer is covered by an annular coating of gold during the vacuum-deposition process. This allows a soldered connection to be made, and ensures good contact with the chromium. A wire is led up the inside of the central shaft and the external connection is made through a screened mercury contact.

Both sides of the capacitor must be insulated from the rest of the rig, which is earthed to act as a screen. This necessitates the addition of 'Tufnol' bushes between the base plate and the bearing races. These are at least 3.17×10^{-3} m (1/8 inch) thick to minimize stray capacitance.

4.3 OPTICAL MEASUREMENTS

4.3.1 Calibration of Fringes

The method of calibration was to observe the position of duochromatic fringes in a system of known geometry, using similar bounding surfaces to those in the rig. The roller and glass disk themselves were not used because the small radius of curvature made it difficult to position fringes accurately. Instead, a plano-convex glass lens of radius 18.3 m (60 feet) was placed against an optically polished steel flat. Monochromatic light of wavelength 546 nm (5460 Å) (from a mercury lamp) was used to form air fringes (concentric rings) in the narrow wedge between the glass and the steel. The arrangement is shown in Fig. 40. The aspheric lens was adjusted to give parallel light and this was reflected by the semi-reflector onto the glass at normal incidence. The fringes were observed through the camera, using a bellows attachment to focus. A color transparency was taken, and projected onto a screen. The diameters of the rings were measured and plotted against thickness, which could be deduced from

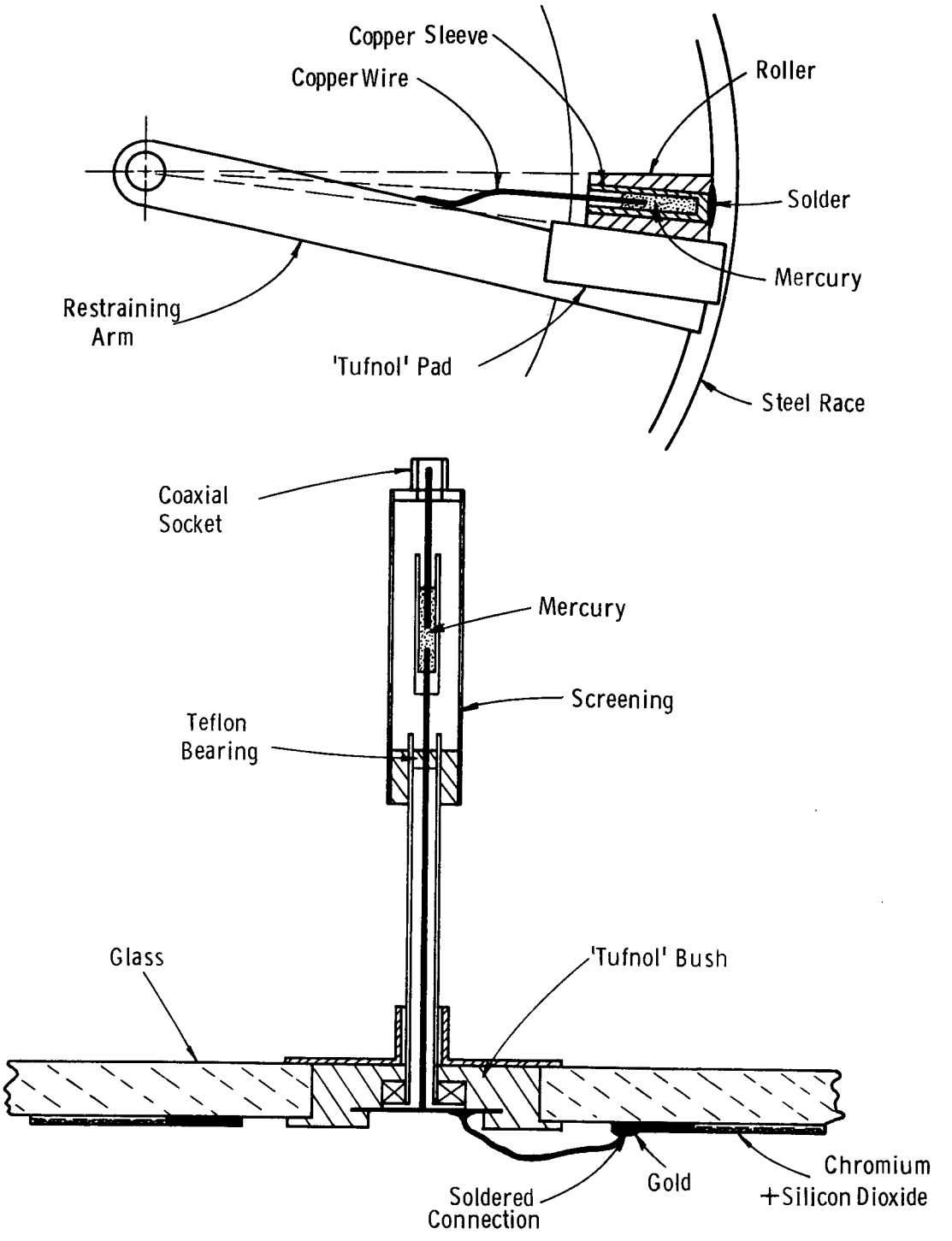

Figure 39. Electrical connections

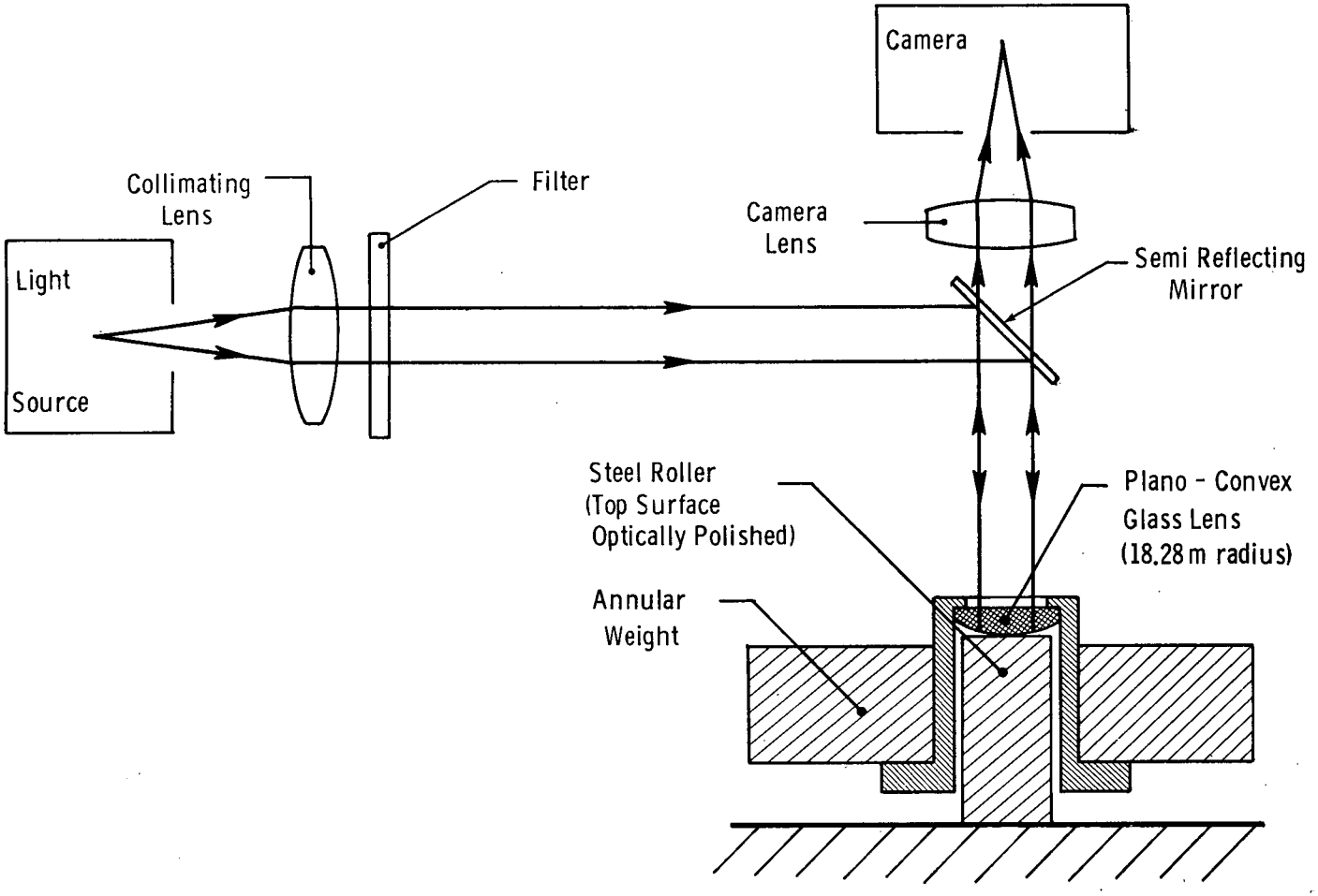

Figure 40. Calibration of fringes

$$N\lambda = 2\, n\, h \cos\theta. \qquad (22)$$

In this case, θ is zero assuming no phase change at the glass/air interface and n is unity, so the relation reduces to:

$$N\lambda = 2\, h. \qquad (23)$$

The curved surface of the glass was then coated with chromium and silicon oxide in the same operation as the glass disk from the rig. This ensured that the coatings were identical. The coated lens was then replaced on the steel flat, but this time the gap was filled with oil of known refractive index. The mercury lamp was replaced by the quartz iodine lamp from the rig, and the 77A filter inserted to give duochromatic light. A color transparency of the duochromatic fringes was made and projected to exactly the same size as the first transparency, using the diameter of the lens as a reference. The diameter of the fringes were measured, and the corresponding thickness was read off directly from the graph after correcting for the refractive index of the oil. The result is given in Fig. 41. Thicknesses relate to air (n =1), so they must be divided by the refractive index of the oil being tested.

4.3.2 Measurement of Film Shape

Fig. 42 show photographs (taken with monochromatic light and without the silicon oxide layer) of the fringe patterns at the end of a flat roller, i.e. one with no end blend. The direction of lubricant flow is from top to bottom. Noticeable features are:

(a) A rear closure running the length of the Hertzian region and broadening with increasing speed.

(b) A much more severe end closure again broadening with increasing speed. The minimum film thickness seems rather insensitive to speed.

(c) Broadening of the Hertzian region at the end of the roller due to a local stress concentration.

The photographs were measured with a traveling microscope to give the film shape along axial and transverse sections. The results are plotted in Figs. 43 and 44.

4.3.3 Variation of Film Thickness with Speed

4.3.3.1 Central Film Thickness, h_o

The fringe colors of the central region were observed at various speeds and at two loads. Duochromatic light was used,

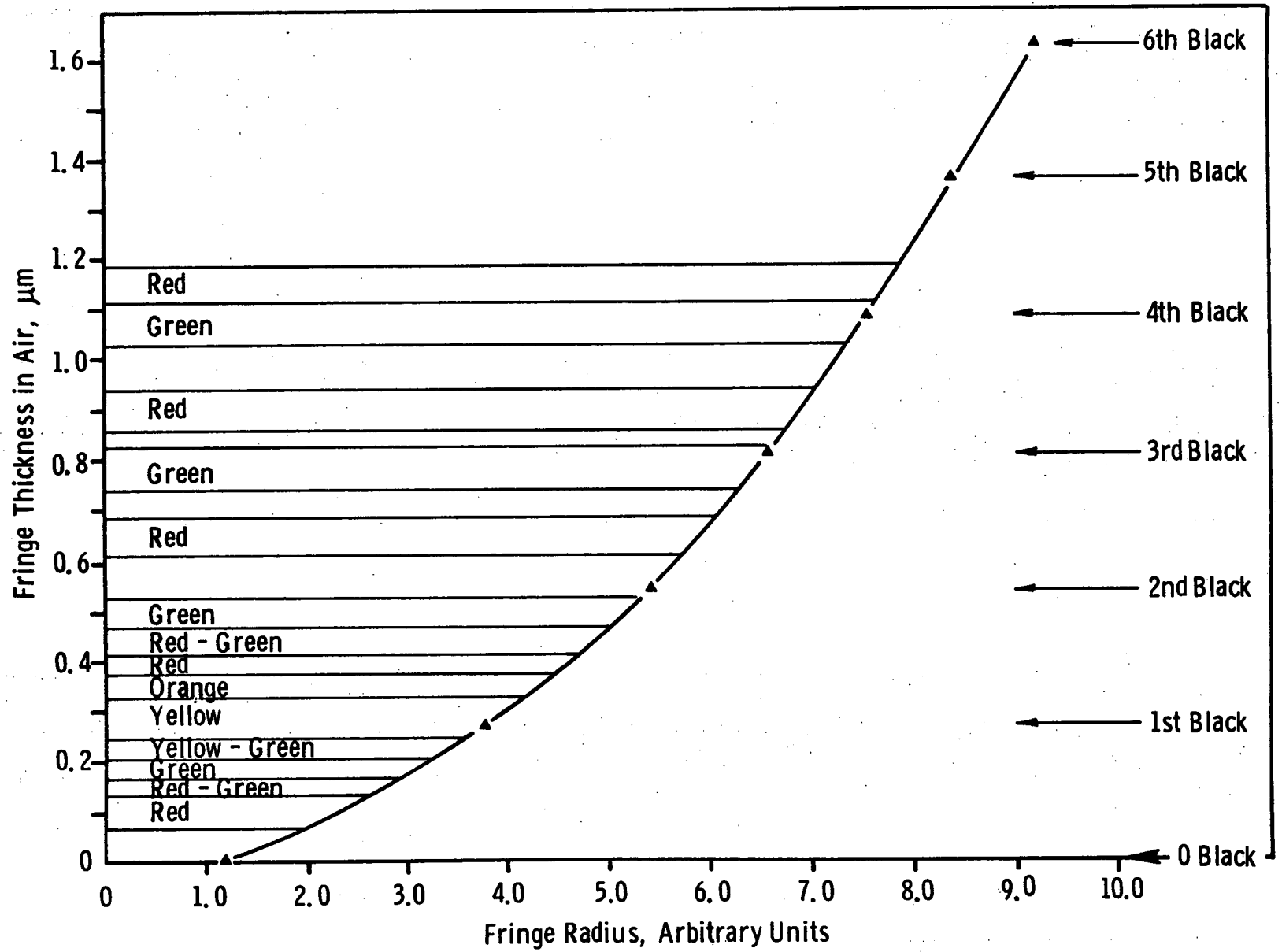

Figure 41. Fringe calibration

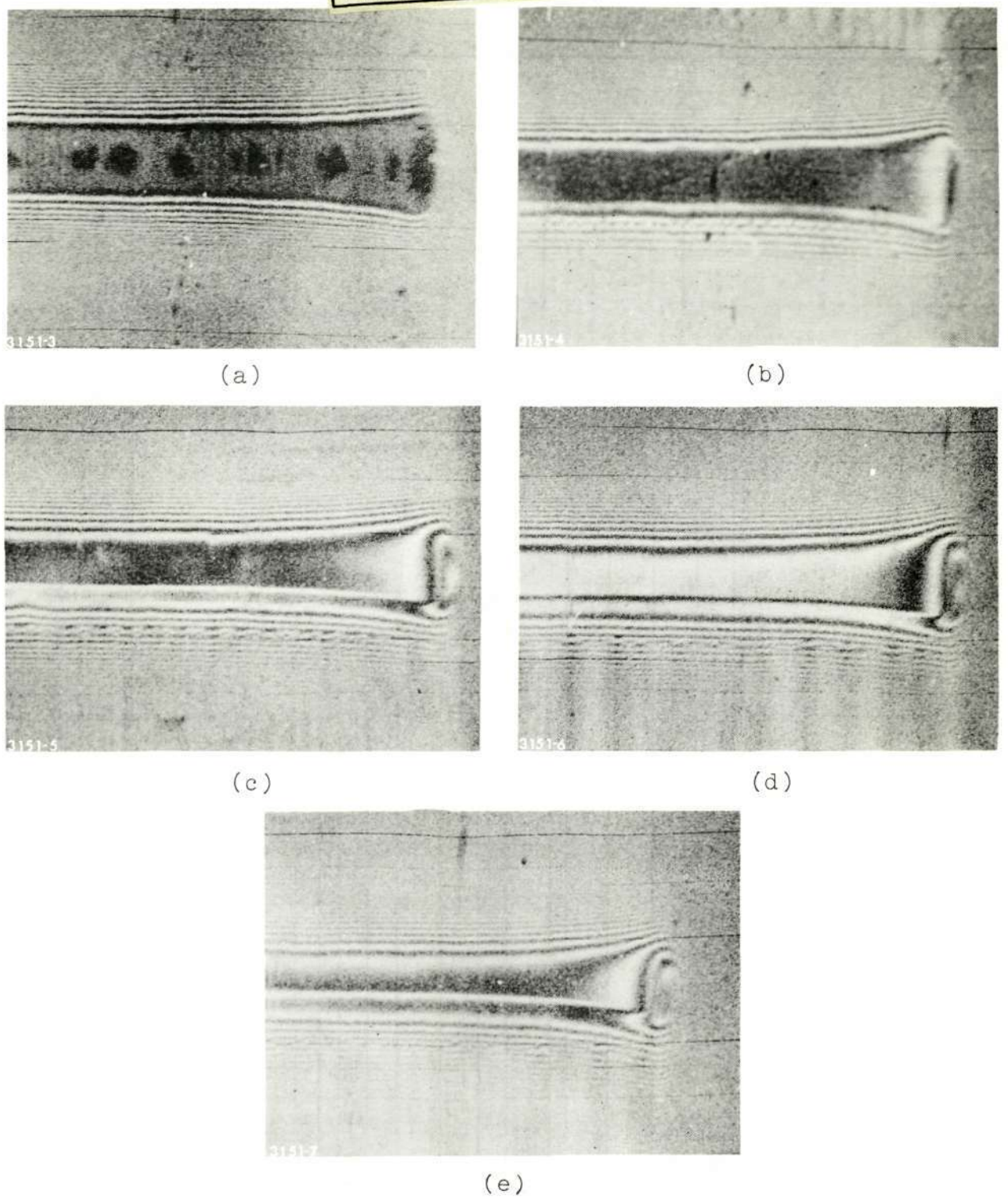

(a) (b)

(c) (d)

(e)

Figure 42. Interference photographs of a line contact. For each the load is 458 N; the speeds are as follows: (a) zero, (b) 0.120 m/s, (c) 0.544 m/s, (d) 0.919 m/s, and (e) 1.64 m/s

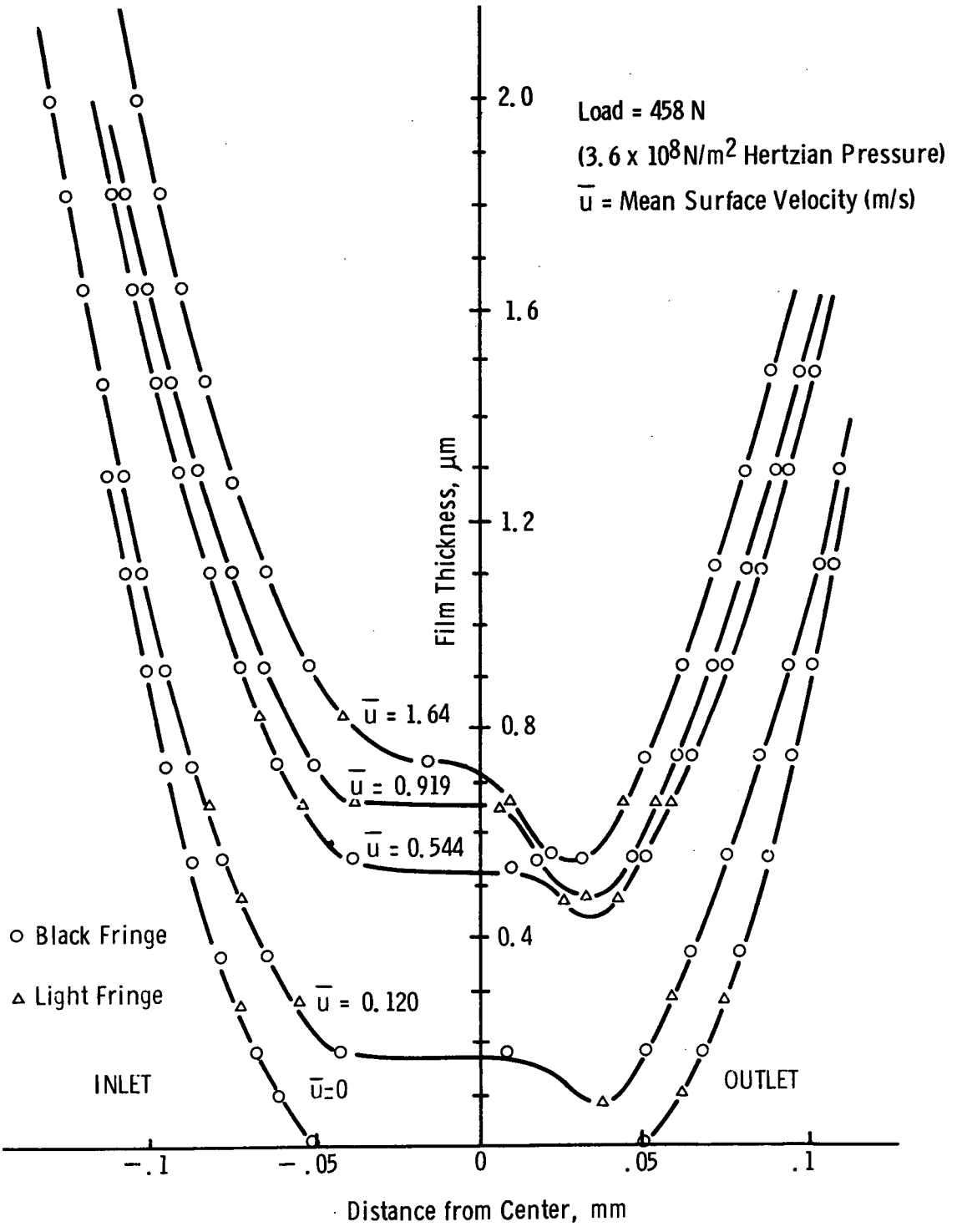

Figure 43. Film shape profile; line contact, transverse section

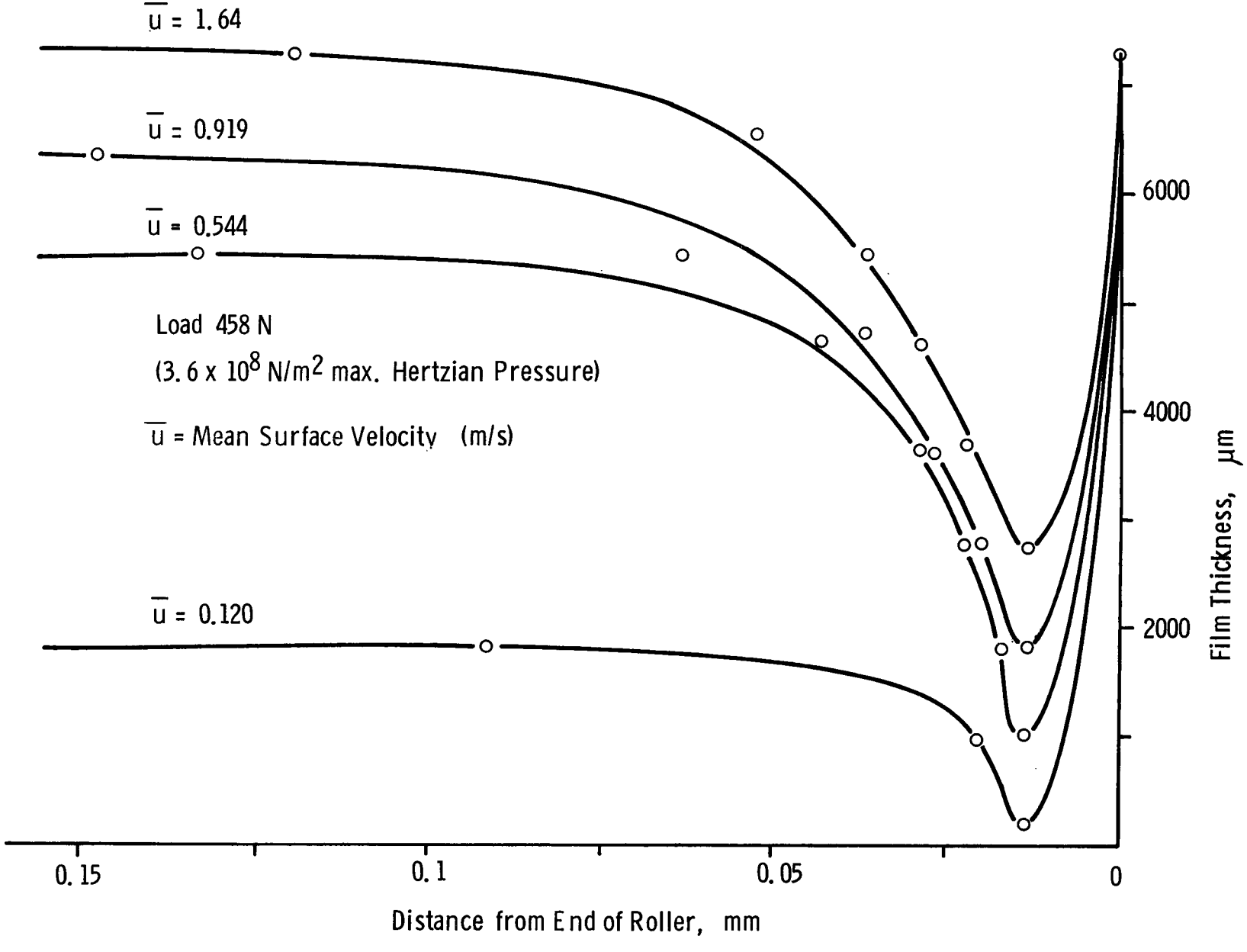

Figure 44. Film shape profile; line contact, axial section

and a silicon oxide layer enabled simultaneous capacitance measurements to be made. Four of the test fluids, a,b,e and q, were used. The temperature of the oil in the inlet region was measured with a small thermocouple placed as close as possible to the contact, and was read from an electronic thermometer. The thermometer was checked against melting ice before each run, and adjusted if necessary.

The results were converted into the usual non-dimensional form, with parameters h_o/R and $\bar{u}\eta_o/E'R$.

The central film thickness, h_o, was evaluated by finding the thickness in air from the fringe calibration chart and dividing by the refractive index, n,of the oil. The value of n was calculated from the refractive index at atmospheric pressure, n_o, using the following relations:

$$n^2 = \frac{1+2A}{1-A} \quad , \tag{24}$$

$$\text{where } A = \frac{\rho}{\rho_o}\left(\frac{n_o^2-1}{n_o^2+2}\right) \tag{25}$$

The density ratio, ρ/ρ_o, was calculated from the Hartung relations:

$$\rho/\rho_o = 1 + \frac{42.8\times10^{-6}}{(\nu_{100})^{0.0385}}.p \tag{26}$$

where ν_{100} is the kinematic viscosity in centistokes at 37.78°C. (100°F.), and p is the average Hertzian pressure. The value of n_o used was that at the temperature of the inlet region at the time of the reading. It was found by linear interpolation between known values at two temperatures.

The value of R used was that at the mid-point of the roller, where all measurements were made, and was measured to be 0.00406 m.

The value of E' was calculated to be 1.20×10^{11} N m^{-2} (17.37×10^6 lbf/in^2).

The viscosity at the inlet, η_o, was found at the test temperature using the Walther-A.S.T.M. formula

$$\log \log (\nu + 0.6) = K - c \log T, \tag{27}$$

where ν is in centistokes and T is the absolute temperature (°K). The constants K and c were found by substituting known values of ν at two temperatures.

2

4.3.3.2 Film Thickness at the Narrowest Point of the Rear Closure, h_{min}

This was measured in exactly the same way as the central film thickness, although the fringe color was much harder to detect since the area under observation was much smaller. Measurements were made on fluid e only, at the same time as the central film thickness measurements.

4.3.3.3 Discussion of Results

Figures 45, 46, 47 and 48 show film thickness versus speed, plotted non-dimensionally. Fluid a and b form rather thin films, and consequently there is a large uncertainty in the film thickness at the lower speeds. However, the points tend to follow straight lines, and their slopes are measured to be approximately:

Fluid	a:	Slope = 0.6
"	b:	" = 0.66
"	e:	" = 0.57
"	q:	" = 0.5

The relatively few readings for fluid q (Fig. 48) may account for the relatively low slope for this lubricant. With the exception of fluid q, however, the slopes are fairly close to the values obtained with point contact.

For fluid e, the minimum film thickness at the rear closure is also plotted non-dimensionally (Figs. 49 and 50) and shows a reduction in film thickness ranging from 13% to 20% (approximately). The largest reduction occurs at the slowest speeds. The reduction also appears to be slightly more severe at the higher load than at the lower.

An estimate for the pressure-viscosity coefficient α for fluid e was obtained from Dowson and Higginson's[23] film thickness formula:

$$H^*_{min} = \frac{1.6U^{*0.7}G^{*0.6}}{W^{*0.13}}, \qquad (28)$$

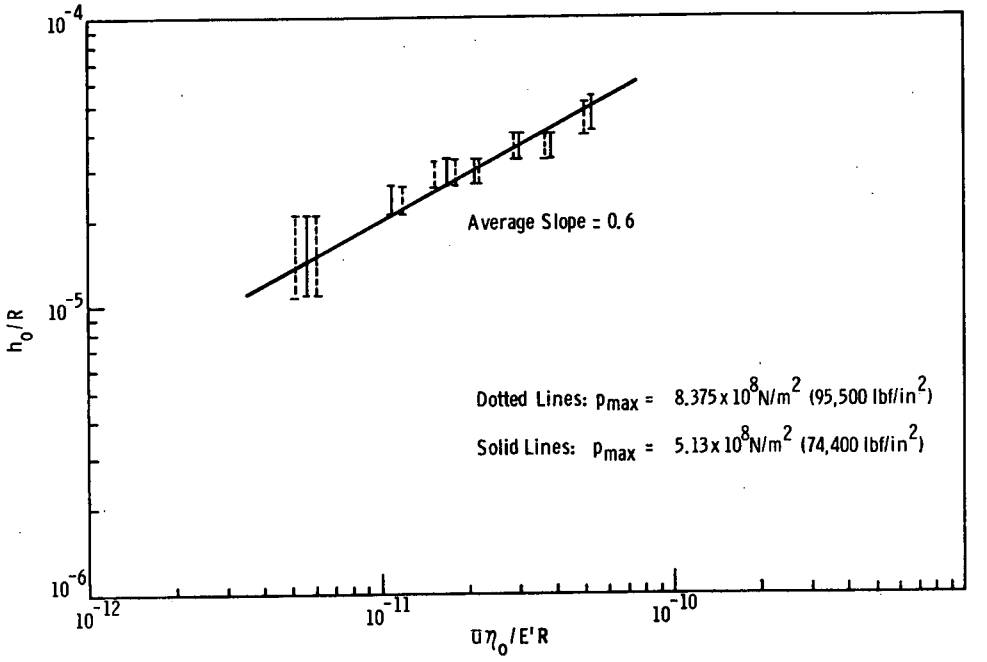

Figure 45. Central film thickness, Fluid a

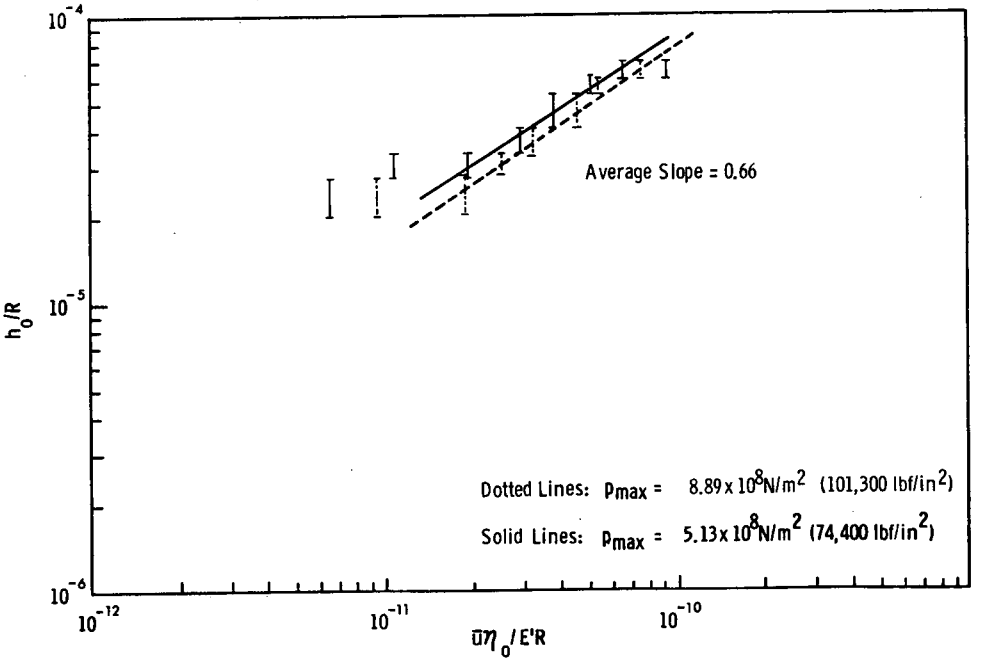

Figure 46. Central film thickness, Fluid b

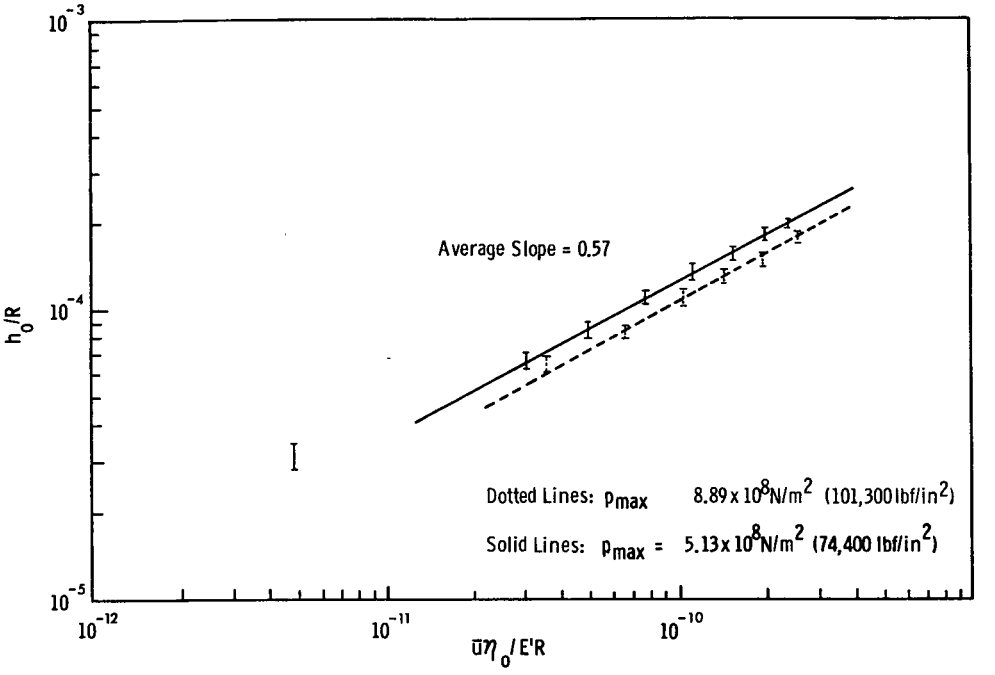

Figure 47. Central film thickness, Fluid e

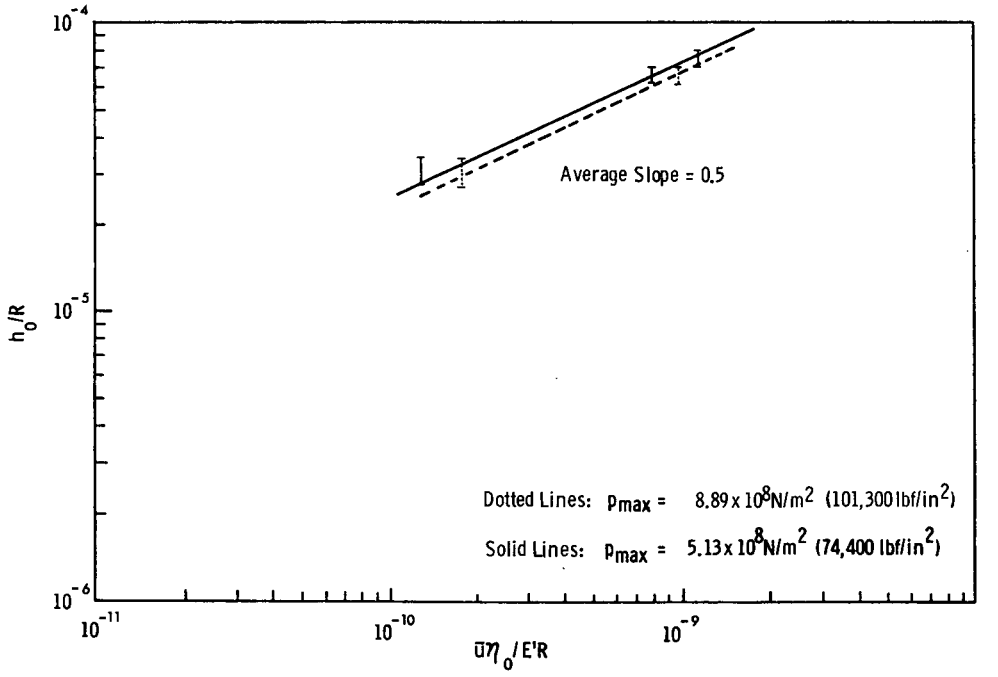

Figure 48. Central film thickness, Fluid q

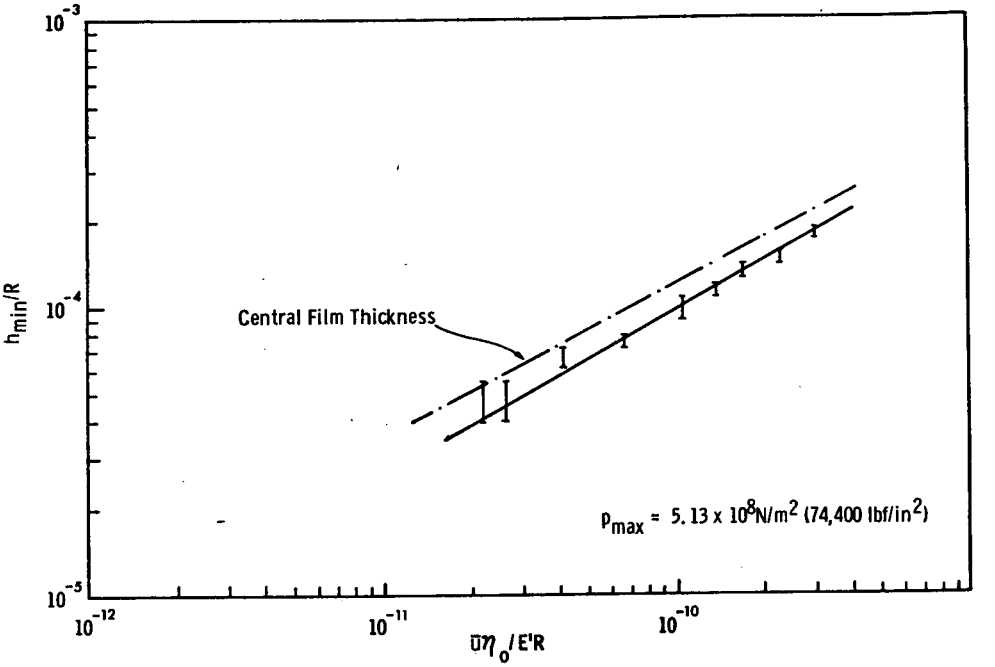

Figure 49. Minimum film thickness at rear closure, Fluid e

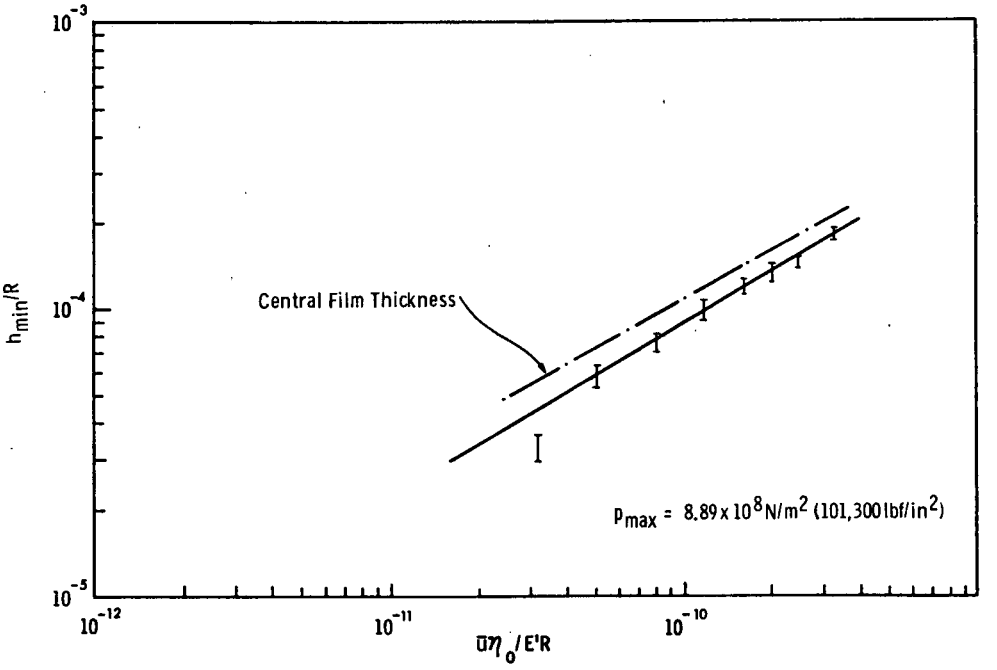

Figure 50. Minimum film thickness at rear closure, Fluid e

where

$H^*_{min} = h_{min}/R$, non-dimensional film thickness parameter,

$G^* = E'\alpha$, " " materials ",

$U^* = \bar{u}\eta_o/E'R$ " " speed ",

and $W^* = W/E'RL$ " " load ".

The curve chosen for measurement of U^* and H^*_{min} was that in Fig. 50, since this had the closest slope to 0.7. A value of 3×10^{-10} was chosen for U^* since this intersected the curve where uncertainties were least. At this point H^* was 1.75×10^{-4} and Eq. 28 gave $\alpha = 4.8\times10^{-8}$ m^2/N (3.3×10^{-4} psi^{-1}).

4.4 CAPACITANCE MEASUREMENTS

4.4.1 Measurement Circuit

The capacitance between the chromium layer and the roller was measured with an Audio Frequency Capacitance Bridge using an external source and detector. The measurement frequency was set at 20 kHz. The detector was a high gain tunable amplifier with a sensitivity of less than 1 μV. The output was fed into the Y amplifier of an oscilloscope, which was set for X-Y operation. The X plates were connected directly to the oscillator. This arrangement gave the form of an ellipse on the screen when the bridge was out of balance, and as balance was approached, the ellipse tended towards a horizontal line. This made the balancing procedure very easy because the major and minor components could be balanced out separately - the major component affected the orientation of the ellipse, and the minor component affected the length of its vertical axis. The complete circuit is shown in Fig. 51.

4.4.2 Silicon Oxide Layer

First attempts at measuring capacitance showed that the frequent bridging of the oil film by asperities was causing a great deal of disturbance to the wave form. This was particularly serious with fluids a,b, and q because they did not form very thick films. It was therefore decided to eliminate all asperity contact by covering the chromium with a thin layer of silicon oxide. This was tried out with a new disk, depositing the chromium and the silicon oxide in the same operation. The thickness of the silicon oxide was monitored during the operation and deposition was stopped when the thickness reached 198nm (1980 Å).

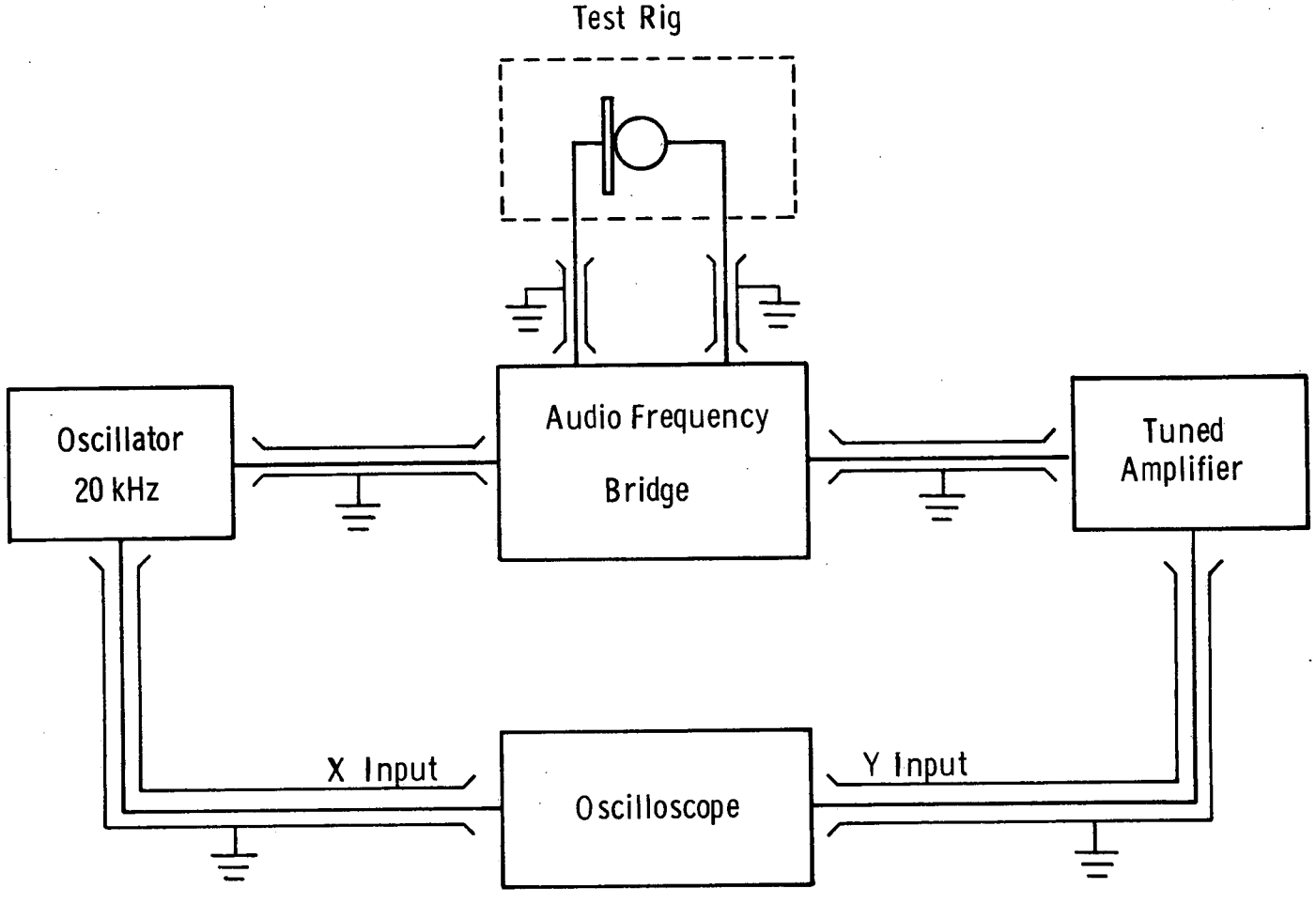

Figure 51. Capacitance measurement circuit

Another great advantage of using a silicon oxide layer is that the full bridge voltage (about 4 volts) can be applied without fear of electrical breakdown. Previously, the voltage had to be kept in the millivolt range, causing a drastic reduction in bridge sensitivity.

4.4.3 Measurement Procedure

Measurements were now quite easily made, and fluids a,b,e and q were evaluated. This was done at the same time as making the optical measurements, and as previously mentioned, runs were made at two loads.

4.4.4 Series Resistance of the Chromium Layer

The chromium layer has a surface resistivity of approximately 50 Ω/cm^2, and at 20 kHz this has a noticeable effect on the measured value of capacitance. The correction of the measured values to give the true values involve converting the parallel parameters of the bridge to the series parameters of the circuit.

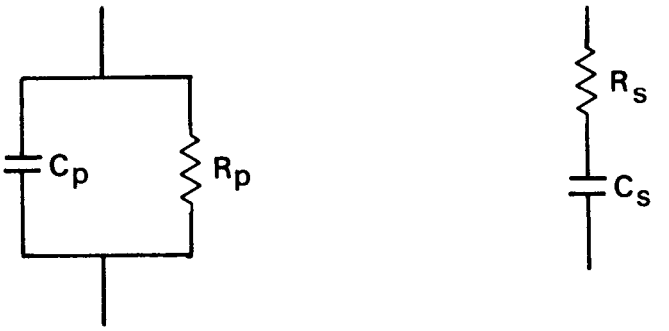

If the impedances of the above circuits are equated, and the real and imaginary parts are separated, we get:

$$\frac{1}{R_s} = \frac{1}{R_p}\left[1 + (\omega R_p C_p)^2\right], \text{ and} \qquad (29)$$

$$C_s = C_p\left[1 + \left(\frac{1}{\omega R_p C_p}\right)^2\right].$$

Thus by measuring C_p and R_p from the bridge we can find the capacitance of the oil film, C_s, and the series resistance of the

chromium, R_s. The value of R_s calculated from each measurement was found to vary only slightly and took the value R_s = 11,000 ± 1,000 ohms, which showed that the conversion was in fact valid. As a result of this, it is found that C_p becomes rather insensitive to changes in C_s, which makes the bridge rather more difficult to balance. An answer to this would seem to be to reduce the measurement frequency, whereupon the effect of the series resistance would become smaller. However, on taking a few measurements at 1 kHz and 8 kHz, it was found that they gave anomalous results. The reason for this was thought to be that relaxation effects were occurring in the silicon oxide, causing an unpredictable dielectric constant. These were probably caused by such things as ionic impurities and interfacial polarization which are known to have an effect at low frequencies. It was therefore necessary to keep the frequency at 20 kHz. It is suggested for future work that a more highly conductive film be tried instead of chromium, such as gold or silver. It is though that there should be a good chance of such a film remaining intact despite its softness, because of the protection afforded by the silicon oxide, which is extremely durable. It is also suggested that the thickness of the metallic coating be increased beyond the optimum value for fringe visibility. This would increase the conductivity at the expense of some fringe visibility.

4.4.5 Calculation of Film Thickness

The method is that used by Dyson, Naylor and Wilson[24] with certain modifications to take into account the silicon oxide layer. The problem is tackled by calculating the capacitance at various selected film thicknesses and drawing a calibration graph. The following assumptions are made:

(a) The shape of the surfaces is the same as in the Hertzian case of dry contact, but with the addition of a constant separation , (h_o+h_s), where h_o is the oil film thickness and h_s is the thickness of silicon oxide.

(b) The inlet and Hertzian sections of the film are completely filled with oil, but at the outlet section, the film of lubricant divides into two parts, each of thickness $h_o/2$, one part adhering to the roller, and the other to the glass disk, and the remainder of the outlet section is composed of air.

A diagram of the model is given in Fig. 52. The shape of the gap between the two surfaces, according to Hertz is given by

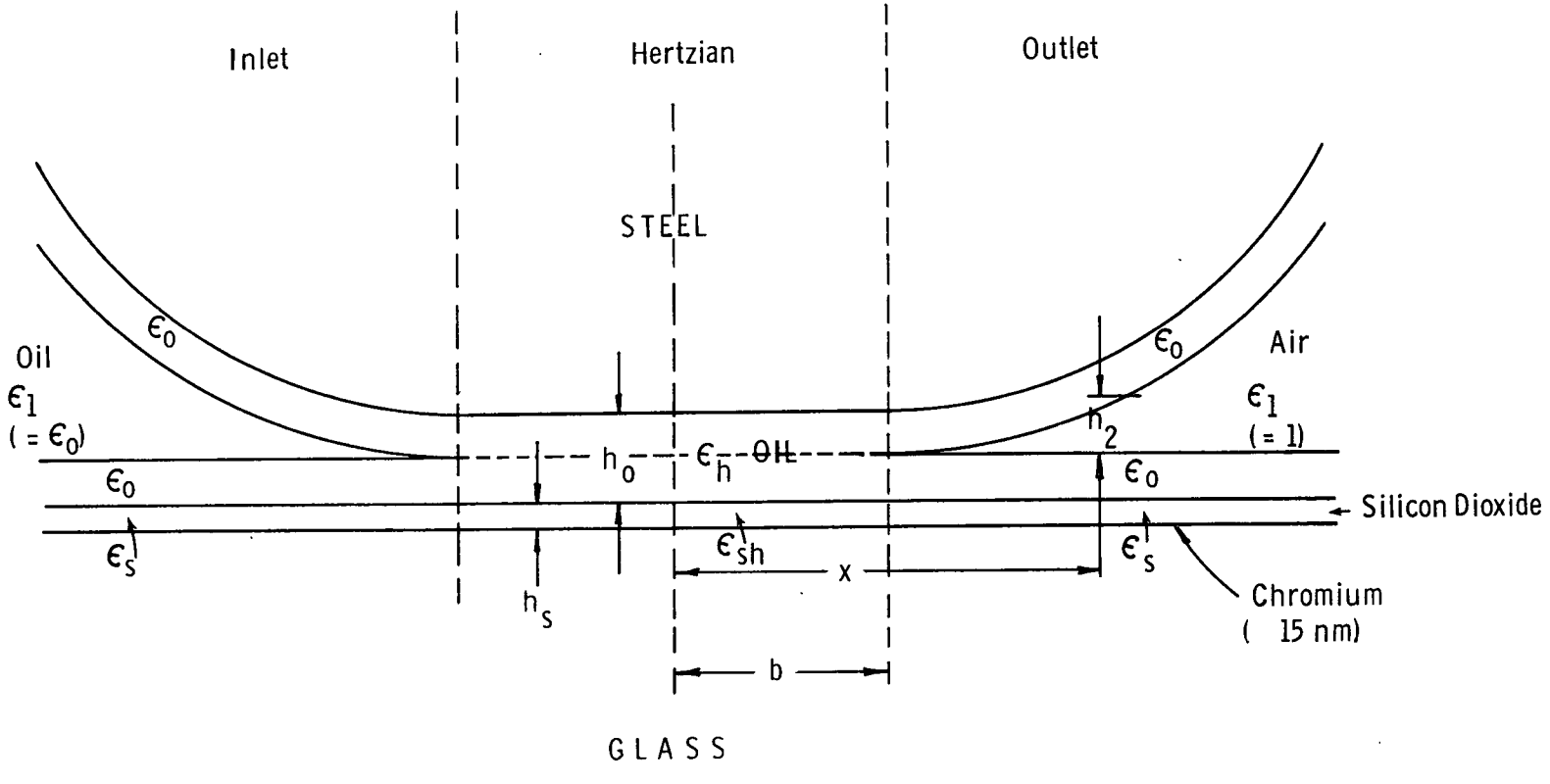

Figure 52. Model of EHL contact for capacitance calculation

$$h_2 = \frac{b^2}{2R}\left\{ |\xi\sqrt{\xi^2-1}| - \ln\left[|\xi| + |\sqrt{\xi^2-1}| \right]\right\}, \qquad (30)$$

where $\xi = x/b \geq 1$.

The total capacitance is divided into three sections

$$C = C_i + C_h + C_o, \qquad (31)$$

where C_i is the capacitance of the inlet section (cm/cm),
C_h " " " " " Hertzian " " " ,
C_o " " " " " outlet " " " ,

also,

$$C_h = \frac{b}{2\chi[h_o/\varepsilon_h + h_s/\varepsilon_{sh}]}, \qquad (32)$$

where ε_h is the permittivity of the oil in the Hertzian region, and
ε_{sh} " " " " " silicon oxide in the Hertzian region.

ε_h and ε_{sh} are estimated at the mean Hertz pressure, $\bar{p}$, which is calculated from the measured value of the half-width, b. Since no data are available for ε_h and ε_{sh}, they are estimated from the values at ambient pressure, ε_o and ε_s, using

$$\varepsilon_{h,sh} = \frac{1+2A}{1-A}, \quad \text{where } A = \frac{\rho}{\rho_o}\left(\frac{\varepsilon_{o,\bar{s}}1}{\varepsilon_{o,s}+1}\right) \qquad (33)$$

For ε_h,

$$\frac{\rho}{\rho_o} = 1 + \frac{42.8\times10^{-6}}{(\nu_{100})^{0.0385}}\,\bar{p}^{\frac{3}{4}}. \qquad (34)$$

For ε_{sh}

$$\frac{\rho}{\rho_o} = 1 + \frac{\bar{p}}{E_s}, \tag{35}$$

where E_s is the Young's modulus of silica.

The inlet and outlet capacitances are given by

$$C_{i,o} = \int_{\pm b}^{\pm\infty} \frac{dx}{4\pi\left[\frac{h_o}{\varepsilon_o} + \frac{h_2}{\varepsilon_1} + \frac{h_s}{\varepsilon_s}\right]}, \tag{36}$$

where $\varepsilon_1 = \varepsilon_o$ for the inlet, and

$\varepsilon_2 = 1$ for the outlet.

The formula for the Hertzian shape is then substitued for h_2 in the above expression, and the substitution

$$\zeta = \frac{1}{\xi} \tag{37}$$

is made to avoid the infinity in the integral. A parameter X is defined

$$X = \frac{b^2}{2R\varepsilon_1}\left(\frac{h_o}{\varepsilon_o} + \frac{h_s}{\varepsilon_s}\right)^{-1}, \tag{38}$$

and that gives

$$Y = \frac{2^{\frac{1}{2}}}{4\pi} X^{\frac{1}{2}} \int_o^1 \frac{d\zeta}{\zeta^2 + X\left\{\left|\sqrt{1-\zeta^2}\right| - \zeta^2 \ln\left[\left|1/\zeta\right| + \left|\sqrt{1/\zeta^2 - 1}\right|\right]\right\}}, \tag{39}$$

where

$$Y = C_{i,o}\left(\frac{\frac{h_o}{\varepsilon_o} + \frac{h_s}{\varepsilon_s}}{R\varepsilon_1}\right)^{\frac{1}{2}}. \tag{40}$$

The above function has been numerically integrated for a range of values of X in Ref. 24 and a table of values compiled. Using this table, values of Y have been found by linear interpolation. This gives C_i and C_o. When C_i, C_o and C_h are added together we have the total capacitance C in e.s.u. cm. per cm. transverse width of roller. To convert to picofarads we use the relation

$$C_c = LC/0.9 \qquad (41)$$

where L is the length of the roller

C_c is the total capacitance in picofarads.

The calculation was done by computer for each fluid at both loads, and a calibration curve for each was drawn (Figs. 53, 54, 55, and 56).

4.4.6 Measurement of the Dielectric Constant of the Silicon Oxide

The bulk value of silicon monoxide is about 5, but a more accurate figure is required, especially as the value for a thin film is probably different from the bulk value, and the exact molecular structure is not known.

To measure this, the rig was assembled dry, and loaded statically at 8 different loads. The capacitance at each load was measured. If a value for ε_s is guessed, the theoretical capacitance can be calculated exactly as in section 4.5 except that now we have $\varepsilon_1 = 1$ for both inlet and outlet sections, and $h_o = 0$. This can now be compared with the measured value, and the value of ε_s adjusted correspondingly. The process is repeated until the theoretical and measured values are within given limits. The iteration process is done by computer. It was found that no single value of ε_s would agree with the calculation at all loads. If agreement was reached at the highest load, then values for lower loads were too small. This could be interpreted by saying that at the lower loads, asperities were keeping the surfaces apart, giving us a false value for the separation, h_s. The value taken was therefore that which agreed at the highest load. This gave a value for the dielectric constant of 5.485 at 20 kHz.

4.4.7 Measurement of Dielectric Constants of Test Fluids

The method of measurement was to use a cell specially designed by A. Smith, of the Lubrication Laboratory, Imperial College. This consisted of two concentric cylindrical surfaces maintained at an exact separation, with suitable screening from external influences. The capacitance was first measured with no fluid in the cell, and then with the test fluid filling the

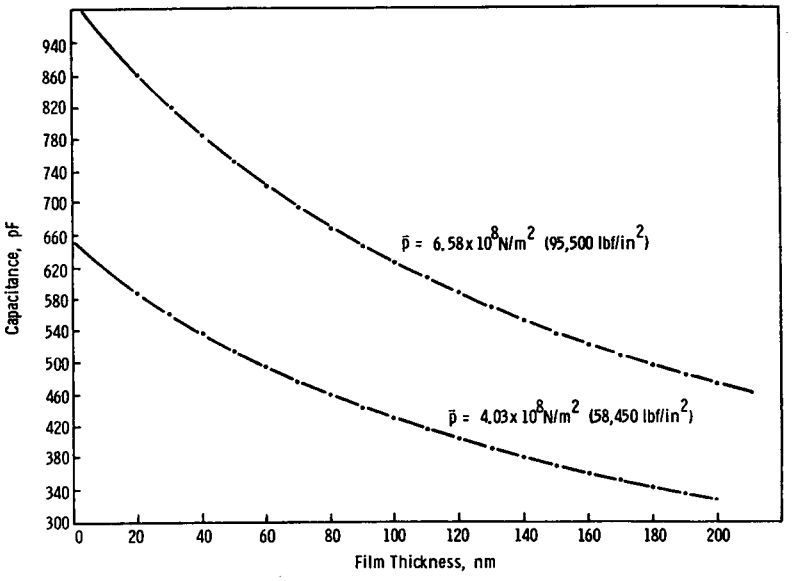

Figure 53. Calibration curve: measured capacitance vs film thickness for Fluid a

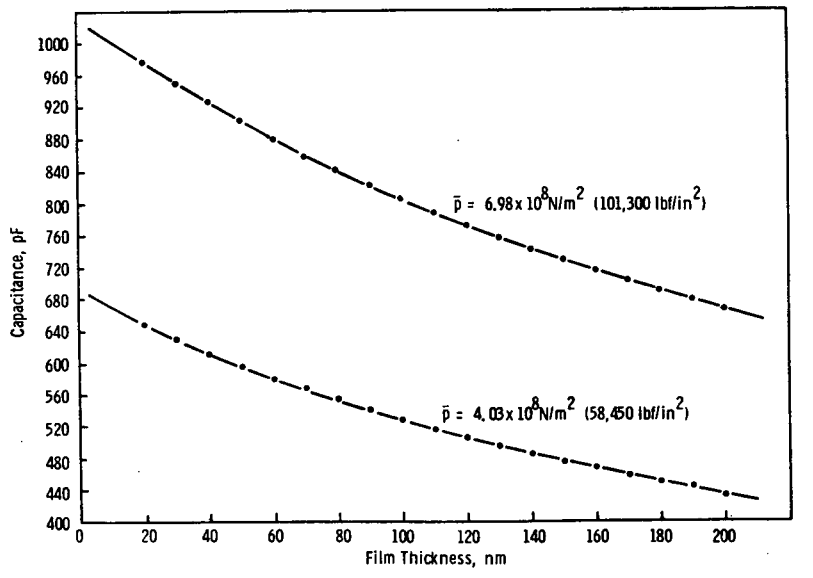

Figure 54. Calibration curve: measured capacitance vs film thickness for Fluid b

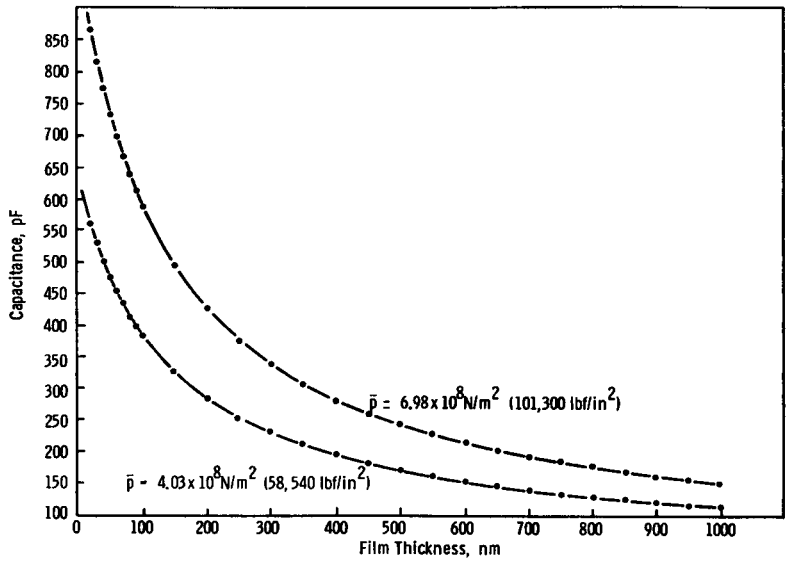

Figure 55. Calibration curve: measured capacitance vs film thickness for Fluid e

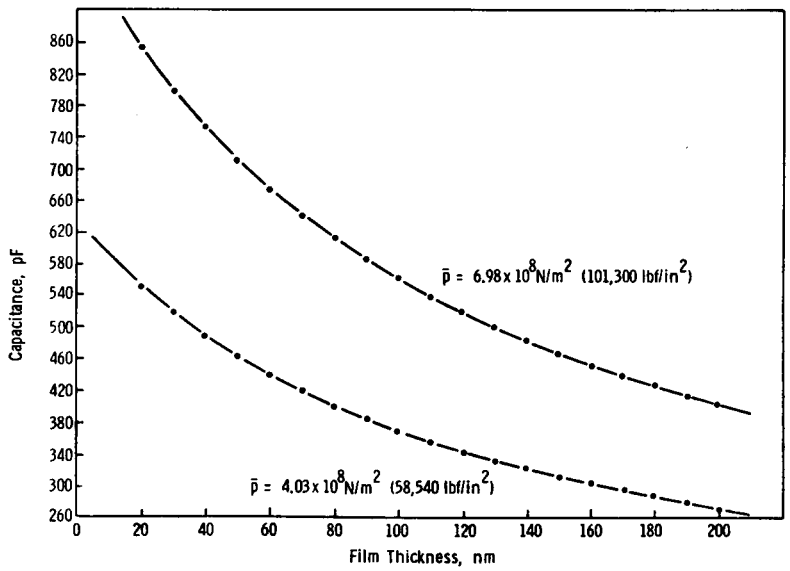

Figure 56. Calibration curve: measured capacitance vs film thickness for Fluid q

gap. The ratio of the two capacitances gave the dielectric constant, estimated to be correct to within 1%. The values for the four test fluids used were

fluid a: 3.555
" b: 5.570
" e: 2.930
" q: 2.731

All measurements were taken at the test frequency of 20 kHz.

4.4.8 Discussion of Results

Non-dimensional film thickness, determined by capacitance, is plotted against non-dimensional speed in Figs. 57, 58, 59 and 60. The points tend to lie on straight lines, but the slopes are in all cases greater than the corresponding slopes determined optically.

To compare these data:

Fluid	Slope (optical)	Slope (capactive)
a	0.6	0.88
b	0.66	0.76, 0.94
e	0.57	0.62
q	0.5	0.56

The difference is most marked for fluids a and b. Figs 61, 62, 63, and 64 show a direct comparision of film thickness determined by the two methods, and it is seen at once that agreement is only close at the higher film thicknesses. The discrepancy is greatest where the film thickness is least. The effect of surface roughness is certainly not negligible at such film thicknesses as shown in Ref. 25, and will cause a departure of this kind, but this effect is certainly not great enough to be wholly responsible in this case. It is concluded, therefore, that this lack of agreement is also partly due to some behavior of the dielectric which has not been taken into account. This could be, for instance, increased polarization due to charges on the oil/silicon oxide interface (interfacial polarization). One check would be to use a higher frequency. Until this can be done, it seems most probable that the capacitance measurements (at small film thickness, especially) are the cause of most of the discrepancies seen in Figs. 61 through 64.

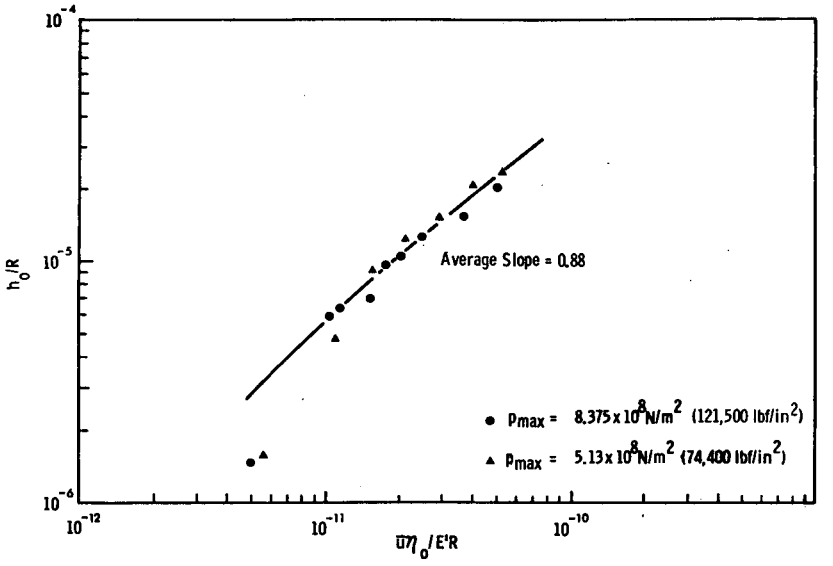

Figure 57. Film thickness from capacitance, Fluid a

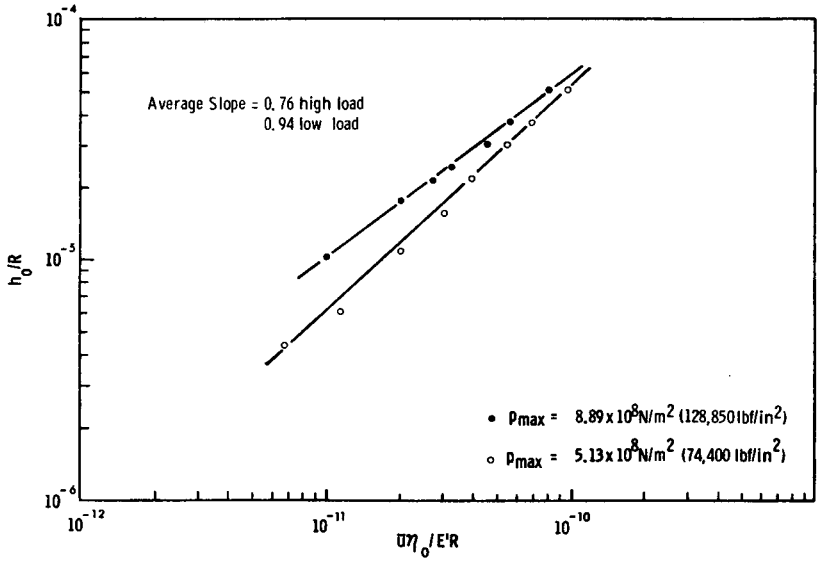

Figure 58. Film thickness from capacitance, Fluid b

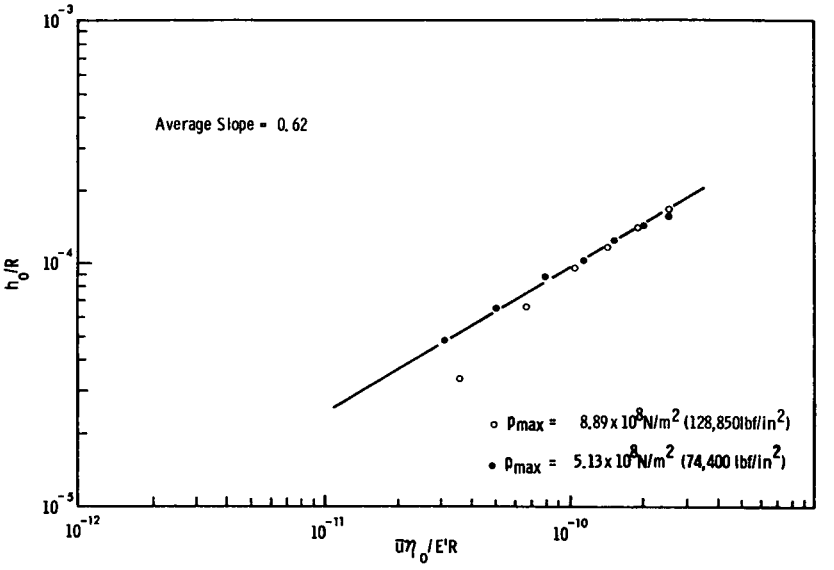

Figure 59. Film thickness from capacitance, Fluid e

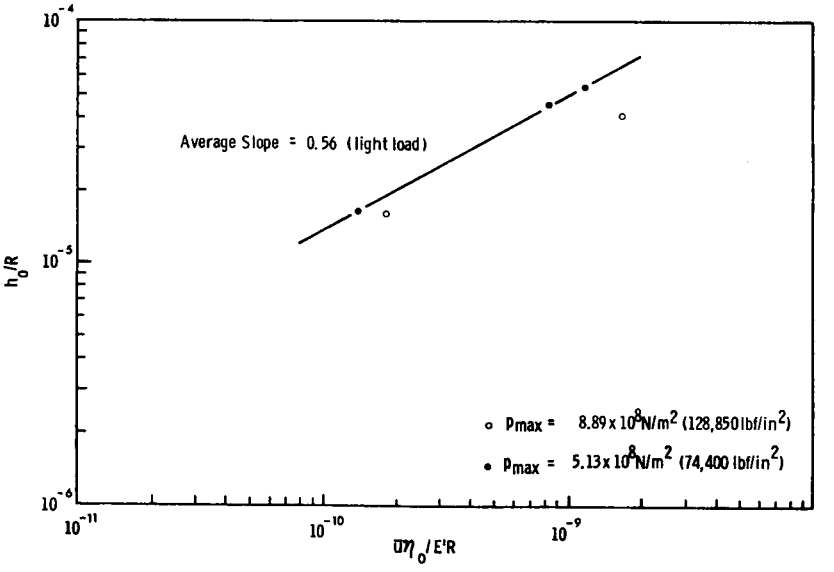

Figure 60. Film thickness from capacitance, Fluid q

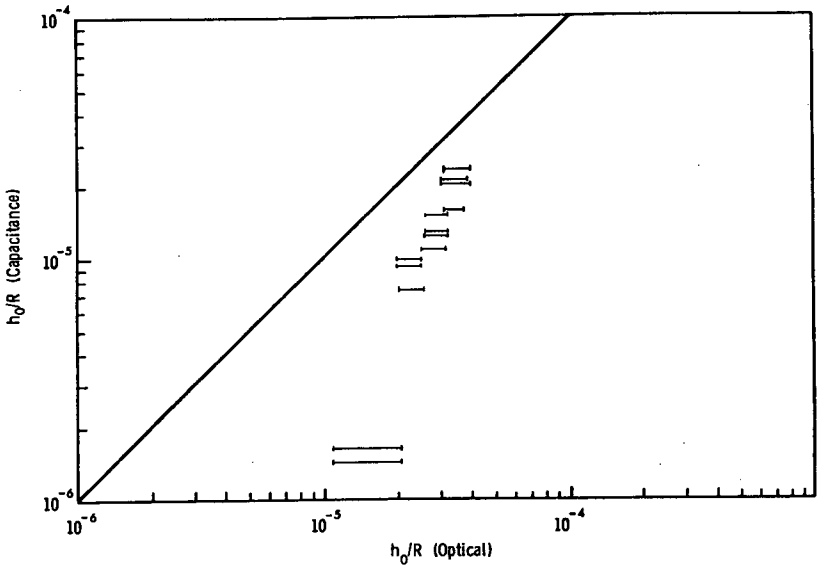

Figure 61. Comparison of film thickness determined by capacitance and optical measurements for Fluid a

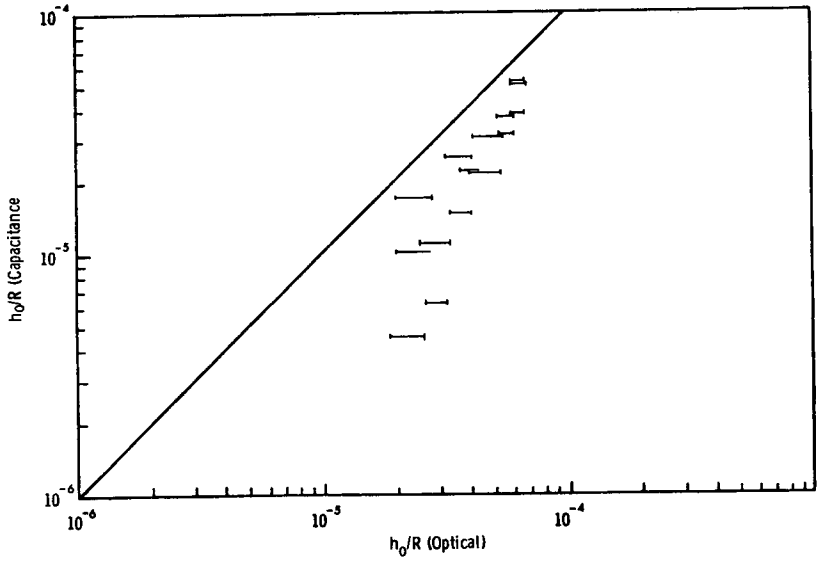

Figure 62. Comparison of film thickness determined by capacitance and optical measurements for Fluid b

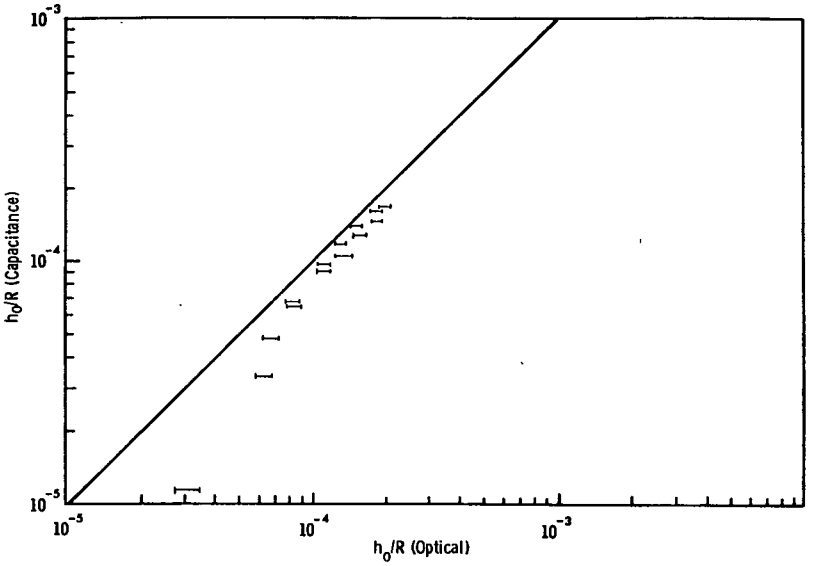

Figure 63. Comparison of film thickness determined by capacitance and optical measurements for Fluid e

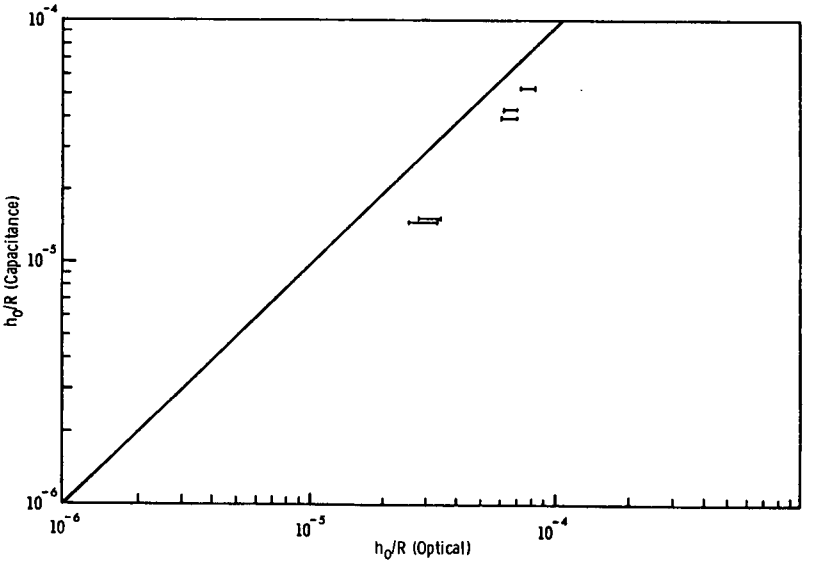

Figure 64. Comparison of film thickness determined by capacitance and optical measurements for Fluid q

4.5 LOW VOLTAGE RESISTANCE MEASUREMENTS

4.5.1 Introduction

Using the same electrical contacts to the roller and chromium layer, but this time with a disk having no layer of silicon oxide, the low voltage electrical resistance of the oil film was investigated, Tests were conducted with fluid b and were designed to give some information on asperity contacts, which provided low resistance bridging of the normally non-conducting film.

4.5.2 Electrical Circuit

The circuit, shown in Fig. 65 consists of a 1 MΩ resistor to limit the current flow to a few microamps when the film is short circuited by asperities and a variable resistor to adjust the applied voltage to the film. The resistance of the chromium layer was about 8 KΩ. An oscilloscope was connected across the terminals on the rig, to give a visual indication of the amount of asperity contact, and a D.C. millivoltmeter was also connected to give a time average of the voltage across the film.

4.5.3 Measurement Procedure

The roller was first loaded statically against the plate with switch S open, and the voltage V_{open} was noted. Switch S was closed, and the voltage dropped to some other value V_{closed}. The potentiometer was adjusted until δV (= $V_{open} - V_{closed}$) was 20 mV. The rig was started up, and the trace on the oscilloscope showed that the voltage was hopping between two limits (V_{open} and V_{closed}), each excursion signifying an asperity contact. The trace was photographed by triggering a single sweep from the camera. The voltage was read from the DC millivoltmeter, and the film thickness was determined optically.

4.5.4 Discussion of Results

At low speeds, the trace was mainly at the lower voltage level, with frequent excursions to the upper level. This represented a high degree of asperity contact with only short periods of time where no bridging took place. As the speed was increased, the trace showed less and less contact, until finally the voltage was almost permanently at its higher level

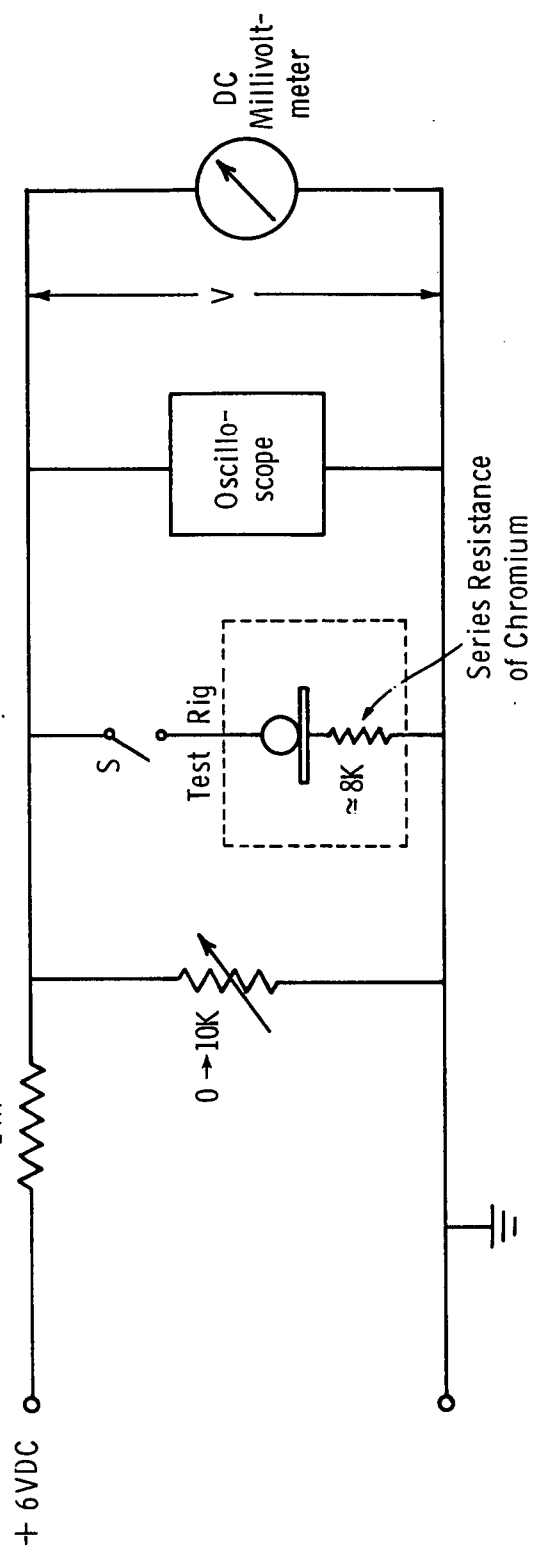

Figure 65. Resistance measurement circuit

with an occasional excursion downwards. This represented conditions where hardly any asperities were contacting. Fig. 66 shows photographs of the traces obtained over the whole range from almost permanent contact to almost zero contact, together with the time average voltages associated with them.

Fig. 67 shows a graph of the time average voltage versus the non-dimensional optical film thickness. Results were taken for fluid b and at the three loads indicated. The voltage approached the open circuit value asymptotically as film thickness was increased, and the applied load seemed to have no effect on the voltage whatsoever. This non-dependence on load is a little surprising, as one would expect the amount of asperity contact to increase with the Hertzian half width b.

One can divide the curve in Fig. 67 visually into two portions by means of the dashed line

$$h_o/R \approx 1.5 \times 10^{-5}. \qquad (42)$$

This represents a film thickness of 60 nm (600 Å or 2.4 μ in) and it is clear that this is approximately equal to the peak-to-valley asperity height of the roller. Although the division is not well defined, one can say generally that below the dashed line the rate of asperity contact is significant and that it depends on film thickness in a manner generally consistent with the known Gaussian distribution of asperity heights. Above the dashed line, the rate of asperity contact is low; and most low resistance paths are probably caused by debris in the oil and local dielectric breakdown.

The non-dependence on load no doubt indicates that flattening of asperities takes place in the Hertzian region, so that one is actually observing asperity contact just outside the Hertzian region. This is further substantiated by the fact that good optical pictures can be obtained even when the film thickness is less than the typical asperity height.

4.6 EFFECT OF ROLLER END PROFILE ON FILM SHAPE

The roller used in section 4.3.2 to measure film shape was not blended at its ends. This caused a stress concentration at the ends which resulted in a broadening of the contact region. A blended roller, with an end profile shown in Fig. 68 was used to see what effect the blending had on the end closure. Fig. 69 is a photograph of the end of the roller running under

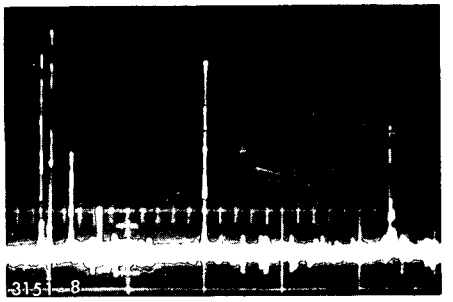

(a) V = 1 mV

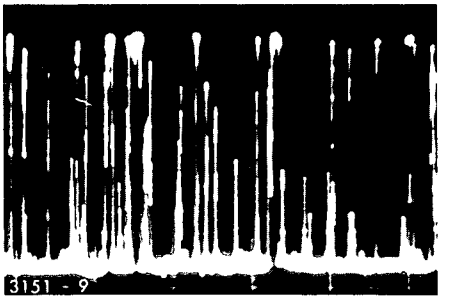

(b) V = 3 mV

(c) V = 6 mV

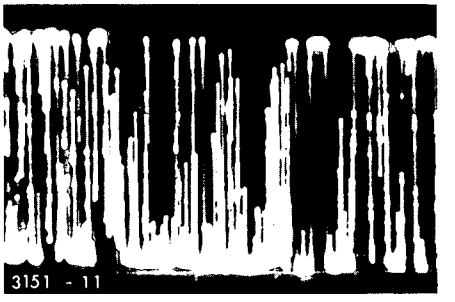

(d) V = 9 mV

(e) V = 12.5 mV

(f) V = 18.25 mV

(g) V = 19.7 mV)

Figure 66. Oscilloscope traces showing frequency of contact and contact resistance

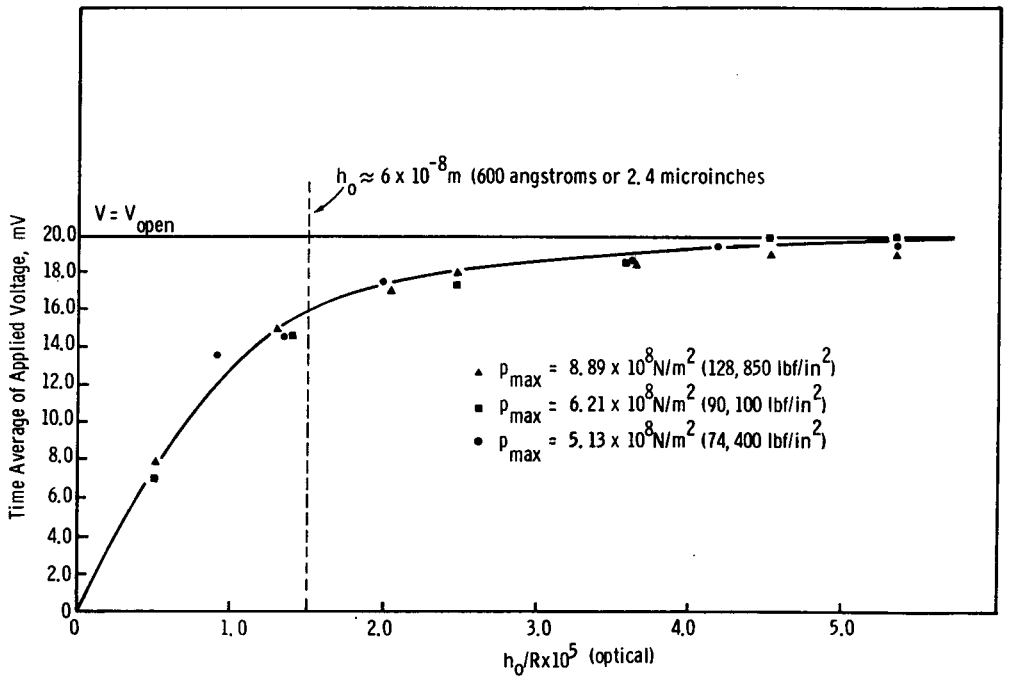

Figure 67. Low-voltage resistance measurements, Fluid b

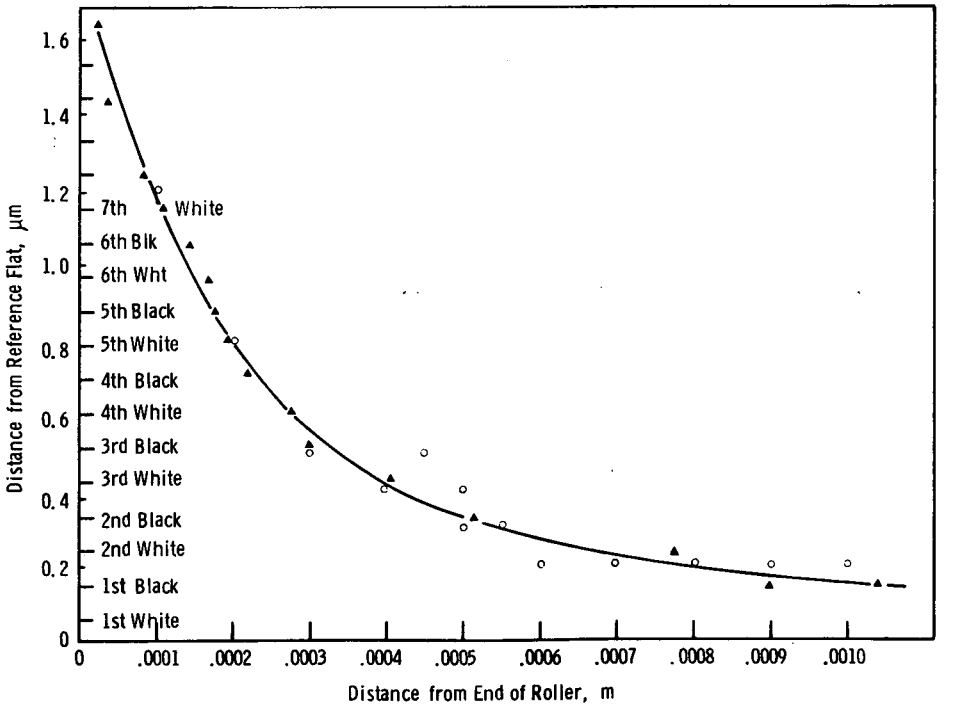

Figure 68. End profile of blended roller (small end) by interferometry

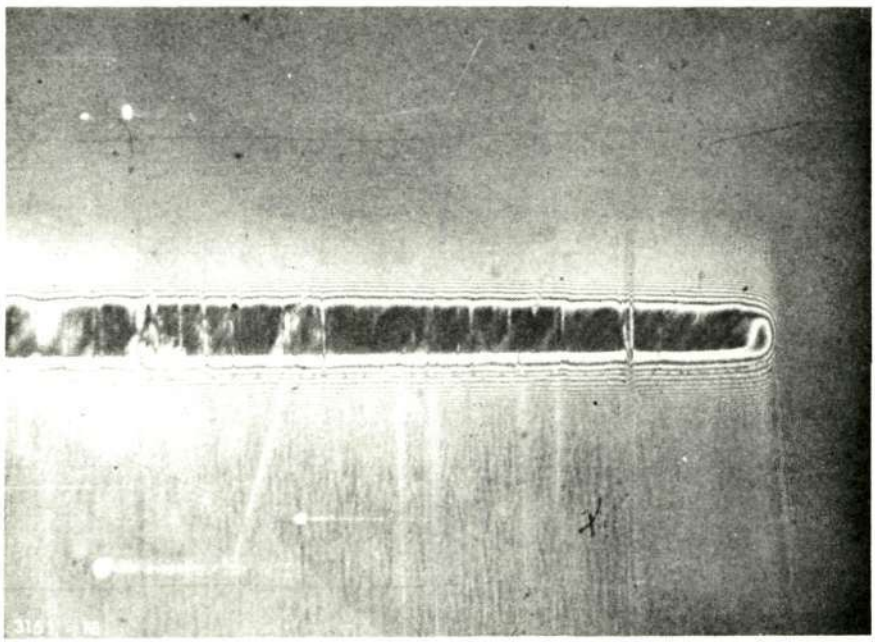

p_{max} = 5.13 x 10^8 Nm^{-2} (74,400 $lbf\text{-}in^{-2}$)

Figure 69. Roller with end blend. $h_o \simeq 325$ nm.

a load corresponding to:

$$p_{max} = 5.13 \times 10^{8} N\ m^{-2} \quad (74{,}400\ lbf\ in^{-2}).$$

If this is compared with the photographs in Fig. 42 it is immediately seen that the end closure contours have taken on a different characteristic shape. The Hertzian region is no longer broadened at the end, and the end closure seems less severe. The contours were measured from the photograph and plotted, in Fig. 70. On comparing this shape with Fig. 44 it is seen that the closure is broader and the reduction in film thickness is not so drastic. The position of the minimum film thickness is now about 3.4×10^{-5}m from the end of the roller compared with a value of about 1.2×10^{-5}m for the non-blended roller.

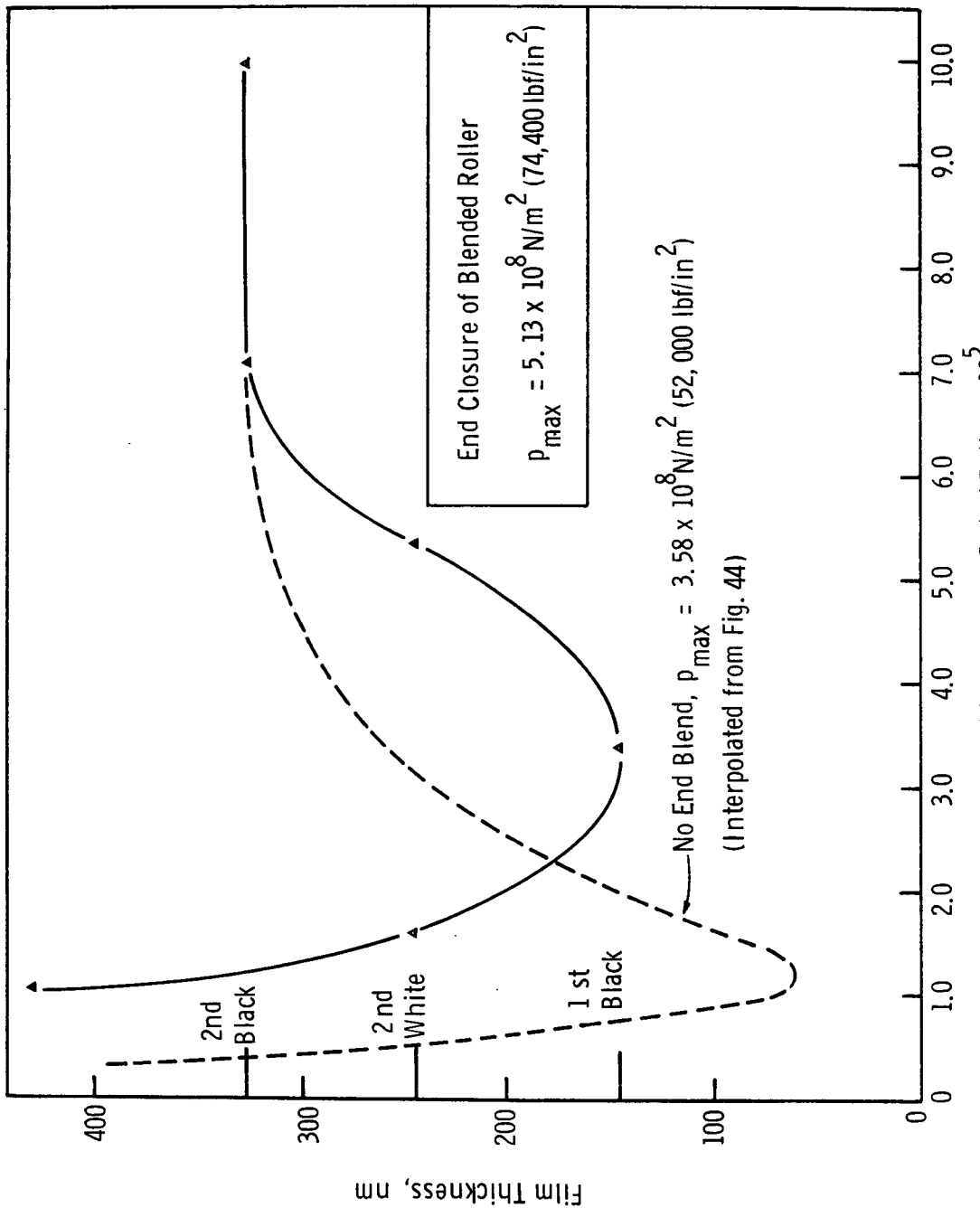

Figure 70. Effect of end blend on roller end closure

5. REFRACTIVE INDEX IN POINT CONTACTS

5.1 DEVELOPMENT OF METHOD

The purpose of this project was to develop an optical method for measuring the refractive index of a fluid in an EHL contact. Although a completely satisfactory method was finally developed, the initial attempt was unsuccessful. A brief description of the steps by which the final method was evolved will be given because it is felt to be useful to the understanding of the measurement of film thickness by optical interferometry.

Film thickness is measured by viewing the interference fringes at normal incidence and then using the standard equation (see Fig. 71)

$$n_3 t \cos\phi = m\lambda, \tag{43}$$

where m = order of the interference,

λ = wavelength of the light,

n_3 = refractive index of the fluid

t = fluid film thickness, and

ϕ = 90° for normal incidence

If m is known, t can be calculated, provided n_3 is also known. However, until now, only estimates of n_3 have been available since it is a function of pressure. With an accurate means of measuring n_3, the distortion can be found absolutely. The pressure distribution then can be obtained by applying standard elasticity theory to the (absolute) measured distortion.

After consultation with Dr. Welford of Applied Optics section of the Physics Department in Imperial College it was thought feasible that the refractive index could be measured in the following manner.

If an interferometric fringe pattern is measured at two different values of θ and ϕ (see Fig. 71 and the fringe orders) are measured at a given position in the contact region then

$$m_1\lambda = n_3 t \cos\phi_1, \tag{44}$$

$$m_2\lambda = n_3 t \cos\phi_2, \text{ and} \tag{45}$$

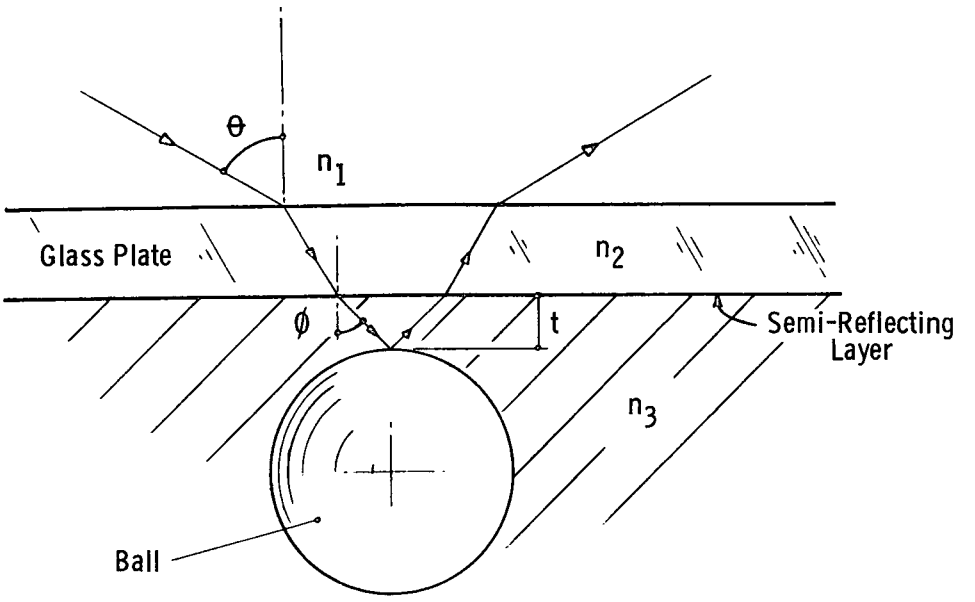

Figure 71. Interference fringes

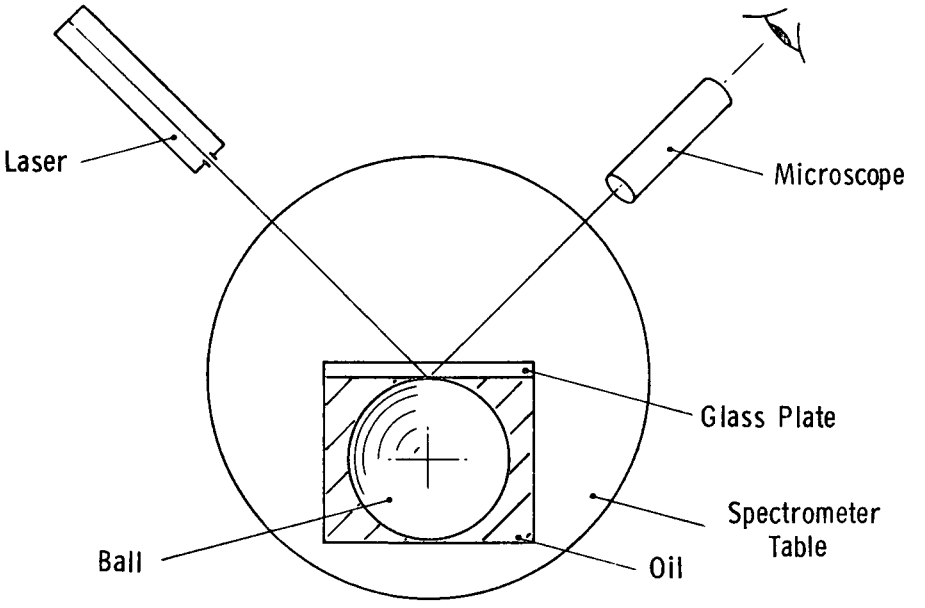

Figure 72. Experimental apparatus

$$\frac{\sin \phi_1}{\sin \theta_1} = \frac{1}{n_3}, \qquad (46)$$

(Snell's law)

$$\frac{\sin \phi_2}{\sin \theta_1} = \frac{1}{n_3}, \qquad (47)$$

if $n_1 \simeq 1$.

Note that this applies even if there is some local change in n_2 provided that the change is stratified. From Eqs. 44 and 45,

$$\frac{m_1}{m_2} = \frac{\cos \phi_1}{\cos \phi_2}; \qquad (48)$$

and, if we use Eqs. 46 and 47 to eliminate cos ϕ_1 and cos ϕ_2,

$$n_3^2 = \frac{m_1^2 \sin^2 \theta_2 - m_2^2 \sin^2 \theta_1}{m_1^2 - m_2^2}. \qquad (49)$$

To test out this theory to see if there were any practical difficulties the apparatus shown in Fig. 72 was constructed.

The glass plate had a semi-reflecting layer of chrome deposited to match the high reflectance of the steel ball. The spectrometer table could be rotated to vary θ, and the fringes were viewed through a microscope which was attached to one of the arms of the spectrometer. Originally the fringes were measured with a filar eyepiece, but later on it was found more convenient and accurate to photograph them. The light source used was a helium laser (λ= 632.8nm) giving a powerful beam of coherent light.

The ball was pressed against the glass plate and the microscope was rotated until the fringes produced by the interference of the laser beam reflected from the ball and from the glass plate, were in the field of view. A photograph of the fringe pattern was taken. The spectrometer table was then rotated to obtain a different value of θ, and the process repeated. The angle θ was found by measuring the angle the spectrometer table had to be rotated through so that the image of the laser beam was reflected normally by the glass plate.

From the photographs the fractional fringe orders at given radii from the center were measured by drawing a graph of fringe order against the radius, and interpolating between the points. The values were then substituted in Eq. 49 to find the refractive index.

The oil was at atmospheric pressure, and so the results obtained experimentally could be compared with those measured with an Abbé refractometer. There appeared to be little correlation, for an oil of refractive index of 1.4, results between 1.3 and 2.5 were obtained. The cause of this unsatisfactory situation was as follows.

When the fringes were viewed at different angles the focus of the microscope had to be adjusted to allow for the variation of optical path length due to the light having to travel obliquely through the glass plate. It is impossible to see, just by looking at the fringes, whether or not they are in focus. This is because fringes produced with a laser light source are almost completely non-localized. In other words, they appear wherever in space the beams from the two surfaces cross - one of the effects caused by the extremely long coherence length of the laser light. The fringes being viewed were formed by an expanding spherical wave from the ball and plane wave from the glass plate. As the spherical wave expands the apparent size of the fringes increase; see Fig. 73. To measure the true image size the microscope must be focused at the interface between the two surfaces. (The separation of the surfaces being negligibly small).

When this fact was realized, a vertical line was deposited on the glass to focus the microscope on. This helped but the results were still not accurate. It was then realized that working through a glass plate at an angle introduces astigmatism. This means that the focal position is different in the horizontal and vertical planes. The microscope was being focused on a vertical line, but the fringes measured were in a horizontal plane. This error was cured by depositing a scale with horizontal lines.

The other source of error was the phase change of the light reflected from the ball. For normal incidence this is known and is unaffected by the polarization of the light. When the light is reflected obliquely the phase change becomes an unknown function of both angle and polarization. It would have been possible to calibrate the apparatus for phase change by substituting the known value for the refractive index in the equation

$$m\lambda = n_3 t \cos \phi + \frac{\delta\lambda}{2\pi} , \qquad (50)$$

where δ is the phase change.

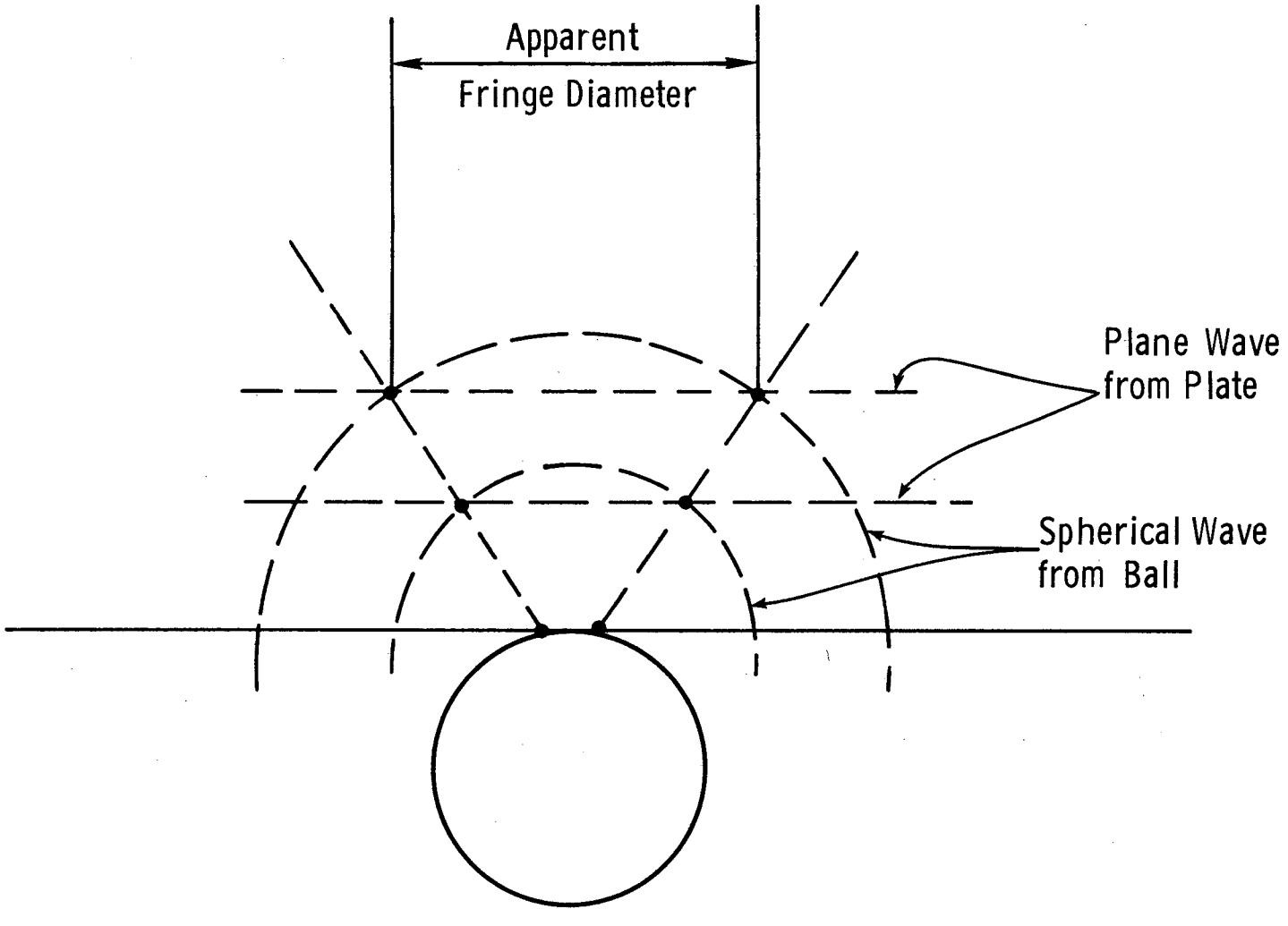

Figure 73. Effect of focus on apparent fringe diameter

As the purpose of the experiment was to check the accuracy of the method this was not considered a very satisfactory way of overcoming the problem. It was solved by using a glass ball for which the phase change is 180° and is not a function of θ or the polarization. The ball was made of the same glass as the front plate and both surfaces were left without any optical coating. This meant that the reflectivity from each surface was exactly equal. Provided that the refractive index of the oil was different from that of the glass, good quality fringes could be observed. The reason for not having a coating was in case the coating itself introduced a phase change which may have changed with incident angle. The reduction in the intensity of the light due to the lower reflectivity of the surfaces was not important as the laser provided enough illumination.

When the experiments were repeated with these modifications the results were much better. The experimental accuracy was now limited by the accuracy with which the fringes could be measured, for a given pair of angles.

The accuracy could be improved by increasing the difference between the fringe orders m_1 and m_2. This can be done by increasing the separation between ϕ_1 and ϕ_2. However if ϕ_2 is increased too much, the spacing between each fringe becomes excessive. The optimum angles for ϕ_1 and ϕ_2 proved to be $\phi_1 = 0$ and $\phi_2 \approx 45°$. Using a flat plate this angle for ϕ_2 was impossible to reach as it made θ_2 imaginary, viz.: by Snell's law,

$n_3 = \sin \theta \; / \; \sin \phi$; and, if $\phi = 45°$ and $n_3 = 1.5$, $\sin \theta = 1.06$

However if a hemispherical piece of glass was substituted for the front plate an angle of 45° for θ_2 could easily be achieved.

The smallest angle for θ_1, that could be reached, without going to a complicated optical system with semi-reflecting mirrors, was 8°. However, as can be seen from,

$$m_1 \lambda = n_3 t \cos \phi_1, \qquad (44)$$

this only changes m_1 by a factor of $\frac{\cos 0°}{\cos 8°} = 1.01$ which makes a negligible effect on the difference between m_1 and m_2.

The hemisphere slightly changes the formula for calculating the refractive index. The pertinent equations are now

$$m_1 \lambda = n_3 t \cos \phi_1 \; , \qquad (44)$$

$$m_2 \lambda = n_3 t \cos \phi_2 \; , \qquad (45)$$

$$\frac{\sin \theta_1}{\sin \phi_1} = \frac{n_3}{n_2} \; , \text{ and} \qquad (51)$$

$$\frac{\sin \theta_2}{\sin \phi_2} = \frac{n_3}{n_2} \; . \qquad (52)$$

The meaning of the symbols is as before; see Fig. 74.

Substituting for cos ϕ_1 and cos ϕ_2 and re-arranging gives

$$n_3^2 = n_2^2\left(\frac{m_1\sin^2\theta_2 - m_2^2\sin^2\theta_1}{m_1^2 - m_2^2}\right); \qquad (53)$$

so, provided n_2, the refractive index of the glass, is known, the index of the film can again be found by measuring θ_1, θ_2, m_1, and m_2.

Figure 75 shows the results from a typical test run. The refractive index of the oil, as measured by an Abbé refractometer was 1.501. The average value from Fig. 75 gives a value of 1.5002. This gives an accuracy of better than 0.1%, which is quite sufficient to measure the absolute distortion with a high degree of accuracy.

5.2 TWO BEAM APPARATUS

5.2.1 Point Contact Entrapments

It was decided to study refractive index in point contact entrapments. A great deal of information about the properties of a fluid can be gained from the study of entrapments, and also they are much more convenient to measure with the technique developed, so the work was concentrated solely on them. They are little pockets of fluid trapped inside the contact area when a ball is brought down against a flat surface in the presence of the fluid (Fig. 76). These entrapments have been predicted theoretically by Christensen[26] and have been observed by Dowson and Jones[35], by Foord, Hammann, and Cameron[6], and by Westlake and Cameron[27]. Christensen predicted that the pressures inside the contact would be considerably higher than the Hertz maximum.

The oil leaks away from the entrapment until eventually the usual Hertzian shape is reached. The depth of the entrapment depends on many factors, such as load, approach velocity and the pressure viscosity characteristics of the oil. A typical depth for a viscous oil with a high pressure viscosity coefficient and a load of 2 kg would be about 3×10^{-6}m with a diameter of about 3×10^{-4}m. As the fluid flows out, both the pressure distribution and the distortion change and so to measure the refractive index and distortion, the fringes must be measured simultaneously at θ_1 and θ_2. A modification was made to the optical system to do this, and an apparatus designed to study oil entrapments.

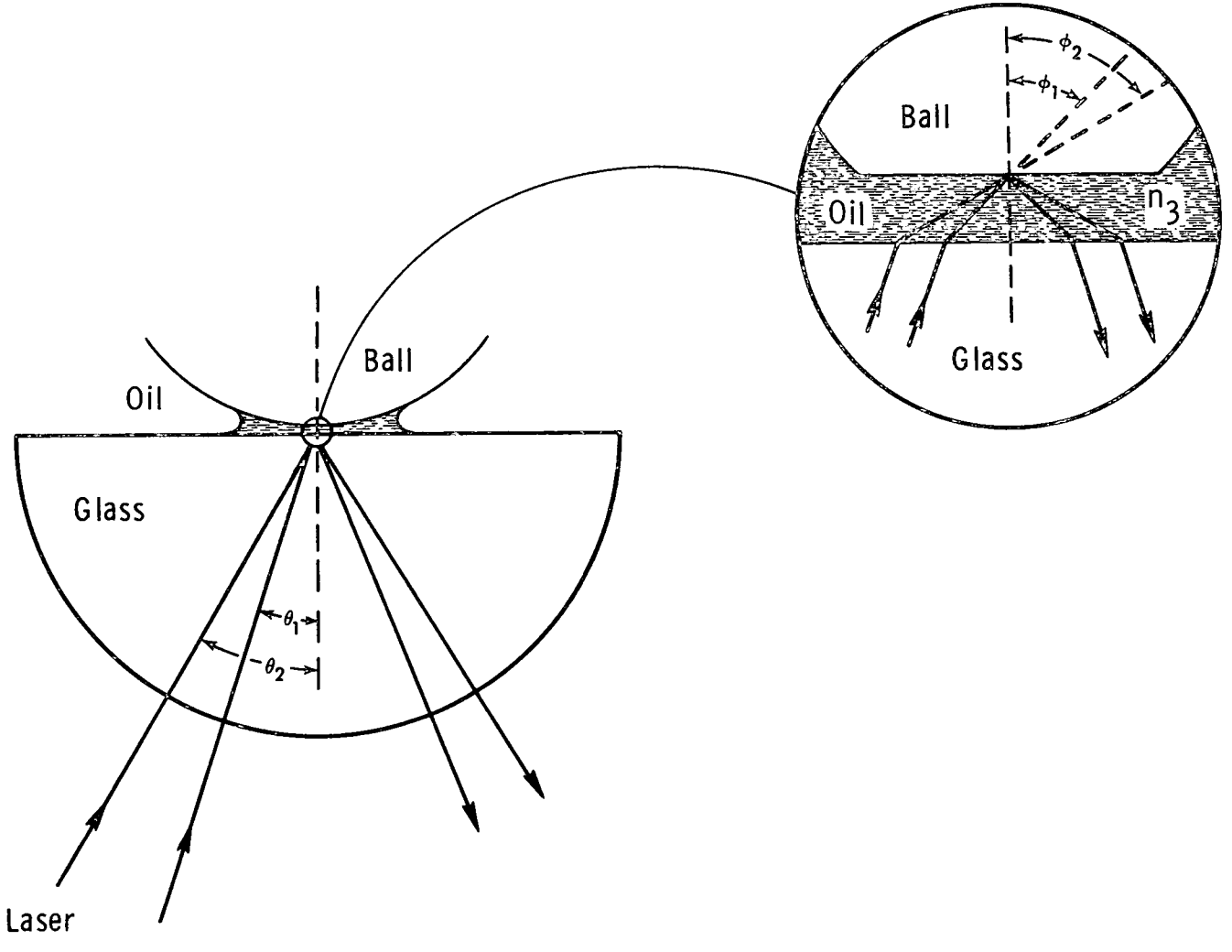

Figure 74. Ball-on-hemisphere set-up

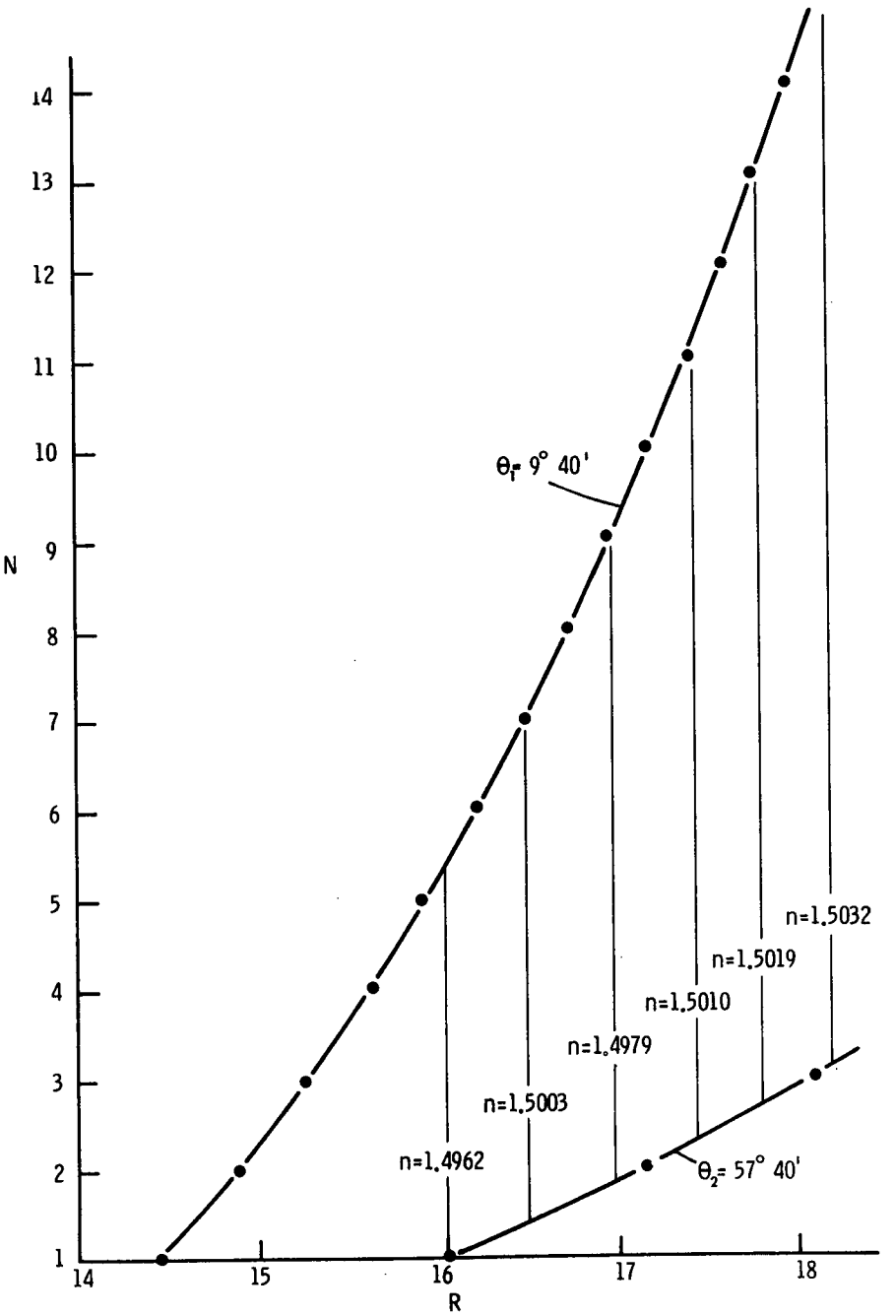

Figure 75. Graph of N (fringe order) plotted against R (fringe diameter) in arbitrary units

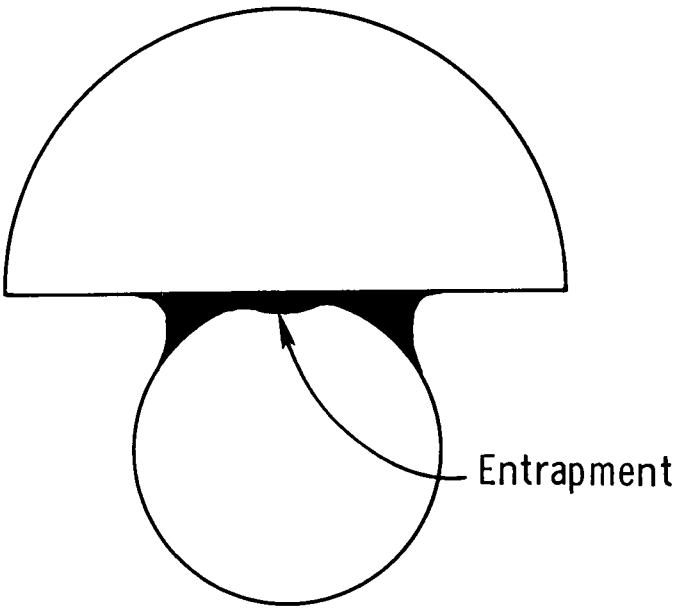

Figure 76. Diagram of entrapment

5.2.2 Apparatus

A diagram of the apparatus is shown in Fig. 77. The velocity of the ball was measured by means of the magnetic bar, which as the ball dropped, produced an E.M.F. in the coil. This E.M.F. was proportional to the velocity of the ball, and was recorded on a U.V. recorder. The ball was released by pin A being withdrawn when the magnetic coil was switched on. The load on the ball could be varied by changing the weights at B. The dashpots were added to slow down the ball, because it was found that reasonable loads of about 2 kg tended to damage the surface of the hemisphere if the ball was allowed to fall freely.

The ball and hemisphere were both made of extra dense flint glass, refractive index 1.74116, according to the manufacturer. The surfaces were optically smooth. The manufacturer also gave Young's modulus = $5.45 \times 10^{10} N/m^2$ (7.9×10^6psi) and Poisson's ratio = 0.2 for the glass. The hemisphere had two photographically deposited scales lines 6.9×10^{-4}cm apart, symmetrically about the center of the flat surface. The outer surface was coated with an antireflection layer.

The ball was fixed in an aluminium cylinder mounted symmetrically above the hemisphere, which was cemented onto a fixing plate. Both ball and the hemisphere were readily removed for ease of cleaning.

The optical system to obtain an image at two angles simultaneously took a great deal of development work. The final system adopted is shown in Fig. 77. For some of the high speed ciné photography, a second laser was used instead of the beam splitter, to increase the illumination.

The incident beam was divided by the beam splitter, and about 90% of the beam was directed on to the entrapment at an angle of about 8° and the rest was directed in at about 47°. This difference being to correct for the greatly increased reflectivity of glass at 47° compared to 8°. Originally θ_2 was made to be 45°, but it was found that the part of the beam which went through, into the ball was reflected back on to the entrapment and destroyed the interference fringes.

The emerging beams were focused by the means of two identical 5 x objectives. The images were then reflected by the optical system shown, so that the two images were side by side on the viewing screen of the camera. The objectives could be moved independently to focus the images and could be locked into position to ensure that the images remained exactly in focus. The path lengths of the two beams were kept equal, so that the magnification would remain equal. To eliminate any possible distortion by an eyepiece, the images were formed without using one.

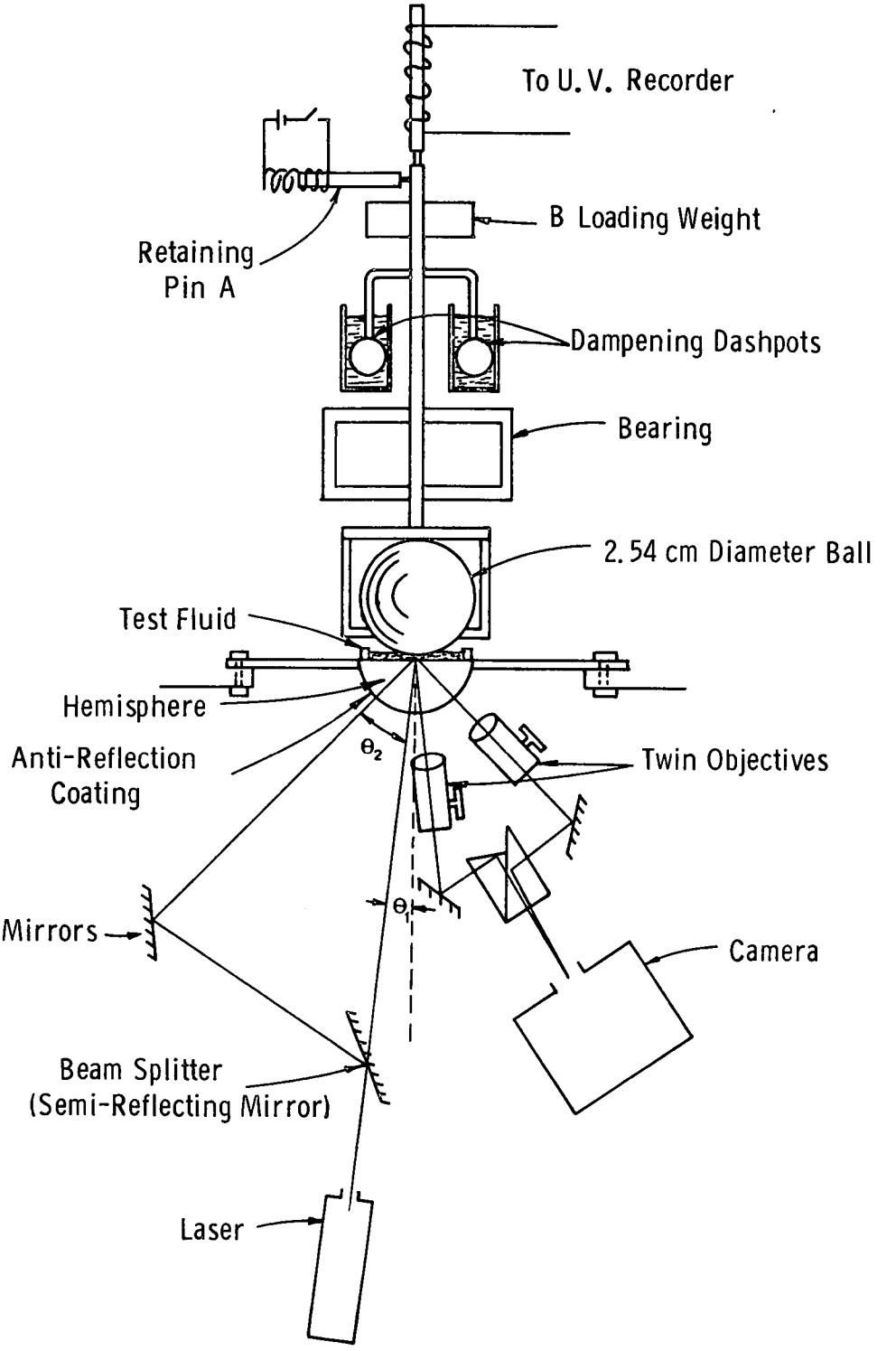

Figure 77. Diagram of apparatus

Initially a motorized Nikon F was used, which took pictures at the rate of 3 per second, but for some of the later work on the formation of the entrapment, it became necessary to use a camera with a faster framing speed. The ideal camera for this was found to be a 16 mm Miliken. This had a framing speed of up to 400 frames per second (fps). When focusing with the Nikon F, the image on the ground glass screen was enlarged with a low power microscope, to increase the accuracy of focusing. The Miliken had a built-in optical system to magnify the image size. The only disadvantage was that the image could not be viewed after the film was loaded in the camera.

5.2.3 Experimental Procedure

The hemisphere and ball were thoroughly cleaned in an ultrasonic cleaner and then were put back in position. A few drops of the fluid to be tested were placed on the center of the hemisphere. Measurements could be made with much smaller quantities of fluid if necessary. The ball was then allowed to rest on the hemisphere, and weights were added to provide the required load. (Usually between 1 and 2 kilograms).

The images of the scale were then very carefully focused on the screen of the camera. This was extremely critical, as a small error could lead to large errors in the results. When the focusing was achieved the objectives were locked into position. The ball was left resting on the surface, in case any distortion caused by the loading, affected the focus.

The ball was then raised about 0.004m from the surface of the hemisphere and locked into position by the locating pin. If the approach velocity of the ball was to be measured, the U.V. recorder was switched on. The camera was then started and the pin removed to allow the ball to drop. For the Miliken, a couple of seconds had to be allowed for the camera to build up to its full framing rate.

The length of time the camera was left running depended very much on the fluid under test. For some fluids all trace of an entrapment had disappeared after less than 1 second. Whereas for others they were still apparent after 5000 seconds.

The magnitudes of θ_1 and θ_2 were found by measuring the angle that the upper half of the apparatus had to be rotated for the beams to be reflected normally by a mirror, which was put in place of the hemisphere.

All the development work was done with a cylinder stock oil of viscosity 10.65 poises at 37.8°C. (100°F.) For the rest of the report this oil will be designated as fluid z. This gave much larger entrapments than any of the seventeen NASA test fluids, which made the test runs easier to perform initially. The seventeen NASA oils were run later.

5.2.4 Analysis of the Photographs

A photograph of an entrapment is shown in Fig. 78, using fluid z, after 3 sec. and with a 2 kilogram load. The left hand side shows the fringes photographed at 8° and the right hand side shows the same entrapment at 47°. The image along C O is contracted due to the cosine term, introduced by the obliquity. The diameters of the fringes along AB and EF were measured using a traveling microscope on the prints enlarged from the 35 mm negatives. When the Miliken was used the fringes were measured directly from the negatives with an analyzer. The fringe diameters were then plotted against fringe order, see Fig. 79.

From this graph the fractional fringe orders at θ_1 and θ_2 can be read off. Due to the symmetry of the entrapment this gives the fringe order corresponding to the same position and therefore film thickness, at both angles.

Equation 53 is

$$n_3^2 = n_2^2\left(\frac{m_1\sin^2\theta_2 - m_2^2\sin^2\theta_1}{m_1^2 - m_1^2}\right). \qquad (53)$$

By substituting for the measured quantities, we can obtain the refractive index inside the entrapment and hence the film thickness from Eqs. 44 and 51, i.e.,

$$n_3 t \cos\phi_1 = m_1\lambda \qquad (44)$$

and

$$\frac{n_3}{n_2} = \frac{\sin\theta_1}{\sin\phi_1} \qquad (51)$$

yield

$$t = m_1\lambda\left(\frac{1}{n_3^2} - \frac{\sin^2\theta_1}{n_2^2}\right)^{\frac{1}{2}} \qquad (54)$$

Figures 80 and 81 show typical entrapments plotted. For clarity only a sample of the photographs measured have been plotted. This now gave an accurate plot of the distortion of an entrapment, along with the refractive index of the fluid. The variation with time of these quantities was also known.

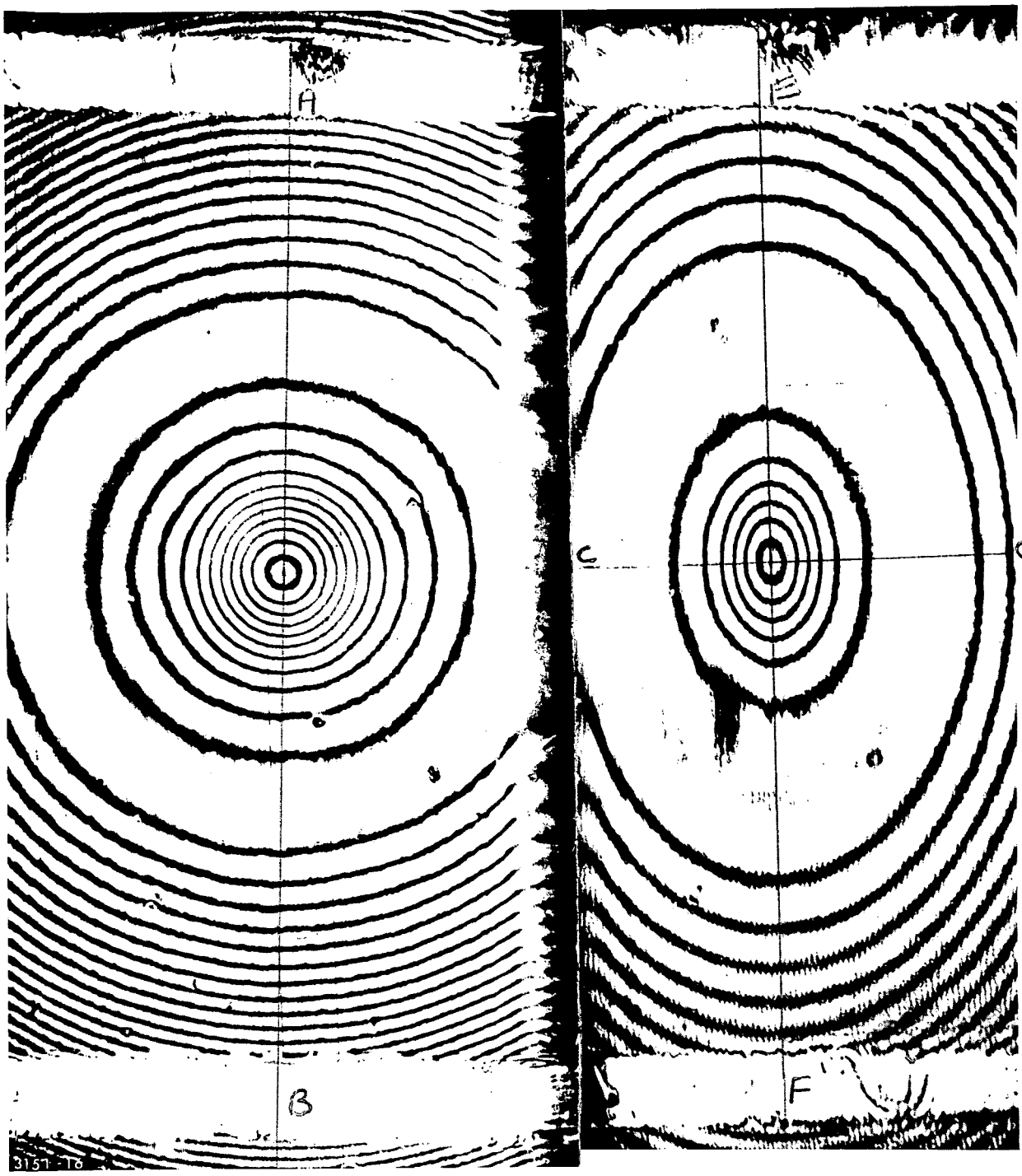

Figure 78. Entrapment with Fluid z (t = 3 sec)

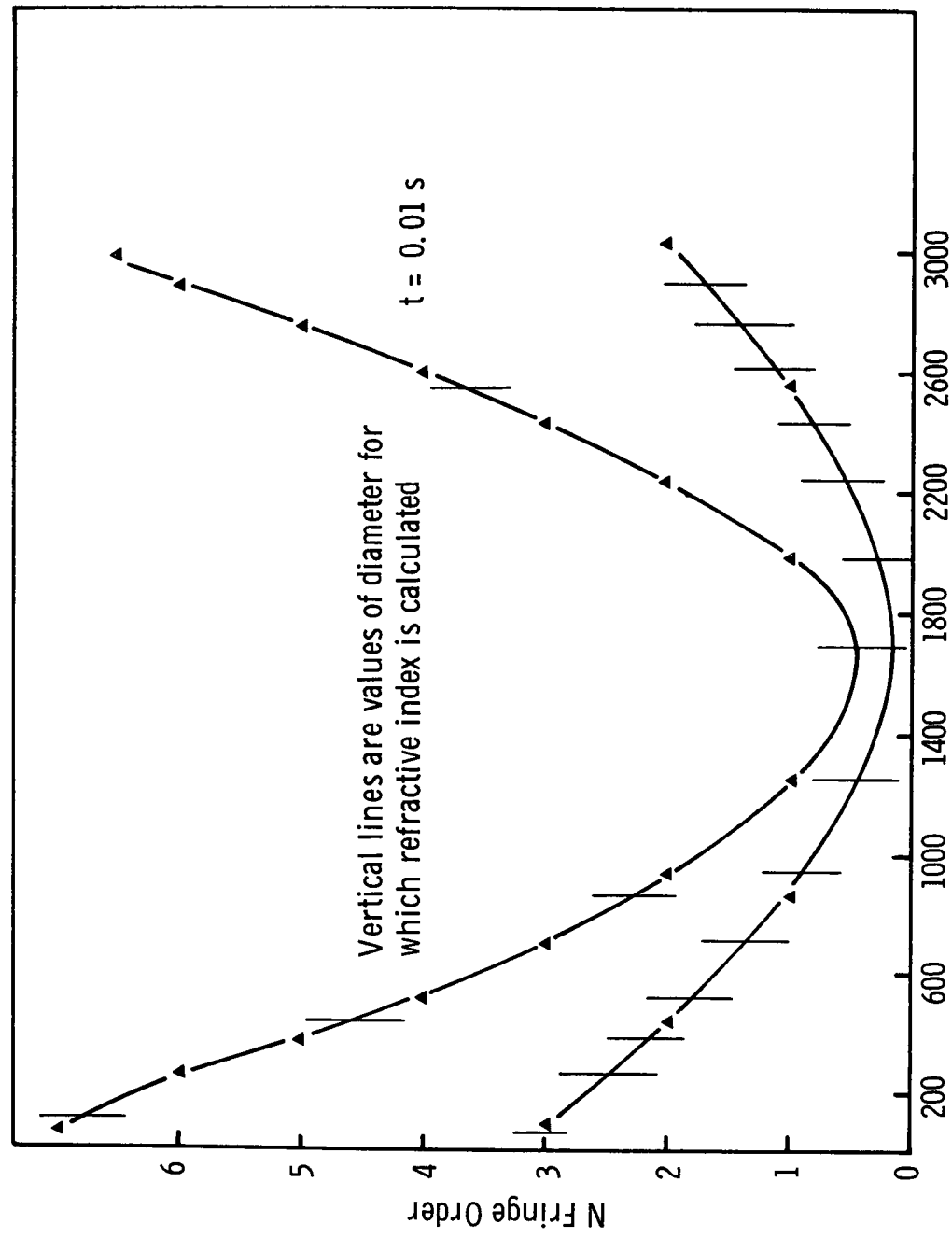

Figure 79. Graph of fringe order against diameter; Fluid e at 26°C

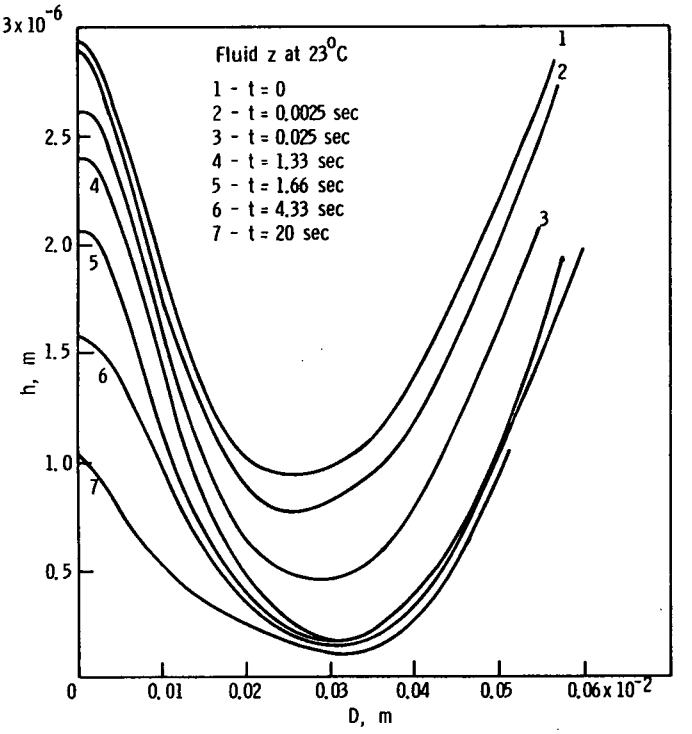

Figure 80. Graph of entrapment depth against diameter; Fluid z at 23°C

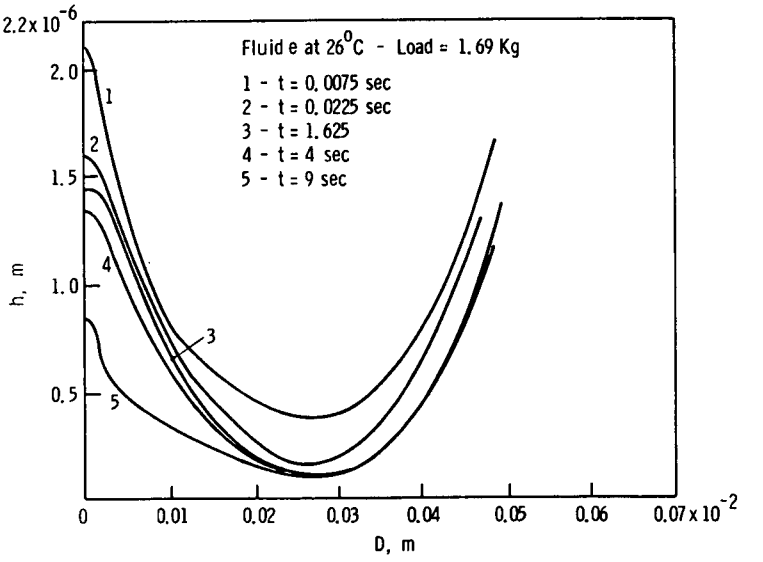

Figure 81. Graph of entrapment depth against diameter; Fluid e at 26°C; load, 1.69 kg

At this point it is convenient to split the research up into six categories.

(a) The determination of the viscosity pressure characteristics of fluids forming sufficiently large entrapments.

(b) The measurement of the approach velocity of the center of the ball (relative to the hemisphere) during the formation of an entrapment. Comparison of these results was then made with the theoretical values predicted by Christensen.

(c) The variation of the refractive index of the fluid with pressure, again for fluids which gave sufficiently large entrapments.

(d) An investigation of the relation between the velocity of approach of the ball and the entrapment size.

(e) Entrapment formation for the NASA fluids.

(f) The variation of the density of the fluid with pressure for fluids which gave large enough entrapments.

These six categories will now be taken up, each in turn.

5.3 VISCOSITY DETERMINATION

To find the viscosity of the fluid, it is first necessary to find the pressure distribution. This was done by a computer program, originally written by D. Evans of the Computing Section, Imperial College (not for this contract).

The program calculates the pressure field over an entrapment. A pressure field is suggested and the resulting deformation is calculated. This is compared with the experimental shape, and the pressure is adjusted in proportion to the fit. This is then used to calculate a new deformation, and this procedure is continued until the computed shape converges to the experimental. A polar grid is used having 18 sectors and 51 rings, the pressure being defined over the inner 21 rings, the first ring being the center point. A normalized pressure field is used for the deformation calculation and then a value for the maximum pressure is obtained by constraining the computed deformation to give the correct difference between the center and edge of the entrapment.

The input is the experimental values derived from the photographs, together with the numerical value of Young's modulus and Poisson's ratio for the ball and plane surface. The deformation is calculated from the formula

$$W = \frac{1-\sigma^2}{\pi E} \iint P \, dr \, d\theta \qquad (55)$$

$$= A \times P_{max} \iint p^* dr \, d\theta,$$

where p* is the normalized pressure.

At each point of the grid, a minor grid, over which the integration is approximated, is set up; this consists of lines at angles of $\pi/24$. For each of these lines, the intersections with the sectors and rings of the main grid are found, and the values of pressure at each point are calculated by interpolating for the values of pressure on the adjacent mesh points of the main grid. The summation $\Sigma_1 p_i dr_i$ is then made for each line, and then the summation of these over θ, giving the approximation $\Sigma\Sigma\ p\ dr\ d\theta$ for the integral required.

The original shape of the ball is approximated locally by a parabaloid. The value for $A \times P_{max}$ is calculated as the multiple of the deformation due to normalized pressure required to give a final shape with zero on the 21st ring and the experimental value for the central deformation on the 1st ring. $\underline{A}$ can be calculated from the values of σ and E fed in, to give a value for P_{max}.

The shape computed is compared with the experimental shape at each point and the pressure is then modified as previously explained. Due to the constraint that the center point, and boundary of the experimental shape and computed shape are already equal, the new pressure distribution is also normalized. A new value for P_{max} is found with the new calculation of the deformation due to this distribution. After five iterations a close fit is usually obtained.

From the pressure distribution the pressure gradient at any given radius can be measured. The volume of fluid inside any given radius can be found by integrating the entrapment shape from the center to the given radius. By measuring the volume for successive photographs and then measuring the rate of change of volume, the rate of fluid flow out of that radius can be deduced.

Using the standard formula for viscosity,

$$\eta = - \frac{\partial P}{\partial r} \frac{h^3}{12} \times \frac{2\pi r}{p_r} , \qquad (56)$$

where r is the radius at which η is being calculated,

$\frac{\partial P}{\partial r}$ is the pressure gradient,

h is the film thickness at radius r, and

q_r is the rate of flow from radius r,

the value for the viscosity can be found.

By varying the value of r, the viscosity can be measured at varying pressures.

A computer program was written to calculate the viscosities. This calculates the viscosity of the fluid at 19 different radii and at each photograph. Only entrapments with a depth of more than about 1.2×10^{-6}m could be used, as the others could not be measured to a sufficiently high accuracy. Unfortunately the only NASA fluid which gave sufficiently large entrapments was fluid e. So the results for the fluid z have been included also. The rate of shear was also calculated by the program.

Figures 82 and 83 show typical pressure plots for fluid e and z. Figures 84 and 85 give plots of log viscosity against pressure. The scatter of the points is caused by (i) small inaccuracies in the measurements of the entrapment which can lead to both the wrong pressure distribution and an incorrect volume flow and (ii) the pressure calculating program uses an iterative method which does not always converge quite correctly. This can produce slightly incorrect pressure values. Both these factors lead to small errors in individual measurements.

From the graphs of $\log_{10}$ viscosity against pressure, the pressure viscosity coefficient (α) was measured at different pressures. The results are given in Table 11.

Comparing the results with the α value measured by R. Gentle (section 3) it can be seen at what pressures his measurements apply. For fluid z, Gentle obtains $\alpha = 2.3 \times 10^{-8} m^2/N$ (1.6×10^{-4} psi^{-1}) with a Hertz max. of $4.1 \times 10^8 N/m^2$ (60×10^3 psi) at 23°C. From Fig. 85 it can be seen that this is equivalent to the α value at a pressure of $2.1 \times 10^8 N/m^2$ (30×10^3 psi). For fluid e, Gentle obtains $\alpha = 3.2 \times 10^{-8} m^2/N$ (2.2×10^{-4} psi^{-1}) with a Hertz max. of $4.1 \times 10^8 N/m^2$ and at 26°C. Figure 84 indicates this is equivalent to the α value at a pressure of $1.2 \times 10^8 N/m^2$ (18×10^3 psi).

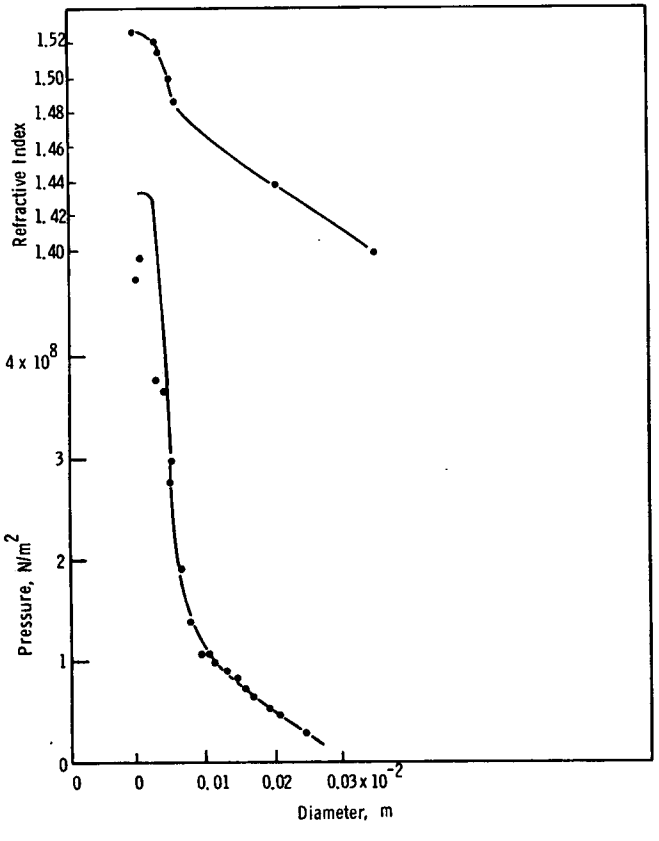

Figure 82. Graph of refractive index and pressure against diameter; Fluid e at 26°C; load 1.7 kg

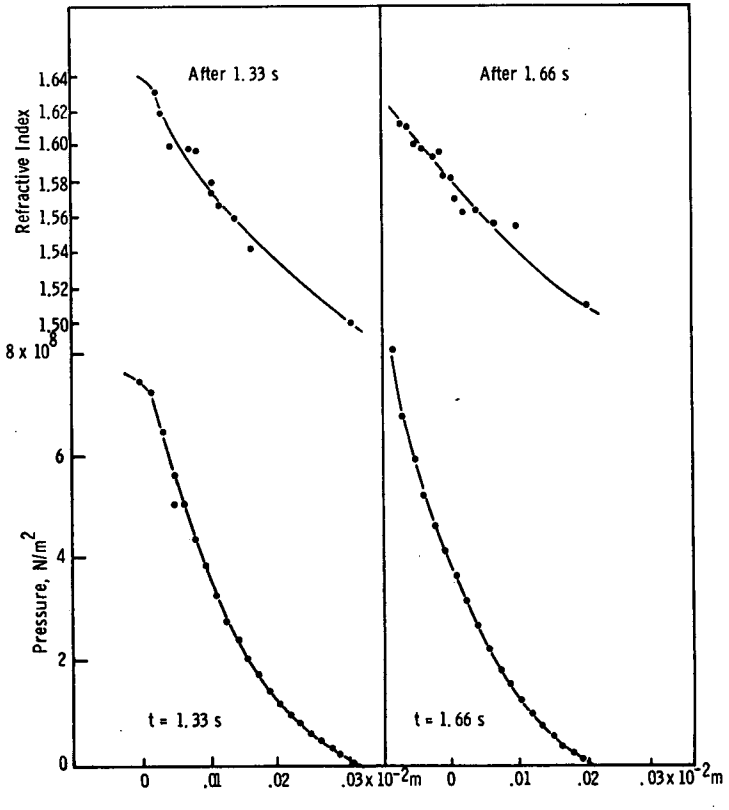

Figure 83. Graph of refractive index and pressure against diameter; Fluid z at 23°C

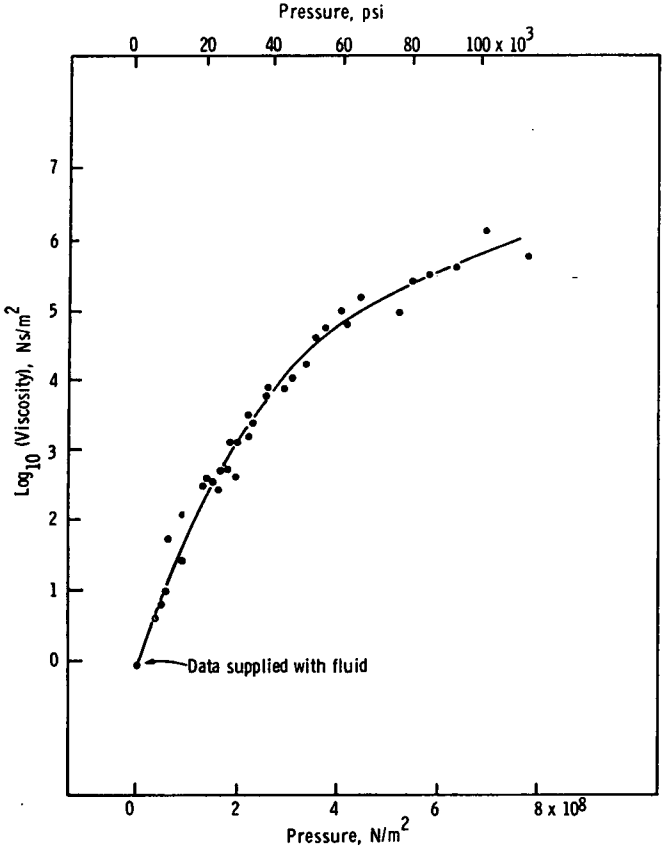

Figure 84. Graph of viscosity against pressure; Fluid e at 26°C

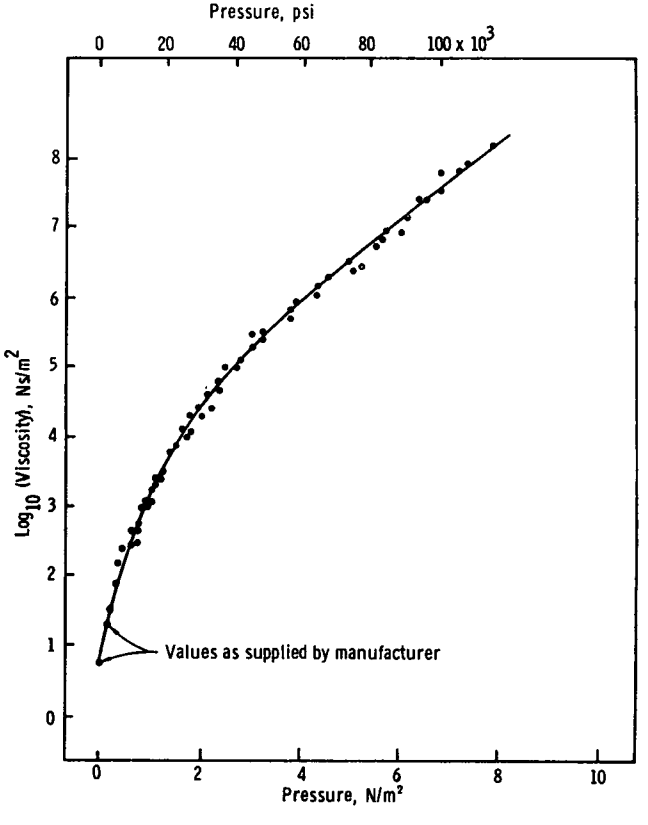

Figure 85. Graph of viscosity against pressure; Fluid z at 23°C

Table 11

PRESSURE-VISCOSITY COEFFICIENT α AT VARIOUS PRESSURES

Fluid e at 26°C

Pressure	α (from Fig. 84)
0	$4.6 \times 10^{-8} m^2/N$ (3.2×10^{-4} psi^{-1})
$0.69 \times 10^8 N/m^2$ (10×10^3 psi)	$4.1 \times 10^{-8} m^2/N$ (2.8×10^{-4} psi^{-1})
$1.03 \times 10^8 N/m^2$ (15×10^3 psi)	$3.6 \times 10^{-8} m^2/N$ (2.5×10^{-4} psi^{-1})
$1.38 \times 10^8 N/m^2$ (20×10^3 psi)	$2.9 \times 10^{-8} m^2/N$ (2.0×10^{-4} psi^{-1})
$2.07 \times 10^8 N/m^2$ (30×10^3 psi)	$2.6 \times 10^{-8} m^2/N$ (1.82×10^{-4} psi^{-1})
$6.21 \times 10^8 N/m^2$ (90×10^3 psi)	$0.67 \times 10^{-8} m^2/N$ (0.46×10^{-4} psi^{-1})

Fluid z at 23°C

Pressure	α (from Fig. 85)
0	$3.9 \times 10^{-8} m^2/N$ (2.74×10^{-4} psi^{-1})
$1.38 \times 10^8 N/m^2$ (20×10^3 psi)	$2.6 \times 10^{-8} m^2/N$ (1.8×10^{-4} psi^{-1})
$2.07 \times 10^8 N/m^2$ (30×10^3 psi)	$2.3 \times 10^{-8} m^2/N$ (1.6×10^{-4} psi^{-1})
$6.21 \times 10^8 N/m^2$ (90×10^3 psi)	$1.36 \times 10^{-8} m^2/N$ (0.94×10^{-4} psi^{-1})

The rate of shear varied from 10^{-1} to $10^{+4}s^{-1}$, it being higher for the larger pressures. This range of shear stress compliments the rolling contact technique, which can measure apparent α values from a rate of shear of $10^{4}s^{-1}$ upwards.

Note also that this method allows η to be determined, since $q_r \propto (h^3/12\eta)(\partial p/\partial r)$, while rolling does not because $q_r \propto \bar{u}h/2 - (h^3/12\eta)(\partial p/\partial r)$, and the $\bar{u}h/2$ term is dominant.

The technique described opens up a whole new range of viscosity measurements. For suitable fluids it now is possible to obtain measurement at viscosities several orders of magnitude higher than by any previous methods. By using harder materials (e.g. sapphire) and a ball with a larger radius of curvature, the technique should be capable of extension to cover a wider range of fluids and to reach much higher pressures.

The results also show a correlation with the result obtained by Gentle (section 3). It is interesting that here a pressure 1.2 to 2.1 x 10^8 N/m^2 has to be taken as the effective pressure at which the α values in the rolling contact test device are determined. In earlier work Westlake and Cameron[27] found that the effective "viscosity" pressure was 7 x 10^7 N/m^2 (10^4 psi).

5.4 APPROACH VELOCITY AND CHRISTENSEN'S SOLUTION

According to Christensen's theoretical work, the following equation should govern the approach of surfaces at the center of the contact.

$$V^{\frac{1}{2}} = Sh, \tag{57}$$

where V is the approach velocity of the surfaces,

h is the film thickness at the center, and

$$S = \frac{6\eta_o\alpha(\pi E\alpha)^2}{16} \times \frac{(\pi\alpha E)^2}{32R} \times 5.1,$$

where η_o is the viscosity of the fluid at atmopsheric pressure,

α is the pressure viscosity coefficient of the fluid, (assumed constant),

E* is the reduced Young's modulus for the two surfaces, and

R is the radius of the ball.

The above equation holds for central pressures greater than 5 x 10^7 N/m^2.

The approach velocity of the center of the contact was measured by finding the slope of the plot of maximum film thickness against time.

The approach velocity used here must be kept distinct from the velocity measured on the recorder which was the maximum velocity of the ball.

Unfortunately until the ball slowed to a velocity of less than about 5×10^{-6}m/s, the fringes were moving too fast for even a shutter speed of 1/2500 s, which was the fastest speed available. For all of the NASA fluids except fluid e, the film thickness was by this time too small to be measured accurately. Hence it was only for fluid e that results could be obtained.

Graphs of the approach velocity against film thickness for fluid e and fluid z are shown in Figs. 86 and 87.

It can be seen that the theoretical relationship predicted by Christensen certainly does not hold. However both graphs appear to consist of at least two straight lines with a sudden change in slope at a velocity of about 1×10^{-6}m/s. The slopes of these lines were measured to see what the apparent α value of the fluid would be given by Christensen's theory. For fluid e, Fig. 86, slope C = $2.8 \times 10^{4}m^{-\frac{1}{2}}s^{-\frac{1}{2}}$ and slope D = $5.73 \times 10^{2}m^{-\frac{1}{2}}s^{-\frac{1}{2}}$ are substituted into Eq. 57 to yield $\alpha = 3.3 \times 10^{-8}m^2/N$ (2.3×10^{-4} psi^{-1}) and $\alpha = 1.6 \times 10^{-8}m^2/N$ (1.1×10^{-4} psi^{-1}), respectively. For fluid z, Fig. 87, slope A = $1.2 \times 10^{4}m^{-\frac{1}{2}}s^{-\frac{1}{2}}$ and slope B = $3.37 \times 10^{2}m^{-\frac{1}{2}}s^{-\frac{1}{2}}$ yield (Via Eq. 57) $\alpha = 2.3 \times 10^{-8}m^2/N$ (1.6×10^{-4} psi^{-1}) and $\alpha = 0.6 \times 10^{-8}m^2/N$ (0.4×10^{-4} psi^{-1}), respectively.

If the α values found from slopes at A and C for fluids z and e are compared with the values found at 2.1 and $1.2 \times 10^{8}N/m^2$, respectively, in the previous section, it can be seen that there is quite a close agreement.

For fluid z the straight line appeared to cross the axis at 1×10^{-7}m which is the value to which the minimum film thickness tended (see Fig. 80). For fluid e the velocity suddenly increased at a film thickness of 13×10^{-7}m and then became constant at a value of 2.5×10^{-7}m/s. This would imply by Christensen's theory that α had fallen to zero.

The theory does not appear to work very well experimentally. This is almost certainly due to the assumption that the pressure viscosity coefficient is constant. Perhaps a closer study of the discrepancies would prove valuable for determining properties of the fluid. From the results it would seem that the fluids behave as though their α value at about $2 \times 10^{8}N/m^2$ was the right value for Christensen's theory, until the velocity drops below about 1×10^{-6}m/s. Then the α value decreases dramatically.

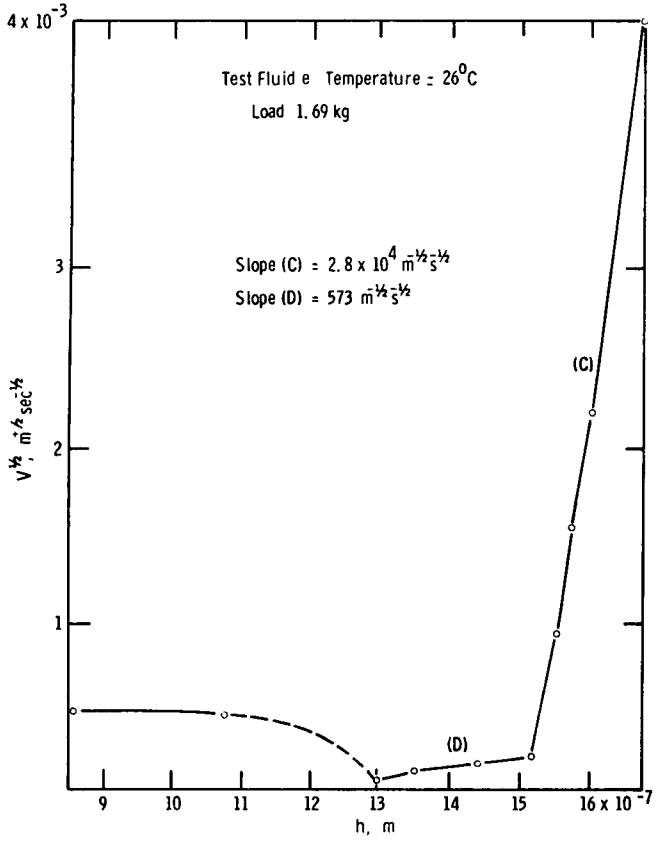

Figure 86. Graph of the square root of the approach velocity of the ball center against film thickness; Fluid e at 26°C; load, 1.69 kg

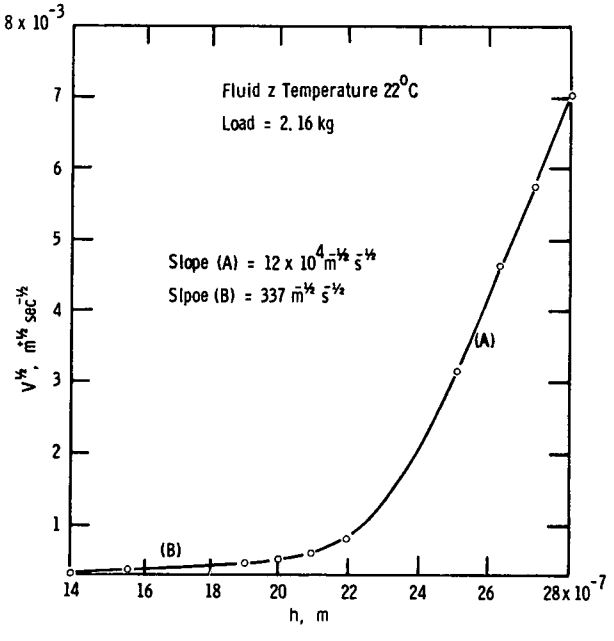

Figure 87. Graph of the square root of the approach velocity of the ball center against film thickness; Fluid z at 22°C; load, 2.16 kg

5.5 REFRACTIVE INDEX AND PRESSURE

The refractive index inside the entrapment was measured in the manner described previously. A graph of refractive index against diameter was then drawn. The refractive index at diameters at which the pressure had been calculated were then read off. See Figs. 82 and 83.

The results for fluids e and z are shown in Figs. 88 and 89. For fluid e the refractive index varies almost linearly with pressure up to about $2 \times 10^8 N/m^2$. The rate of change of the index with pressure then drops. For fluid z the refractive index increased almost linearly with pressure up to about $7 \times 10^8 N/m^2$. The results above this pressure are not very accurate, due to the fact that very small errors in the maximum deformation could effect the maximum pressure calculated by the computer program. This is a consequence of the fact that large changes of this central maximum pressure do not alter the shape very much, as the area it acts over is small.

The technique provides a novel way of measuring the change of refractive index with pressure for suitable fluids. For the first time it has actually been possible to measure the change of refractive index in an E.H.L. contact.

5.6 APPROACH VELOCITY AND ENTRAPMENT SIZE

The approach velocity was measured on the U.V. recorder as previously described. The approach velocity was plotted against the maximum entrapment depth. This was done with fluid z using loads of 2 kilograms and relatively high velocities.

There was found to be no correlation between the entrapment size and the initial velocity of the ball. This was a most suprising result and further measurement of the approach velocity were therefore not carried out. It was not until the Miliken camera was used that the explanation of this anomaly became apparent. At some critical value of the approach velocity the ball bounces after the initial entrapment is formed. An example of this is shown in photographs, Fig. 97, which is described in the next section. The ball comes down again within one frame which is 1/400 sec., but the resulting entrapment is much smaller in size, and does not appear to have any direct correlation with the entrapment before the bounce.

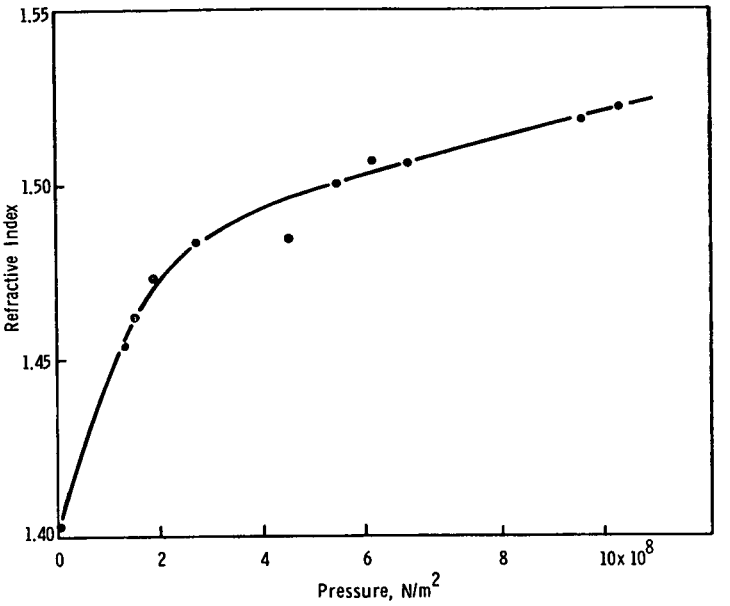

Figure 88. Graph of refractive index against pressure; Fluid e at 26°C

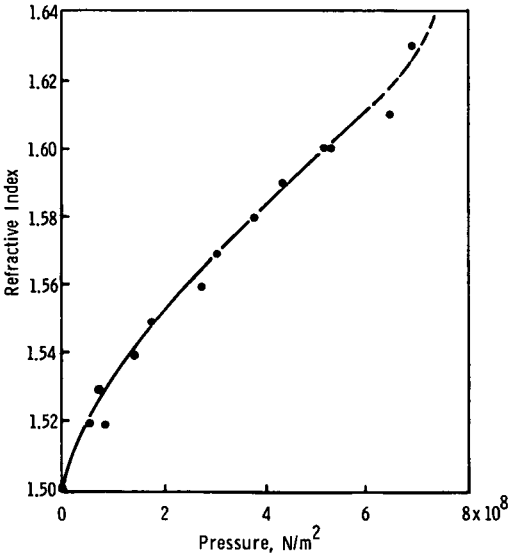

Figure 89. Graph of refractive index against pressure; Fluid z at 23°C

For the measurement to have much validity the conditions would have to be altered to prevent the ball bouncing. Until these conditions are known the above method does not appear to have very much use.

5.7 ENTRAPMENT FORMATION

All the NASA test fluids (except fluids d, j, and n, which were too thin) were tested using the high speed Miliken camera at 400 fps. Enlargements were then made of the first few frames and compared with the ones from other fluids. Comparatively low loads, of about 1 kg, were used for most of the fluids.

Fluid b

This is shown in Fig. 90. The first photograph shows the ball approaching the hemisphere with an entrapment approximately 4×10^{-7}m deep, and the second that it has bounced away from the surfaces. Cavitation is clearly seen around the edges of the contact, which is still partly visible in picture 4. Notice that the size of the entrapment has greatly decreased. Pictures 5 and 6 show air bubbles released by the cavitation which remain for a comparatively long time.

Fluid l

This is shown in Fig. 91. It is very similar to fluid b except that the entrapment in Picture 1 is smaller, about 2×10^{-7}m; in picture 3 it is shallower than the first order fringe. Cavitation and air bubbles are again apparent.

Fluid f

The results are given in Figs. 92 and 93. This fluid formed a larger entrapment than any of the other test fluids, except e. Picture 2 again provides evidence of cavitation, although not quite so pronounced as either of the two previous fluids, b and l. After 0.1 s, there is still a fringe visible in the center (Picture 6). Notice also the air bubbles. These tend to float out from the contact, dissolving slowly. This can be seen very clearly by comparing Picture 5 and 6.

Fluid q

This fluid (Figs. 94 and 95) formed a small entrapment, which disappeared after 0.015 s. Some cavitation can be seen in Picture 5 as the ball bounces off from the flat surface.

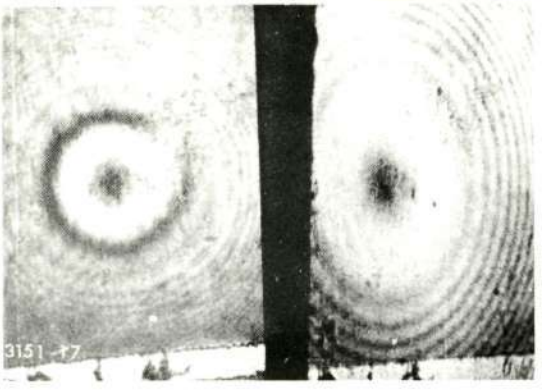

t = 0 sec

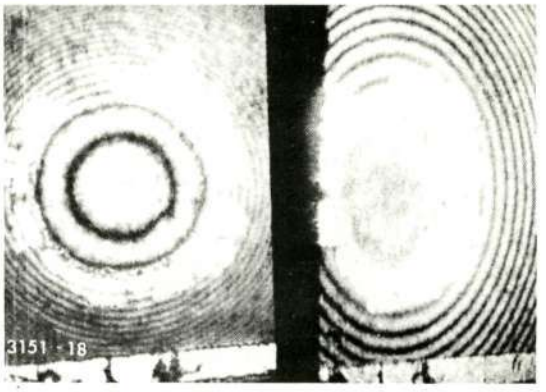

t = 0.0025 sec

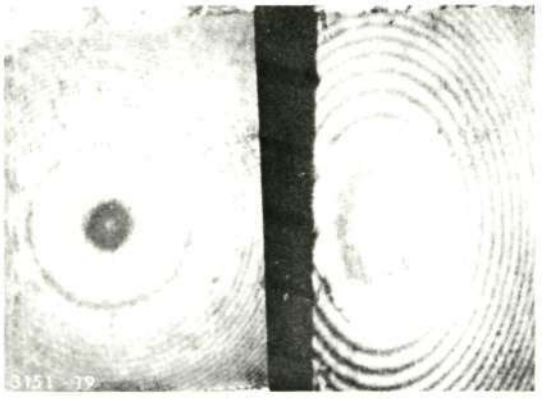

t = 0.005 sec

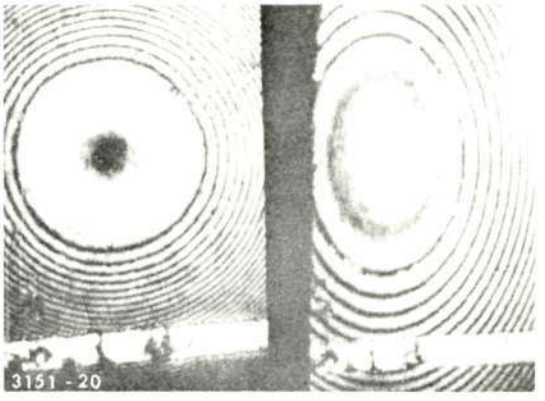

t = 0.0075 sec

t = 0.01 sec

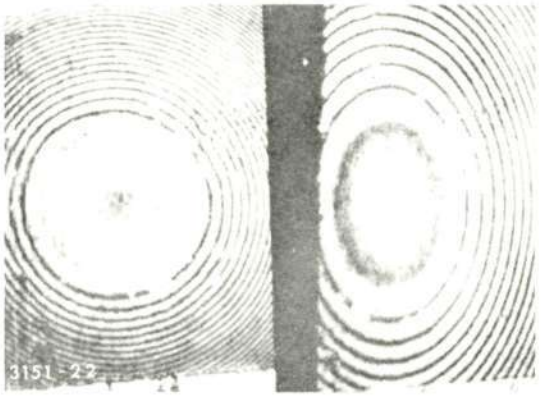

t = 0.0125 sec

Figure 90. Entrapment with Fluid b as a function of time; temperature, 24.8°C; load, 1.03 kg

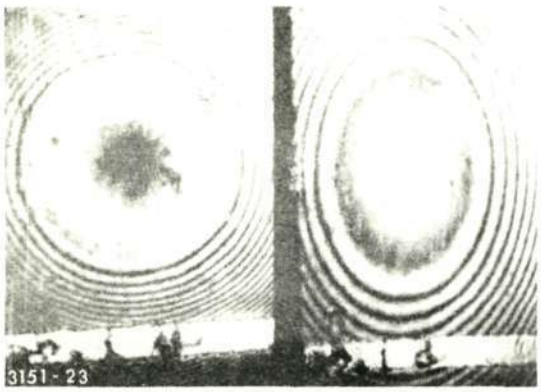

t = 0 sec

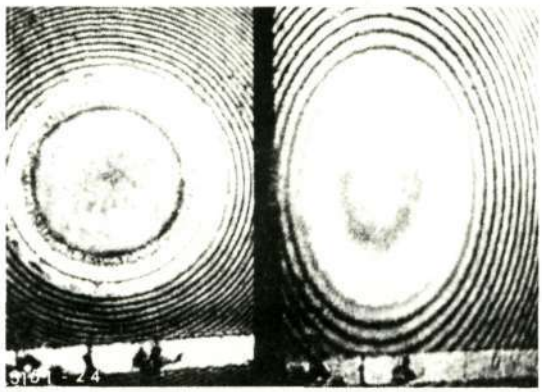

t = 0.0025 sec

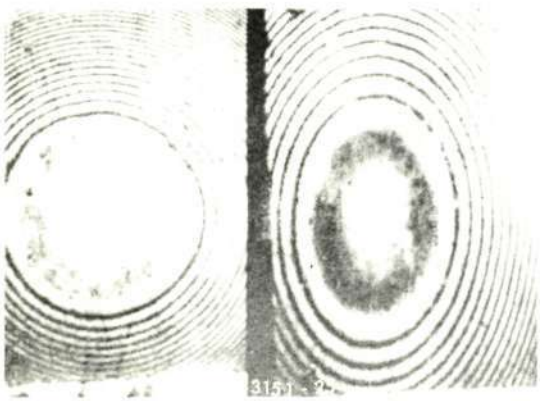

t = 0.005 sec

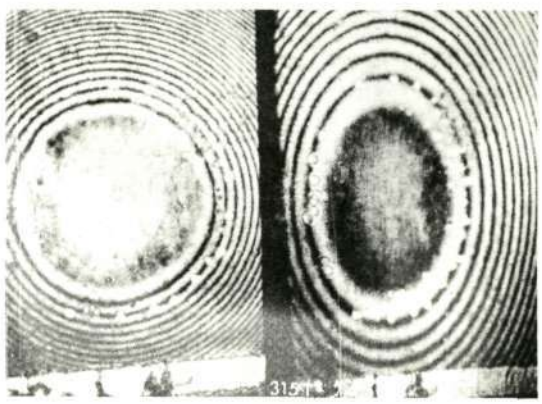

t = 0.0075 sec

t = 0.0075 sec

Figure 91. Entrapment with Fluid 1 as a function of time; temperature, 23.2°C; load, 1.03 kg

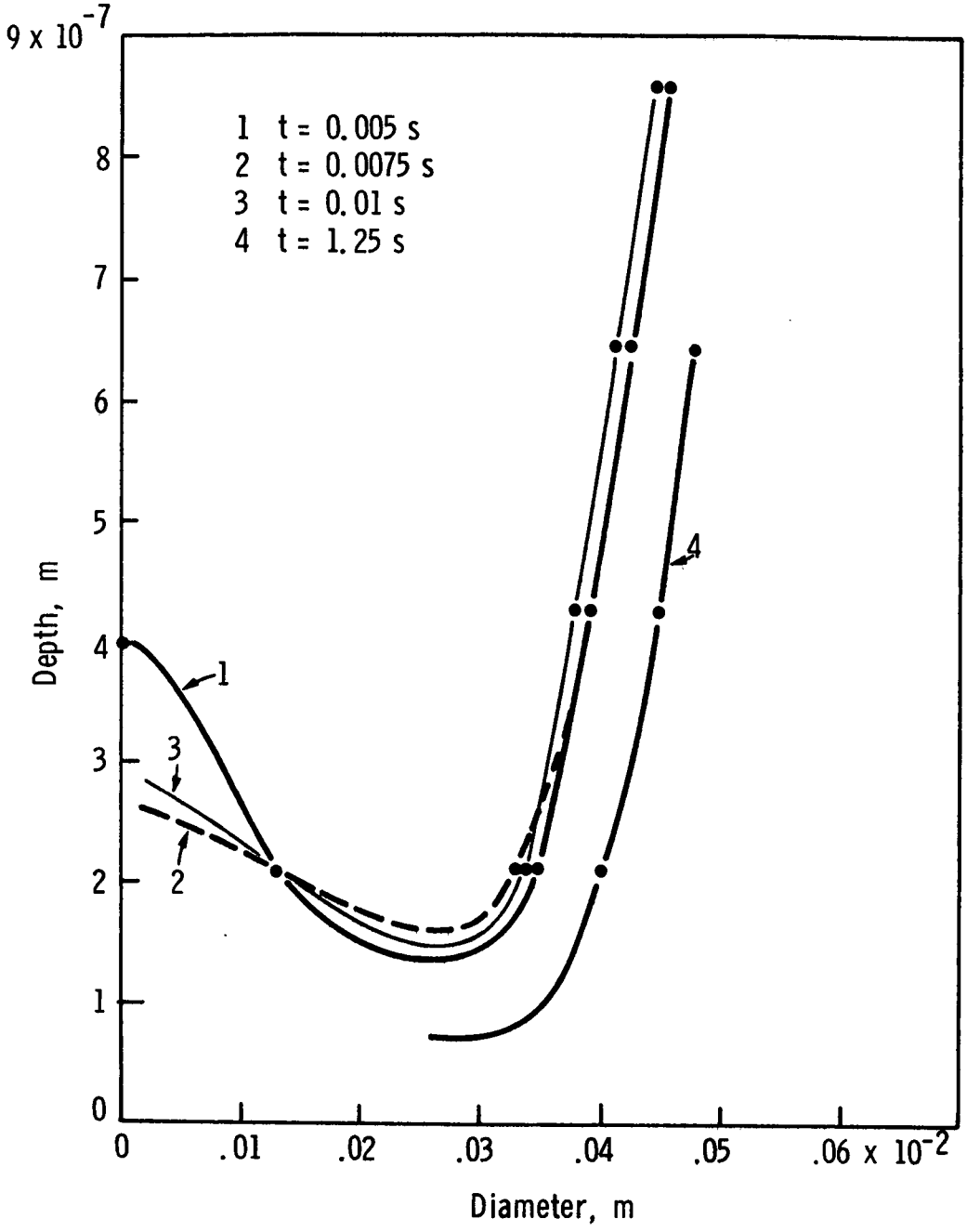

Figure 92. Graph of entrapment depth against diameter; Fluid f

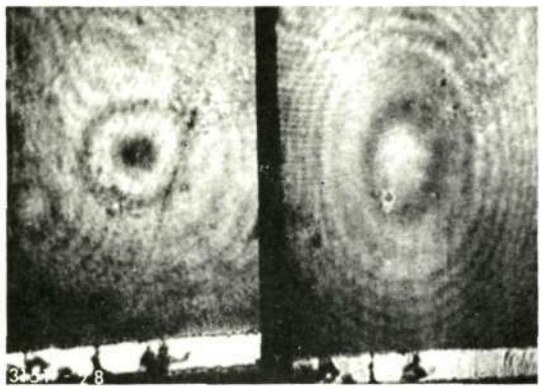

t = 0 sec

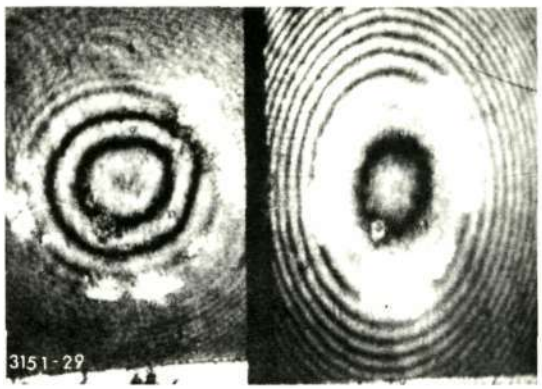

t = 0.0025 sec

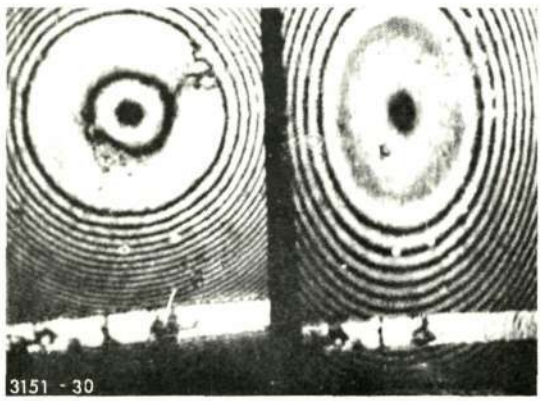

t = 0.005 sec

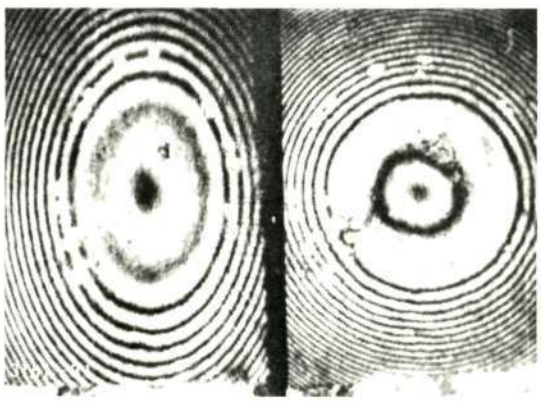

t = 0.0075 sec

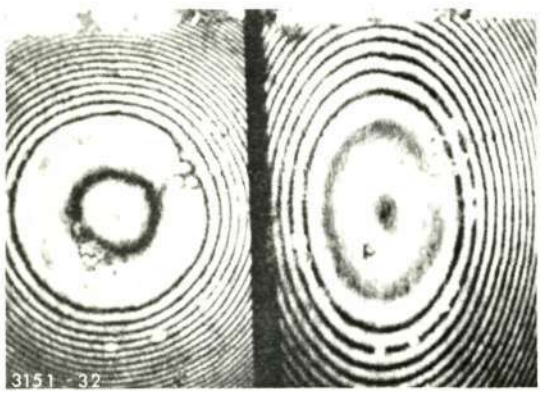

t = 0.010 sec

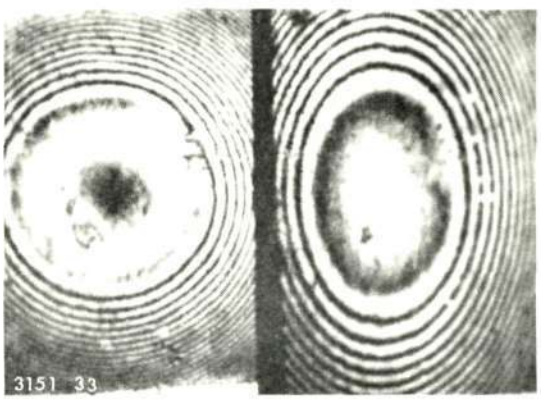

t = 0.1 sec

Figure 93. Entrapment with Fluid f as a function of time; temperature, 24.6°C; load, 1.039 kg

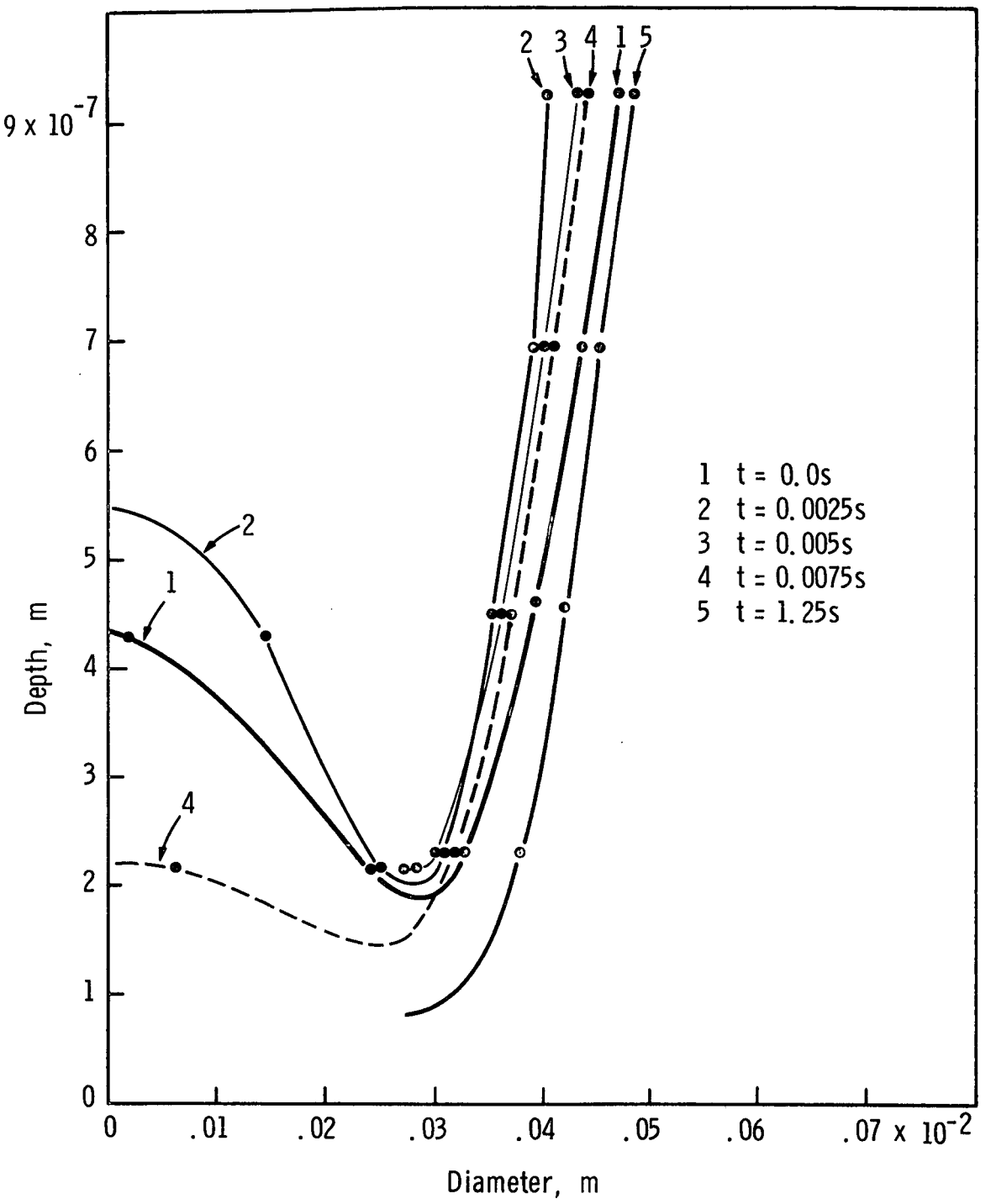

Figure 94. Graph of entrapment depth against diameter; Fluid q at 24.6°C

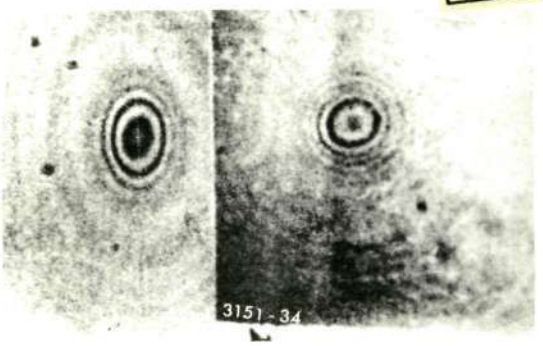

t = 0 sec, Fluid z
T = 23°C, load = 2.16 kg

t = 0.0025 sec, Fluid z
T = 23°C, load = 2.16 kg

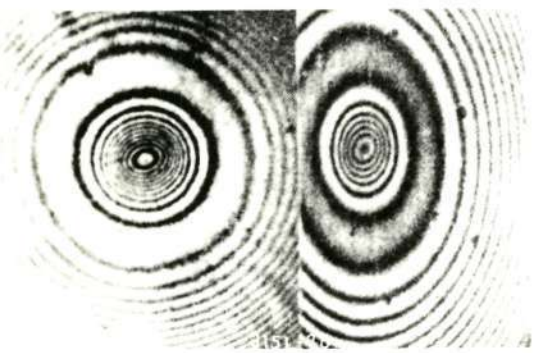

t = 0.005 sec, Fluid z
T = 23°C, load = 2.16 kg

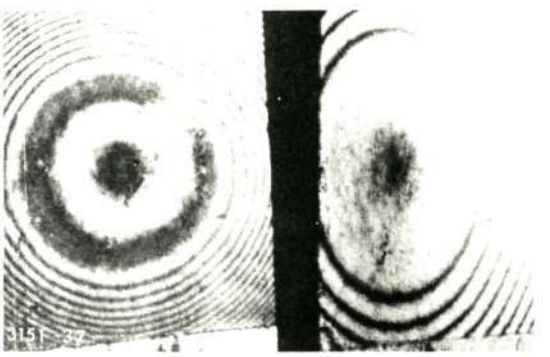

t = 0 sec, Fluid q
T = 24.6°C, load = 1.03 kg

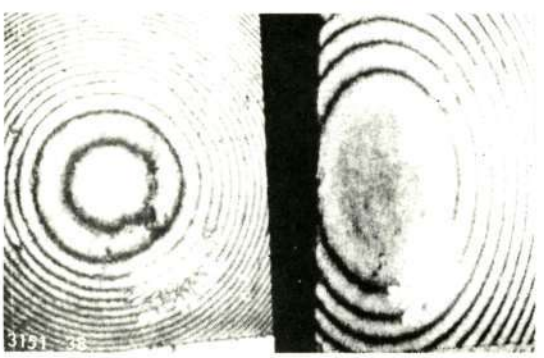

t = 0.0025 sec, Fluid q
T = 24.6°C, load = 1.03 kg

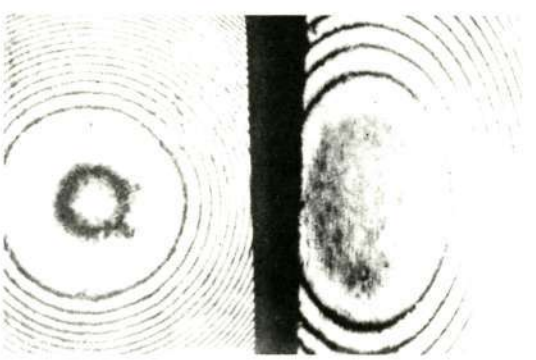

t = 0.005 sec, Fluid q
T = 24.6°C, load = 1.03 kg

Figure 95. Entrapments with fluids z and q as a function of time

Fluid z

This is included here (Fig. 95) because it was the only fluid that did not bounce when the high speed pictures were taken. Notice there is no sign of cavitation.

In section 5.6 a higher approach velocity was used than in this part of the work, and there clear evidence was found of bouncing.

Fluid a and c

Profiles of the ball after 1 s are plotted in Fig. 96. Only on the initial frame did these fluids form entrapments deeper than the first order fringe.

Fluids g, h, i, m, p, and k

These fluids were all similar in that again no significant entrapment was observed.

Fluid o

This produced an entrapment of one fringe, corresponding to a depth of about 5×10^{-7}m. More than 0.02 s elapsed before this fringe disappeared. The only fluids to form longer lasting entrapments were fluid e and f.

Fluid e

Several runs were done with this fluid at varying loads and temperatures.

The following observations were made from the pictures from Figs. 97 through 100.

i) The maximum cavitation occurred at a load of 2.16 kg and a temperature of 21.8°C. This can be seen in Picture 2, Fig. 97

ii) The maximum entrapment depth before the ball bounced also happened at a temperature of 21.8°C and a load of 2.16 kg.

iii) The minimum entrapment size after the ball bounced occurred again at a temperature of 21.8°C and a load of 2.16 kg.

iv) From Figs. 99 and 100 it can be seen that the entrapment is much deeper before bouncing and shallower afterwards for a load of 2.16 kg than for a load of 1.69 kg, at the same temperature of 26°C.

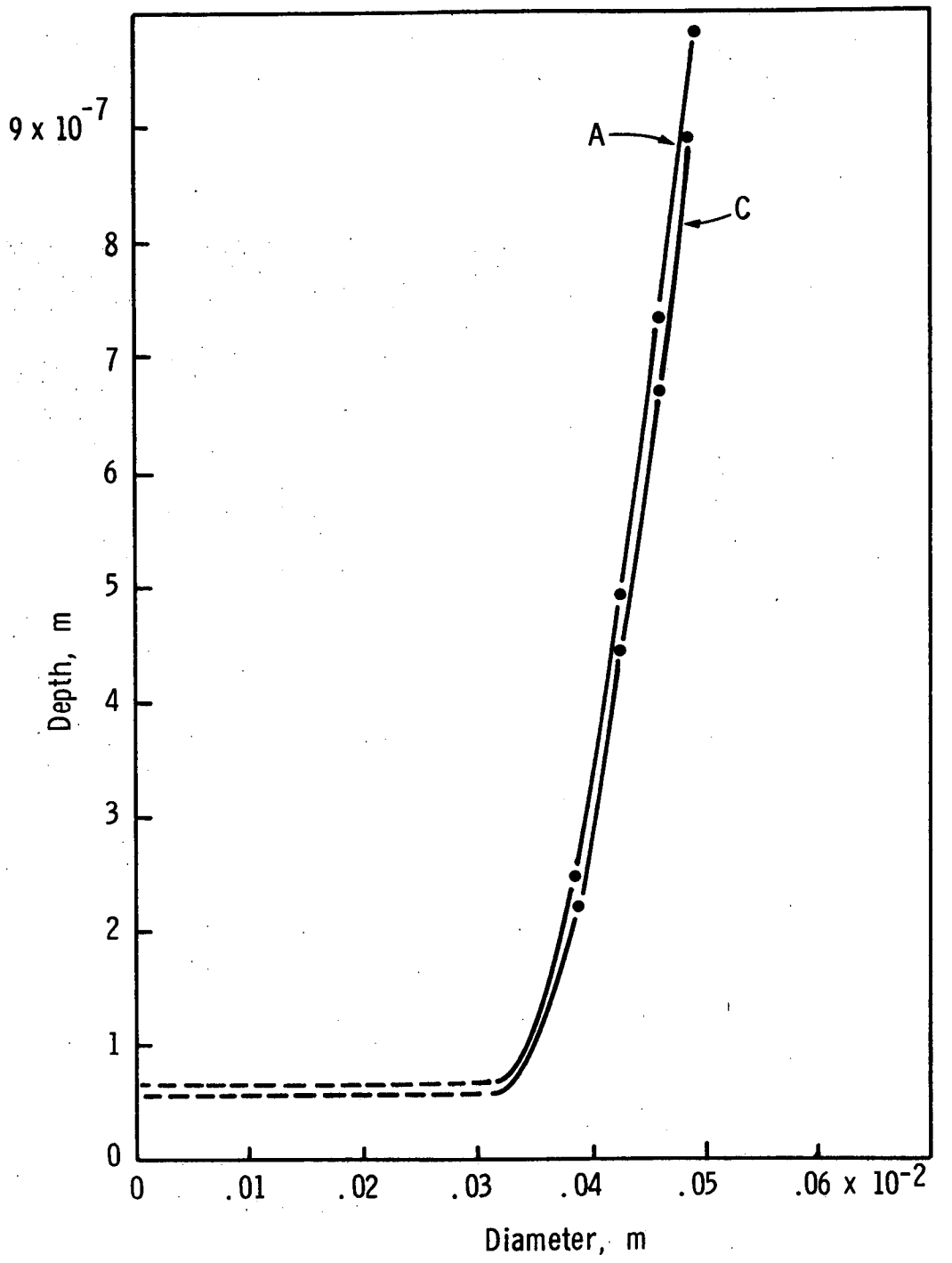

Figure 96. Graph of entrapment depth against diameter; Fluids a and c at 26°C; load, 1.03 kg; t = 1.0 sec

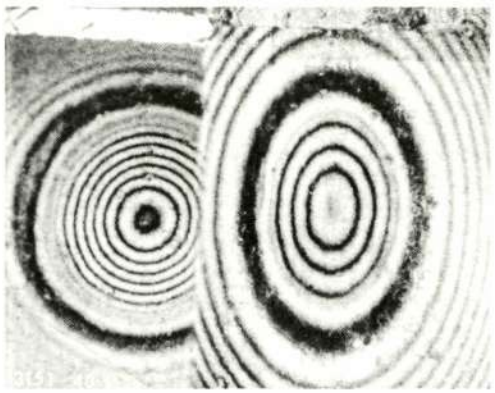

t = 0 sec

t = 0.0025 sec

t = 0.005 sec

Figure 97. Entrapment with Fluid e as a function of time; temperature, 21.8°C; load 2.16 kg

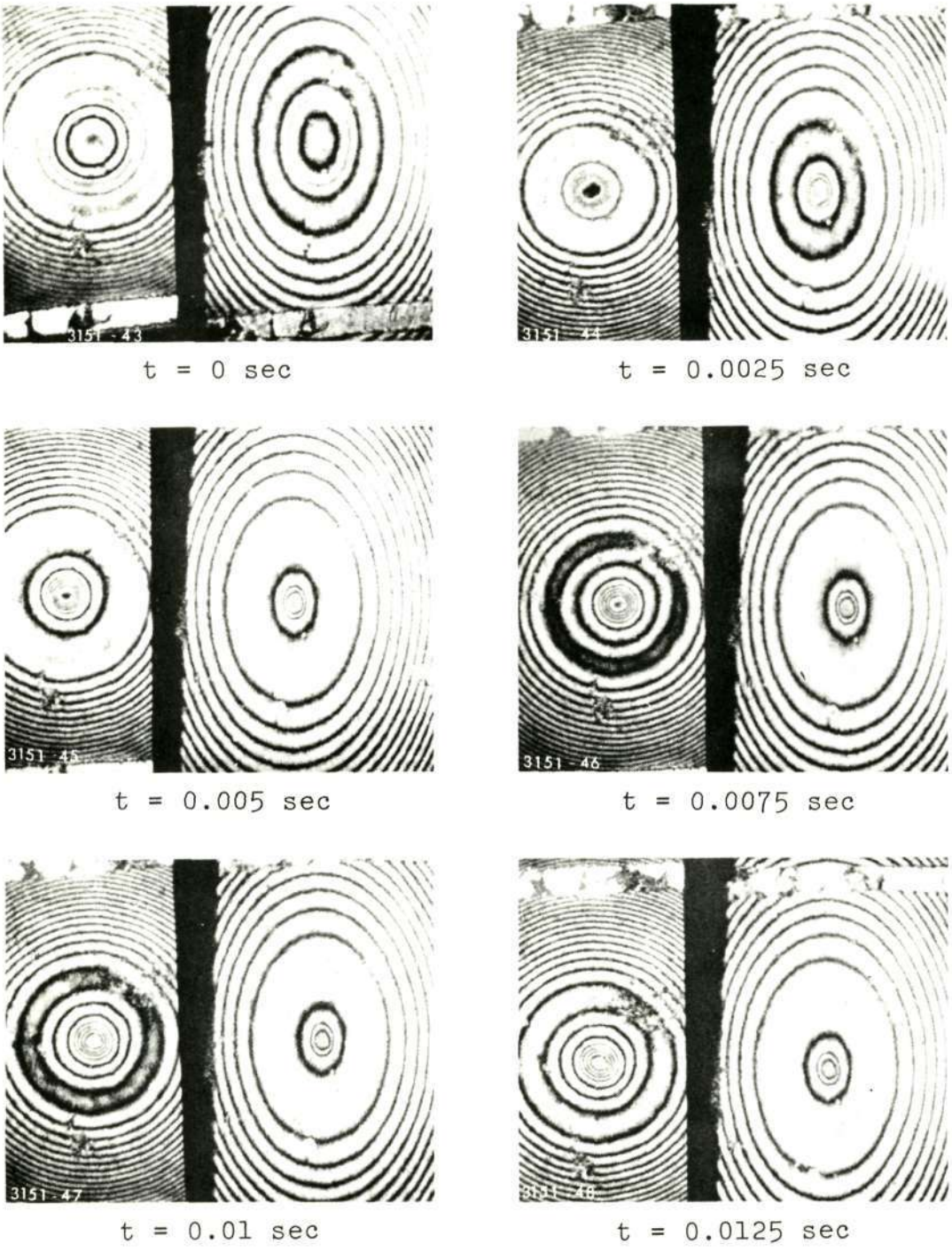

Figure 98. Entrapment with Fluid e as a function of time; temperature, 23.5°C; load, 1.03 kg

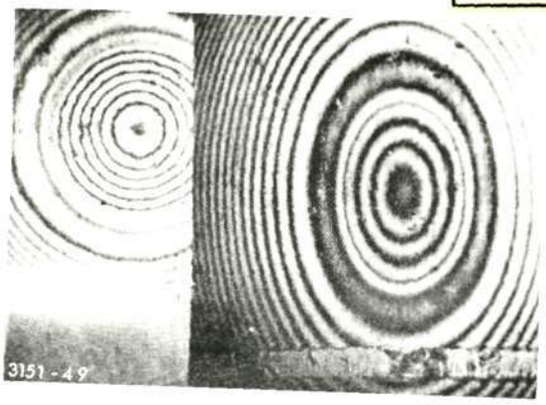

t = 0 sec

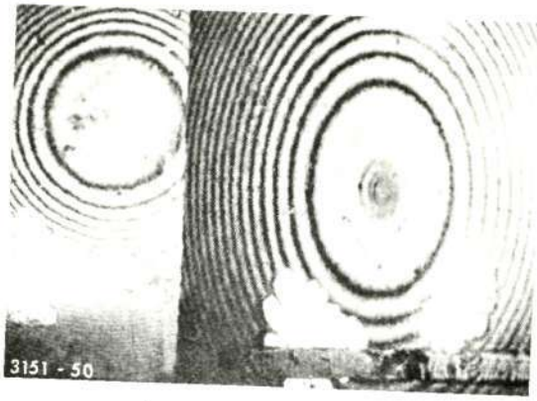

t = 0.0025 sec

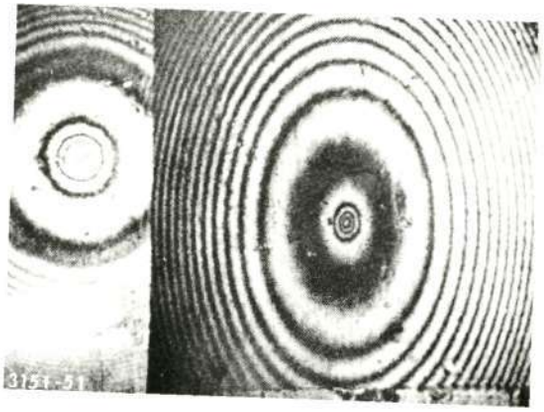

t = 0.005 sec

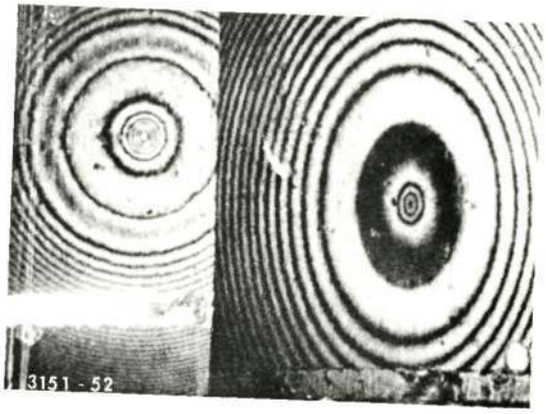

t = 0.0075 sec

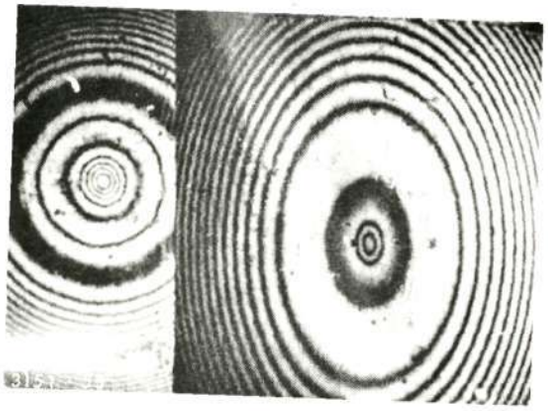

t = 0.01 sec

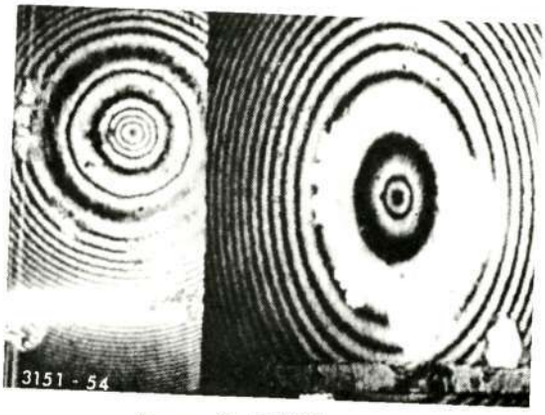

t = 0.0125 sec

Figure 99. Entrapment with Fluid e as a function of time; temperature, 26°C; load, 2.16 kg

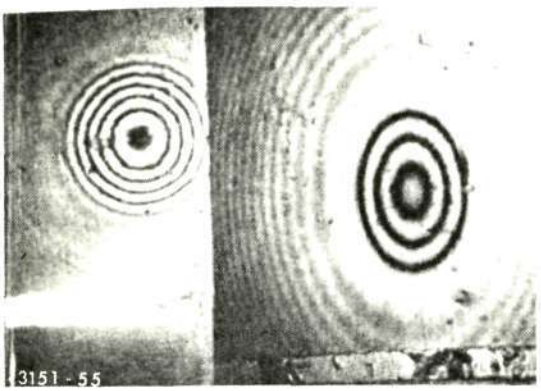

t = 0 sec

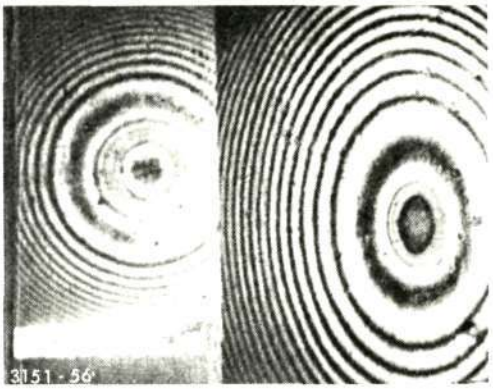

t = 0.0025 sec

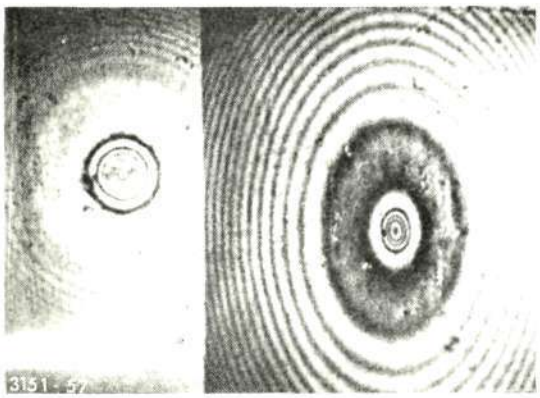

t = 0.005 sec

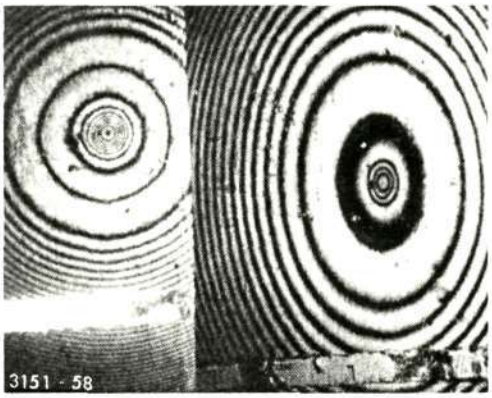

t = 0.0075 sec

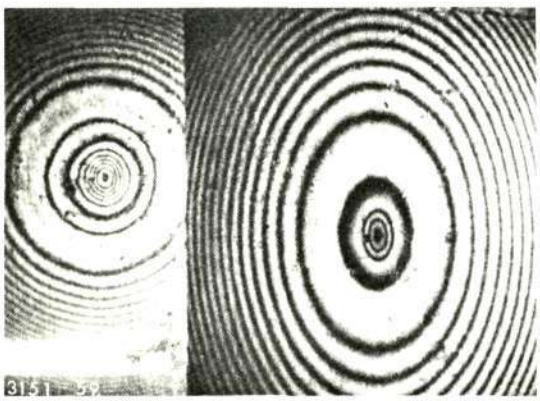

t = 0.01 sec

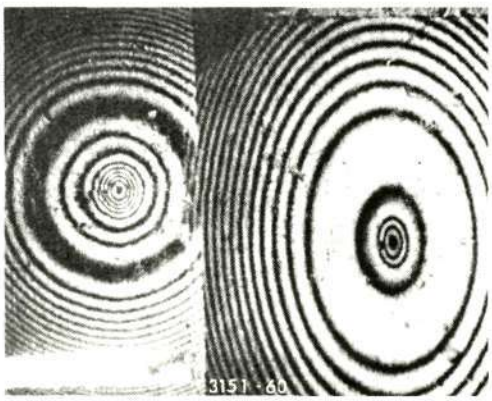

t = 0.0125 sec

Figure 100. Entrapment with Fluid e as a function of time temperature, 26°C; load, 1.69 kg

From these observations the following was deduced: Before the ball bounces the maximum depth of the entrapment is formed by the largest load and lowest temperature. These conditions also produce the largest amount of cavitation. After the ball has bounced there is a critical load which produces the maximum depth of entrapment. A higher load produces more cavitation and allows more fluid to escape. A lower load produces hardly any cavitation, (see picture 2, Fig. 98), and so very little fluid loss. However the entrapment is smaller as the original entrapment, before the bouncing effect, is very much smaller. The critical load for maximum entrapment size is around 1.6 kg.

Some interesting examples of cavitation can be seen in the results. With further development this technique may well provide very useful information into the rheological properties of fluids.

The results for fluid e show quite clearly that before the ball bounces the entrapment size can be increased by increasing the load or by decreasing the temperature, (which obviously is equivalent to increasing the fluid viscosity). After the ball bounces, however, there is a maximum entrapment depth which occurs at some critical load and temperature. Below this load the entrapment before the bounce is very small and above it, too much fluid escapes when the ball bounces.

5.8 DENSITY MEASUREMENT IN ENTRAPMENT

In section 5.5 the variation of the refractive index with pressure was found. From the Lorenz - Lorentz relationship we have

$$\frac{1}{\rho}\,\frac{n^2-1}{n^2+2} = \text{constant}, \tag{58}$$

thus

$$\rho/\rho_o = \frac{n^2-1}{n_o^2-1}\,\frac{n_o^2+2}{n^2+2}\,, \tag{59}$$

where n is the refractive index at pressure P and density ρ, and n_o is the refractive index at atmospheric pressure and density ρ_o.

By substituting the measured values of the refractive index into Eq. 59, we find the change in density. These are shown in Fig. 101 for fluids e and z. It is interesting to note that the rate of change of density of fluid e drops considerably at about $4 \times 10^8 N/m^2$ (60,000 psi). The bulk modulus at atmospheric pressure for fluid e was given in section 2.3 to be $1.86 \times 10^9 N/m^2$ (270,000 psi). If the slope of the curve through the intercept is measured, it gives a bulk modulus of $1.83 \times 10^9 N/m^2$ (265,000 psi). This falls well within the limits of experimental error.

This method provides a convenient way of measuring the fluid density and is the first time this has actually been done in an EHL contact.

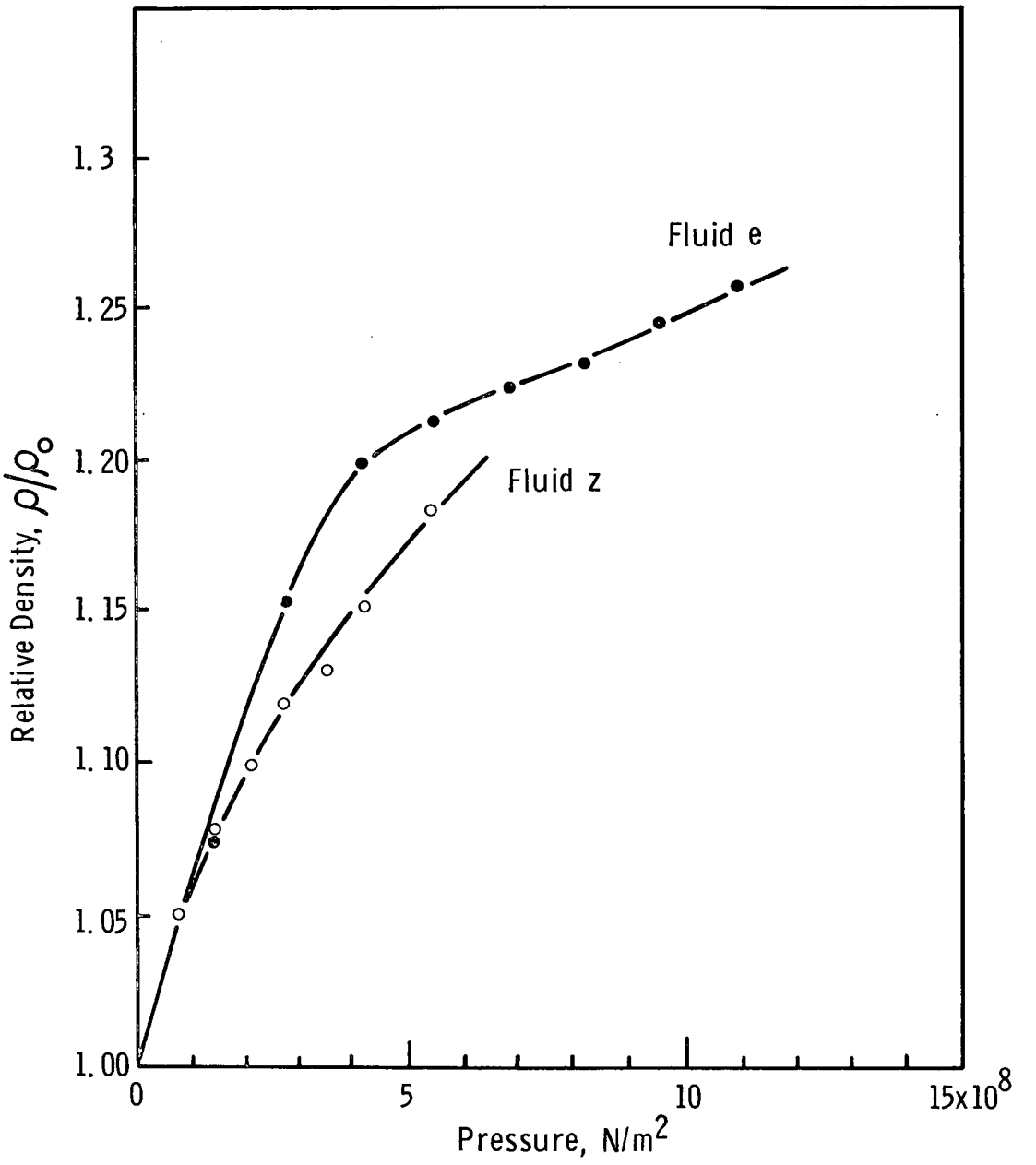

Figure 101. Graph of relative density against pressure

6. SOFT FILM STUDIES

6.1 FLUIDS TESTED

Of the seventeen test fluids listed in Table 1 fourteen were tested in this part of the project. The three omitted were fluids d, g, and p: octacosane, dihydrocedrene, and dimethylsilicone (100 cs), respectively. Fluid d is a solid at the temperature of measurement and unsuitable without dilution; it and fluid g are both expected to behave similarly to the other hydrocarbons studies. It is expected that fluid p would behave similarly to fluid q, the other silicone. The fluids omitted were substituted by four other fluids; stearic acid in hexadecane (cetane) solutions, with weight/weight concentrations of 0.4%, 0.1%, and 0.05%, and Hercolube, an ester fluid. These four new fluids were found more suitable for the study of soft films. Several of the fluids were diluted with cetane to lower their viscosities to a convenient range; this was not expected to alter their soft-film-forming properties excessively.

6.2 APPARATUS

6.2.1 Introduction to Apparatus

The apparatus was devised to overcome the biggest drawback in all squeeze film experiments, i. e. the possibility that unwanted dirt particles are seriously affecting or causing the "thick film" results. This problem and that of surface asperities are overcome by using mercury to displace the fluids being tested. The mercury will flow round any such protuberances and only be separated from the solid face by any fluid film remaining.

The test fluid film thickness is calculated from the capacitance measured between a known area of metal on the solid surface and the mercury with the lubricant as the dielectric. The variation of this film thickness with time is noted both for thinning of the fluid under the hydrostatic pressure of the mercury and for the thinning of the fluid as shear is applied by moving the mercury past the film.

Two types of apparatus are used. The cell apparatus in which the shear is applied to the mercury and the ball apparatus, which is used to test the fluids for any "thick film" formation, because it is simpler and quicker to use than the cell apparatus.

6.2.2 The Cell Apparatus

The cell apparatus has been improved over a lengthy period of time to its present form, which is reliable, easy to clean and comparatively versatile, though not too durable.

The form of these cells can be seen from Fig. 102. Each cell contains three capacitor plates, usually of chrome, although one cell with iron capacitors has been used. These capacitor plates are deposited on a microscope slide using a vacuum deposition apparatus. The shape of each plate, which is 1 cm^2 ($10^{-4}m^2$) in area plus a short thin connection strip, is produced with the aid of a mica mask, cut to the relevant dimensions, placed between the heated source of the metal and the slide in the vacuum apparatus. Lengths of wire are stuck to the connection strip using a conducting epoxy resin.

The completed slide is attached to a Teflon block. This block is shaped to reduce the effective cross section of the cell to whatever value is required for each cell. The top of the block has an indentation slightly wider than 1 cm ($10^{-2}m$) cut into it. The floor of this indentation is polished and either end is rounded off to reduce turbulence. The capacitor plates face onto this indentation, and the slide is adhered to the ridges on each side with an epoxy resin.

This completed section is placed in the glass cell casing under the window through which the connecting wires are drawn. It is secured and made flush with the casing using more epoxy resin which also serves to insulate the connecting wires and the conducting epoxy resin.

The cell casing is made of glass. So that reproducible sized casings could be obtained a carbon mold of the necessary shape and dimensions was built. The window in this casing is necessary for the cell's construction and to allow for the connection wires. It was initially included so that the films could be observed through a microscope by interferometry. Of the three vertical glass tubes, one in the cell and two in the fitting cone, two are used as manometers, for the calculation of the shear, and one for the introduction of the test fluids. One of the manometer tubes is also used as an electrode inlet for the wire connecting the mercury forming the other capacitor plate, to the bridge.

Glass is used for the cells for several reasons. It adsorbs very little and is easily cleaned. During an experiment the mercury and fluid are observable everywhere, not just at the capacitor plates, so if anything is amiss it can be seen. The thick films are of chemical origin and glass will contaminate neither the mercury nor the test fluid.

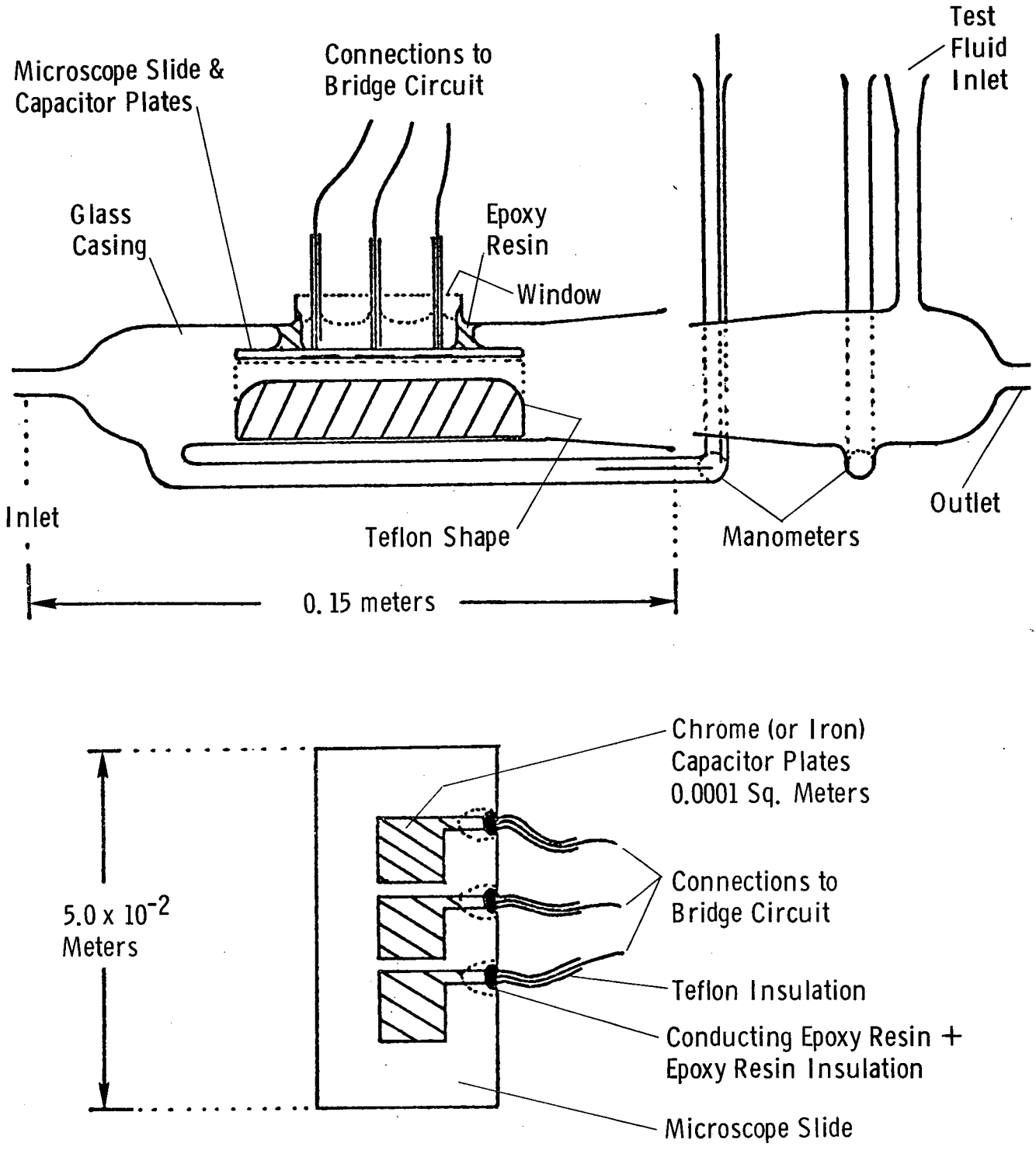

Figure 102. Cell apparatus and detail of capacitor plates

The Teflon was chosen as it is easy to work, easy to clean and adsorbs little.

To check that the epoxy resin in no way contaminates the test fluid, pure hexadecane was left in the cell for several hours and then thinned by the mercury. There proved to be no anomalous variations in the thinning of the hexadecane with time. In fact, the way the cell is constructed very little, if any, of the test fluid comes into contact with the epoxy resin.

The disadvantages of these cells are as follows:

(a) They are not very durable. If there is an electrical fault it usually proves irreparable.

(b) Due to the construction method, a new cell takes at least 14 days to complete and test.

(c) These cells cannot be used for tests at high or low temperatures, as only moderate variations from transient temperatures cause the glass to crack and the epoxy resins to deteroriate, especially at the wire-capacitor plate electrical connection.

6.2.3 The Apparatus for Moving the Mercury

As can be seen in Fig. 103 the set up is in five basic parts of which the cell section has already been described.

The peristaltic pump was chosen to force the mercury through the circuit because nowhere does the mercury leave the silicon rubber tubing and risk the contamination that might occur in other types of pump. The pump motor speed is altered by means of a variable transformer so that the mercury flow can be varied i. e. the constant head sustained. A suppressor was fitted across the brushes of the pump motor to reduce the sparking and therefore the interference produced on the autobalance bridge readings. From this pump the mercury is forced into the constant head device. This cuts out the throb in the mercury flow caused by the pump and is also used to regulate the flow of mercury through the cell and hence the shear on the "thick film". After flowing through the cell the mercury falls into a spherical container with an outlet stem at the bottom which is graduated in cubic centimeters ($10^{-6}m^3$). By stopping the flow below this stem and timing the rise of the mercury level over these graduations the flow of the mercury can be measured exactly, from which the shear applied to the "thick film" can be calculated. The mercury then flows into the reservoir, which also takes the overflow from the constant head device. The mercury is sucked from the very bottom of this reservoir into the pump, so that, as the mercury is very much heavier than the test oils, any

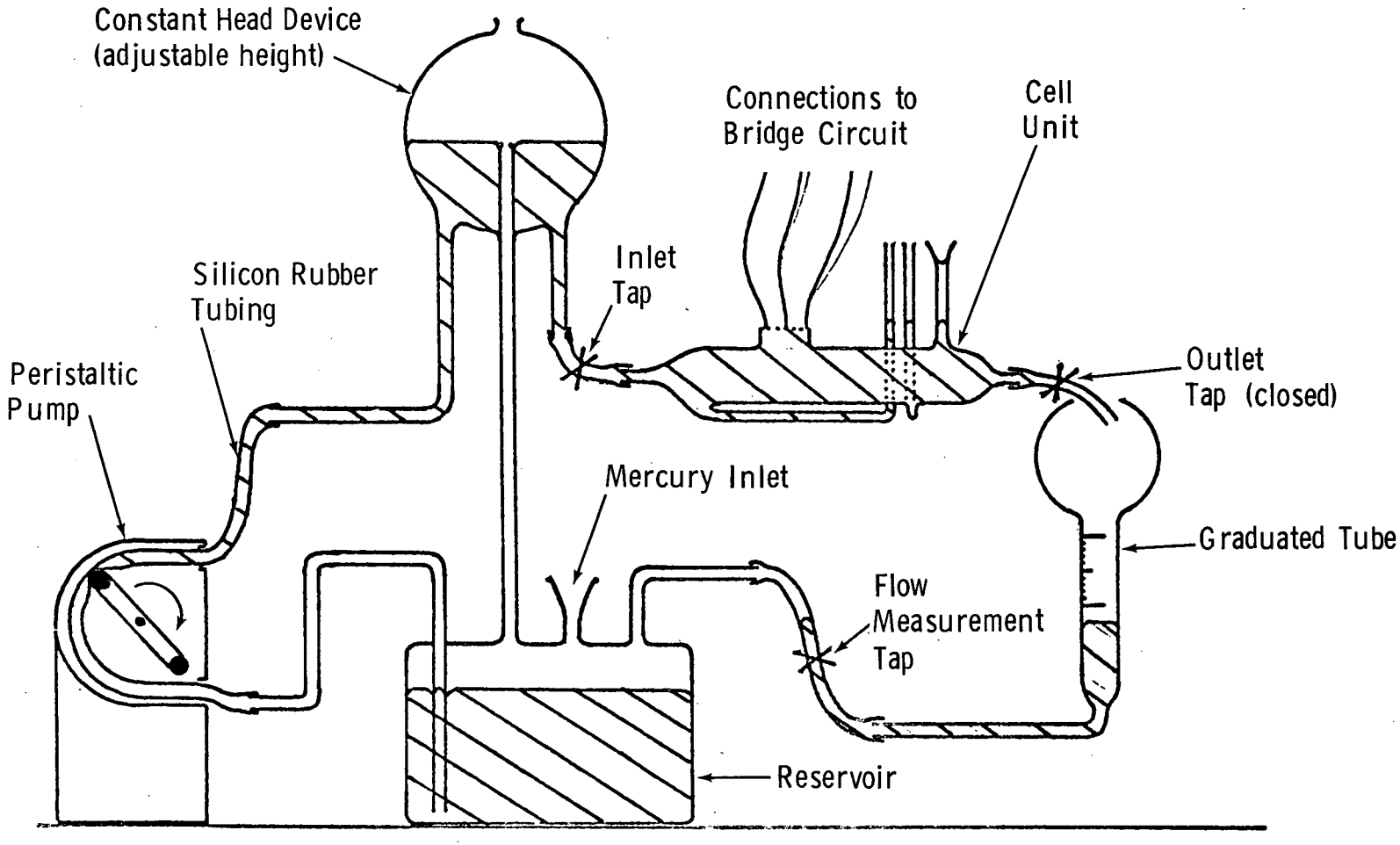

Figure 103. Mercury flow system (shown in "film growing" position)

substantial amounts of oil that are carried this far in the circuit are trapped there. In fact the spherical container and constant head device act as traps in a similar way, so the possibility of oil being carried around the circuit is negligible.

These sections are all of glass for the same reasons mentioned for the cell in 6.2.2 above, and each section can be broken down into smaller parts for the sake of easy cleansing and replacement when necessary.

The flow circuit is completed by the same silicon rubber tubing used in the pump. This simplifies the movement of the constant head device for variation of the shear and enables, with the use of clips, the flow to be varied or stopped wherever necessary. This tubing is semi-transparent and easy to clean. It was tested for contamination in the same way as the epoxy resin in 6.2.2 with similar negative results.

6.2.4 The Calculation of the Shear

As already mentioned, the shear applied to the oil film can be calculated both from the measurement of the flow rate through the cell, and by the measurement of the pressure drop across it. The expressions for the shear τ are

$$\tau = 6\eta q/h_c^2, \text{ and} \tag{60}$$

$$\tau = \tfrac{1}{2}h_c dp/dx, \tag{61}$$

where

q = rate of flow,
η = viscosity of the mercury,
h_c = depth of the cell cross-section,
dp = pressure difference, and
dx = length of restricted cross-section.

For low shear rates, i.e. low values of flow, these formulas gave matching results for the shear, but as the shear applied has been increased by decreasing h_c the results have diverged. This is due to the inevitable shock wave at the entrance to the restricted cross-section. It is felt, however, that these formulae will hold for the last capacitor along the cell, where the flow distribution will have had time to become parabolic. The results quoted from shear experiments, therefore, are taken from this capacitor.

6.2.5 The Electrical System

The electrical capacitance of the mercury-oil film-metal surface systems in both the cell and ball apparatus is measured

in order to calculate the thickness of the test fluid film which acts as the dielectric of the capacitor. A modified Wayne-Kerr Autobalance Universal Bridge, type B641, is used in making these measurements. This bridge operates on the transformer ratio arm principle[28], and unmodified, presents to the test capacitor, over the capacitance range met in these experiments, a peak voltage of 40 mV. This voltage is sufficient to cause dielectric breakdown of the oil film, thus invalidating the measurements. The voltage applied to the oil film is therefore reduced by inserting an attenuator between the E terminals of the bridge and the capacitor, and an amplifier between the capacitor and the I terminals of the bridge. Fig. 104 shows much simplified circuit diagrams of the unmodified and modified bridge circuits respectively. The original bridge applied a voltage V_x to the unknown admittance, through which current i_x is passed. Adjusting the standards Gs and Bs brings i_s into balance with i_x. By inserting the attenuator R_1 and R_2 the voltage across Y_x is reduced to V_x/A. The resulting current i_x/A is boosted by the amplifier to give the output current i_xB/A. By setting B equal to A, the bridge can be used in the same way as before modification.

In practice A and B are each set at 1,000, thereby reducing the peak voltage applied to the oil film to 40 μV. This voltage is sufficiently small to avoid breakdown of oil films down to 50 nm (500Å) thick. During experimental work, so that thinner films could be measured, an extra variable attenuator, able to reduce the voltage by factors of 10, 100 or 1,000 was built. This is inserted in the circuit in series with the other attenuator. Its major use was to overcome saturation effects which can cause incorrect readings. The complete system, see Fig. 105, is calibrated to give capacitance measurements of an accuracy of ±2%.

The greatest problems with this apparatus were the noise amplification and interference with the amplifier by the other circuitry, especially the peristaltic pump motor. The noise problem was overcome in the design of the amplifier, the work of Smith[29]. The interference was greatly reduced by shielding the input transformer in the amplified circuit with mu-metal. A further improvement was the replacement of the batteries with a 15 volt power supply.

If necessary the capacitance readings are fed to a pen recorder through a differential amplifier. This amplifier has a gain of 0.1 and acts as a buffer, short period averager and impedance matching device.

The thickness of the oil film is derived from the capacitance measurements from in the equation

$$h = \frac{A_c \varepsilon_p \varepsilon_o}{C} \quad , \qquad (62)$$

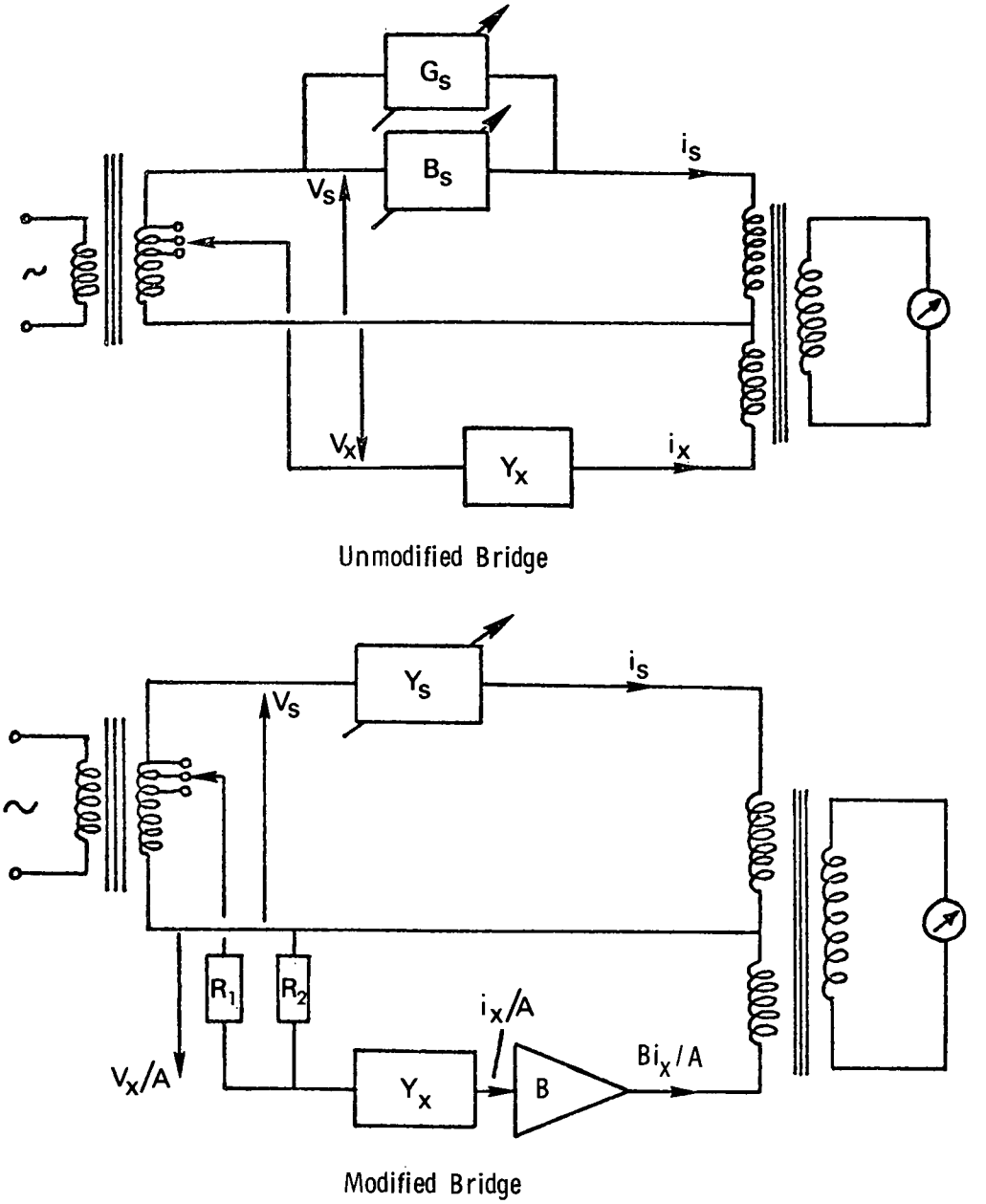

Figure 104. Unmodified bridge (top) and modified bridge (bottom)

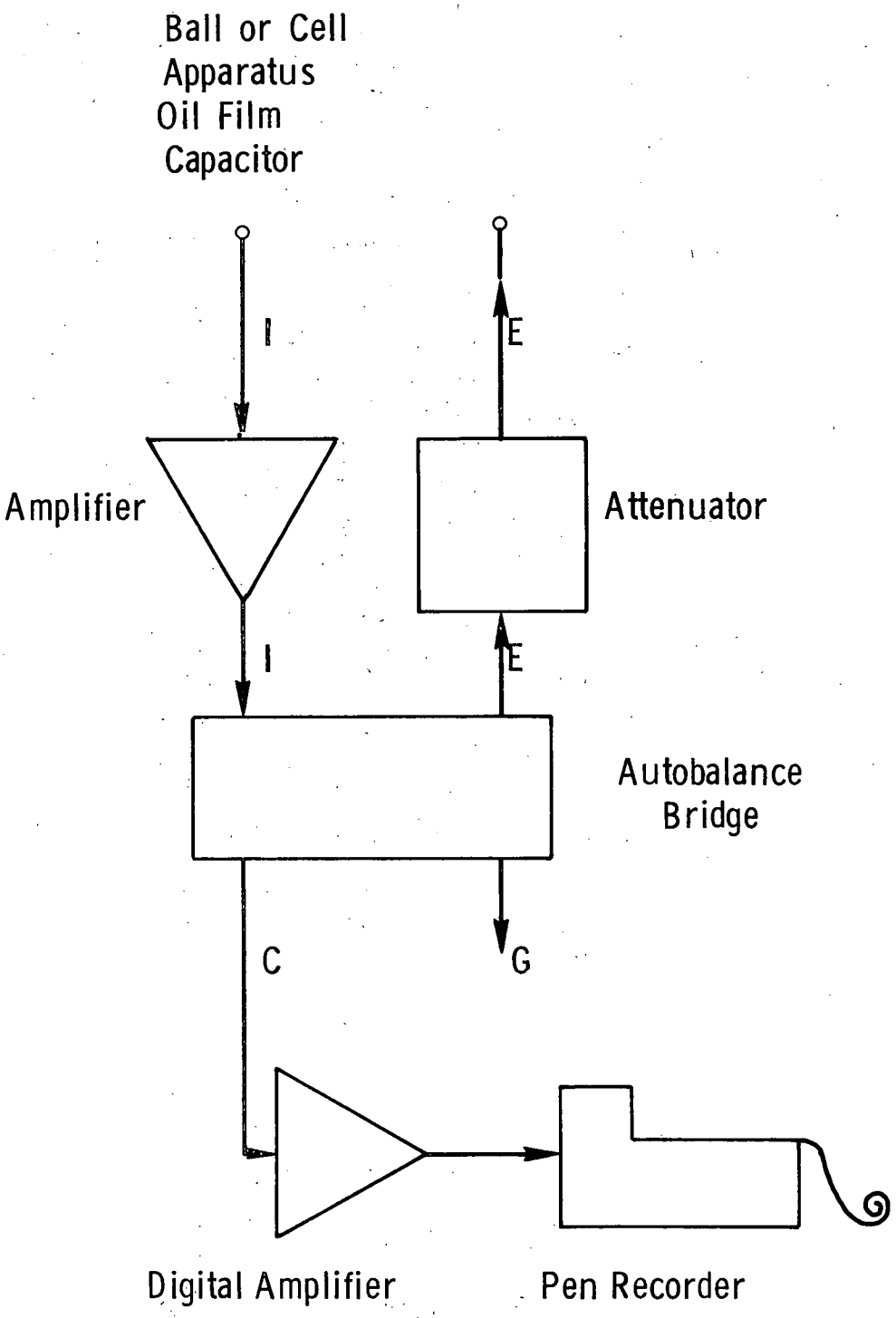

Figure 105. Diagramatic representation of electrical system

where A is the surface area of the capacitor plate, or ball, ε_o is the rationalized permittivity of free space, C is the capacitance registered on the bridge and ε_p is the relative permittivity of the dielectric, i.e. the oil.

The possibility of variation of ε_p, the relative permittivity of the test fluid, from that of the bulk value is discusses fully by Smith[29], who indicates that any change could be no more than 20%. In fact, by considering the mechanisms of the polarizability of the dielectric he shows that any such change will be much less than the above 20%. The measurements of film thickness made using white light interferometry, as described later, give very close agreement with the values calculated from the capacitance measurements, indicating that the dielectric constants of the bulk fluids used for these calculations can be relied upon.

6.2.6 The Ball Apparatus

This apparatus is easy to clean, handle and reproduce. It greatly speeded up the process of testing the fluids for any "thick film" properties and was also useful for comparison with theoretical predictions.

Fig. 106 shows the apparatus. It consists, basically, of a polished steel ball of 6.4 x 10^{-3}m (¼ in) diameter, with an insulated copper wire attached, the insulation being of Teflon. The same epoxy resins as used in the cell apparatus are used here. This wire fits through a stopper whose cone matches the socket of a test tube in which mercury and, later, the test fluid are held. Also through this stopper passes a coiled steel wire, the diameter of the coil being just less than that of the test tube cross-section, i.e. 1.5 cm. This coil acts to protect the ball and its adherent oil film from coming into contact with the test tube walls, and is also the electrical connection from the bridge to the mercury acting this time as a spherical capacitor plate concentric with the ball.

During an experiment the ball is moved up and down from the test fluid into the mercury, and so that there is always perfect electrical contact between the mercury and steel wire coil this is made of sufficient length never to leave the mercury once it is immersed, and therefore the end is never covered by a film of oil which would interfere with the capacitance readings.

The film thickness on the ball is deduced from the capacitance measured between the steel wire and ball using the same formula as that for the flat capacitors in the cell apparatus.

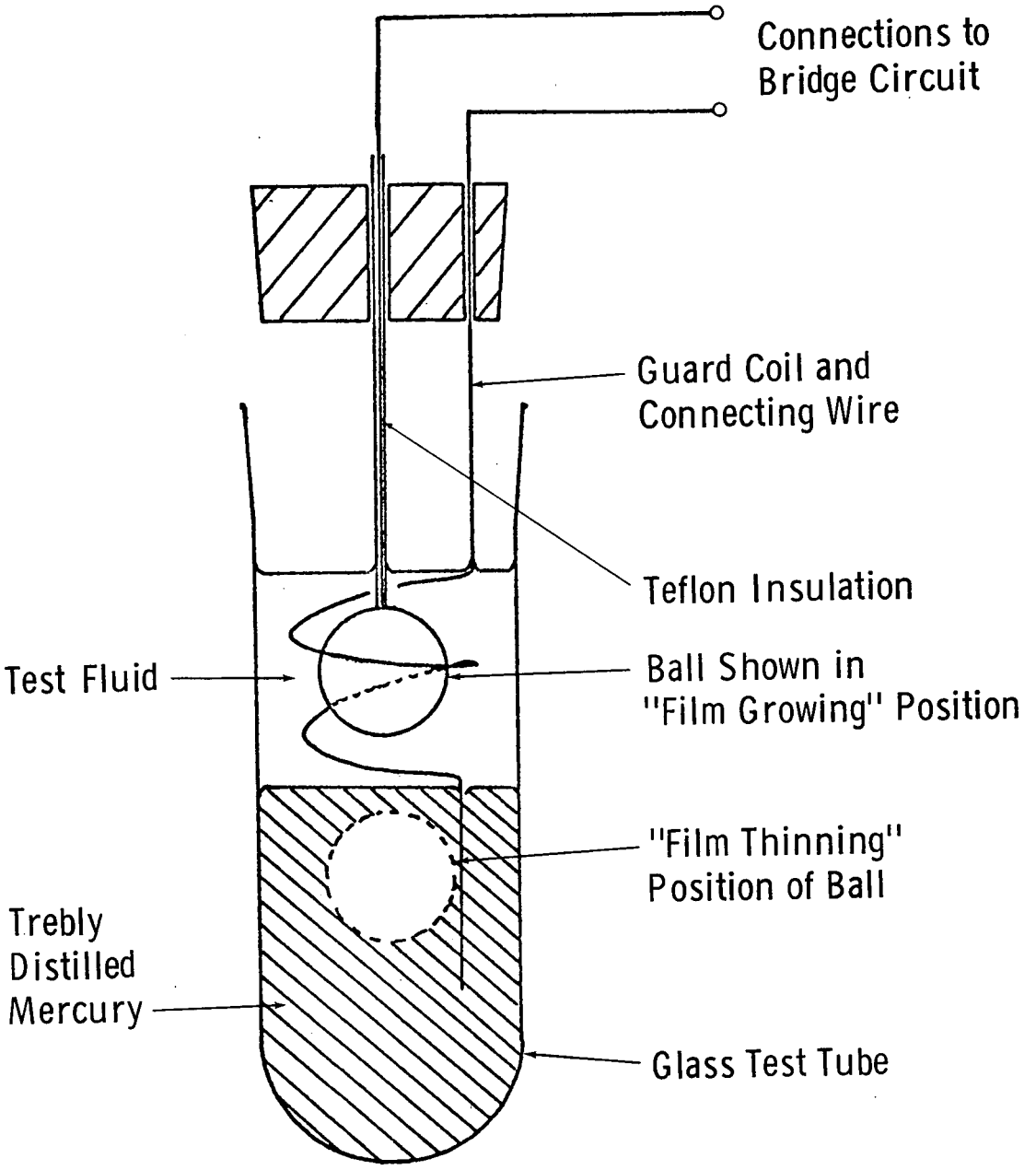

Figure 106. Ball apparatus

This expression is, in fact, deduced for the concentric sphere case, whence a parallel plate capacitor is taken to be a section of a concentric sphere capacitor of infinite radius.

6.2.7 Optical Arrangement

The apparatus used for optical measurements of the distribution and thickness of the oil films, see Fig. 107, consists of the white light stereo microscope arrangement used by Gentle in this report (Section 3). The cell apparatus is easily adapted for optical use by using chrome capacitor plates of ∿ 25% semi-reflectivity.

The color fringes observed on the film are very useful. They successfully check that the capacitance readings are correct and that if electrical breakdown occurs, it is just that and not physical breakdown.

6.2.8 Ionic Bombardment Cleansing Apparatus

Originally the cell apparatus was built to be able to be linked to the vacuum pump and high voltage wiring of an ionic bombardment cleaning apparatus. It was discovered, however, that this cleaning process negated any possibility of the chemisorbed "thick films" occurring for any fluid. As the purpose of this cell apparatus is to measure the resistance to shear of such films this cleansing process was discarded in favor of a wet cleaning process, using an ultrasonic agitation bath and various solvents. This omission simplified the design of the cell and the flow circuit.

The relative qualities of the wet and the ionic bombardment cleaning processes is discussed with the analysis of the results.

6.3 EXPERIMENTAL METHOD

6.3.1 Cleaning Procedure and Fluid Preparation

In the flowing mercury apparatus all but the actual cell and the silicon rubber tubing are of glass and therefore cleaned by the action of chromic acid with the addition of distilled water, which raises the acid temperature markedly. These glass sections then are rinsed thoroughly, first in distilled water, secondly in acetone before being arranged and used.

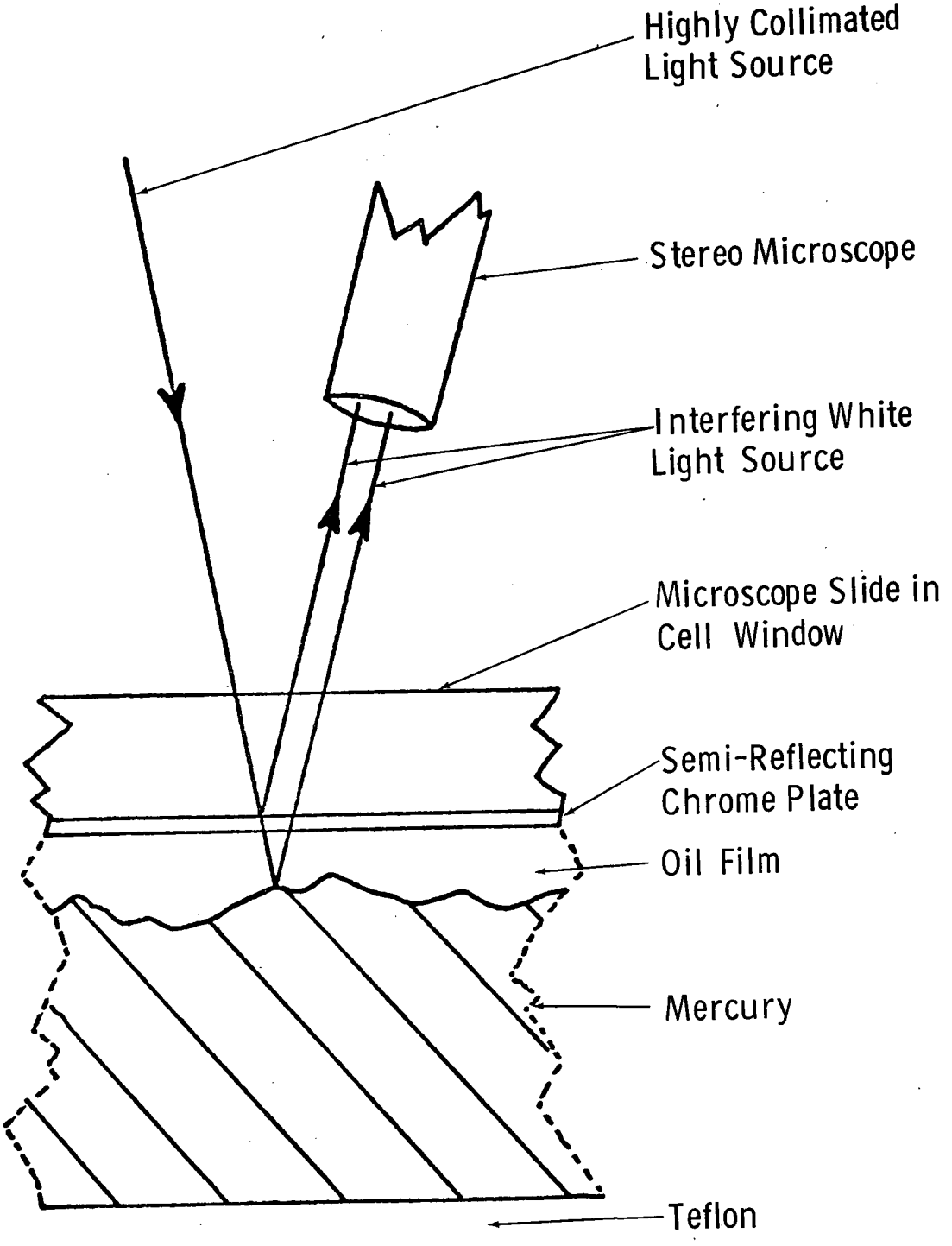

Figure 107. Optical arrangement in cell apparatus

The actual cell cannot be cleaned in this way due to the action of the chromic acid and the great temperature variation. Instead, a wet cleansing process is used, involving an ultrasonic agitating bath with various solvents. Firstly, the cell undergoes ultrasonic agitation in an alkaline detergent solution for ten minutes and is then rinsed thoroughly in tap water and distilled water. The cell is then placed in an emulsifier solution containing tetrachloro-tetrafluoro-ethane and similarly agitated for another ten minutes, followed by the above rinsing process. After a five minute period of agitation in distilled water the cell is rinsed several times in acetone and finally submitted to a further 10 minutes agitation, in more acetone. The cell is dried immediately after this by slight warming, quickly placed correctly in the flow circuit and used.

The silicon rubber tubing is replaced after every experiment as it is seen to be contaminated by the mercury over a period of several days. The same cleansing process as that used for the cell is employed for this tubing with the periods of agitation reduced to 5 minutes for all the immersions, to prevent the silicon rubber adsorbing substantially any of the cleansing fluids. Once the tubing has been dried by warming it is placed in the apparatus and used as soon as possible.

Both these cleaning processes can be relied on to enable surfaces to be completely wetted by distilled water. The ionic bombardment cleaning process, however, unfailingly yielded surfaces from which a lubricant solution will retract. The relationship between the cleansing processes and the "thick film" growth is discussed later.

For the ball apparatus, the ball and protective coil section are cleaned similarly to the cell in the ultrasonic agitation bath, whereas the containing glass test tube is cleaned with chromic acid. Both are dried by warming and used quickly.

For the purification of the test fluids, the procedure was suited to the chemistry of the fluid being tested.

For the hydrocarbons (i.e. fluids c, f, g, j and k - see Table 1) the principal contaminants are the result of air oxidation. These are removed by

storing over silica gel
passing the fluid over a small silica gel column within two days of use
storing in the dark in the absence of oxygen.

For the esters (i.e. fluids a, h, i, and o) the fear of hydrolysis to acid and alcohol was shown by Gentle (in Section 3)

and by the results produced by the ball apparatus, to be unfounded. A similar purification procedure as used for the hydrocarbons was therefore adopted.

The 2-ethylhexyldiphenylphosphate (fluid m) was passed over alumina prior to use. Fluids l and n were used untreated. The remaining three fluids were tested untreated (i.e. b, e, and q).

The degassing procedure was found not to affect the thinning plots, and therefore discarded.

Hexadecane the normal solvent used in the stearic acid experiments, used to lower the highly viscous test fluids was stored over silica gel in a darkened tube prior to use. After this treatment pure hexadecane alone when tested gave no "thick film" in either apparatus.

6.3.2 Measurement of Film Thinning, With and Without Shear

Before any experiment is started the bridge circuit is checked. Firstly the calibration of the bridge itself is checked with capacitors of accurately known values which cover the range corresponding to the experimental results. The amplifier and attenuator are then included in the circuit, and, using the same capacitors, the bridge is again calibrated by varying the fine adjustment on both the amplifier and the attenuator. This calibration is repeated whenever a range alteration is made on the variable attenuator.

6.3.2.1 Ball Apparatus

The glass test tube is three quarters filled with trebly distilled mercury, the ball section is lowered into the tube so that the ball itself is fully covered, the two terminals are connected to the bridge circuit and the capacitance and conductance registered. This is to test for faults in the electrical connections to the ball, as the capacitance reading should be zero, and to note the maximum conductance possible in the circuit for comparison with later readings during the experiment.

The ball is then raised clear of the mercury surface, although the guard coil remains partly submerged, and the test fluid introduced in quantity enough to cover the ball. The apparatus is left like this for a "growing period", which, with few exceptions, was set at 30 minutes for the test fluids. The ball, with its now adherent oil film, is again lowered into the mercury. Simultaneously a clock is started and the bridge circuit switched on. The variation of the capacitance of the oil film with time is then noted on the pen recorder, or by

eye if more than one of these ball experiments is being carried out. A full thinning curve, which can take anything from one day to thirty days to fall below 10^{-8}m (100Å) is then plotted on log-log paper for later analysis.

At any time a capacitance reading can be made on any one of three sequential decades on the bridge, with the use of the two decade display panels included. This facet can be used while an experiment is running to check that no saturation is registering in the results. If any signs of saturation are present, then a higher decade is selected, and, if necessary, the extra attenuator is switched into the circuit.

6.3.2.2 Cell Apparatus

About 200 cc of trebly distilled mercury is introduced to the reservoir, some of which is pumped into the constant head device from where the mercury is allowed to flow until it covers the capacitor plates in the cell. As for the ball apparatus, the capacitance and conductance of this dry mercury-metal contact is noted. By opening a tap at the exit of the cell the mercury level is lowered until the capacitor plates are 3-4 mm clear. The test fluid is then poured onto the surface of the mercury until the capacitors are covered. Any air bubbles trapped in the narrow channel where these plates are situated, are freed by angling the cell back and forth, then the apparatus is left for a similar "growing period" to that used with the ball apparatus. The tap at the entrance to the cell is then opened, allowing mercury from the constant head device to rise above the now oil covered capacitor plates, a clock and the bridge circuit being switched on simultaneously. As in the ball experiments, the thinning of the oil films with time is charted, although by eye in this case as there are three capacitor plates per cell, and the entire thinning is finally plotted on log-log graph paper.

When a "thick film" is shown to be present on metal substrates, i.e. the capacitance readings remain constant for more than 24 hours creating a plateau on the log-log plot of film thinning with time, shear is applied to these semi-solid films by moving the mercury past them.

6.3.2.3 Initial Procedure

In the early experiments the bridge circuit was switched on while the mercury was pumped past the film to register the effect of the shear. The results obtained were later found to be of no value, due partly to saturation, which had not then been fully allowed for, but mainly through "sparking" which many workers in this field have encountered. This effect is discussed

in the results section, but, as the potential applied across these oil films is so low, the electrical breakdown of the films which sparking could cause, if it occurred, was not considered until quite recently. These breakdowns were, instead, interpreted as physical, i.e. it was thought that "thick films" had been swept away by the mercury resulting in high conductance readings approaching the values for dry metal-mercury contact. New cells were built with larger and larger cross-sections, to reduce the shear, until it appeared that these oil films could barely resist a shear of 0.1 N/m^2 (1.0 $dynes/cm^2$) when the possibility of sparking was considered.

This electrical breakdown was first investigated in the ball apparatus. Solutions of 0.1% w.w. stearic acid in hexadecane were allowed to thin to classic examples of "thick films" on two balls. One ball was then subjected to rotation in the mercury, with the bridge circuit switched on, causing breakdown, whether electrical or physical, almost immediately. The second ball was similarly treated but with the bridge circuit switched off. After two minutes of this treatment the motion was stopped and the bridge circuit switched on. No breakdown was registered, indeed the film seemed hardly affected. This procedure was repeated five times with the same result. Finally the ball was again rotated, but with the bridge circuit on, and, as for the first ball, breakdown quickly followed. From this it seemed clear that sparking is inevitable if the potential across the film by the bridge circuit is present while there is relative motion between the mercury and oil film.

6.3.2.4 Final Procedure

This confirmation of the occurrence of sparking resulted in the procedure finally used when shear is applied to the oil films.

Before the mercury is set in motion by the pump the bridge circuit is switched off. The constant head device and the taps are then adjusted to give the flow rate desired and the pump is allowed to sustain this constant flow, and therefore constant shear, for a two minute period, during which the flow is measured as described earlier. The bridge circuit is then closed and the capacitance and conductance readings noted. The circuit is then quickly opened, the constant head device and taps adjusted to give an increased shear, and the mercury set in motion for another two minutes. This process of applying shear in incremental steps is continued until the "thick film" is reduced to less than 100Å (10^{-8} m), unless the maximum shear the cell is capable of is reached first. The variation of the capacitance, and hence the film thickness, is then plotted against the shear applied.

6.3.3 Interferometric Procedure

When a film is being thinned either by hydrostatic pressure of the mercury, or by shearing the film with flow of the mercury, the color interference patterns produced by the motion, or lack of motion of the oil film is observed. Five orders of fringes can be discerned in this arrangement, which corresponds to an observeable thickness range of 1.2×10^{-6}m down to 2.0×10^{-7}m (12,000Å to 2,000Å).

The phase change in the reflected light at the mercury oil interface cannot, however, be measured on this apparatus, but it is felt that the calibration used by Gentle (Section 3) is equally applicable for the cell apparatus as the optics of the two systems are almost identical.

Although the capacitance measurements give the impression that the film is thinning comparatively uniformly over the capacitor area, the fringe patterns show this is far from the case, especially in the later stages. Correlation between capacitance and interferometric observations, therefore, is obtained by assessing the proportion of the total area occupied by each color and summing the equivalent capacitances for each color to give the total capacitance of the film.

6.4 ANALYSIS OF RESULTS

All experiments were carried out between 20°C and 22°C. Figures 108 through 114 summarize all of the data on squeeze film thickness to be discussed below. Table 12 gives the capacitance/conductance data corresponding to these figures. In Fig. 108 the cell apparatus was used without shear; in Figs. 113 and 114 shear was applied. The other figures refer to the ball apparatus.

6.4.1 Thick Films Produced

(a) With the ball apparatus and solutions of 0.1% stearic acid in cetane, the variation of film thickness with "growing time" is demonstrated in Fig. 112, i.e., the longer a film is grown, the thicker it is. In fact the 100 minute period is well over those with which appreciable variations of final film thickness occur.

(b) In the cell apparatus, the variation of final film thickness with concentration of stearic acid in cetane is demonstrated in Fig. 108. Again, the greater the additive concentration, the greater the final film thickness. Comprehensive relationships of this nature are disclosed by Smith[29], in detail.

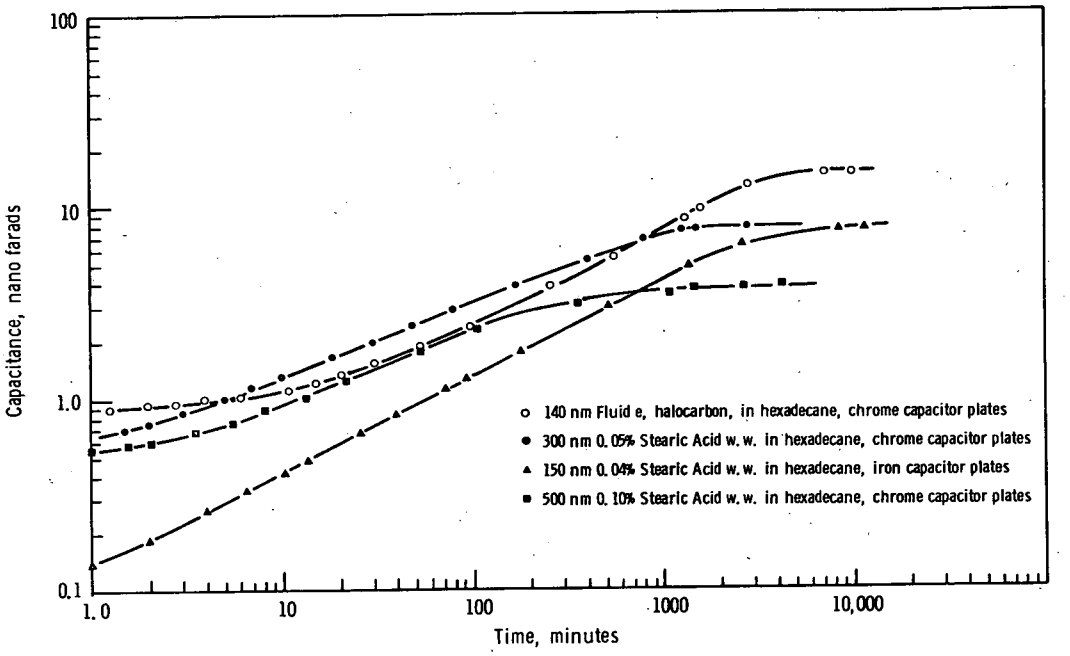

Figure 108. Thick films. Thinning for cell apparatus

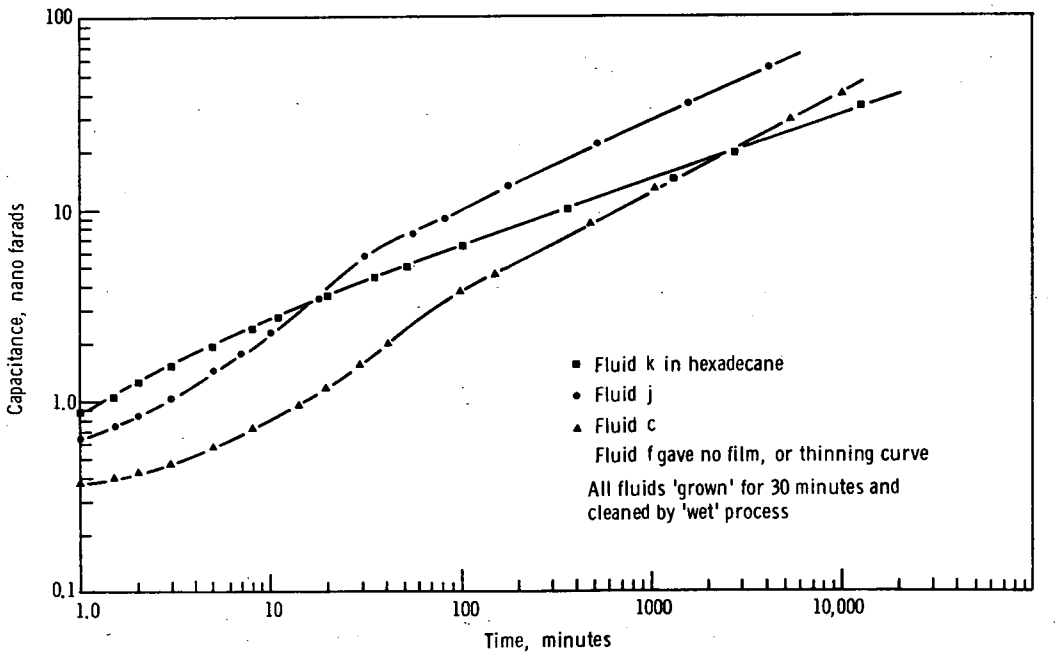

Figure 109. Hydrocarbons. Ball apparatus

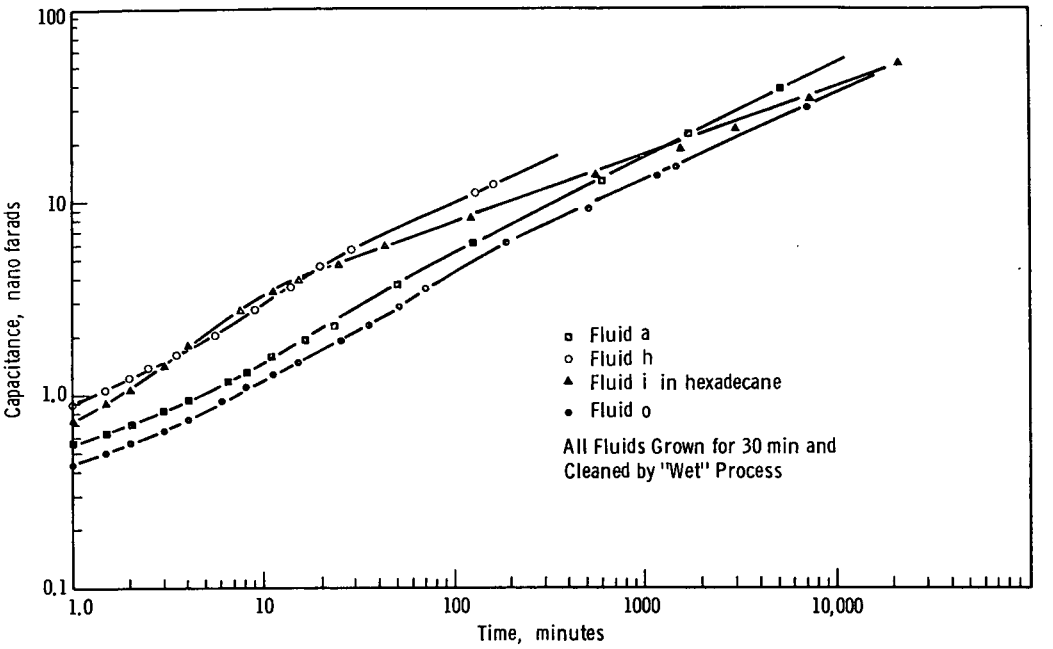

Figure 110. The esters. Ball apparatus

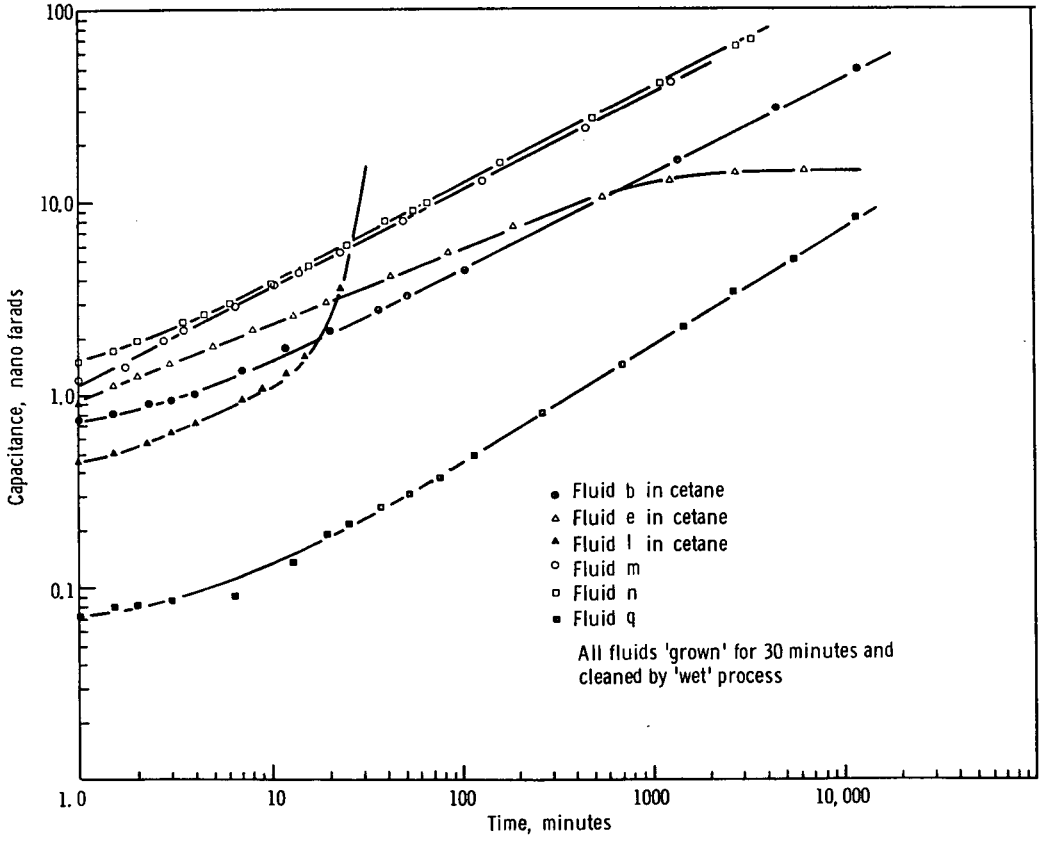

Figure 111. Remaining NASA fluids tested. Ball apparatus

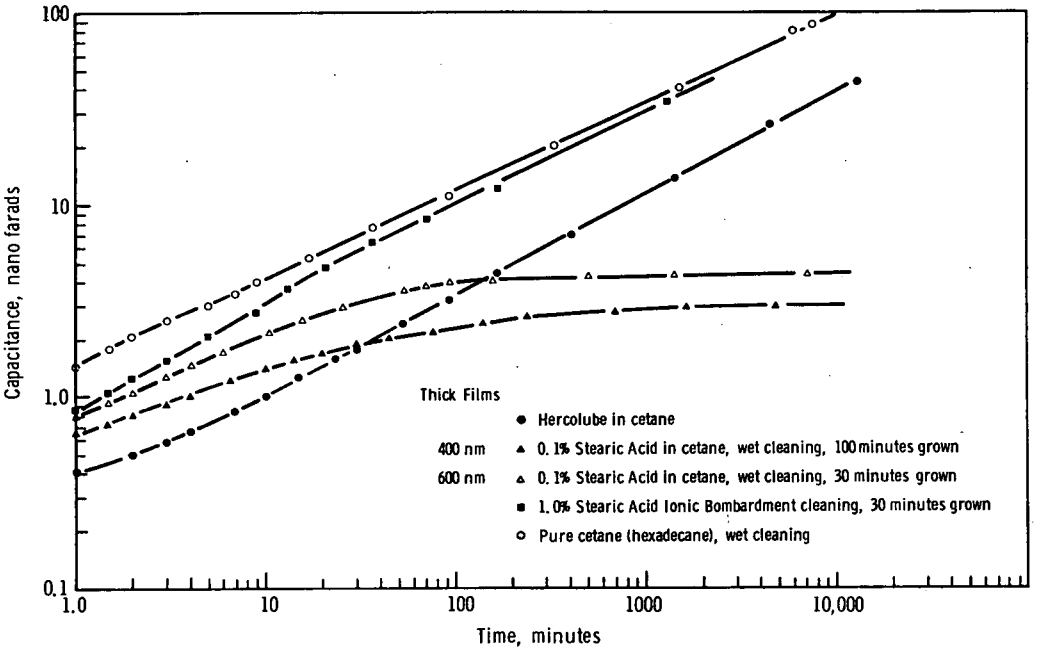

Figure 112. Non-test fluids. Ball apparatus

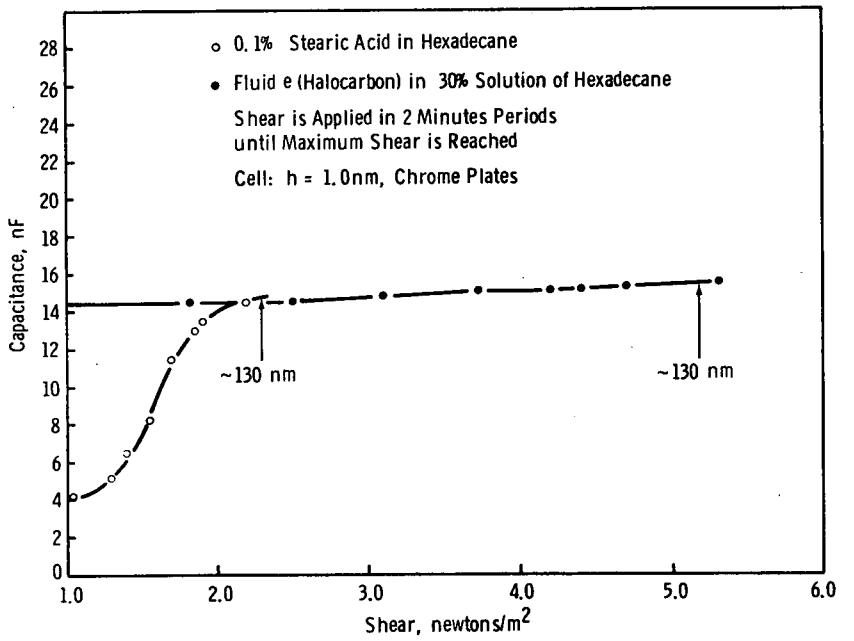

Figure 113. Thinning of thick films under tangential shear

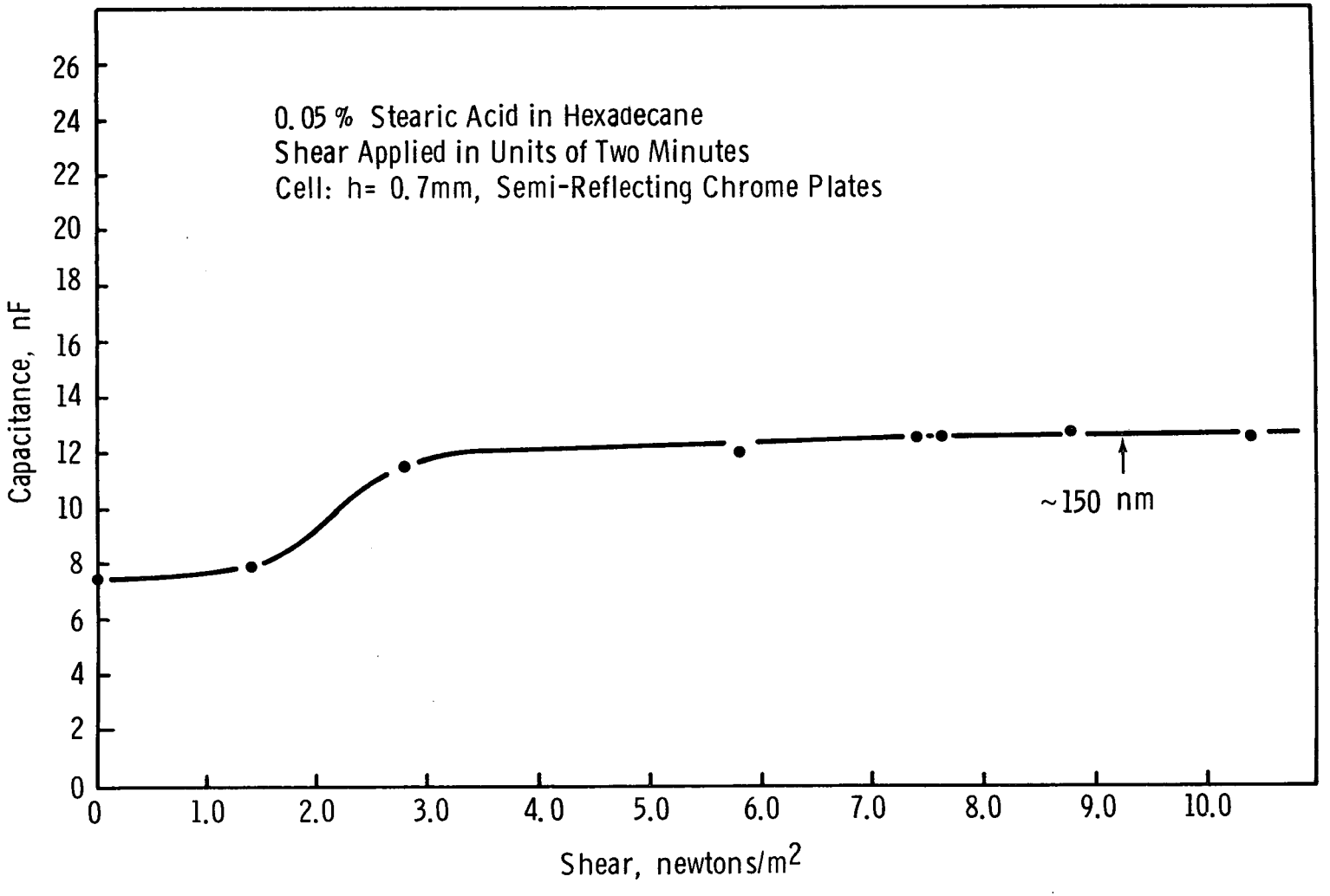

Figure 114. Thinning of thick film under shear

Table 12

SOFT FILM CAPACITANCE DATA

Fluid: a - pentaerythritoltetravalerat·

Growing Started: 3:30 Thinning Started: 4:05 Grown: 35 min.

Dry Mercury-Metal Contact Conductance: 3.7 mmhos

Ball Apparatus

Time in Minutes	Capacitance in Nanofarads	Conductance in μmhos	
1.0	0.57	0	
1.5	0.65	0	
2.0	0.72	0	
3.0	0.84	0	
4.0	0.95	0	
6.5	1.18	0	
8.0	1.3	0	
11.0	1.55	0	
16.0	1.9	0	
23.0	2.25	0	
58.0	3.75	0	
124	6.05	0	
605	13.0	2.0	
1,700	23.0	35	
5,100	38.5	62	i.e. no thick film

Fluid: b - polyethyleneglycol (10% solution in cetane)

Growing Started: 3:28 Thinning Started: 4:00 Grown: 32 min.

Dry Mercury-Metal Contact Conductance: 3.2 mmhos

Ball Apparatus

Time in Minutes	Capacitance in Nanofarads	Conductance in μmhos	
1.0	0.76	0	
1.5	0.8	0	
2.25	0.91	0	
3.0	0.94	0	
4.0	1.0	0	
7.0	1.35	1.0	
12.0	1.75	1.5	
20	2.15	2.0	
36	2.80	2.5	
50	3.3	3.5	
102	4.45	6.5	
351	6.95	38.0	
1,360	16.3	44	
4,320	31.0	285	
11,510	~50	~3,000	i.e. no thick film

Table 12 (continued)

SOFT FILM CAPACITANCE DATA

Fluid: c - squalane (in hexadecane, ~10% w.w.)

Growing Started: 2:28 Thinning Started: 2:58 Grown 30 min.

Dry Mercury-Metal Contact Conductance: 3.5 mmhos

Ball Apparatus

Time in Minutes	Capacitance in Nanofarads	Conductance in μmhos	
1.0	0.37	0	
1.5	0.395	0	
2.0	0.42	0	
3.0	0.47	0	
5.0	0.575	0	
8.0	0.71	0	
14.0	0.95	0	
19.0	1.15	0	
29.0	1.55	0	
41.0	1.95	1.0	
98	3.7	17	
148	4.5	55	
480	8.3	113	
1,050	13.0	217	
5,400	29	170	
9,800	39	150	
20,000	no reading	2,900	i.e. no thick film

Fluid: e - halocarbon (~10% solution in cetane)

Growing Started: 3:50 Thinning Started: 4:24 Grown: 34 min.

Dry Mercury-Metal Contact Conductance: 3.1 mmhos

Ball Apparatus

Time in Minutes	Capacitance in Nanofarads	Conductance in μmhos	
1.0	0.9	0	
1.5	1.15	0	
2.0	1.25	0	
3.0	1.45	1.0	
5.0	1.8	1.5	
8.0	2.2	1.5	
13.0	2.6	1.5	
19.0	3.0	1.5	
42.0	4.1	1.5	
82	5.45	1.5	
186	7.5	3.0	
540	10.5	5.0	
1,220	13.3	17	
2,700	14.5	17	
6,150	15.0	20	i.e. thick film (repeated) ~150 nm

Table 12 (continued)

SOFT FILM CAPACITANCE DATA

Fluid: f - cyclododecylcyclododecane (∿10% solution in cetane)

Growing Started: 4:50 Thinning Started: 5:20 Grown: 30 min.

Dry Mercury-Metal Contact Conductance: 2.7 mmhos

Ball Apparatus

Time in Minutes	Capacitance in Nanofarads	Conductance in μmhos	
0.25	∿200.0	∿1,800	
0.5	∿200.0	∿2,000	
0.75	∿200.0	∿2,700	
1.0	∿200.0	∿2,700	
repeated, grown for 100 min.			
0.25	∿180.0	∿1,400	no film, and
0.5	∿180.0	∿2,000	no thinning curve!
1.0	∿180.0	∿2,600	

Fluid: h - di(2-ethylhexyl)adipate

Growing Started: 4:25 Thinning Started: 4:55 Grown: 30 min.

Dry Mercury-Metal Contact Conductance: 3 mmhos

Ball Apparatus

Time in Minutes	Capacitance in Nanofarads	Conductance in μmhos	
1.0	0.88	0	
1.5	1.05	0	
2.0	1.2	0	
2.5	1.35	0	
3.5	1.6	0	
5.5	2.0	0	
9.0	2.7	0	
14	3.55	1.0	
20	4.5	4.0	
28	5.5	8.0	
130	11.0	30	
160	12.0	40	
190	unmeasurable	∿3,000	i.e. no thick film

Table 12 (continued)

SOFT FILM CAPACITANCE DATA

Fluid: i - di(2-ethylhexyl)3,3,4,4-tetramethyladipate
(∿10% solution in hexadecane)

Growing Started: 3:57 Thinning Started: 4:30 Grown: 33 min.

Dry Mercury-Metal Contact Conductance: 2.65 mmhos

Ball Apparatus

Time in Minutes	Capacitance in Nanofarads	Conductance in μmhos	
1.0	0.75	0	
1.5	0.90	0	
2.0	1.1	0	
3.0	1.45	0	
4.0	1.8	0	
7.5	2.75	0	
11.0	3.4	1.0	
15.0	3.95	1.0	
24.0	4.8	1.5	
42.5	6.0	1.5	
123	8.4	3.0	
552	13.5	4.0	
1,540	18.5	∿15.0	
2,950	23.5	20.0	
7,200	33.5	20.0	
21,000	53.0	200	i.e. no film

Fluid: j - bicyclohexyl

Growing Started: 2:55 Thinning Started: 3:25 Grown: 30 min.

Dry Mercury-Metal Contact Conductance: 3.0 mmhos

Ball Apparatus

Time in Minutes	Capacitance in Nanofarads	Conductance in μmhos	
1.0	0.63	0.5	
1.5	0.74	0.5	
2	0.84	0.5	
3	1.02	0.9	
5	1.45	2.0	
7	1.75	2.0	
10	2.25	2.5	
18	3.5	4.0	
31	5.7	6.0	
55	7.3	6.0	
80	8.75	7.5	
174	13.0	20.0	
510	21.75	42.0	
1,570	35.5	140	
4,150	∿53	∿2,200	
5,000	no reading	∿3,000	i.e. no thick film

Table 12 (continued)

SOFT FILM CAPACITANCE DATA

Fluid: k - 1,4-bicyclohexylbutane (∿10% solution in cetane)

Growing Started: 5:10 Thinning Started: 5:45 Grown: 35 min.

Dry Mercury-Metal Contact Conductance: 2.7 mmhos

Ball Apparatus

Time in Minutes	Capacitance in Nanofarads	Conductance in μmhos	
1.0	0.88	0	
1.5	1.05	0	
2.0	1.25	0	
3.0	1.5	0	
5.0	1.9	0	
8.0	2.35	0	
11.0	2.65	0	
20.0	3.5	0	
35.0	4.35	1.0	
51.0	5.0	1.5	
101.0	6.35	2.5	
365.0	9.7	4.5	
1,290	14.0	25	
2,730	19.5	60	
12,500	33.5	92	i.e. no film

Fluid: l - oleic acid in cetane (∿10% volume)

Growing Started: 3:00 Thinning Started: 3:29 Grown: 29 min.

Dry Mercury-Metal Contact Conductance: 3.4 mmhos

Ball Apparatus

Time in Minutes	Capacitance in Nanofarads	Conductance in μmhos	
1.0	0.46	0	
1.5	0.51	2.0	
2.25	0.57	1.0	
3.0	0.64	17.0	
4.0	0.72	2.0	
7.0	0.95	5.0	
9.0	1.1	1.0	
12.0	1.3	1.0	
15.0	1.6	2.0	
23.0	∿3.6	∿270	
30.0	no reading	∿3,300	i.e. no thick film, but sudden conductance increase

Table 12 (continued)

SOFT FILM CAPACITANCE DATA

Fluid: m - 2-ethylhexyldiphenylphosphate

Growing Started: 4:47 Thinning Started: 5:17 Grown: 30 min

Dry Mercury-Metal Contact Conductance: 3 mmhos

Ball Apparatus

Time in Minutes	Capacitance in Nanofarads	Conductance in μmhos	
1.0	1.2	1.5	
1.75	1.4	1.5	
2.75	1.95	3.0	
3.5	2.2	3.5	
6.5	2.9	7.0	
10.5	3.75	24.0	
14.0	4.35	29.0	
23.0	5.5	40.0	
49	8.0	60.0	
130	13.0	170	
450	24.0	530	
1,260	42.0	1,200	
2,000	no reading	∿3,000	i.e. no thick film

Fluid: n - 3,3'-dichlorodiphenylether

Growing Started: 5:05 Thinning Started: 5:35 Grown: 30 min.

Dry Mercury-Metal Contact Conductance: 3.0 mmhos

Ball Apparatus

Time in Minutes	Capacitance in Nanofarads	Conductance in μmhos	
1.0	1.5	2.0	
1.5	1.7	3.5	
2.0	1.95	4.0	
3.5	2.4	5.5	
4.5	2.6	7.0	
6.0	3.0	8.5	
10.0	3.7	13.0	
16	4.65	19.0	
25	6.0	35	
39	8.2	52.5	
55	9.0	180.0	
65	10.0	224	
160	16.0	720	
500	27.0	1,050	
1,110	40.5	∿1,500	
2,750	∿65	∿2,400	
3,240	69	2,530	
4,000	unmeasurable	∿3,000	i.e. no thick film

Table 12 (continued)

SOFT FILM CAPACITANCE DATA

Fluid: o - 1,1,7-trihydroperfluoroheptylperfluoroglutarate

Growing Started: 3:53 Thinning Started: 4:23 Grown: 30 min

Dry Mercury-Metal Contact Conductance: 3 mmhos

Ball Apparatus

Time in Minutes	Capacitance in Nanofarads	Conductance in μmhos	
1.0	0.44	0	
1.5	0.51	0	
2.0	0.56	0	
3.0	0.66	0	
6.0	0.92	0	
4.0	0.75	0	
8.0	1.1	0	
11.0	1.25	0	
15.0	1.45	0	
25.0	1.9	1.0	
35.0	2.3	1.5	
50	2.85	2.0	
70	3.55	2.5	
185	6.15	5.5	
510	9.2	25	
1,155	13.5	145	
1,430	15	140	
7,000	32	∿2,320	
7,500	no reading	∿3,000	i.e. no thick film

Fluid: q - dimethylsilicone (1000 cs)

Growing Started: 3:39 Thinning Started: 4:09 Grown: 30 min.

Dry Mercury-Metal Contact Conductance: 3.0 mmhos

Ball Apparatus

Time in Minutes	Capacitance in Nanofarads	Conductance in μmhos	
1.0	0.07	0	
1.5	0.08	0	
2.0	0.08	0	
3.0	0.085	0	
6.5	0.09	0	
13	0.135	0	
19.5	0.190	0	
25	0.215	0	
37	0.26	0	
52	0.31	0	
75	0.37	0	
115	0.485	0	
266	0.800	0	
700	1.42	0	
1,475	2.27	2.0	
2,665	3.5	8.0	
5,440	5.1	9.0	no apparent thick film,
11,410	8.35	20.0	although sudden
13,000	unmeasurable	∿3,000	conductivity increase

Table 12 (continued)

SOFT FILM CAPACITANCE DATA

Fluid: Hercolube in cetane (∿10% vol.)

Growing Started: 2:40 Thinning Started: 3:15 Grown: 35 min.

Dry Mercury-Metal Contact Conductance: 3.7 mmhos

Ball Apparatus

Time in Minutes	Capacitance in Nanofarads	Conductance in μmhos	
1.0	0.41	0	
2.0	0.5	0	
3.0	0.58	0	
4.0	0.65	0	
7.0	0.82	0	
10.0	0.99	0	
15.0	1.23	0	
23.5	1.55	0	
30	1.75	0	
52	2.35	0	
93	3.15	0	
159	4.25	0	
411	6.95	3.8	
1,410	13.3	65.0	
4,380	26	105	
12,100	43	135	i.e. no thick film

Fluid: 0.1% stearic acid in cetane, wet cleaning process

Growing Started: 3:45 Thinning Started: 4:15 Grown: 30 min.

Dry Mercury-Metal Contact Conductance: 3 mmhos

Ball Apparatus

Time in Minutes	Capacitance in Nanofarads	Conductance in μmhos	
1.0	0.8	0	
1.25	0.87	0	
1.5	0.94	0	
2.0	1.05	0	
2.5	1.2	0	
3.0	1.3	0	
4.0	1.45	0	
6.0	1.7	0	
10.5	2.15	0	
15.5	2.45	0	
25	2.9	0.5	
30	3.05	0.5	
53.5	3.55	2.0	
70	3.7	2.5	
92	3.85	20	
150	4.0	25	
500	4.2	25	
1,400	4.3	20	
7,000	4.4	20	i.e. thick film ∿400 nm

Table 12 (continued)

SOFT FILM CAPACITANCE DATA

Fluid: 0.1% stearic acid in cetane cleaned in glow discharge apparatus

Growing Started: 4:20 Thinning Started: 4:50 Grown: 30 min.

Dry Mercury-Metal Contact Conductance: 3 mmhos

Ball Apparatus

Time in Minutes	Capacitance in Nanofarads	Conductance in μmhos	
1.0	0.83	0	
1.5	1.05	0	
2.0	1.25	0.5	
3.0	1.55	0.5	
5.0	2.1	1.0	
8.0	2.7	1.5	
13.0	3.65	1.5	
20.5	4.75	2.0	
35	6.3	3.5	
70	8.3	4.0	
165	11.8	170	
1,280	35.0	2,200	
2,000	unreadable	∿3,000	i.e. no film

Fluid: pure hexadecane, wet cleaned ball

Growing Started: 3:50 Thinning Started: 4:27 Grown: 37 min.

Dry Mercury-Metal Contact Conductance: 3.2 mmhos

Ball Apparatus

Time in Minutes	Capacitance in Nanofarads	Conductance in μmhos	
1.0	1.45	2.0	
1.5	1.8	3.0	
2.0	2.05	3.5	
3.0	2.5	5.0	
5.0	3.0	7.5	
7.0	3.45	10.5	
9.0	3.9	12.0	
17	5.2	16.5	
37	7.5	23.5	
90	11.0	35.0	
325	20	55.0	
1,500	40	105	
5,700	80	40	
7,200	85	280	i.e. no thick film

Table 12 (continued)

SOFT FILM CAPACITANCE DATA

Fluid: 0.05% stearic acid in hexadecane

Growing Started: 5:25 Thinning Started: 6:00 Grown: 35 min.

Dry Mercury-Metal Contact Conductance: 300 μmhos

Cell Apparatus - Semi-reflecting chrome plates for optical check of Film Thickness

Time in Minutes	Capacitance in Nanofarads	Conductance in μmhos	
1.5	0.7	2.0	
2.0	0.74	2.0	
3.0	0.85	5	
5.0	1.0	5	
7.0	1.15	5	
10.0	1.3	5	
18	1.6	5	
30	1.9	5	
48	2.4	5	
78	2.9	5	
170	3.75	5	
405	5.15	5	
795	6.6	9	
1,250	7.4	34	
1,500	7.5	37	
2,800	7.55	33	i.e. thick film ~ 300 nm (optically checked)

Fluid: 0.1% stearic acid in cetane

Growing Started: 6:31 Thinning Started: 7:00 Grown: 29 min.

Dry Mercury-Metal Contact Conductance: 6.4 mmhos

Cell Apparatus, Chrome Plates (1 cm^2)

Time in Minutes	Capacitance in Nanofarads	Conductance in μmhos	
1.0	0.55	0	
1.5	0.575	0	
2.0	0.6	0	
3.5	0.675	0	
5.5	0.75	0	
8.0	0.85	0	
13.5	1.02	0	
21.5	1.25	0	
51.0	1.8	0	
106	2.3	0	
365	3.05	1.5	
1,100	3.45	4.0	
1,400	3.7	4.0	
2,660	3.75	4.0	
4,160	3.75	45	i.e. thick film ~ 500 nm

Table 12 (continued)

SOFT FILM CAPACITANCE DATA

Fluid: 0.4% stearic acid in hexadecane

Growing Strated: 6:05 Thinning Started: 6:40 Grown: 35 min.

Dry Mercury-Metal Contract Conductance: 8.7 mmhos

Cell Apparatus - Iron Capacitors (1 cm^2)

Time in Minutes	Capacitance in Nanofarads	Conductance in μmhos	
1	0.14	0	
2	0.185	0	
4	0.26	1.0	
6.25	0.33	1.0	
10.25	0.41	1.0	
13.5	0.48	1.0	
25.5	0.68	1.0	
40.5	0.82	1.0	
70.5	1.1	1.0	
90.5	1.25	1.0	
180	1.75	1.0	
520	2.95	1.0	
1,415	4.8	53	
2,600	6.2	51	
8,400	7.5	74	
11,200	7.6	70	i.e. thick film ~ 150 nm (area of capacitor less than for chrome due to deterioration of metal substrate)

Fluid: e - halocarbon ~30% solution in hexadecane

Growing Started: 3:30 Thinning Started: 4:10 Grown: 40 min.

Dry Mercury-Metal Contact Conductance: 5.4 mmhos

Cell Apparatus - Chrome Plates (1 cm^2)

Time in Minutes	Capacitance in Nanofarads	Conductance in μmhos	
1.25	0.9	1.0	
2.0	0.95	1.5	
2.75	0.95	1.5	
4.0	1.0	1.5	
6.0	1.05	1.5	
11.0	1.1	2.0	
15.0	1.2	2.0	
20.5	1.3	2.0	
31.5	1.5	2.0	
53.0	1.75	2.0	
96	2.25	2.0	
255	3.7	5.5	
1,320	8.5	21	
1,560	9.5	23	
2,770	12.5	23	
2,950	13.0	25	
7,100	14.5	35	
9,700	14.5	33	i.e. thick film ~ 140 nm

Table 12 (continued)

SOFT FILM CAPACITANCE DATA

Fluid: 0.05% stearic acid in cetane w.w.

Cell Specification - Semi-reflecting Chrome Plates, h = 0.70 mm

Flow cc/sec	Shear (N/m^2)	Time Period (min.)	Capacitance (nF)	Conductance μmhos
0	0	0	7.5	37
1.0	1.4	2	7.9	33
2.0	2.8	2	11.5	30
4.0	5.8	2	12.0	30
5.0	7.4	2	12.5	30
5.1	7.6	4	12.5	35
6.0	8.8	4	12.5	35
7.1	10.4	16	12.5	45

i.e. film of 12.5 nF $\cong$ 150 nm remaining after max shear for cell, 10.4 N/m^2 applied (optically checked)

Fluid: 0.1% stearic acid in hexadecane

Cell Specification - Chrome plates, h = 1.0 mm

Flow cc/sec	Shear (N/m^2)	Capacitance (nF)	Conductance (μmhos)	Time Period (min.)
0	0	3.75	45	0
1.0	0.75	3.8	30	2
1.4	1.05	4.2	30	2
1.7	1.3	5.1	33	2
1.9	1.4	6.5	40	2
2.1	1.55	8.2	43	2
2.3	1.7	11.5	231	4
2.5	1.85	13.0	370	4
2.6	1.9	13.5	320	8
2.95	2.2	14.5	205	10
2.95	2.2	14.5	140	30

i.e. after applying max shear for cell - 2.2 N/m^2 - film thinned to constant value 14.5 nF $\cong$ 140 nm

Table 12 (concluded)

SOFT FILM CAPACITANCE DATA

Fluid: e - halocarbon (30% solution in hexadecane)

Cell Specification - Chrome Plates, h = 1.0 mm

Flow cc/sec	Shear (N/m^2)	Time Period Mins.	Capacitance Nanofarads	Conductance μmhos
0	0	0	14.5	33
2.3	1.7	2	14.5	42
3.4	2.5	2	14.5	150
4.2	3.1	2	14.8	35
4.85	3.6	2	15.0	20
5.6	4.2	2	15.0	11
6.0	4.4	2	15.1	10
6.4	4.7	28	15.3	95
7.2	5.3	12	15.3	107
7.2	5.3	70	15.5	39

i.e. film of 15.5 nF $\triangleq$ 130 nm remaining after max shear of 5.3 N/m^2 applied for 70 min.

(c) Comparison of the 0.1% stearic acid in hexadecane films for both the stainless steel ball apparatus (see Fig. 112) and chrome cell apparatus (see Fig. 108) show final film thicknesses, although close, are apparently greater on the steel surface. Unrecorded results with fluid e (a halocarbon) suggest the same conclusions.

On the other hand, the cell apparatus with iron capacitors gives a very thick film for 0.4% stearic acid in cetane (see Fig. 108) as opposed to the meager 150 nm (1,500Å) film on stainless steel. There are other difficulties resulting from the use of pure iron in the cell apparatus. It proves exceedingly difficult to deposit in the vacuum apparatus - the glass substrate must be heated first, which increases the danger of contamination. The wet cleaning procedure leaves the metallized surface holed and scratched, probably due to the above contamination and, of course, the metal can be seen to rust during a test, the presence of a hydrated oxide layer being necessary for the formation of both thick films and rust. In the light of these factors it seems fair to discard the results obtained with iron capacitor plates.

(d) The films observed in fluid e, i.e., the polychlorotrifluoroethylene oil, may well be explained by the decomposition of the fluid into fatty acids (see Figs. 108 and 112). Hopefully the fluid is stable enough not to do this quickly after being passed over silica gel. The films may, therefore, be explained by the very much stronger hydrogen bonding of fluorine as opposed to the chlorine present, and the high degree of polarisation in the long chain molecule. The causes of the films would then be mainly physical in comparison with the chemisorbed stearic acid-cetane films.

(e) In Fig. 112, it is interesting to compare the thinning graphs of pure cetane on a wet cleaned ball and 0.1% stearic acid in hexadecane grown on a ball cleaned by the ionic bombardment process. Firstly the fact that no thick film remains with the stearic acid-cetane solution is indicative of their cause. The ionic bombardment cleaning process results in a metal surface free of any contamination whatsoever. If the mechanism of these thick films was purely physical, this should not effect their formation. The ultrasonic vibration cleaning process results in a metal surface free of all contamination except that present in the fluids, especially the final fluid. This results in a hydrated oxide remaining on the metal after cleansing, hence the "wet cleansing" designation of the process. The reaction of stearic acid with a metal to form soap needs the presence of both oxygen and water so a film of soap fibrils would only

form for the wet cleansing process, assuming that both acid and hexadecane are pure enough not to provide water molecules themselves. Once again, a complete discussion of the thick film formation is given by Smith[29].

Secondly, the fact that the two lines are not identical is interesting. Pure hexadecane alone should give the classic thinning curve for an oil film undergoing squeezing due to hydrostatic pressure of mercury, i.e. it should fit the mathematically produced relationship. In fact, it does, perfectly. It has a gradient of ½ within all reasonable error, and is the fastest thinning of all the test fluids that are in solutions of hexadecane to reduce their viscosity. Assuming the thick film formation is purely chemical, however, then the 0.1% stearic acid in cetane fluid should give an equivalent straight line if the chemisorbed film cannot form due to the cleaning process. The only major difference between the stearic acid molecules and hexadecane molecules if chemical considerations are negated is that the stearic acid molecule is polar, whereas the hexadecane like all pure hydrocarbons is non polar. The possibility of "ordered liquid" films is considered by Hardy[30] and more recently Allen and Drauglis[31] among others, as a possible explanation for these thick films. Such a purely physical effect could cause the increase in viscosity necessary to produce the difference in these two graphs. Comparisons of the values of the constant, B, derived in Appendix A with that of cetane and fluid j, another pure hydrocarbon for other test fluids reveal a decrease in the value of B, corresponding to an increase in the fluid viscosity, in several cases. For this comparison see Table 13 in Appendix A.

6.4.2 Thinning of Thick Films Under Shear

(a) Early results obtained for the application of shear to these thick films, as already explained, have been invalidated because of sparking across the oil film.

Sparking, i.e. a voltage discharge across the film causing high conductance and the passage of current through the film, has been observed by many workers in this field, notably Needs[32] and Brüninghaus[33]. The causes of this effect are uncertain, in this case, but two possible reasons come to mind.

As already mentioned, these thick films are not smooth at the mercury interface, but consist of many "peaks and valleys". The mercury surface, as shown optically, follows these asperities and finally the voltage will be high enough, somewhere in the film, for sparking to take place and current to pass.

The second reason is really the latter half of the above, with the voltage build up being attributed to a "streaming potential" along the interface.

Whatever the causes, once sparking has occurred the current passed and instantaneous high temperatures produced, over microscopic regions, will cause pitting of the metal surface and vaporisation of mercury into the film. This debris will lower the conductance of the film, making more sparking inevitable. Thus total electrical breakdown results from the escalation of this process.

The proof of electrical breakdown occurring without physical breakdown has already been indicated in experiments with the ball apparatus. Nevertheless, an enforced "sparking situation" was produced in the chrome cell whilst being observed interferometrically. Although the bridge registered complete breakdown, no difference in the film was observed optically.

(b) Since the new procedure for shearing the fluids had been used it has been discovered that the thick films are very much stronger than was at one time believed. In fact, physical breakdown under shear has not yet been achieved. Nevertheless, several interesting points appear in Fig. 113 and 114.

A relatively low shear of between 1.0 and 3.0 N/m^2 will produce a rapid decrease in the film thickness. This decrease, however, is arrested when the films are of the order of 130 nm (1,300Å), and cannot be thinned further with the maximum shear presently available i.e. 100 N/m^2. Long periods of this maximum shear, 70 minutes in one case, have no added effect, the films are stable.

The original thick film depth, dependent on growing time and concentration, seems unimportant. All surplus film matter is swept away, leaving this apparently sturdy 150-130 nm (1,500-1,300Å) layer. Fluid e appears to fit in neatly with the behavior of the stearic acid-hexadecane soap-fibril films.

6.4.3 Interferometric Observations

As most of these results have been mentioned once they are briefly noted:

The changing nature of the film can be observed as it thins. The mercury-oil interface is never uniform, but initially it is much smoother than the thick-film stage, when most superfluous hexadecane has been squeezed out.

Proof that electrical breakdown is not accompanied by physical breakdown is simply observed.

The final thickness of the thick film can be checked with the capacitance readings, and the possibility of variation of the dielectric constant, ε, invalidated.

The nature of a film that has undergone shear, as opposed to one that has not is different in two major ways.

Firstly the sheared film has a more uniform appearance, i.e. large monochromatic "plateaus", basically the color corresponding to the thickest part of the film, usually red or orange. In these plateaus there are indentations of deep blue, but very little rising above - the direction of a depth change can be deducted from the fringe color order. A film that has not undergone shear appears much rougher, i.e. has several orders of fringes corresponding to a greater depth variation.

The second major difference between the two types of thick film is that with shearing circular patches appear in the basically monochromatic picture. These appear to be grey, but on closer inspection consist of very many fringes, transcending all the orders and appearing white in the middle. They would appear to be, therefore, hemispherical outcrops of height at least 1.2 μm (12,000Å) from the film. Observably, their diameters vary between 1.0×10^{-4}m and 5.0×10^{-4}m(5×10^{6}Å). As these hemispherical globules appear and grow only under shear it seems likely that they represent the remaining free cetane trapped in the soap fibrils being squeezed out of the network as it settles. This, however, is pure speculation.

The 0.05% stearic acid in hexadecane film (see Fig. 108) was checked quantitatively, using the formula

$$C_d = \frac{\varepsilon_p \varepsilon_o A_c}{d} \quad , \qquad (63)$$

where d is the optical film thickness, and C_d the corresponding capacitance.

Using Gentle's calibration (Section 3), i.e.

First Order:	Yellow	fringes	= 2.0 x 10^{-7}	meter	
	Red	"	= 2.7	"	"
	Blue	"	= 3.4	"	"
	Green	"	= 4.3	"	"
Second Order:	Yellow	"	= 4.7	"	"

The observations were:

50% area 1st order yellow, i.e., $C_{Y1} = 4.8$ nF,
30% area 1st order Green/blue, i.e., $C_{G1} = 1.45$ nF, and
20% area 2nd order Yellow, i.e., $C_{Y2} = 0.85$ nF.

$\therefore C_{total} = C_{Y1} + C_{G1} + C_{Y2} = 7.1$ nF

This compares with capacitance reading $C_d = 7.5$ nF.

6.4.4 The Test Fluids (ball apparatus): Figures 109, 110, and 111.

Of these, fluids a, b, c, h, j, n, m, and o give straight line gradients of exactly 0.5, within experimental error, appearing, on the surface, to fit the theoretically predicted thinning curve perfectly. The fact that the constant, B, varies for several of them, indicating large differences between the given and calculated values of the viscosity is most interesting. See Appendix A.

Fluids i and k, an ester and hydrocarbon respectively give straight lines of equal gradient 0.35. This suggests an increase in viscosity with time, not just a constant increment for all time.

It is feasible that the oleic acid, fluid l, should become conducting due to the bend in its structure and its relatively high conductivity, i.e. electronic availability. The behavior of fluid f, apparently a pure hydrocarbon, and fluid q, apparently a good dielectric, both becoming conducting at high film thicknesses, the former instantly, is hard to explain. These results, however, were repeated at least twice.

The formation of a thick film of almost infinite viscosity by fluid e has already been discussed.

The thinning of hercolube, a mixture, basically, of esters appears consistent with the theory.

7. SUMMARY OF RESULTS

It was the purpose of this investigation to study the effect that lubricant properties have on film thickness in rolling/sliding contact and to determine the cause of any variations from existing theory. Several variations of the optical elastohydrodynamic (EHD) method were employed for most of this work. Other related measurements, such as traction, were also made. A wide range of experimental conditions and fluid properties was investigated.

7.1 DISCUSSION OF RESULTS

Briefly the objectives, principal results, and conclusions may be summarized as follows. Five major projects were involved.

7.1.1 Test Fluids

Seventeen fluids of widely differing physical properties and molecular structure were selected for intensive study. These fluids were:

a. Pentaerythritoltetravalerate
b. Polyethylene glycol
c. Squalane
d. Octacosane
e. Polychlorotrifluoroethylene oil
f. Cyclododecyl cyclododecane
g. Dihydrocedrene
h. Di(2-ethyl hexyl)adipate
i. Di(2-ethyl hexyl)3,3,4,4 tetramethyl adipate
j. Bicyclohexyl
k. 1,4-Bicyclohexyl butane
l. Oleic acid
m. 2-Ethylhexyldiphenylphosphate
n. 3,3'-Dichlorodiphenyl ether
o. 1,1,7-Trihydroperfluoroheptylperfluoroglutate
p. Dimethyl silicone (100 cs)
q. Dimethyl silicone (1000 cs)

Fluids i. and o. were new compounds systhesized for this project, the remainder were either on hand or commercially available.

To aid in the interpretation of the experimental results, the following physical properties were obtained for those of the seventeen fluids where adequate amounts were available: density, viscosity, specific heat, compressibility, thermal conductivity, and glass transition/freezing temperature. In most cases data were obtained at more than one temperature.

7.1.2 Film Thickness and Traction in Point Contacts

The application of the classical laws governing the formation of an EHD film were studies, with particular attention paid to deviations from these laws. Non-Newtonian fluid behavior and the effect of fluid inertia, gas solubility, oxygen content of the atmosphere, wetting of the metal bearing surfaces, and friction polymer formation were among the phenomena considered. Of particular importance was the simultaneous measurement of traction and film thickness. This area proved fruitful and hence the effort in that direction was expanded to include studies over a wide speed range and with continuous variation of slide/roll ratio.

The short conclusion of this section of the program has been that there are no marked deviations from classical behavior in the formation of the film with the proviso that the question of pressure freezing (a classical effect) be taken into account.

This pressure freezing was first detected using a fluid which was outside the 17 chosen for the program but which has been much used in similar studies. This is 5 phenyl-4 ether. This feature was extensively studied and a theory of traction developed which uses the concept of pressure freezing forming granules of a glass-like material.

The fact that the film thickness did not change any measureable amount with small amounts of traction means that traction *per se* cannot be explained by non-Newtonian effects. The argument is as follows.

A number of studies have recently been published which have shown that the film thickness h is uniquely determined by three standard dimensionless EHD parameters: speed ($\eta\bar{u}/E'R$), material ($\alpha E'$), and load ($W/E'R^2$), which are derived from the absolute viscosity η, rolling speed $\bar{u}$, reduced Young's modulus E', reduced ball radius R, pressure/viscosity coefficient α, and load W. These give straight lines on log-log plots from 0.05 μm or so up to high values of speed where the viscous heating in the inlet zone starts to play a part. It has also been remarked by a number of authors that the oil film thickness is almost entirely dependent on the conditions in the inlet zone. The effective pressure at which the pressure viscosity coefficient should be determined is not the maximum Hertzian contact, p_{max}, but some lesser value generated in the inlet region and determined by conditions in that region. In these studies, this effective pressure is about 20% of p_{max}. Further, the maximum rate of shear is at a point in the inlet zone, about one Hertz width from the edge of the Hertz contact. This rate of shear is of the order of $(\bar{u}/h)$. It is several orders of magnitude larger in the inlet sweep than it is in the contact zone itself. Any non-Newtonian effects show up when the film thickness (h/R) is plotted against the speed parameter ($\eta\bar{u}/E'R$).

All the 17 fluids tested gave linear log film thickness--log speed plots. Hence under pure rolling they behaved as Newtonian fluids.

The traction problem may be stated as follows.

For a given area of contact, if the film thickness h is steady, the frictional drag F is proportional to $\eta(U_1-U_2)/h$, where U_1 and U_2 represent the ball and disk speed, respectively. Now for steady conditions of load and temperature, $h\propto(\eta\bar{u})^{0.7}$ where $\bar{u}=(U_1+U_2)/2$. Hence, $F\propto\eta^{0.3}(U_1-U_2)/\bar{u}^{0.7}$. But careful measurements show that as $(U_1-U_2)\to 0$, $F\propto\frac{(U_1-U_2)}{\bar{u}}$. For this to be so (in the classical theory) η must vary as $1/\bar{u}^{0.3}$. There is no obvious reason why it should. The fact that at very low value of sliding, the film thickness still obeys the pure rolling law excludes heating as the cause. It also excludes (and this is important) any further terms in the Navier-Stokes equations not usually taken into account. It has therefore effectively decoupled the inlet from the Hertz zone.

It is for this reason that so much work was put into this part of the project.

The extremely high pressures in the contact zone and the very low rates of shear make it quite understandable that the conditions are different there. It is not often appreciated that in pure rolling at the center of the Hertz zone where dp/dx is zero, the shear stress is also zero. At this point the pressure is at its maximum and the viscosity will also be maximum. The heat generated will be zero, and, assuming no heat is convected, the temperature will be ambient. This makes the viscosity a maximum and it is consequently very, very large.

Under these conditions the transition of the fluid into a glass is quite likely. The consequences of this suggestion are incorporated into a theory of traction. This is highly speculative and needs considerable further study to bring it from an interesting hypothesis to a proven theory. The theory has predicted that at high pressures, which can only be achieved with sapphire as disk, there should be some very interesting effects if the "glass" theory of traction is true. It would clearly be of value to be able to carry on with this work and study at greater depth traction at high pressures, i.e., over 10^9 Nm^{-2} (150,000 psi).

K. L. Johnson of Cambridge, using a disk machine has also established with mineral oils that there is a critical pressure at 10^9 Nm^{-2} (150,000 psi). It would be interesting and also valuable to extend the work to 2.3×10^9 Nm^{-2} (350,000 psi),

at least, as it is at these pressures that ball bearings operate.

This section of this project then has shown the fluids follow the classical laws for formation of the lubricant film. Traction, however, is quite different and here the glass transition seems a very plausible explanation of many of the observed effects.

7.1.3 Film Thickness in Line Contacts

A line contact optical EHL apparatus was used to compare film thickness measured by optical, capacitance, and resistance methods. This was done for the reason that capacity measurements with a point contact are prone to every form of interference (as the signal is so small). In line measurements the signal is an order of magnitude larger. Almost all the published work is with line contact apparatus so the comparison would be of more use in such a configuration. The same considerations also apply to the electrical resistance tests.

The device employed for the line contact tests uses a completely new concept in optical EHL work. It is in essence a counter rotating single tapered roller thrust bearing. The bottom race is a steel plate with a conical track. The cone angle is equal to the total cone angle of a 12.7 mm (1/2 in) long roller of 6.35 mm (1/4 in) mid-diameter. The roller is located in a fixed cage and drives the top "race" which is a 12.7 mm (1/2 in) flat glass-plate, semichromed on the under side. Immediately above the roller is a hydrostatic pocket with a glass window in it. The pocket, pressurized by oil, loads the glass onto the roller with an almost completely even pressure. As oil and glass have the same refractive index, light passes through the window, the pressurized oil, and glass track with no refraction. The data from this apparatus have opened up several important subjects. These are briefly listed.

They have shown that it is possible to obtain capacity measurements using a layer of silica over the chrome reflecting layer, and at the same time measuring the film thickness optically. This has three advantages: (1) the silica acts as a spacer layer, thus allowing very thin films to be measured; (ii) it is an electrical insulator and thus rough surfaces can be used for the mating surface (normally, very smooth disks have to be used to avoid breakdown, a restriction now relaxed); (iii) the semi-reflecting metal layer, being protected by the silica, can be soft. Hence, a gold layer which is transparent at much greater conductivities than chrome can be used.

These bonuses only appeared at a late stage in the tests. They constitute a strong recommendation to continue the work so that they can be fully exploited.

The conclusion drawn from the optical and capacity measurements are that the two systems give comparable results. While it would be surprising if this was not the case, it is satisfying that it is.

The electrical resistance tests again agree with the optical. The marked decrease of asperity contact for $h > 0.06$ μm is interesting. This is of the order of the peak-to-valley height of the asperities on the roller. Also, of greater importance, is that the time average of contact is not a function of load (or area). This must mean that the contacts occur outside the Hertz zone. Inside they are either squashed down or are covered with a layer of vitrified oil. Again further tests are necessary for the resolution of these questions.

An extra series of tests in this part of the work was the determination of the effect of end blending in the roller.

Though some results had been published by Gohar and Cameron in Trans. ASLE on end closures, no data was known for the difference between blended and unblended rollers. The use of interferometry was found to be of great service in determining the exact amount of end blend actually present in any given roller, not an easy thing to measure accurately. Secondly, running blended rollers gives a very dramatic example of the reduction in closure consequent on a carefully chosen blend. This part of the study, brief though it was, has shown both the value of this apparatus and also the desirability of further work.

7.1.4 Refractive Index in Point Contacts

The purpose of this task was to find a means for measuring refractive index in an EHL contact.

All techniques for oil film thickness measurement require the knowledge of some property of the lubricant at a high pressure. The X-ray method requires a knowledge of the fraction of the radiation absorbed in the contact. Capacity needs the dielectric constant averaged over the contact. The optical technique requires the refractive index at all points. The first two need averaged values, hence for absolute accuracy the pressure distribution must be known as well as the pressure dependence of the quantity required (absorbence or dielectric constant). In the optical system the refractive index at all points in the contact area is needed.

The initial approach to this problem involved the observation of critical angle of reflection. However, Dr. Welford of the Technical Optics group of the Physics Department

at Imperial College suggested a very elegant method using interference with light entering at two angles.

This technique was decided upon. An apparatus was built to measure the refractive index entrapped in a contact produced by a ball dropping onto a plane. The advantage of the dropping ball will be considered later.

Once the refractive index at all parts of the contact could be determined accurately, the deformation at every spot could then be found absolutely. At this juncture a considerable extension of the task was undertaken. First, the density can be computed from refractive index using the Lorenz-Lorentz relation. As part of another research project (independent of this project), a computer program has been developed to find the local pressure consequent on any measured distortion. This is simply the inverse Boussinesq problem. The pressures inside the contact could be then computed from the fringes knowing, to a good degree of accuracy, the refractive index. Once the pressures were known everywhere a relation was produced of the variation of refractive index with pressure, not only the variation across the contact.

An unexpected extension to the work was next undertaken. The change in the entrapment was followed with time---either while the ball was falling or after it touched the lower plate. The change in volume of the dimple could then be computed---the density ρ already being known from refractive index. Reynold's equation in polar coordinates is, for the axially symmetrical case here, $\frac{\partial}{\partial r}\left(\frac{\rho h^3 \partial p}{\eta \partial r}\right) = 12\, \partial(h\rho)/\partial t$. The solution of this equation enables the viscosity at all points to be determined. Such a solution is possible as h, ρ and p are everywhere known.

This very simple device has now been turned into a machine for determining refractive index as a function of pressure and more importantly, it has become a high pressure viscometer and densitometer.

A study of the results presented in the main body of the text shows that with glass, pressures up to 8.4×10^8 Nm^{-2} (120,000 psi) are attained and viscosities up to 10^8 poise. The viscosities are 2 to 3 orders of magnitude higher than those attainable in any high pressure viscometer yet built. This is of course due to the very large driving pressure gradient. The pressures in the center of the entrapment are of the order of 8.4×10^8 Nm^{-2}, the diameter is about 0.25 mm, and hence the average radial pressure gradient is 3.4×10^{12} Nm^{-3} (24 million psi/inch)! The film is so thin that this does not stop the fluid from remaining isothermal. The rates of shear are low --

from 1/10 to 10^4 sec^{-1}. This is very convenient, since the rolling ball device, when acting as a high pressure viscometer is in the high shear rate range, from 10^4 to 10^7 sec^{-1}.

The apparatus was built primarily to answer the question put to it, viz., to find the refractive index in an EHD contact, not to measure pressures or viscosities. These are clearly of major importance and a new machine has been thought out to incorporate damping and to allow sapphire strikers to be used of differing radii. No reason can be foreseen that should prevent pressures well above 3.4×10^9 Nm^{-2}(1/2 million psi) being attained and correspondingly high viscosities being measured. This is an important extension and should be pursued.

A device has been projected to use this double interferometry to study rolling contacts. It uses some of the techniques devised for the line contact apparatus (though it may be preferable to start as a point contact). If the exact shape of the exit constriction can be measured, the pressures can be computed directly from them. This will require a microscope of very considerable resolving power and of much larger magnification than we have so far used. These questions have been discussed with the Technical Optics Section (Imperial College, London), who were responsible for suggesting the method used here. They say that such an object lens could indeed be computed out and made. Once the absolute shape of the exit constriction is found, the pressure in the zone then follows and the elusive pressure spike proved for the first time.

In passing it was possible to apply Christensen's theory of a falling sphere and it was found to diverge from practice. This was due (it is thought) to the interesting finding that above about 2.8×10^8 Nm^{-2} (40,000 psi) and viscosities of 10^7 poise the pressure viscosity coefficient α drops steeply. The effect had been previously found by K. L. Johnson using traction experiments.

In sum then this part of the work achieved its goal of measuring refractive index in an EHD contact. It also measured pressures and as well determined viscosities up to 8.4×10^8 Nm^{-2} (120,000 psi) and 10^8 poise.

7.1.5 Soft Film Studies

Work on the problem of soft films began at a time when the mechanism of their formation was unclear and even their existence was uncertain. Since then it has become clear that the soft films normally found on steel are in fact 2-dimensional greases formed by chemical attack. There is in normal mineral oil enough active material to react with the surface of the steel and form a soap. This forms a fragile network of soap fibrils which enmesh the

lubricant. These are responsible for most of the "rigid" films reported in the literature.

This was reported by A. J. Smith and A. Cameron to the Faraday Society at a Discussion at Cambridge in September 1970 The tests were all carried under static conditions. The apparatus for these studies caused the oil under test to be displaced by mercury. In earlier reports published elsewhere, 2 solid plates were brought together and could therefore be influenced by dirt in the oil. The use of mercury in place of one of the plates obviated this problem.

In the work reported to the Faraday Society great stress was layed on making the capacitance measurements (from which the film thickness was obtained) at very low voltages. A special bridge system was developed and sometimes less than 1 microvolt was impressed across the film. In this way no electrical breakdown was induced.

The findings of this project were that none of the 17 test fluids—with one exception—formed any soft films at all. With hindsight, in view of the work reported to the Faraday Society—which was not available at the time the project was planned—this was only to be expected. The exception was fluid e, polychlorotrifluoroethylene oil. Fluid e produced a thinner film which did not break down.

These results were of value for the other tasks. The absence of a soft film proved that the cleaning process used for the other film thickness studies was adequate. The ball soft film device, employing a ball dipped in mercury, with very low 1/2 microvolt potential difference, had been demonstrated to measure down to <u>one monolayer</u> of stearic acid—2 nm (20 Å)—so it was fully sensitive enough to check the cleaning process. It also proved that the fluids used in the tests did not have any surface active contaminants—with of course the obvious exception of oleic acid and the rather strange fluid e.

A part of this project was a considerable study of the theory of the thinning of these films with time. This is a branch of hydrodynamics that had not been studied. It is the squeeze film effect where the pressure gradient is known--being merely the difference in density of mercury and fluid--and one of the "plates" is a liquid--mercury.

When the experimental data from all the 17 test fluids which did not thin too fast are analyzed, it appears that the <u>rate</u> of thinning is not the same in all cases, even though the viscosity of the liquids is taken into account. This gives strong evidence for a change in viscosity near the surface even though a rigid soft film is not formed.

An interesting comparison has been achieved with a static film. The capacitance and the optical thickness were measured together. The results clearly show that the original capacitance technique was valid. It also provides a new way of measuring the dielectric constant for very thin films. This is of importance for micro circuits and for the design of electric condensers.

Since, with the exception of fluid e, the 17 test fluids did not form soft films, it was decided to study the system from the Faraday Society paper, stearic acid in cetane, in greater detail. The shear strength of the soft film - under shear produced by flowing the mercury - was investigated. It was found that under the combined influence of both shear and the electric field of the capacitance measurement, very little shear, usually much less than 1 Nm^{-2} (10 dynes/cm^2), was required to induce electrical breakdown of the soft film. A new technique, in which shear and electric field are applied alternately instead of simultaneously, shows the film is far more stable than that. At 3 Nm^{-2} (30 dynes/cm^2), there is no sign of breakdown. An apparatus has been designed using a steel cylinder in a torsional mode to apply shear up to 150 Nm^{-2} (1500 dynes/cm^2). Measurements have not yet been made with this apparatus.

7.2 CONCLUSIONS

Highlights from the project are listed below:

A new theory of traction based on glass transition, of which there is evidence, is presented. The experimental data argues against relaxation (or similar effects) being the solution of the traction problem.

The line contact apparatus shows that the optical, capacity, and resistance techniques all give comparable results. The use of a silica layer over the semi-reflecting metal film enables capacity tests to be carried out with much rougher surfaces than formerly possible. Resistance measurements suggest the asperities are deformed before entering the Hertz zone. The effect of end blending the roller is clearly shown and more regard should be paid to this in practical roller bearing manufacture.

Refractive index was measured in an EHL contact. The dimple or entrapment formed with a dropping ball was used for the contact. Further than this, the variation of density and pressure in the contact was evaluated and also the device was then used as a high pressure viscometer. The variation of viscosities (up to 10^8 poise) with pressure to 8.4×10^8 Nm^{-2}(120,000 psi) was readily measured. The rates of shear were from 10^{-1}

to 10^4 sec^{-1}. This extends the capability of measuring pressure viscosities over the entire shear range, as the rolling optical EHD apparatus measures from 10^4 to 10^7 sec^{-1}.

None of the 17 test fluids formed rigid soft films of the type found with stearic acid in cetane on steel (except that fluid e, polychlorotrifluoroethylene oil, gave a thin film). However, there is evidence of viscosity variation near the surface even when there is no soft film. In the stearic acid system, the soft film was found to be exceedingly susceptible to electric breakdown if the film was under the gentlest of shear stress (less than 0.5 Nm^{-2}). In the absence of an electric field, the soft film could tolerate far greater stresses (more than 3 Nm^{-2}, perhaps much more).

7.3 RECOMMENDATIONS FOR FURTHER WORK

In a "state of the art" project of this nature—if it was well founded at its inception—some features seem to demand continuation. These are listed.

Traction. Some major features of traction only appear at 10^9 Nm^{-2} (150,000 psi) Hertz stress and upwards. Apparatus is available to study this region and the work should continue.

Line Contact. Using a silica layer, rough surfaces can be studied. Finishing processes capable of industrial use can be studied with this machine and optimized.

"Refractive Index". The viscosity of fluids and their densities can be measured to pressures and thicknesses not available anywhere. This work is most important.

Soft Film. The limit of shear strength of soft films should be determined, but more important, the technique should be employed to study viscosity variations near the surface.

APPENDIX A

MATHEMATICAL APPROACH TO THINNING FILM

The conditions of flow within the cell apparatus, when the oil film is thinning under hydrostatic pressure of the mercury, may be approximately described by considering elementary conditions of equilibrium of the oil film, with the aid of several assumptions. This derivation stems from a more general treatment by Askwith, Cameron, and Crouch.[34]

Figure 115 represents an element of fluid within the oil film, dimensions dx, dy, dz. The forces acting on this element are due to hydrostatic pressure and viscous shear, all other forces being assumed negligible in this derivation, e.g., inertial forces. Equating these forces in the x-direction gives

$$pdydz + [\tau_{xy} + \frac{\partial \tau_{xy}}{\partial y} dy]dxdz = \tau_{xy}dxdz + [p + \frac{\partial p}{\partial x}dx]dy, \quad (A-1)$$

which gives

$$\frac{\partial \tau_{xy}}{\partial y} = \frac{\partial p}{\partial x} \quad (A-2)$$

Similar relations for $\partial p/\partial y$ and $\partial p/\partial z$ can be found. If, however, x is the direction of gravitational force, then we have

$$\frac{\partial p}{\partial x} = (\rho_{mercury} - \rho_{oil})g = \rho' g, \quad (A-3)$$

where ρ' represents the density difference of oil and mercury and g the acceleration due to gravity. If inertial forces are ignored, $\partial p/\partial y$ is zero and $\partial p/\partial z$ is also zero due to the symmetry of the problem in the xz and yz planes. We can therefore write

$$\frac{\partial \tau_y}{\partial y} = \rho' g. \quad (A-4)$$

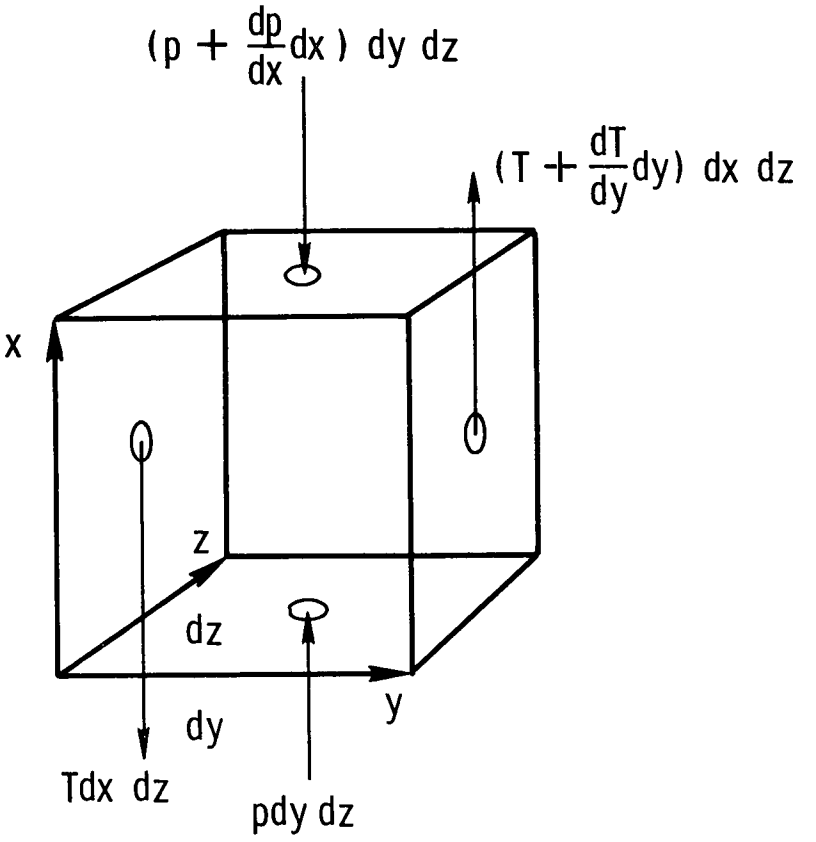

Figure 115. Forces acting on an element of the oil film

Applying Newton's law of viscous flow, i.e., $\tau_y = \eta \partial u_x / \partial y$, where u_x represents the fluid flow in the x-direction, yields

$$\rho' g = \eta \frac{\partial^2 u_x}{\partial y^2} \tag{A-5}$$

if η is assumed constant. Let $g\rho'/\eta = K$, a constant, Then

$$\frac{\partial^2 u_x}{\partial y^2} = K. \tag{A-6}$$

This equation suggests a parabolic velocity profile of u_x with y, i.e.,

$$u_x = u_{x\ max}\ (y/h)^2, \tag{A-7}$$

where $u_{x\ max}$ represents the value of u_x at y = h. Therefore, from Eq. A-6,

$$\frac{\partial^2 u_x}{\partial y^2} = \frac{2u_{x\ max}}{h^2} = \frac{2u_x}{y^2} = K, \tag{A-8}$$

i.e.,

$$u_x = \frac{K}{2} y^2. \tag{A-9}$$

Now $q_x = \int_o^h u_x dy$, where q_x represents the oil flow in the x-direction. Therefore, using Eq. A-9, we obtain

$$q_x = \frac{K}{2}\left[\frac{1}{3}y^3\right]_o^h = \frac{Kh^3}{6} \quad . \qquad \text{(A-10)}$$

Considering the equilibrium of flow in Fig. 116, we get

$$\frac{\partial q_x}{\partial x} - w = 0, \qquad \text{(A-11)}$$

where w represents the velocity of the mercury-oil interface, i.e., -dh/dt. Therefore

$$\frac{\partial q_x}{\partial x} + \frac{dh}{dt} = 0 \qquad \text{(A-12)}$$

Substituting Eq. A-10 into Eq. A-12 gives

$$\frac{K}{6}\frac{\partial h^3}{\partial x} + \frac{dh}{dt} = 0, \qquad \text{(A-13)}$$

but, as $\partial h^3/\partial x = 3h^2 \partial h/\partial x$, then

$$\frac{K}{2} h^2 \frac{\partial h}{\partial x} + \frac{dh}{dt} = 0. \qquad \text{(A-14)}$$

This is a simplified version of the equation currently being solved by iteration with the aid of a computer and is solved analytically to give the boundary conditions necessary for the program. As all the assumptions made in this derivation are valid for the case where the film has thinned for a reasonably long time, i.e., 10^3 seconds, this solution may be legitimately used in comparison with the later regions of the thinning curves.

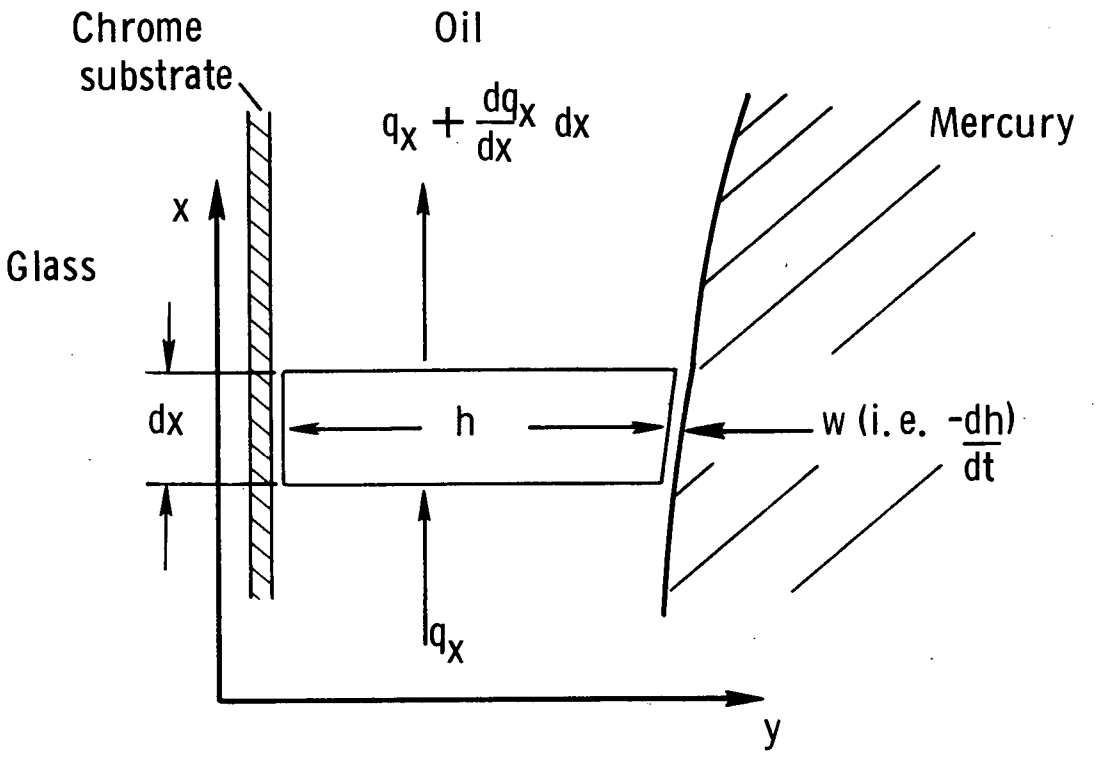

Figure 116. Flow specification in element of film, height dx

Solution of Eq. A-14. It simplifies matters to nondimensionalize this equation first. Let

$$X = x/L_s, H = h/H_m, \text{ and } T = KH_m^2 t/L_s, \tag{A-15}$$

where H_m represents the maximum film thickness for time zero and x zero. L_s represents the full span in the x-direction, and X, H, and T are nondimensional depth, film thickness, and time, respectively. This gives

$$H^2\frac{dH}{dX} + \frac{dH}{dT} = 0. \tag{A-16}$$

As H is a function of time and depth it may be written $H = H(X)H(T)$. Using this in Eq. A-16 gives

$$\frac{[H(T)]^3[H(X)]^2}{2}\frac{dH(X)}{dX} + H(X)\frac{dH(T)}{dT} = 0, \tag{A-17}$$

i.e.,

$$\frac{H(X)}{2}\frac{dH(X)}{dX} = -\frac{dH(T)}{dT}\cdot\frac{1}{[H(T)]^3}, \tag{A-18}$$

and these two expressions must equal a constant, call it C, as they are functions of different variables. Thus these equations become

$$-\frac{dH(T)}{[H(T)]^3} = CdT, \text{ and}$$
$$\frac{H(X)dH(X)}{2} = CdX. \tag{A-19}$$

Both expressions in Eq. A-19 can be integrated separately to give

$$\frac{1}{2[H(T)]^2} = CT + C_1, \text{ and}$$

$$\frac{[H(X)]^2}{4} = CX + C_2, \tag{A-20}$$

where C_1 and C_2 are both constants of integration. Thus

$$H(T) = \left[\frac{1}{2(CT+C_1)}\right]^{1/2}, \text{ and}$$

$$H(X) = [4(CX+C_2)]^{1/2}, \tag{A-21}$$

whence

$$H = H(X)H(T) = \left[\frac{2(CX+C_2)}{(CT+C_1)}\right]^{1/2}. \tag{A-22}$$

Now, as $h = H_m$ at $x = 0$ and $t = 0$, this boundary condition can be written non-dimensionally as $H = 1$ when $X = 0$ and $T = 0$. This substitution gives

$$1 = \left[\frac{2C_2}{C_1}\right]^{1/2}, \text{ i.e. } C_1 = 2C_2. \tag{A-23}$$

Thus Eq. A-22 becomes

$$H = \left[\frac{2(CX+C_2)}{(CT+2C_2)}\right]^{1/2}. \tag{A-24}$$

An assumed boundary condition at $X = 1$ and $T = 0$, i.e., $x = L_s$ and $t = 0$, is $H = 1.1$. This assumption is fair in the light of interferometric observations of the variation of the film thickness with depth. This substitution gives

$$1.1 = \left[\frac{2(C+C_2)}{2C_2}\right]^{1/2}, \text{ i.e., } C = 0.21\ C_2. \tag{A-25}$$

Therefore Eq. A-24 becomes

$$H = \left[\frac{0.42X+2}{0.21T+2}\right]^{1/2}. \tag{A-26}$$

Returning the dimensional variables to Eq. A-26 via Aq. A-15, we have

$$h = H_m \left[\frac{7x+1}{\frac{7}{2} KH_m^2 t+1}\right]^{1/2}, \qquad \text{(A-27)}$$

where $L_s = 3x10^{-2}m$ is the measured value.

For comparison with the graphic results, the variation of capacitance C_t with time is required, i.e.,

$$C_t = \frac{\varepsilon\varepsilon_o A_c}{h}, \qquad \text{(A-28)}$$

where ε, ε_o, and A_c are defined in Section 6. Thus, combining this expression with Eq. A-27, we obtain

$$C_t = \frac{\varepsilon\varepsilon_o A_c}{H_m} \left[\frac{7}{2} KH_m^2 t+1\right]^{1/2} \int_{1x10^{-2}}^{2x10^{-2}} [7x+1]^{-1/2}\, dx, \qquad \text{(A-29)}$$

where the integral sums the capacitors of height dx which make up area A_c. This expression works out to be

$$C_t = \frac{\varepsilon\varepsilon_o A_c}{H_m} \left[\frac{7}{2} KH_m^2 t+1\right]^{1/2} (1.0x10^{-2}). \qquad \text{(A-30)}$$

The factor K in MKS units is of the order of 10^8. Since this expression is only valid after 10^3 seconds, the quantity 1 in the brackets may be neglected, which gives

$$C_t = \frac{\varepsilon\varepsilon_o A_c}{10^2} \sqrt{\frac{7}{2} Kt}, \text{ for } t > 10^3 \text{ sec.} \qquad \text{(A-31)}$$

If we remove the viscosity η and density difference p' from K and replace the group of constants $10^{-2}\ \varepsilon_o A_c g^{1/2}$ with one constant B, we have

$$C_t = \varepsilon B(p't/\eta)^{1/2}, \text{ for } t > 10^3 \text{ sec.} \qquad \text{(A-32)}$$

Although this relationship has been derived for the cell apparatus, it is proposed that it is also applicable to the ball apparatus (with B some other constant of the apparatus) if the time criterion is met. The order of the film thickness observed on the balls after periods of 10^3 seconds is 10^{-6}m, i.e., four orders of magnitude greater than the ball radius 6.4×10^{-3}m. Thus this assumption seems to be justified. The fact that the graphs obtained from the two types of apparatus are of similar form after such a time period makes this assumption highly credible.

Those fluids which have capacitance versus time graphs which exactly fit this theory, i.e., $C_t \propto t^{1/2}$, can be discussed in the light of this theory. The other fluids appear to have varying viscosity and thus cannot be treated by this analysis. For those fluids for which $C_t \propto t^{1/2}$, it is possible to calculate B by inverting Eq. A-32,

$$B = \frac{C_t}{\varepsilon} (\eta/p't)^{1/2}. \qquad \text{(A-33)}$$

This expression provides a means of obtaining the viscosity of one liquid relative to another. In Table 13, the value of B is given for 6 fluids which met the criterion of $C_t \propto t^{1/2}$. Then, assuming the starred (*) value, the viscosity yielded by B is compared to the measured bulk viscosity for the other 5 fluids.

It has been mentioned that a computed iterative technique is being employed to solve a more complex form of Eq. A-14. It is hoped that this solution will predict the film thinning-time relationship from 1 second onwards to a high degree of accuracy, and that it will verify Eq. A-32.

Table 13

VISCOSITIES DERIVED FROM THINNING FILM

Fluid	B from Eq. A-33 $10^{-9}F(m^5s^{-2}kg^{-1})^{1/2}$	η thinning / η bulk
pure cetane	3.25×10^{-9}	1*
stearic acid in cetane - dry cleaning	2.9×10^{-9}	1.25
bicyclohexyl, fluid j.	3.2×10^{-9}	1.03
pentaerythritoltetravalerate, fluid a.	2.7×10^{-9}	1.45
dimethylsilicone (1000 cs), fluid g.	2.48×10^{-9}	1.71
di(2-ethylhexyl)adipate, fluid h.	$\sim0.5\times10^{-9}$	$\sim$42.0

APPENDIX B
LIST OF SYMBOLS USED

Symbol	Description
a	Half-width of Hertz point contact
A	Slope of exponential traction plots
A_c	Area of capacitor plates
b	Half-width of Hertz line contact
C	Theoretical Capacitance, across oil film (e.s.u.)
C_c	Theoretical Capacitance, across oil film (picofarads)
C_d	Capacitance deduced optically
C_h	Theoretical Capacitance of Hertzian region (e.s.u.)
C_i	Theoretical Capacitance of Inlet region (e.s.u.)
C_o	Theoretical Capacitance of Outlet region (e.s.u.)
C_p	Capacitance measured at bridge
C_s	Measured capacitance of lubricant film
C_t	Capacitance calculated at time t
d	Optical oil film thickness in capacitors
E	Young's Modulus
E'	Reduced Young's Modulus
f	Traction coefficient = F/N
F	Traction force
G*	Nondimensional materials parameter
g	Acceleration due to gravity
h	Test fluid film thickness
h_c	Depth of Cell Apparatus cross section

Symbol	Description
h_o	Central oil film thickness
h_r	Film thickness at r
h_s	Thickness of silicon oxide layer
h_z	Separation outside Hertzian contact
h_{min}	Minimum film thickness
H_m	Maximum film thickness at zero time and x
H^*	Nondimensional film thickness parameter
L	Length of line contact
L_s	Maximum depth of oil film in mercury
m	Order of interference fringe
n	Refractive index at mean Hertzian pressure
n_2	Refractive index of glass plate + hemisphere
n_3	Refractive index of fluid
n_o	Refractive index at ambient pressure
N	Integer
p	Pressure
$\bar{p}$	Mean Hertzian pressure
p_{max}	Maximum Hertz contact pressure
p^*	Normalized maximum pressure
q	Rate of flow of mercury
q_r	Rate of flow of oil at r
q_x	Rate of flow of oil at x
r	Radius at which viscosity calculated
R	Reduced ball (or roller) radius

Symbol	Description
R_p	Resistance measured at bridge
R_s	Series resistance of chromium layer
t	Local film thickness
T	Temperature
$\bar{u}$	Rolling speed $[1/2(U_1 + U_2)]$
U_1	Ball speed (driving)
U_2	Disk speed (driven)
u_x	Velocity of oil in x direction
$u_{x_{max}}$	Maximum velocity of oil in x direction
U^*	Nondimensional speed parameter
v	Approach velocity of ball center
V	Voltage
w	Velocity of mercury-oil interface
W	Load
W^*	Nondimensional load parameter
α	Pressure/viscosity coefficient
δ	Phase change on reflection
ε	Relative permittivity of oil at ambient pressure
ε_h	Permittivity of oil at mean Hertzian pressure
ε_s	Permittivity of silicon oxide layer at ambient pressure
ε_{sh}	Permittivity of silicon oxide layer at mean Hertzian pressure
ε_o	Rationalized permittivity of free space
ε_1	Permittivity in gap outside Hertzian region

Symbol	Description
λ	Wavelength of light
η	Absolute viscosity
η_o	Absolute viscosity at ambient pressure
σ	Poisson ratio
Σ	Slide/Roll ratio: $\left[\frac{U_1-U_2}{\bar{u}}\right]$
ρ	Density
ρ_o	Density at ambient pressure
ρ'	Density difference between mercury and oil
θ	Angle of incidence
θ_L	Angle of laser beam in glass
ϕ	Angle of laser beam in the oil
τ	Shear applied to "thick films"
ω	Frequency
ω_d	Local deformation of the ball
ν	Kinematic viscosity
ξ	x/b
ζ	$1/\xi$

REFERENCES

1. Grubin, A. N., "Contact stresses in toothed gears and worm gears," Cent. Sci. Res. Inst. for Tech. and Mech. Eng. (Moscow), Book no. 30, D.S.I.R., Trans. no. 337, 1949.

2. Dowson, D., and Higginson, G. R., (a) "A numerical solution to the elastohydrodynamic problem," Jour. Mech. Eng. Sci. 1, 1959, pp. 6-9. (b) "The effect of material properties on the lubrication of elastic rollers," Jour. Mech. Eng. Sci. 2, 1960, pp. 188-94.

3. Crook, A. W., "Lubrication of rollers. II. Film thickness with relation to viscosity and speed. III. A theoretical discussion of friction and the temperatures in the oil film," Phil. Trans. 254, 1961, pp. 223-58.

4. Sibley, L. B., and Orcutt, F. K., "Elastohydrodynamic lubrication of rolling contact surfaces," Trans. ASLE 4, 1961, pp. 234-49.

5. Cameron, A. and Gohar, R., "Theoretical and experimental studies of the oil film in lubricated point contact," Proc. Roy. Soc. (London) A 291, 1427, 26 April 1966, pp. 520-536.

6. Foord, C. A., Hammann, W. C., and Cameron, A., "Evaluation of lubricants using optical elastohydrodynamics," Trans. ASLE 11, 1, Jan. 1968, pp. 31-43.

7. Foord, C. A., Wedeven, L. D., Westlake, F. J. and Cameron, A. "Optical elastohydrodynamics," Proc. Inst. Mech. Engrs. (London) 184, part 1, no. 28, 1969-70, pp. 487-503.

8. Westlake, F. J., "An interferometric study of ultra-thin fluid films," Ph.D. Thesis, Imperial College, London University, 1970.

9. Wedeven, L. D., "Optical measurements in elastohydrodynamic rolling contact bearings," Ph.D. Thesis, London University, 1970.

10. Tedder, J. M., "The use of trifluoroacetic anhydride and related compounds in organic synthesis," Chem. Rev., 55, 787 (1955).

11. Parish, R. C., and Stock, L. M., "A method for the esterification of hindered acids," J. Org. Chem., 30, 927 (1965).

12. Baizer, M. M., Anderson, J. D., Wagenknecht, J. H., Ort, M. R., and Petrovich, J. P., "Electrolytic reductive coupling as a synthetic tool," Electrochimica Acta, 1967, Vol. 12, 1377.

13. Baizer, M. M., and Anderson, J. D., "Electrolytic reductive coupling 11. Derivatives of mono-olefinic α,β-unsaturated acids," J. Electrochem. Soc., 111, 223 (1964).

14. Tolansky, S., An Introduction to Interferometry (Longmans, London, 1955).

15. Golder, H. Q., "Apparatus for measuring shear strength of soils," Engineering 153, 3989, 26 June 1942, pp. 501-503.

16. Jefferis, J. A. and Johnson, K. L., "Sliding friction between lubricated rollers," Proc. Instn. Mech. Eng. 182, part 1, no. 14, 1967-8, pp. 281-91.

17. Cheng, H. S., and Sternlicht, B., "A numerical solution for the pressure, temperature, and film thickness between two infinitely long, lubricated rolling and sliding cylinders, under heavy loads," Trans. ASME., J. Basic Eng. D 87, 3, Sept. 1965, pp. 695-707.

18. Kannel, J. W., and Walowit, J. A., "Simplified analysis for tractions between rolling-sliding elastohydrodynamic contacts," Trans. ASME, J. Lubrication Tech. F 93, 1, Jan. 1971, pp. 39-46.

19. Dyson, A., "Frictional traction and lubricant rheology in elastohydrodynamic lubrication," Phil. Trans. Roy. Soc. (London) A266, 1170, 1970, pp. 1-33.

20. Allen, C. M., Townsend, D. P., and Zaretsky, E. V., "Elastohydrodynamic lubrication of a spinning ball in a nonconforming groove," Trans. ASME, J. Lubrication Tech., Jan. 1970, pp. 89-96.

21. Plint, M. A., "Traction in elastohydrodynamic contacts," Proc. Instn. Mech. Eng. 182, part 1, no. 14, 1967-8, pp. 300-306.

22. Jacobson, B., "On the lubrication of heavily loaded spherical surfaces considering surface deformation and solidification of the lubricant," Acta Polytechnica Scandinavica, Mech. Eng. Series no. 54, Royal Swedish Academy of Engineering Sciences, Stockholm, 1970.

23. Dowson, D. and Higginson, G. R., Elasto-Hydrodynamic Lubrication (Pergamon Press, Oxford, 1966).

24. Dyson, A., Naylor, H. and Wilson, A. R., "The measurement of oil film thickness in elastohydrodynamic contacts," Proc. Instn. Mech. Eng. 180 part 3B, Elastohydrodynamic Symposium, paper no. 10, Univ. of Leeds, 1965, pp. 119-134.

25. ten Napel, W. E. and Bosma, R., "Influence of surface roughness on the capacitive measurement of film thickness in elastohydrodynamic contacts," Proc. Inst. Mech. Eng. (London), 185, no. 37, 1970-71, pp. 635-9.

26. Christensen, H., "The oil film in a closing gap," Proc. Roy. Soc. (London) A 266, 1326, 20 March 1962, pp. 312-328.

27. Westlake, F. J. and Cameron, A., "High speed photographic study of lubricated contacts using optical interferometry," J. Photographic Sci. 17, 4, 1969.

28. Wayne-Kerr Monograph No. 1, The Transformer Ratio-Arm Bridge (Wayne-Kerr Ltd., New Malden, Surrey).

29. Smith, A. J., "The thinning of liquid films on metal surfaces," Ph.D. Thesis, Imperial College, London University, 1971.

30. Hardy, W., Collected Works (Cambridge University Press, Cambridge, 1936).

31. Allen, C. M. and Drauglis, E., "Boundary layer lubrication: monolayer or multilayer," Wear 14, 1969, pp. 363-384.

32. Needs, S. J., "Boundary film investigations," Trans. ASME. 62, 4, May 1940, pp. 331-9.

33. Brüninghaus, L., "The electrical conduction of liquid hydrocarbons," Ann. Off. Combust. Liq, 4, 1929, pp. 515-27.

34. Askwith, T. C., Cameron, A., and Crouch, R. F., "Chain length of additives in relation to lubricants in thin film and boundary lubrication," Proc. Roy. Soc. (London) A 291, 1427, 26 April 1966, pp. 500-519.

35. Dowson, D. and Jones, D. A., "An optical-interference method of measurement of time-dependent elastohydrodynamic film profiles," Proc. Inst. Mech. Engrs. (London) 182, part 3G, 1967-68, pp. 49-52.